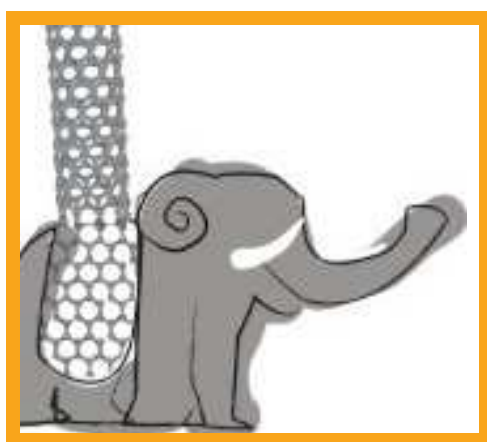


Carbon-Based Low Dimensional Materials

*-Proceedings of the 2nd CARBOMAT Workshop-
Catania (Italy) Dec. 5-7, 2011*



**Edited by
Silvia Scalese & Antonino La Magna**



**Consiglio Nazionale delle Ricerche
Istituto per la Microelettronica e Microsistemi**

Carbon-Based Low Dimensional Materials -Proceedings of the 2nd CARBOMAT Workshop-

Edited by S. Scalese and A. La Magna

© Edizioni CNR 2012

ISBN 978-88-8080-124-5

Printed in Catania (Italy), March 2012

Abstracting and non-profit use of the material is permitted with credit to the source. Statements and opinions expressed in the chapters are these of the individual contributors and not necessarily those of the editors or publisher. No responsibility is accepted for the accuracy of information contained in the published articles. Authors have the right to republish it, in whole or part, in any publication of which they are an author or editor, and to make other personal use of the work.

Conference Chairs

Silvia Scalese
Antonino La Magna

Organizing Committee (CNR-IMM)

Markus Italia
Antonio Marino
Giovanna Leanza
Aldo Spada

Scientific Committee

Giuseppe Angilella (University of Catania)
Giuseppe Compagnini (University of Catania)
Ioannis Deretzis (CNR-IMM)
Filippo Giannazzo (CNR-IMM)
Antonino La Magna (CNR-IMM)
Giovanni Neri (University of Messina)
Silvia Scalese (CNR-IMM)
Viviana Scuderi (CNR-IMM)

CONTACTS:

CARBOMAT 2011

c/o CNR-IMM
Strada VIII, n. 5
Zona Industriale
I-95121 Catania
Italy

Phone: +39 - 095- 5968- 220/235

Fax: +39 - 095- 5968 - 312

Website: <http://carbomat.imm.cnr.it>

Email: carbomat@imm.cnr.it

SPONSORS:



SIGMA-ALDRICH®

The Sponsors are greatly acknowledged for their support.

INTRODUCTION

Over the past several decades there has been an explosive growth in research and development related to nanomaterials and, among them, a huge interest has been devoted to carbon nanostructures. It is remarkable that two Nobel prizes (Chemistry 1996 to R. F. Curl Jr., SH. W. Kroto and R. E. Smalley "for their discovery of fullerenes"; Physics 2010 to A. Geim and K. Novoselov "for groundbreaking experiments regarding the two-dimensional material graphene") have been awarded for researches on these topics.

The strength of carbon nanomaterials lies in the fact that most of their properties can be modified and adjusted, depending on the target application. The morphology, surface chemistry, as well as the physical properties of carbon nanomaterials can be varied by tuning the synthesis procedures, or by suitable post-synthesis treatments. This flexibility in the production processes is also supported by the exceptional properties of the basic (non-functionalized) pristine structures including huge electron mobility, record breaking strengths etc. The mixing of non-conventional properties and nano-manufacturing potentiality makes the carbon nanomaterials a key-ingredient of the current nanoscience.

Although nanomaterials such as fullerenes, graphene or carbon nanotubes (CNTs) are very popular and already available from several suppliers, their controlled synthesis remains a dynamic field of research, and improvements in the selectivity of desired nanomaterials, as well as in the purity and quality are being continuously achieved. The presence of impurities, structural defects and heteroatoms may have remarkable effects on the properties and, hence, on the applications. Almost unlimited possibilities open to researchers coming from multidisciplinary areas (materials science, physics, chemistry and biology) who can contribute, with complementary skills, to “invent” new materials for electronics, transportation, energy production and storage, or medicine.

In this framework, the CARBOMAT Workshop aims to bring together researchers working in the field of nano-sized carbon based materials (nanotubes, fullerenes, linear chains, graphene, etc.) in order to present and discuss state-of-the-art results.

The main topics of the Workshop are: synthesis, functionalization, characterization, theoretical modelling and applications of low-dimensional carbon structures.

For several applications, a key role is played by the interactions between C nano-materials and a suite of elements, chemical groups, metals, antibodies, DNA molecules, enzymes, etc. In this second edition, a special session was focused on the interactions of carbon nanostructures with chemical groups and functional molecules, and to the use of such systems for innovative sensors.

We would like to thank all the invited speakers and the regular participants, for their precious contribution to the high scientific level of the Workshop. Because of their stimulus to the often heated discussions during and after the presentations the workshop was successful. We believe that the proceedings of the CARBOMAT Workshop collected in this volume represent valuable examples of the complexity, interdisciplinarity and unquestionable fascination of the current research on the C based nanoscience.

The Conference Chairs

Silvia Scalese & Antonino La Magna

INDEX

	Page
1. Effect of graphene/substrate interface on the electronic transport properties <i>F. Giannazzo, E. Rimini, V. Raineri</i>	1
2. Raman studies of graphene growth on Ni and Cu by chemical vapor deposition <i>G. Faggio, G. Messina, S. Santangelo, V. Morandi, L. Ortolani, R. Rizzoli, G.P. Veronese</i>	5
3. Spin coupling around a carbon vacancy in graphene <i>M. Casartelli, S. Casolo, G. F. Tantardini, R. Martinazzo</i>	9
4. Cyclotron resonance and renormalization in graphene and its bilayer <i>K. Shizuya</i>	12
5. Transport properties of graphene across strain-induced nonuniform velocity profiles <i>F. M. D. Pellegrino, G. G. N. Angilella, R. Pucci</i>	16
6. First principle study of ballistic thermal conductance of graphene antidot lattices for thermoelectric applications <i>H. Karamitaheri, M. Pourfath, N. Neophytou, M. Pazoki, and H. Kosina</i>	19
Raman monitoring of strain induced effects in mechanically deposited single layer graphene <i>P. Russo, G. Compagnini, C. D'Andrea, O. M. Maragò, P. G. Gucciardi, J. -C. Valmalette</i>	23
7. Carbon nanostructures for gas sensing applications <i>M. Penza</i>	27
8. Synthesis, characterization and sensing properties of electrospun CNTs/polymer/ metal oxides composites <i>P. Frontera, A. Donato, S. Trocino, P. L. Antonucci, G. Neri</i>	33
9. NO ₂ sensor based on ultra-thin titania coating on carbon nanofibers <i>N. Donato, M. Latino, G. Neri, D. Spadaro, C. Marichy, M.-G. Willinger, N. Pinna</i>	37
10. An inkjet deposition system for water-based solutions of MWCNT/PMA for sensing applications <i>N. Donato, D. Aloisio, E. Patti, G. Scolaro, G. Neri, D. Spadaro, S. Trocino, A. Donato, M. Latino</i>	41
11. Liquid phase functionalization of carbon nanotubes: morphology and surface modification <i>C. Milone, E. Piperopoulos, S.H. Abdul Rahim, M. Lanza, S. Santangelo, S. Galvagno</i>	45
12. Single Wall Carbon nanotubes deposited on stainless steel foil as counter electrode for dye sensitized solar cells <i>G. Calogero, O.M. Maragò, P. G. Gucciardi, G. Di Marco</i>	49
13. Nanodiamonds: hints for bio-technical applications <i>S. Orlanducci, E. Tamburri, I. Cianchetta, D. Sordi, M. L. Terranova, D. Passeri, M. Rossi</i>	53
14. Change of mechanical and physical properties of an epoxy resin induced by carbon nanotube presence <i>V. Brancato, A.M. Visco, A. Pistone, M. Fazio, D. Iannazzo, A. Piperno, S. Galvagno</i>	56
15. Experimental and calculated optical properties of polyynes and cumulenes chains prepared by laser ablation in liquids <i>G. Forte, L. D'Urso, E. Fazio, S. Patanè, F. Neri, O. Puglisi, G. Compagnini</i>	60
16. Influence of the microstructure of carbon nanotubes on the catalytic wet air oxidation of <i>p</i> -coumaric acid <i>E. Fazio, E. Piperopoulos, S.H. Abdul Rahim, M. Lanza, S. Santangelo, G. Mondio, F. Neri, C. Milone</i>	64

17. Towards the control of structural properties of CNTs produced by arc discharge in liquid environments <i>S. Scalese, V. Scuderi</i>	68
18. Temperature characterization of the sheet resistance of MWCNTs/PDDAC based sensitive films <i>N. Donato, D. Aloisio, D. Spadaro, M. Latino, A. Giberti, C. Malagù</i>	71
19. Raman optical trapping of carbon nanotubes and graphene <i>M. G. Donato, P. G. Gucciardi, S. Vasi, M. Monaca, R. Sayed, G. Calogero, P.H. Jones, O.M. Maragò</i>	75
20. Synthesis of graphene nanoribbons and other carbon nanostructures <i>F. Cataldo</i>	79
21. Taguchi-optimised production of MWCNT-based nanocomposites by catalytic route <i>S. Santangelo, G. Messina, G. Faggio, E. Piperopoulos, M. Lanza, C. Milone</i>	82
22. Use of the electric fields for the manipulation of MWCNTs <i>V. Scuderi, A. La Magna, A. Pistone, N. Donato, G. Neri, S. Scalese</i>	86
23. Shaping of diamonds in 1-D nanostructures and other strategies for fabrication of low-dimensional diamond-based components <i>M. L. Terranova, V. Guglielmotti, S. Orlanducci, V. Sessa, E. Tamburri, F. Toschi, M. Rossi</i>	90
24. Self-Assembling of Graphitic Nanoplatelets <i>R. Matassa, S. Orlanducci, V. Guglielmotti, D. Sordi, E. Tamburri, M. L. Terranova, D. Passeri, M. Rossi</i>	93
25. Deposition of carbon nanowalls at the electrodes during electrical-field-assisted laser ablation in water <i>M. Sinatra, G.C. Messina, P. Russo, G. Compagnini, O. Puglisi, S. Scalese</i>	97
26. Organic molecules encapsulated in single wall carbon nanotubes – challenges for theoretical modeling <i>M. Kertesz, T. Yumura</i>	100
27. <i>Ab initio</i> predictions of covalent and metallic intercalations of epitaxial graphene systems on SiC substrates <i>I. Deretzis, A. La Magna</i>	104

Appendix 1: Information about the location

Appendix 2: List of Participants

EFFECT OF GRAPHENE/SUBSTRATE INTERFACE ON THE ELECTRONIC TRANSPORT PROPERTIES

F. Giannazzo ^{1*}, E. Rimini ¹, V. Raineri ¹

¹ CNR-IMM, Strada VIII, 5 95121 Catania, Italy

* E-mail: filippo.giannazzo@imm.cnr.it

ABSTRACT

The scattering mechanisms limiting the electronic transport properties have been investigated by measuring two-dimensional maps of the electron mean free path (l) in graphene on substrates with different dielectric permittivities, i.e. SiO₂ ($\kappa_{\text{SiO}_2}=3.9$), 4H-SiC (0001) ($\kappa_{\text{SiC}}=9.7$) and SrTiO₃ (001) ($\kappa_{\text{STO}}=330$). From the analysis of local l versus gate bias curves, nanoscale maps of the densities of charged impurities (N_{CI}) and resonant scattering centres (N_{RS}) have been extracted. A clear correlation between the minima in the l maps and the maxima in the N_{CI} maps is obtained for graphene on SiO₂ and 4H-SiC, indicating charged impurity scattering as the main source of the lateral inhomogeneity of l on low- κ substrates. On the contrary, the l and N_{CI} maps are uncorrelated in graphene on SrTiO₃, while a clear correlation is found between l and N_{RS} maps. This demonstrates a very efficient dielectric screening of charged impurity in graphene on SrTiO₃ and the role of resonant scattering centres as limiting factor for electron mean free path.

1. INTRODUCTION

The excellent transport properties in graphene allowed the observation of several peculiar electronic phenomena and opened the way to challenging device applications [1,2]. Giant carrier mobility ($\mu > 10^5 \text{ cm}^2 \text{ V}^{-1} \text{ s}^{-1}$) and micrometer electron mean free path (l) have been recently reported in graphene under proper experimental conditions, i.e. in suspended ultra-clean membranes [3] or in graphene encapsulated between inert and ultra-flat boron nitride layers [4,5]. However, significantly lower values of l and μ are typically measured under practical conditions, i.e. in graphene devices on common dielectric substrates, at room temperature (RT) and under ambient environment. Literature values of mobility spread over a wide range, depending on the graphene synthesis method, on the substrate, but also on the processes used for graphene device fabrication. The road to electronic device applications of graphene imposes a deep knowledge of the nanoscale mechanisms dominating the charge carrier mobility in graphene supported by a substrate, at room temperature and under atmospheric environment. Since the early transport experiments, the electron scattering mechanisms in graphene have been discussed widely and controversially. Current electronic transport models in graphene suggest only few mechanisms which can explain

the common experimentally observed proportionality between conductivity (σ) and carrier density (n) at low n . Among them, charged impurities scattering [6] and resonant scattering [7] are currently regarded as the most probable candidates to influence the drift mobility and the electron mean free path. The interaction of graphene two-dimensional-electron-gas (2DEG) with surface polar phonons of the substrate has been also indicated as a strong degradation mechanism for graphene electron mean free path [8]. In this work, we used a method based on scanning capacitance microscopy/spectroscopy to obtain 2D maps of the electron mean free path (l) in graphene deposited on substrates with different dielectric permittivities, i.e. SiO₂ ($\kappa_{\text{SiO}_2}=3.9$), 4H-SiC (0001) ($\kappa_{\text{SiC}}=9.7$) and the very-high- κ perovskite strontium titanate, SrTiO₃ (001), briefly STO ($\kappa_{\text{STO}}=330$).

2. EXPERIMENTAL DETAILS

Graphene flakes were obtained by mechanical exfoliation of highly oriented pyrolytic graphite (HOPG) and deposited on (i) 300 nm SiO₂ thermally grown on highly doped Si substrate – G-SiO₂, (ii) 2 μm low doped epitaxially grown SiC layer on highly doped 4H-SiC(0001) – G-SiC, and (iii) 30 μm single-crystal SrTiO₃ (001) – G-STO. Preliminary identification of graphene flakes was done under optical microscope [9,10]. Flakes showing lowest optical contrast were then fully characterized by micro-Raman spectroscopy and by tapping mode Atomic Force Microscopy (t-AFM) to identify single layers of graphene (SLG) [10]. Local Capacitance measurements were carried out at room temperature and under ambient conditions using a Veeco DI3100 AFM with Scanning Capacitance Microscopy (SCM) application module. AFM operated in contact mode using platinum coated doped Si tips. A DC bias ramp was applied to the sample back-gate to sweep the Fermi level in graphene from the hole to the electron branch. For the samples in this study, the back-gate is provided by the Si under SiO₂ (for G-SiO₂), by the SiC substrate under the lowly doped epi-SiC layer (for G-SiC) and by a Ni-Au film under the STO layer (for G-STO). In addition, an AC modulating bias at 100 kHz frequency is superimposed to the DC bias to induce an excess of charges (holes/electrons) from the nanometric tip contact to graphene. This charge in excess diffuses in graphene over an effective area A_{eff} around the tip contact, whose extension depends on the gate bias [11,12,13]. An ultra-high-sensitive ($10^{-21} \text{ F/Hz}^{1/2}$) capacitance sensor is

connected to the tip, and measures the capacitance variations induced by the modulating bias, using a lock-in method. The capacitance measured when the tip is in contact with graphene (C_{gr}) is compared to the capacitance when the tip is in contact with the bare substrate (C_{sub}). In the latter case C_{sub} is the capacitance of a parallel plate capacitor with area A_{tip} , the tip contact area, i.e. $C_{sub}=A_{tip}\kappa_0\kappa_{sub}/t_{sub}$, being κ_0 the vacuum permittivity, κ_{sub} the substrate permittivity and t_{sub} its thickness. Instead, C_{gr} is the capacitance of a parallel plate capacitor with area A_{eff} , i.e. $C_{gr}=A_{eff}\kappa_0\kappa_{sub}/t_{sub}$. Local capacitance-voltage characteristics were measured on regular arrays of dots (tip positions) on graphene. For each position A_{eff} is evaluated as $A_{eff}=A_{tip}C_{gr}/C_{sub}$. It has been recently demonstrated that this effective area is related to the “local” electron mean free path l in graphene as $l=(A_{eff}/\pi)^{1/2}$ [12,13].

3. RESULTS AND DISCUSSION

Fig. 1(a), (b) and (c) show the measured l at two different tip positions on G-SiO₂, G-SiC and G-STO as a function of the gate bias V_g .

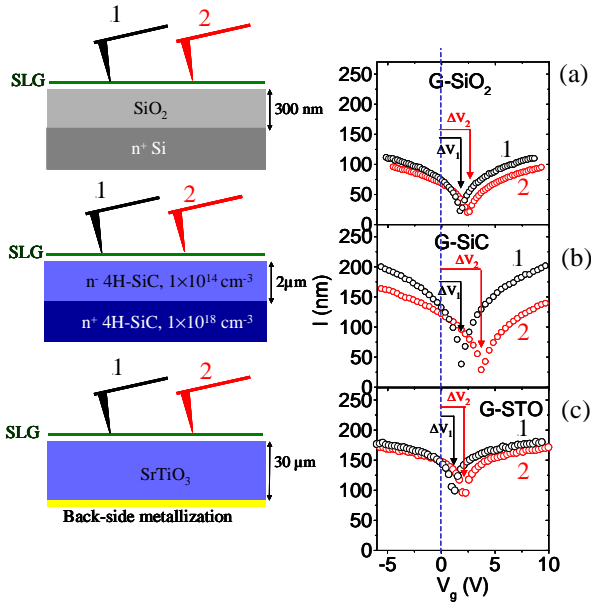


Fig.1 Measured electron mean free path l at two different tip positions on G-SiO₂ (a), G-SiC (b) and G-STO (c) as a function of the gate bias V_g .

Each curve exhibits ambipolar behavior with electron and hole branches and a minimum corresponding to the neutrality point. The position (V_{NP}) of this minimum on the V_g axis is related to a net density of charged impurities (N_{CI}) in the locally probed area, which causes a shift of the neutrality point with respect to $V_g=0$. The small positive shifts observed in the representative curves of Fig.1(a), (b) and (c) indicate the presence of a low density of positive charges on the sample surface, probably associated with water adsorbates. This density clearly changes from point to point on graphene surface.

The local density of charged impurities at each tip position can be extracted from the value of V_{NP} in the l - V_g characteristic, using the relation $N_{CI}=(\kappa_0\kappa_{sub}V_{NP})/(qt_{sub})$, where q is the electron charge.

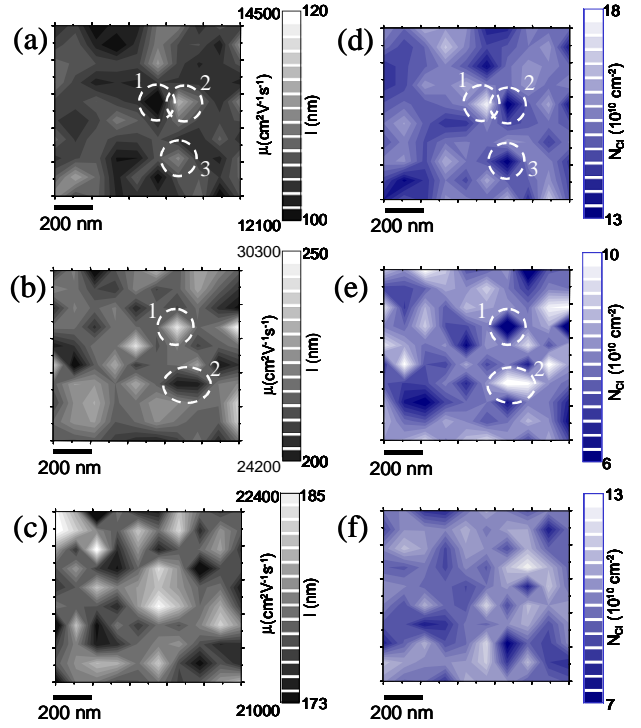


Fig.2 Two-dimensional maps of the local electron mean free path (l) for G-SiO₂ (a), G-SiC (b) and G-STO (c). Maps of the CI density at the same positions on G-SiO₂ (d), G-SiC (e) and G-STO (f).

In Fig.2, two-dimensional maps of the CI density for G-SiO₂ (d), G-SiC (e) and G-STO (f) are reported. Each map was extracted peaking V_{NP} from a set of l - V_g curves collected by scanning of the tip on a regular array of 10×10 positions spaced by 100 nm. For graphene on SiO₂, a CI density ranging from 1.3×10^{11} to 1.8×10^{11} cm⁻² depending on the position is found. For graphene on SiC, N_{CI} ranges from 0.6×10^{11} to 1.0×10^{11} cm⁻². Finally, for graphene on STO, N_{CI} in the range 0.7×10^{11} – 1.3×10^{11} cm⁻² is found. The maps of the local electron mean free path (l) measured on the same arrays are also shown in Fig.2(a), (b) and (c). For consistency in the comparison between measurements of l in graphene on substrates with different thickness and permittivities, l values at the same electron density of $n=5\times 10^{11}$ cm⁻² were reported in the three maps.

In graphene on SiO₂ the electron mean free path exhibits lateral variations from ~100 to ~120 nm, in graphene on SiC from ~200 to ~250 nm, whereas the spread in graphene on STO is much lower, from ~173 nm to ~185 nm. Using the relation $\mu=q/\hbar(\pi n)^{-1/2}$ between carrier mobility μ and electron mean free path l at a carrier density n , these spreads correspond to “local” variations of the mobility from ~12100 to ~14500 cm²V⁻¹s⁻¹ for G-SiO₂, from ~24200 to ~30300 cm²V⁻¹s⁻¹ for G-SiC, and from ~21000 to 22400 cm²V⁻¹s⁻¹ for G-STO.

A clear correlation between the l maps and the corresponding N_{CI} maps is found for G-SiO₂ and G-SiC, with the maxima of the l distribution located at the same positions of the minima in the N_{CI} distribution. To guide the eye, the positions of representative maxima and minima in the l maps are indicated in Fig. 2(a) and (b) and the corresponding positions in the N_{CI} maps are also identified in Fig. 2(d), (e). Instead, no clear correlation can be observed in the case of G-STO. This suggests that CI have a strong effect on the electron mean free path in graphene deposited on substrates with lower dielectric permittivity, whereas they are efficiently screened in graphene on very high κ dielectrics. The lower spread in the l values for G-STO is consistent with this scenario. Nevertheless, the electron mean free path in graphene on STO results to be lower than in graphene on SiC and only ~ 1.6 times than in graphene on SiO₂. This can only be explained considering additional scattering sources limiting l together with CI. These sources become the dominant scattering factors whenever long range Coulomb potential from CI is efficiently screened. As recently reported by Ni et al. [14], resonant scatterers can play this role.

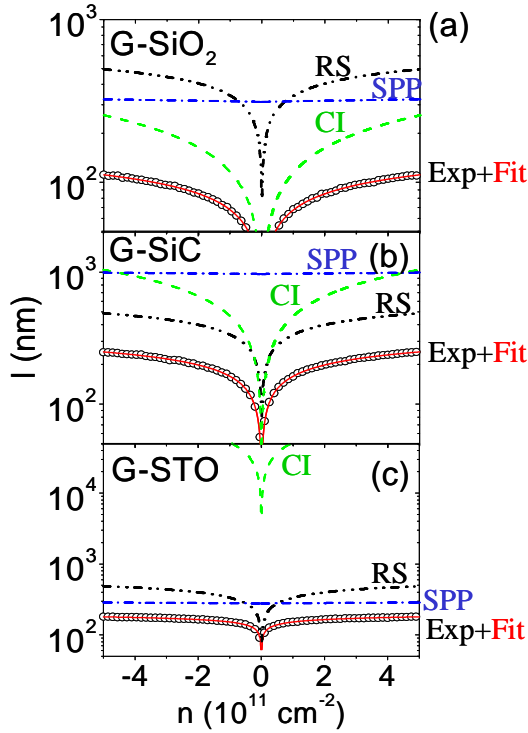


Fig.3 Electron mean free path l vs the electron density (open circles) at a fixed position in G-SiO₂ (a), G-SiC (b) and G-STO (b). Circles represent the experimental data, the solid lines represent the fit. The RS, CI and SPP contributions to the electron mean free path are also reported.

In the following, the density of resonant scatterers N_{RS} at different positions will be extracted by fitting the behavior of l vs the carrier density n for each curve in the array. In Fig.3 open circles represent the measured l vs the electron density at a fixed position in G-SiO₂ (a), G-SiC (b) and G-STO (b), whereas the solid lines represent the

fit. Three contributions to the electron mean free path have been considered, i.e. RS, CI and SPP, i.e.

$$l^{-1} = l_{RS}^{-1} + l_{CI}^{-1} + l_{SPP}^{-1} \quad (1)$$

The resonant scatterers term l_{RS} is expressed as [15],

$$l_{RS}(n) = \frac{\sqrt{\pi n}}{\pi^2 N_{RS}} \left[\ln \left(\sqrt{\pi n} R_0 \right) \right]^2 \quad (2)$$

where N_{RS} is the RS density and R_0 the effective radius of RS, which is commonly assumed as $R_0 \approx 2a$, being $a \approx 0.14$ nm the bond length in graphene [16].

The charged-impurity term l_{CI} is expressed as [15],

$$l_{CI}(n) = \frac{16\kappa_0^2 \kappa^2 \hbar^2 v_F^2}{Z^2 q^4 N_{CI}} \left(1 + \frac{q^2}{\pi \hbar v_F \kappa_0 \kappa} \right)^2 \sqrt{\pi n} \quad (3)$$

where \hbar is the Planck's reduced constant, v_F is the electron Fermi velocity in graphene ($=1 \times 10^6$ m/s), Z is the net charge of the impurity (assumed to be 1), and κ is the average between the permittivity of the substrate κ_{sub} and the vacuum permittivity ($\kappa_{vac}=1$).

Finally, the electron mean free path l_{SPP} associated to scattering by a surface polar phonon mode with energy E_i is expressed as [17,18]

$$l_{SPP,i} = \sqrt{\frac{\beta}{E_i}} \frac{\hbar v_F}{q^2} \frac{4\pi\kappa_0}{F_i^2} \frac{q v_F}{N_{SPP,i}} \frac{\exp(k_0 z_0)}{q} \frac{\hbar \sqrt{\pi}}{q} \quad (4)$$

where $k_0 \approx [2E_i/(\hbar v_F)]^2 + \chi n]^{1/2}$, $\chi \approx 10.5$, $\beta \approx 0.153 \times 10^{-4}$ eV, and $z_0 \approx 0.35$ nm the separation between the polar substrate and graphene. $N_{SPP,i}$ is the SPP phonon occupation number, given by the Bose-Einstein statistics. F_i^2 is the Fröhlich coupling constant which gives the magnitude of the polarization field and depends on the substrate permittivity.

	SiO ₂	STO	SiC
κ_{sub}	3.9	330	9.7
E_1 (meV)	58.9	57	
E_2 (meV)	156.4	92	116.0
F_1^2 (meV)	0.237	0.67	
F_2^2 (meV)	1.612	1.082	0.734

Table I Dielectric permittivity, surface polar phonons energy and Fröhlich constants of SiO₂, STO and SiC

The only fitting parameter used in Fig.3(a), (b), (c) is the density of resonant scatterers N_{RS} , whereas the literature values for the surface polar phonons modes and for the Fröhlich constants of the three substrates are reported in Table 1. In addition to the fit on the experimental data (red line), the individual contribution l_{RS} , l_{CI} and l_{SPP} are also reported in Fig.3(a), (b) and (c).

The same fitting procedure has been repeated for all the 100 l - n curves in the array. The SPP scattering has been assumed independent on the surface position, whereas N_{RS} changed for the different curves. The obtained maps

of N_{RS} values are reported in Fig.4(d), (e) and (f), and are compared with the electron mean free path maps in Fig.4(a), (b) and (c). It is worth noting a clear correlation between the N_{RS} map (Fig.4(f)) and the electron mean free path map (Fig.4(c)) in graphene on STO, whereas no correlation can be found between the N_{RS} maps and the l maps in graphene on SiO_2 and SiC.

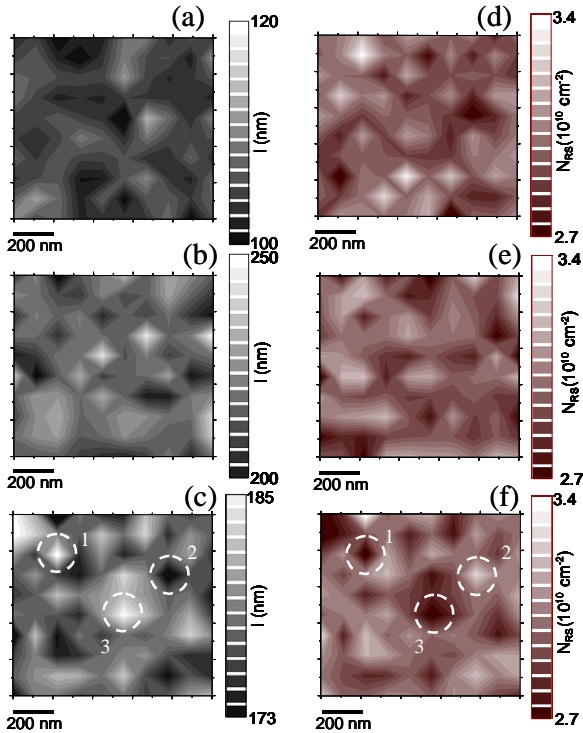


Fig.4 Two-dimensional maps of the local electron mean free path (l) for G- SiO_2 (a), G-SiC (b) and G-STO (c). Maps of the RS density at the same positions on G- SiO_2 (d), G-SiC (e) and G-STO (f).

4. CONCLUSION

In conclusion, we evaluated the local electron mean free path (l) in graphene demonstrating that maps with a high resolution can be achieved. Such maps revealed themselves as a groundbreaking instrument to comprehend the scattering mechanisms limiting the transport properties in graphene at room temperature. The control on such properties is a key topic in the road to applications. By applying the described method we could obtain information on the different contributions to the scattering comparing graphene by mechanical exfoliation of HOPG deposited on different dielectrics such as SiO_2 (G- SiO_2), 4H-SiC(0001) (G-SiC) and strontium titanate (G-STO). Both the adopted deposition method and local electrical measurements do not introduce damage in exfoliated graphene. Laterally inhomogeneous densities of CI and RS have been imaged. The RS distribution exhibits an average value $\sim 3 \times 10^{10} \text{ cm}^{-2}$ independently on the substrate. A clear correlation between the minima in the l map and the maxima in the N_{CI} map is obtained for graphene on SiO_2 and 4H-SiC, indicating that CI are the main source of the lateral inhomogeneity of l in graphene

on low- κ substrates. On the contrary, the l and N_{CI} map are uncorrelated in graphene on STO, while a clear correlation is found between l and N_{RS} map. This demonstrates the very efficient dielectric screening of CI in graphene on high- κ STO and the role of RS as limiting factor for electron mean free path.

5. ACKNOWLEDGEMENTS

The authors want to acknowledge S. Di Franco and N. Piluso from CNR-IMM, Catania for the assistance in sample preparation and in Raman analyses, respectively. This publication has been supported, in part, by the European Science Foundation (ESF) under the EUROCORES program EuroGRAPHENE, within the GRAPHIC-RF coordinated project.

6. REFERENCES

- [1] A.H. Castro Neto, F. Guinea, N.M.R. Peres, K.S. Novoselov, A.K. Geim, *Rev. Mod. Phys.* **81**, 109–162 (2009).
- [2] A.K. Geim, *Science* **324**, 1530–1534 (2009).
- [3] K. I. Bolotin, K. J. Sikes, J. H. Hone, L. Stormer, P. Kim, *Phys. Rev. Lett.* **101**, 096802 (2008).
- [4] C.R. Dean, A.F. Young, I. Meric, C. Lee, L. Wang, S. Sorgenfrei, K. Watanabe, T. Taniguchi, P. Kim, K. L. Shepard, J. Hone, *Nature Nanotechnology* **5**, 722–726 (2010).
- [5] A.S. Mayorov, R.V. Gorbachev, S.V. Morozov, L. Britnell, R. Jalil, L.A. Ponomarenko, P. Blake, K.S. Novoselov, K. Watanabe, T. Taniguchi, A. K. Geim, *Nano Lett.* **2011**, 2396–2399 (2011).
- [6] T. Ando, *J. Phy. Soc. Jpn.* **75**, 074716 (2006).
- [7] N.M.R. Peres, F. Guinea, A.H. Castro Neto, *Phys. Rev. B* **73**, 125411 (2006).
- [8] S. Fratini, F. Guinea, *Phys. Rev. B.* **77**, 195415 (2008).
- [9] S. Sonde, F. Giannazzo, V. Raineri, E. Rimini, *J. Vac. Sci. Technol. B.* **27**, 868–873 (2009).
- [10] F. Giannazzo, S. Sonde, V. Raineri, G. Patanè, G. Compagnini, F. Aliotta, R. Ponterio, E. Rimini, *Phys. Status Solidi C.* **7**, 1251–1255 (2010).
- [11] F. Giannazzo, S. Sonde, V. Raineri, E. Rimini, *Nano Lett.* **9**, 23–29 (2009).
- [12] F. Giannazzo, S. Sonde, V. Raineri, and E. Rimini, *Appl. Phys. Lett.* **95**, 263109 (2009).
- [13] F. Giannazzo, S. Sonde, R. Lo Nigro, E. Rimini, V. Raineri, *Nano Lett.* **11**, 4612–4618 (2011).
- [14] Z.H. Ni, L.A. Ponomarenko, R.R. Nair, R. Yang, S. Anissimova, I.V. Grigorieva, F. Schedin, P. Blake, Z.X. Shen, E.H. Hill, K.S. Novoselov, A.K. Geim, *Nano Lett.* **10**, 3868–3872 (2010).
- [15] T. Stauber, N. M. R. Peres, F. Guinea, *Phys. Rev. B.* **76**, 205423 (2007).
- [16] J.H. Chen, W.G. Cullen, C. Jang, M.S. Fuhrer, E.D. Williams, *Phys. Rev. Lett.* **102**, 236805 (2009)
- [17] V. Perebeinos, P. Avouris, *Phys. Rev. B.* **81**, 195442 (2010).
- [18] S. Sonde, F. Giannazzo, C. Vecchio, R. Yakimova, E. Rimini, V. Raineri, *Appl. Phys. Lett.* **97**, 132101 (2010)

RAMAN STUDIES OF GRAPHENE GROWTH ON NI AND CU BY CHEMICAL VAPOR DEPOSITION

G.Faggio^{1*}, G. Messina¹, S. Santangelo¹, V. Morandi², L. Ortolani², R. Rizzoli², G.P. Veronese²

¹ *Dept. of Mechanics and Materials, University "Mediterranea" of Reggio Calabria, Italy*

² *Nat. Res. Council - Inst. of Microelectronics & Microsystems, Bologna, Italy*

*E-mail: gfaggio@unirc.it

ABSTRACT

Graphene has attracted a lot of interest for fundamental studies as well as for potential applications. Various techniques have been developed to produce graphene and recently the growth of large area graphene by Catalytic Chemical Vapor Deposition (C-CVD) has occupied a relevant role. In this work, Raman spectroscopy and Scanning Electron Microscopy (SEM) measurements are carried out on graphene films grown on thin Ni and Cu catalyst films by CVD at atmospheric pressure. The complementary Raman and SEM characterization shows that films grown on Ni are multilayers, while very thin graphene flakes (from 1- to 3-layer) are grown on Cu.

1. INTRODUCTION

Graphene, single sheet of carbon atoms arranged in hexagonal structure, has attracted great interest for its potential applications in a wide variety of fields.

The most simple method for the production of graphene is mechanical exfoliation of graphite, but this method can only produce small size samples of the order of a few tens of microns and is not scalable [1].

Recently, graphene growth by Catalytic Chemical Vapor Deposition (C-CVD) on metal substrates has received great attention since large-area films with high spatial uniformity can be easily grown and transferred to other substrates [2]. Most literature currently focuses on graphene synthesis using Cu foils as substrate, whereas less attention has been dedicated on syntheses on thin catalyst films deposited on substrates. In particular, employment of Si-based substrates allows easier integration in Si-based technology processes, and mainly in the fabrication of Si-graphene hybrid devices, such as MEMS. For example, a pre-patterning of the metal substrate can produce graphene patterns of well-defined geometries at controlled locations [3].

For electronic applications it is imperative to grow large single crystals of graphene with low defectiveness. This requires an accurate optimization of the growth parameters. In this context Raman spectroscopy has been extensively used to evaluate the structural properties of graphene [4,5]. The main features of the Raman spectrum of graphene are the G-peak at $\sim 1580 \text{ cm}^{-1}$ due to the in-plane bond-stretching of all pairs of sp^2 -carbon atoms in both rings and chains, the D-peak at $\sim 1350 \text{ cm}^{-1}$ due to a

breathing mode of six-atom rings, and the 2D-peak at $\sim 2700 \text{ cm}^{-1}$, that is the second order of the D-peak. The D-peak requires disorder or defects for its activation, while 2D-peak is always present, even when no D-peak is present. The shape, linewidth and position of 2D-peak are commonly used to evaluate the number of graphene layers [4]. By increasing the number of layers ($n \geq 2$) the 2D-peak becomes much broader and up-shifted with respect to single-layer (1L) graphene. In CVD graphene, the difference in the lineshape of the 2D-peak between 1L and few layer graphene could not so sharp as in exfoliated graphene, due to the lower electronic coupling between layers with not-ordered stacking. A narrow lorentzian line ($\sim 30\text{-}40 \text{ cm}^{-1}$) can be used to fit the 2D-peak of both 1L and bilayer (2L) CVD graphene [3]. In unintentionally doped graphene samples, the G to 2D intensity ratio (I_G/I_{2D}) can be used as a qualitative parameter to evidence the presence of very few sheets of graphene [3].

In this work, we report on the growth of graphene films on Ni and Cu thin films deposited on SiO_2/Si substrates by CVD from a mixture of methane and hydrogen. After growth, graphene films were transferred to SiO_2/Si substrates and analyzed by Raman spectroscopy, Scanning Electron Microscopy (SEM) and Transmission Electron Microscopy (TEM). The complementary Raman and TEM characterization shows that graphene multilayer films are obtained on Ni films, while very thin graphene flakes from 1L to 3-layers (3L) are obtained on Cu films.

2. EXPERIMENTAL

Graphene membranes have been grown by CVD in a hot-wall furnace, resistively heated up to 1000°C . As substrates, Ni (700 nm thick) and Cu (300 nm thick) thin films have been e-beam evaporated on SiO_2 (250 nm)/Si substrates. Different methane (CH_4) fractions, ranging from 0.3% to 100%, have been used for the graphene growth, using hydrogen and/or argon as a reducing and carrier gases. Processes have been performed at atmospheric pressure. The growth stage lasted 5 minutes and the process was then terminated by means of two different protocols. In the first one, samples have been rapidly cooled down by a fast extraction of 1-2 minutes to a furnace zone where the temperature was $300\text{-}350^\circ\text{C}$. In the second protocol, samples have been freely cooled down to 600°C using the same gas mixture of the

deposition step and then further cooled down below 400°C in H₂/Ar mixture. Final cooling step to room temperature was performed in Ar for both protocols. Then graphene membranes have been transferred on functional substrates for subsequent electrical, morphological and structural characterization by using a standard protocol. A 300 nm thick polymethyl-methacrylate (PMMA) layer has been deposited on the samples and then FeCl₃ (or a FeCl₃/HCl mixture) was used for metal etching and membrane release. Scooping of the PMMA/graphene layer was performed with SiO₂/Si substrates or C-lacey grids for TEM analysis. PMMA supporting layer was then removed by means of acetone vapour.

Transferred membranes have been characterized by means of field emission Scanning Electron Microscopy (FE-SEM, LEO 1530), and by high-resolution TEM (FEI-TECNAI F20 operating at 120 keV).

The Raman scattering measurements have been carried out at room temperature with an Instrument S.A. Ramanor U1000 double monochromator, equipped with a microscope Olympus BX40 for micro-Raman sampling and with an electrically cooled Hamamatsu R943-02 photomultiplier for photon-counting detection. The 514.5 nm (2.41 eV) line of an Ar⁺ ion laser (Coherent Innova 70) has been used to excite Raman scattering. Using a X100 objective, the laser beam was focused to a diameter of approximately 1 μm. Care has been taken to minimize heating or damage of the sample by choosing low laser power (below 1 mW at its surface).

3. RESULTS AND DISCUSSION

Figure 1 shows SEM image of graphene grown on Ni at low CH₄ concentration (0.35%), after the transfer onto SiO₂/Si substrate. The transferred film appears continuous and different contrast regions indicate variation in the film thickness. The image shows the formation of graphene wrinkles (white lines in Fig.1). The wrinkles are attributed to the different thermal expansion coefficient between graphene and the underlying metal substrate [2].

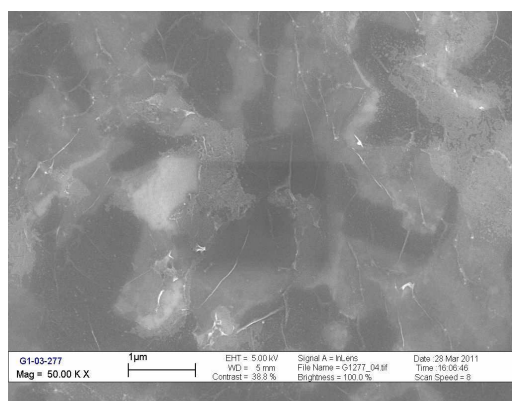


Figure 1. SEM image of the graphene sample grown on Ni thin film at low (0.35%) CH₄ concentration, after the transfer onto SiO₂/Si substrate.

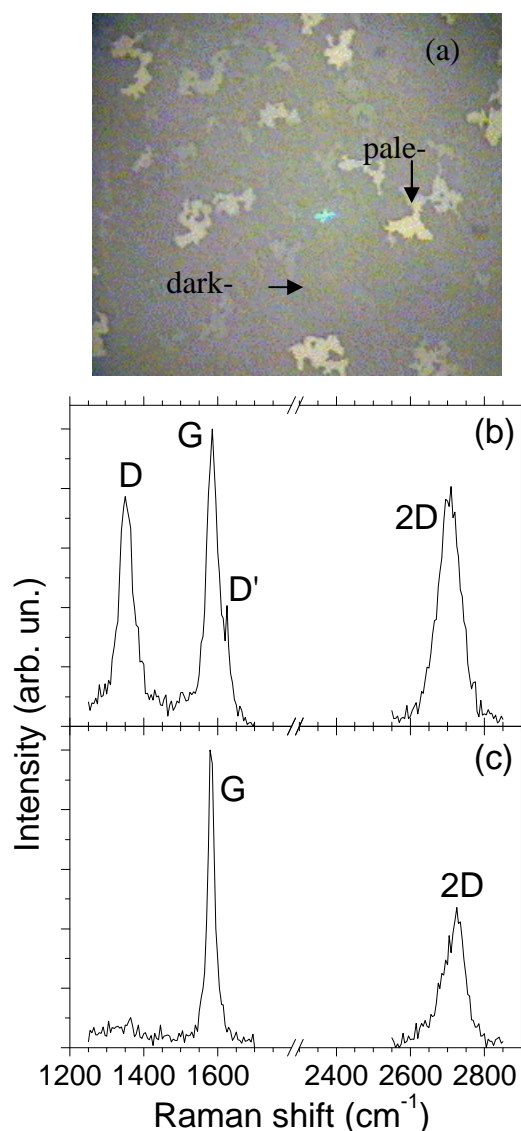


Figure 2. Optical image and Raman spectra of graphene grown on Ni at low (0.35%) CH₄ concentration ((b) dark-grey zone; (c) pale-grey zone).

Raman spectroscopy provides a quick structural characterization of the graphene films. Figure 2 shows optical image and Raman spectra of the transferred graphene film grown on Ni at low CH₄ concentration (0.35%). As can be seen, the optical image (Fig.2a) shows different contrast zones that we indicate as dark-grey zone and pale-grey zone. The Raman spectrum of the dark-grey zone (Fig. 2b) shows a G-peak centered at ~ 1585 cm⁻¹ with a full width at half maximum (FWHM) of ~ 37 cm⁻¹ and a 2D-band centered at ~ 2700 cm⁻¹ with a FWHM of ~ 66 cm⁻¹. In addition, D (~ 1350 cm⁻¹) and D' (~ 1620 cm⁻¹) peaks are also observed, indicating the presence of defects in graphene. The pale-grey zone of the same sample shows (Fig. 2c) the absence of D and D' peaks, a narrow G-peak (FWHM~21cm⁻¹) and a 2D-band similar in shape to that of graphite. Moving from dark-grey to pale-grey zone the I_G/I_{2D} intensity ratio undergoes an increment from 1.2 to 2.6 respectively. These results indicate that the dark-grey zones are graphene multilayers with high structural disorder, while the pale-grey zones

are graphene multilayers with a very low density of defects.

Graphene samples grown on Ni at higher methane concentrations show a greater thickness and lack of homogeneity.

It has been proposed that CVD growth of graphene on Ni is due to a C segregation and precipitation process and that fast cooling rate in conjunction with thin films are needed to suppress the formation of multiple graphene layers [6]. However, to date it seems very difficult to grow uniform graphene films on Ni due to the polycrystalline nature of the catalyst films and the preferential precipitation of C at the grain boundaries [3]. Different treatments will be investigated in order to increase Ni grain size and then graphene uniformity.

By using a metal catalyst with low C solubility as Cu, it is possible to improve the quality of graphene films. CVD growth of graphene on Cu occurs by a surface adsorption process and so large-area graphene films with uniform thickness can be obtained [6].

As concern graphene samples grown on Cu films, SEM analysis shows that, at high CH₄ concentration (20%), the transferred films are not continuous and are not homogeneous in thickness. Moreover, Raman analysis shows the presence of nano-crystalline graphite with high structural disorder. These results clearly show that graphene synthesis on Cu by CVD at atmospheric pressure [7] and high CH₄ concentrations is not a self-limiting process, unlike low pressure synthesis process [6].

Figure 3 shows SEM image of graphene grown on Cu at low (0.35%) CH₄ concentration after the transfer onto SiO₂/Si substrate. The transferred film is not continuous and the graphene domains are small-sized (~ 1 μm), comparable to the diameter of the laser beam used in the Raman measurements.

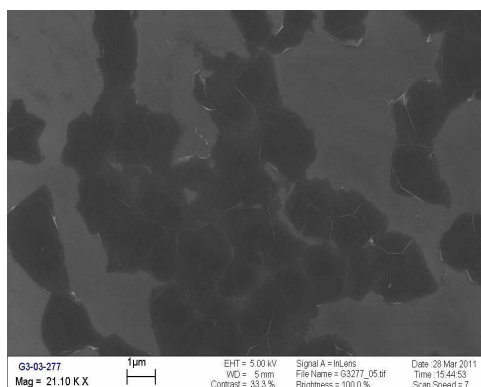


Figure 3. SEM image of the graphene sample grown on Cu thin film at low CH₄ concentration (0.35%), after the transfer onto SiO₂/Si substrate

The Raman analysis has been performed on both the center of the sample and its periphery. At the center of the sample, the Raman spectrum (Fig.4) consists of a narrow G-peak (FWHM~20cm⁻¹) and of a large Lorentzian 2D-band (FWHM~56cm⁻¹). A I_G/I_{2D} ~ 1.8 value is measured. The Raman analysis results indicate that the probed domains are graphene multilayers.

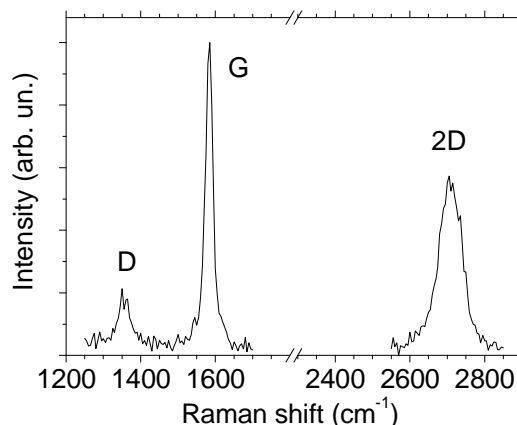


Figure 4. Raman spectrum of graphene grown on Cu at low (0.35%) CH₄ concentration (center of the sample).

At the periphery of the sample, we observe a narrowing of the 2D-band (FWHM~49cm⁻¹) and a lowering of I_G/I_{2D} ratio down to 1.1 (Fig. 5a) and 0.9 (Fig.5b) value for two different locations. Raman spectra with these characteristics are commonly associated to 1L, 2L and 3L CVD graphene[3]. The low (Fig.5a) or narrow (Fig.5b) D peak is not due to the presence of a large amount of structural defects [8], but it is probably due to the edges of small-sized flakes [9] or to misalignment of adjacent domains.

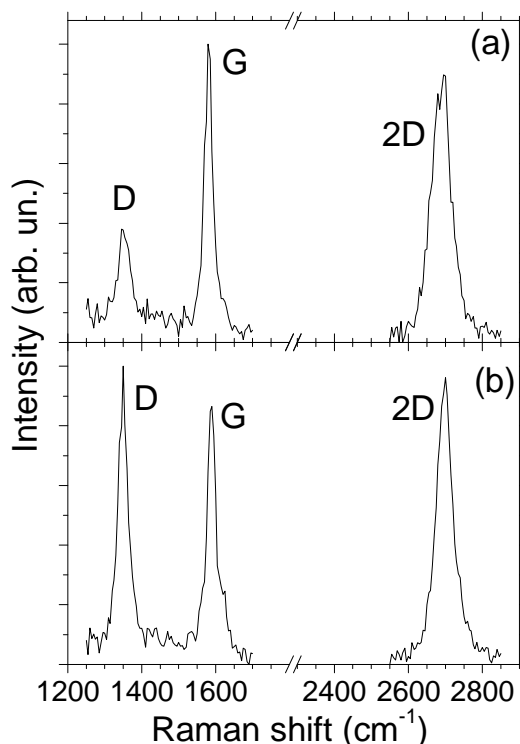


Figure 5. Raman spectra of graphene grown on Cu thin films at low CH₄ concentration (0.35%) taken at two different locations in the periphery of the sample.

Figure 6 shows TEM images taken on the graphene film grown on Cu thin film at low methane concentration (0.35%) after transfer on a TEM grid. A careful analysis

of the folded edges of the graphene flake shows that the analyzed sheet has from 1 to 3 layers, in accordance with the Raman results.

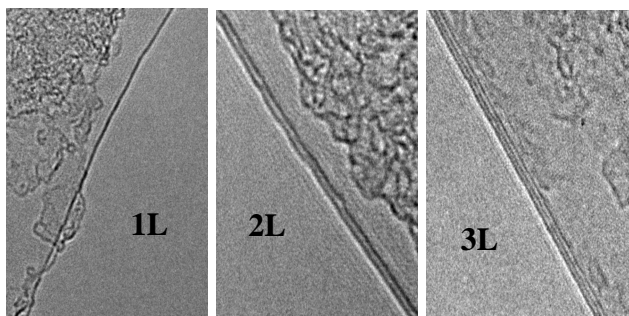


Figure 6. TEM images of graphene films grown on Cu at low CH_4 concentration. The dark fringes, 1 on the left, 2 on the center and 3 on the right, indicate that the analyzed flakes are 1L, 2L and 3L graphene.

4. CONCLUSIONS

In this work, we have reported preliminary results of CVD growth of graphene on Ni and Cu thin films at atmospheric pressure.

We have evidenced that in CVD graphene the differences in the lineshape of the 2D-peak between single-layer and bilayer could not be so sharp as in exfoliated graphene, due to the lower electronic coupling between layers with not-ordered stacking. A narrow lorentzian line ($\sim 30\text{cm}^{-1}$) can be used to fit the 2D-peak of a CVD-bilayer.

A I_G/I_{2D} intensity ratio less than unit is commonly found in the literature in case of 1L and 2L CVD graphene. So, without any claim to exactly count the number of layers, the I_G/I_{2D} ratio can be used to evidence the presence of very few layer graphene.

As concern the results of CVD growth on Cu at atmospheric pressure, Raman spectroscopy has evidenced the growth of multilayer graphene even at low methane concentrations, confirming that, the CVD growth on Cu at atmospheric pressure is not a self-limiting process, unlike the low-pressure process.

The use of low CH_4 concentration goes in the right direction to grow few layer graphene. In the next future we plan to optimize the growth parameters to obtain continuous few layers films at atmospheric pressure.

REFERENCES

- [1] K.S. Novoselov, A.K. Geim, S.V. Morozov, D. Jiang, Y. Zhang, S.V. Dubonos, I.V. Grigorieva, A.A. Firsov, *Science* **306**, 666 (2004)
- [2] X. Li, W. Cai, Jinho An, S. Kim, J. Nah, D. Yang, R. Piner, A. Velamakanni, I. Jung, E. Tutuc, S. K. Banerjee, L. Colombo, R.s. Ruoff, *Science* **324**, 1312 (2009)
- [3] A. Reina, X. Jia, J. Ho, D. Nezich, H. Son, V. Bulovic, M. S. Dresselhaus and J. Kong, *Nano. Lett.* **9**, 30 (2009)
- [4] A.C. Ferrari, J. C. Meyer, V. Scardaci, C. Casiraghi, M. Lazzeri, F. Mauri, S. Piscanec, D. Jiang, K. S. Novoselov, S. Roth and A. K. Geim, *Phys. Rev. Lett.* **97**, 187401 (2006)

- [5] L.M. Malard, M. A. Pimenta, G. Dresselhaus, M. S. Dresselhaus, *Phys. Reports* **473**, 51 (2009)
- [6] X. Li, W. Cai, L. Colombo and R. S. Ruoff, *Nano Lett.* **9** 4268 (2009)
- [7] S. Bhaviripudi, X. Jia, M. S. Dresselhaus and J. Kong, *Nano Lett.* **10** 4128 (2010)
- [8] A.C. Ferrari and J. Robertson, *Phys. Rev. B* **61** 14095 (2000)
- [9] C. Casiraghi, A. Hartschuh, H. Qian, S. Piscanec, C. Georgi, A. Fasoli, K. S. Novoselov, D. M. Basko and A. C. Ferrari, *Nano. Lett.* **9**, 1433 (2009)

SPIN COUPLING AROUND A CARBON VACANCY IN GRAPHENE

M. Casartelli^{1*}, S. Casolo¹, G. F. Tantardini^{1,2}, R. Martinazzo^{1,2**}¹ *Dipartimento di Chimica Fisica ed Elettrochimica, Università degli Studi di Milano, via Golgi 19, 20133 Milano, Italy*² *Istituto di Scienze e Tecnologie Molecolari, CNR, via Golgi 19, 20133 Milano, Italy*

* E-mail: marina.casartelli@unimi.it

** E-mail: rocco.martinazzo@unimi.it

ABSTRACT

Recent years have witnessed an ever growing interest in true two-dimensional materials and, in particular, in graphene. Beside the extraordinary optical, mechanical and electric properties, the latter acquires interesting magnetic properties in the presence of lattice defects, that may be used for designing and fabricating logic, spintronic and magnetic storage devices. Similarly to covalently bound adatoms, each carbon atom vacancy creates a midgap state as a consequence of the removal of a p_z orbital from the π - π^* electronic systems. However, a vacancy also introduces low energy states related to the three dangling bonds left in the σ network. The question then arises of how the unpaired electrons couple to each other around the defect. Here, we address this problem by exploring the energy landscape of the lowest energy states with the help of *first-principles* electronic structure calculations, for periodic and cluster models. We show that the ground-state can be mechanically switched between a high-spin, stable configuration and a low-spin, bi-stable configuration, provided spin conversion is allowed by the switcher, *e.g.* an STM tip.

1. INTRODUCTION

Graphene, thanks to its extraordinary electronic and mechanical properties, is a potential candidate for a number of applications. Being one-atom thick, it is extremely sensitive to the presence of adsorbed atoms and molecules and, more generally, to defects such as vacancies, holes and/or substitutional dopants. This property, apart from being directly usable in molecular sensor devices, can also be employed to tune graphene electric and magnetic transport properties.

Among defects, lattice vacancies play a special role, which is rather unique in this context. They can be easily produced by irradiating graphene (or graphite) with highly energetic particles (either heavy ions or electrons) which are able to overcome the ~ 20 eV threshold for the C atom displacement. Similarly to adsorbed species which form covalent bonds with C atom sites, they perturb the π electron systems by creating resonant scattering centers for the conduction electrons [1]. Differently from other defects, they bring states from the σ band right at the Fermi level, where coupling may

occur with the π states, and possibly gives rise to a net magnetic moment [2]. We investigate here this issue with the aim of understanding the irradiation-induced magnetism experimentally found in carbon based materials, and uncovering potentially interesting magnetic structures for nanoscale applications.

2. METHODS

We have studied the formation of a carbon vacancy in a single layer graphene with the help of *first principles* calculations. Calculations were performed using Periodic Density Functional Theory (DFT) with the projector-augmented wave (PAW) method in the frozen core approximation, as implemented in the Vienna *ab initio* simulation package suite (VASP) [3]-[8]. The PBE [9][10] functional within the generalized gradient approximation was adopted, within the spin-unrestricted (polarized) framework. Different graphene supercells were considered (from 2×2 to 10×10) and the 6×6 was found large enough, yet computationally manageable, for the present purposes. The energy cutoff was set to 500 eV, and a $6\times 6\times 1$ k-point mesh was chosen in a way to include all the special points in the Brillouin zone. In addition, we performed wavefunction and DFT calculations on a relatively large carbon cluster with hydrogen terminated edges (Polycyclic Aromatic Hydrocarbon); the size and the shape of the cluster were selected with the help of Tight-Binding (TB) calculations in such a way to prevent the formation of edge localized states which could interfere with defect-induced states at the Fermi level. Full and restricted geometry optimizations on this cluster were performed at the DFT-B3LYP level of theory, and single point calculations were performed at the restricted- and unrestricted-Hartree-Fock levels (for both closed and open-shell situations), as well as at the more accurate multi-configuration Self-Consistent Field level known as Complete Active Space SCF (CASSCF). The latter are still underway, and a detailed analysis of their results will be presented in a forthcoming publication.

3. RESULTS AND DISCUSSION

Upon removal of a carbon atom from a perfect graphene lattice a three-fold (D_{3h}) structure is obtained, with three σ

dangling bonds on the graphene layer and a “hole” in the π electronic system. The latter is known to give rise to a semi-delocalized state at the Fermi level -appearing as a sharp peak in the (local) density of state (DOS) in the neighborhood of the vacancy [2][11]- which slowly decays away from the defect and effectively resides on one of the two graphene sublattice only [1]. Indeed, such state arises from the presence of the (approximate) electron-hole symmetry and the creation of a sublattice imbalance upon vacancy formation, see e.g. [1].

In general, sublattice imbalance governs the spin-coupling in the (bipartite or “alternant”) π system, as nicely shown by Lieb [12], who proved that in the ground-electronic state any bipartite system has a net spin S given by half the sublattice imbalance (a sort of Hund’s rule for imbalanced-induced midgap states). This result, however, is of little use when considering coupling (interaction) with σ electrons, as we do in the following.

In the ideal, threefold geometry, the three σ dangling bonds, *i.e.* at the Fermi level, span the A_1', E' irreducible representations of the D_{3h} group, and hybridize, forming a molecular state of lower energy (a_1'), and leaving a singly occupied, doubly degenerate state (e'). One further singly occupied state is the π midgap state mentioned above, which is of A_2' symmetry (a_2'). This gives rise to an overall doubly degenerate electronic state $^{1,3}E'$ which undergoes a Jahn-Teller distortion confirmed by the DFT calculations (see below). Further low-lying electronic states arise from $\pi \rightarrow \sigma$ ($\{..e^2\}$ configurations) or $\sigma \rightarrow \pi$ electron transfer ($\{..a^2\}$ configuration), but only the $^1E'$ state of the first is doubly-degenerate and could give the observed distortion. Structural optimization with a spin-polarized Kohn-Sham determinant give substantial lattice reconstruction for any supercell considered, in agreement with previous results [2][13], though to different extent depending on the supercell size. For reasonably sized supercells, two of the undercoordinated C sites get closer to each other, closing a pentagon upon formation of a C-C bond, while the remaining two electrons sit on the C atom opposite to the pentagon (“lone” C in the following).

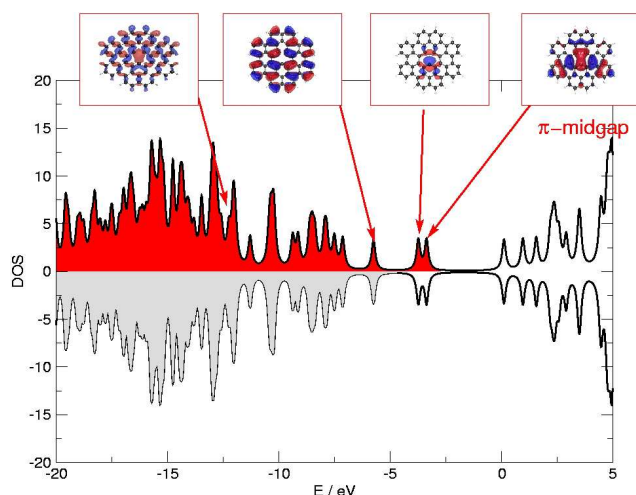


Figure 1 DOSs in the C_{2v} distorted structure, as computed at the ROHF level on the cluster model, and properly broadened. Upper and lower panels for spin-up and spin-down. Also shown a number of representative orbitals.

The overall magnetic moment is now $1.4 \mu_B$, corresponding to a non-pure spin-state, the structure is still planar and the point group symmetry of the system is C_{2v} . Calculations on the cluster model give similar results, and show the re-arrangement of the single particle levels occurring upon structural relaxation. This is displayed in Fig.1 for the simplest case of the triplet, restricted open shell HF solution. Similar results were obtained with unrestricted HF both for the triplet and the singlet state, though, of course, with a different occupation of the spin-orbitals. On the other hand, restricted HF in the singlet forces the unpaired electrons to be paired in a hybrid molecular orbital which is midway between the dangling σ and the π -midgap state, with some energy penalty. Thus we conclude that the structure is *open-shell* both for the triplet and for the singlet states. A more accurate analysis based on CASSCF calculations is underway and will be presented in a forthcoming paper. Based on the above results, we consider the above solution obtained in the periodic setting as resulting from the “interaction” between two states which have the same open-shell configuration and differ only for the coupling of the two lone electrons.

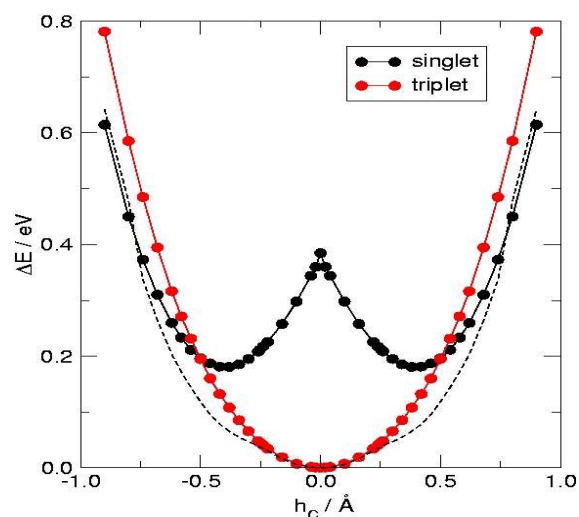


Figure 2 Energy of the “triplet” and “singlet” states as function of the “lone” C atom height, when optimizing the remaining coordinates. Also shown as dashed lines the results of magnetization-unconstrained calculations.

To support this interpretation, we performed magnetization constrained (spin-polarized) calculations, where we set the total magnetic moment to be zero or two Bohr magnetons, approximately corresponding to the singlet and the triplet states above.

The results are shown in Fig.2 as functions of the “lone” C height from the surface, which turns out to be the most important geometrical parameter governing the electronics. Notice that a full geometrical optimization on the remaining coordinates has been performed for each value of the C atom height, and for each possible magnetization. Fig.2 strongly suggests that the unconstrained energy curve results from a “mixture” of the triplet and singlet states. Such a mixture is possible in the adopted DFT setting because allowance is made to

partial occupation of Kohn-Sham single particle states. Thus, in the following we focus on the “singlet” and “triplet” states only.

Again from Fig.2, we see that the triplet state has essentially a flat geometry, whereas in the singlet the “lone” carbon atom moves out-of-plane, reducing the overall symmetry to C_s . Two equivalent situations occurs in this case, with the C atom above or below the plane, thereby giving rise to a *bi-stable* system. The planar (singlet) configuration is likely to be (accidentally) doubly-degenerate, but this is yet to be investigated in detail. We just notice here that for $h=0$ the singlet geometry is only slightly distorted from the threefold structure of the “ideal” vacancy and thus an essentially double degenerate state may occur either from the configuration $\{..e^1a^1\}$ or from $\{..e^2\}$.

To fully understand the geometrical rearrangement around the vacancy, and possibly exploit the crossing of the spin manifolds already apparent in Fig.2, we map the most relevant part of the configuration space of the system, namely the above out-of-plane displacement h and a pentagonal distortion coordinate q , designed to give the ideal structure for $q=0$ and the pentagonal one for $q=1$. The results of this study are reported in Fig.3 where the differences between the singlet and triplet energy surfaces become more apparent.

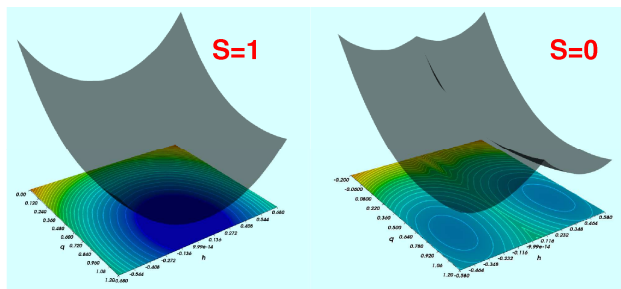


Figure 3: Potential energy surfaces for the “triplet” and “singlet” states as a function of the out-of-plane displacement h and of the pentagonal distortion coordinate q .

The detailed electronic structure of these two vacancy-induced states, and the way they change with geometry, is less trivial to analyse and requires a detailed comparison of selected wavefunction calculations which are underway on the cluster model. Here, we just notice that our results support the idea that both the triplet and the singlet state are always of the (same) open-shell character, with one electron in the (localized) dangling σ orbital and one electron in the semi-delocalized π (midgap) orbital. This is made clear in the DFT spin density iso-surfaces shown in Fig.4, which show in both cases a non-vanishing value. [Note: for the “singlet” this has to be considered an *artifact* of the spin-polarization, simply signalling the presence of an intrinsically “multi-determinantal” state as the open-shell singlet is].

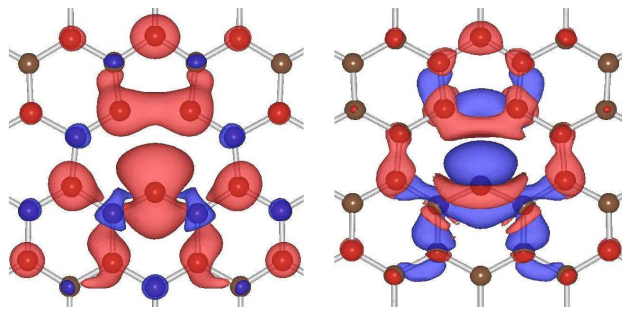


Figure 4: Spin density iso-surfaces for “triplet” (left) and “singlet” (right) states. Both have an open-shell configuration.

4. CONCLUSIONS

We reported preliminary results of a detailed *first-principles* study of the electronic and geometrical structural changes occurring upon formation of a C atom vacancy in graphene. Present results clearly show that the two lowest-lying states correspond to a “singlet” and a “triplet” pairing of the two unpaired electrons left upon formation a new σ C-C bond. The triplet has a single equilibrium configuration, with the lattice planar though Jahn-Teller distorted. The singlet is slightly higher in energy but it becomes the ground-state when the “lone” C atom is moved above or below the plane, thereby giving rise to an interesting *bi-stable* system. Since the energy gap is at most 0.4 eV in the important region of configuration space, the exchange coupling can be estimated to be less than 1 eV in this region. Overall, these results show that vacancies are more intriguing than currently believed, and may turn out to be useful “dots” for a number of nanoscale applications.

5. REFERENCES

- [1] R. Martinazzo, S. Casolo, G.F. Tantardini, *Physics and Applications of Graphene – Theory*, InTech, Chapter 3, 2011
- [2] O.V. Yazyev, L. Helm, *Phys. Rev. B*, **75**, 125408 (2007)
- [3] G. Kresse, J. Hafner, *Phys. Rev. B* **49**, 14251 (1994)
- [4] G. Kresse, J. Hafner, *Phys. Rev. B* **47**, 558 (1993)
- [5] G. Kresse, J. Furthmuller, *Comput. Mater. Sci.* **6**, 15 (1996)
- [6] G. Kresse, J. Furthmuller, *Phys. Rev. B* **54**, 11169 (1996)
- [7] P. E. Bloch, *Phys. Rev. B* **50**, 17953 (1994)
- [8] G. Kresse, D. Joubert, *Phys. Rev. B* **59**, 1758 (1999)
- [9] J. P. Perdew, K. Burke, M. Ernzerhof, *Phys. Rev. Lett.* **77**, 3865 (1996)
- [10] J. P. Perdew, K. Burke, M. Ernzerhof, *Phys. Rev. Lett.* **78**, 1396 (1997)
- [11] S. Casolo, O.M. Løvrvik, R. Martinazzo, G.F. Tantardini, *J. Chem. Phys.*, **130**, 054704 (2009)
- [12] E.H. Lieb, *Phys. Rev. B*, **62**, 1201 (1989)
- [13] A.A. El-Barbary, R.H. Telling, C.P. Ewels, M.I. Heggie, P.R. Briddon, *Phys. Rev. B*, **68**, 144107 (2003)

CYCLOTRON RESONANCE AND RENORMALIZATION IN GRAPHENE AND ITS BILAYER

K. Shizuya

*Yukawa Institute for Theoretical Physics,
Kyoto University, Kyoto 606-8502, Japan
E-mail: shizuya@yukawa.kyoto-u.ac.jp*

ABSTRACT

We report our recent study of cyclotron resonance in graphene, with focus on the many-body effect on the resonance energies. The genuine many-body corrections turn out to derive from vacuum polarization, specific to graphene, which diverges at short wavelengths and which requires renormalization of velocity and, for bilayer graphene, interlayer couplings as well. As a result, the renormalized velocity and interlayer coupling strengths run with the magnetic field, and many-body corrections are uniquely determined from one resonance to another. Theory is compared with the experimental data for both monolayer and bilayer graphene.

I. INTRODUCTION

Graphene and its multilayer give rise to rich spectra of cyclotron resonance, with resonance energies varying from one transition to another within the electron band or the hole band, and, notably, even between the two bands [1]. This is in sharp contrast to conventional quantum Hall (QH) systems with a parabolic dispersion, where cyclotron resonance takes place between adjacent Landau levels, hence at a single frequency $\omega_c = eB/m^*$ which, according to Kohn's theorem [2], is unaffected by Coulomb interactions [?]. The nonparabolic electronic spectra in graphene evade Kohn's theorem and offer the challenge of detecting many-body corrections to cyclotron resonance [3–5].

Experiment has so far verified, via infrared spectroscopy, some characteristic features of cyclotron resonance in monolayer [6, 7] and bilayer [8, 9] graphene. Data generally show no clear sign of the many-body effect, except for one [6] on monolayer graphene. For bilayer graphene only a limited number of data are available so far. The data show a weak electron-hole asymmetry, and generally defy a good fit by theory.

In this paper we would like to report our recent study of many-body corrections to cyclotron resonance in graphene and its bilayers [10]. We construct an effective theory of cyclotron resonance within the single-mode approximation and point out the following:

(1) The genuine nonzero many-body corrections arise from vacuum polarization, specific to graphene, which diverges logarithmically at short wavelengths.

(2) Both intralayer and interlayer coupling strengths require renormalization, which then allows one to determine many-body corrections uniquely from one resonance to another. The renormalized velocity v_1^{ren} and inter-layer cou-

pling γ_1^{ren} thereby run with the magnetic field B , decreasing gradually with increasing B .

(3) Theory is favorably compared with the experimental data on graphene.

II. MONOLAYER GRAPHENE

Monolayer graphene supports as charge carriers massless Dirac fermions at two inequivalent valleys (K and K'), and they, in a magnetic field, lead to a tower of unequally-spaced Landau levels $|n, y_0\rangle$ of energy

$$\epsilon_n = s_n \omega_c \sqrt{|n|} \quad \text{with } \omega_c \equiv \sqrt{2} v_0 / \ell, \quad (2.1)$$

labeled by integers $n = \pm 0, \pm 1, \pm 2, \dots$, and the center coordinate $y_0 \equiv \ell^2 p_x$ with the magnetic length $\ell \equiv 1/\sqrt{eB}$; $s_n \equiv \text{sgn}[n] \rightarrow \pm 1$; the ‘‘light velocity’’ $v_0 \sim 10^6$ m/s leads to the basic cyclotron energy $\omega_c \equiv \sqrt{2} v_0 / \ell \approx 36.3 \times v_0 [10^6 \text{m/s}] \sqrt{B[\text{T}]} \text{meV}$. Each Landau level is fourfold degenerate (in spin and valley) when Zeeman coupling is ignored. Supplying a tiny sublattice asymmetry reveals that the $n = 0$ level is doubly degenerate and electron-like with $\epsilon_0 = 0_+$ at one valley while it is hole-like with $\epsilon_0 = -0$ at another valley. See Fig. 1(a).

Let us expand the electron field $\psi(\mathbf{x}, t)$ in terms of the Landau-level eigenmodes $\psi_n(y_0, t)$ and write the charge density $\rho_{-\mathbf{p}} = \int d^2\mathbf{x} e^{i\mathbf{p}\cdot\mathbf{x}} \psi^\dagger \psi$ as [11]

$$\rho_{-\mathbf{p}} = \sum_{k, n=-\infty}^{\infty} g_{\mathbf{p}}^{kn} R_{\mathbf{p}}^{kn},$$

$$R_{\mathbf{p}}^{kn} = \gamma_{\mathbf{p}} \int dy_0 \psi_k^\dagger(y_0) e^{i\mathbf{p}\cdot\mathbf{r}} \psi_n(y_0), \quad (2.2)$$

where $\gamma_{\mathbf{p}} = e^{-\frac{1}{4}\ell^2 \mathbf{p}^2}$; $\mathbf{r} = (i\ell^2 \partial / \partial y_0, y_0)$ stands for the center coordinate. The coefficient matrix $g_{\mathbf{p}}^{kn}$ is given by

$$g_{\mathbf{p}}^{kn} = \frac{1}{2} b_k b_n (f_{\mathbf{p}}^{|k|-1, |n|-1} + s_k s_n f_{\mathbf{p}}^{|k|, |n|}), \quad (2.3)$$

where $b_n = 1$ for $n \neq 0$ and $b_0 = \sqrt{2}$; $s_n = \text{sgn}[n] \rightarrow \pm 1$; $f_{\mathbf{p}}^{kn} = \sqrt{n!/k!} (-\ell p / \sqrt{2})^{k-n} L_n^{(k-n)}(\frac{1}{2}\ell^2 \mathbf{p}^2)$ for $k \geq n \geq 0$, and $f_{\mathbf{p}}^{nk} = (f_{-\mathbf{p}}^{kn})^\dagger$; $p = p_x - ip_y$. The Coulomb interaction is written as

$$H^{\text{Coul}} = \frac{1}{2} \sum_{\mathbf{p}} v_{\mathbf{p}} : \rho_{-\mathbf{p}} \rho_{\mathbf{p}} :, \quad (2.4)$$

where $v_{\mathbf{p}} = 2\pi\alpha / (\epsilon_b |\mathbf{p}|)$ with $\alpha = e^2 / (4\pi\epsilon_0) \approx 1/137$ and the substrate dielectric constant ϵ_b .

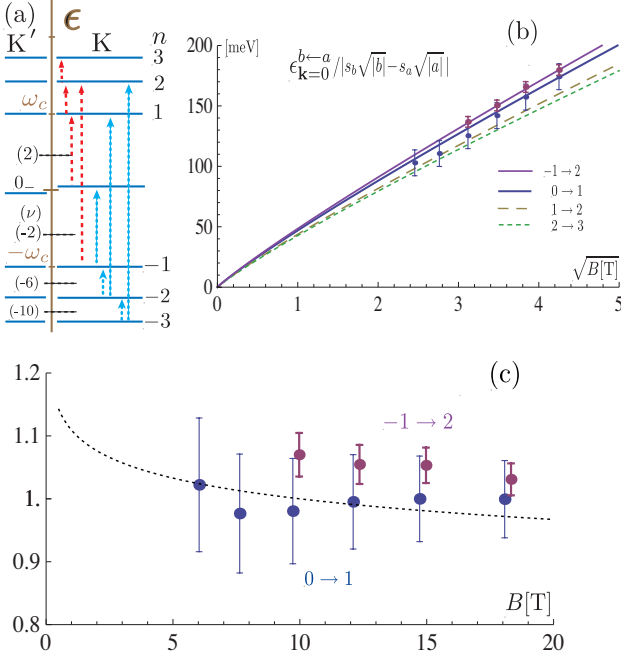


FIG. 1: (a) Cyclotron resonance; circularly-polarized light can distinguish between transitions indicated by different types of arrows. (b) Rescaled cyclotron-resonance energies as a function of \sqrt{B} , with $v_0^{\text{ren}}|_{B=10\text{T}} \approx 1.13 \times 10^6$ m/s and, as a typical value, $V_c \approx 12 \sqrt{B[\text{T}]} \text{ meV}$ ($\epsilon_b \approx 5$). The experimental data are quoted from Ref. [6] with error bars inferred from the original data. (c) The same data plotted in units of $\omega_c = \sqrt{2} v_0^{\text{ren}}|_{B=10\text{T}}/\ell$ as a function of B . The dotted curve represents a possible profile of the running of $v_0^{\text{ren}}|_B$, normalized to 1 at $B = 10\text{T}$.

III. CYCLOTRON RESONANCE AND RENORMALIZATION

Let us note that the charge operator $R_{\mathbf{p}}^{kn}$ in Eq. (2.2) annihilates an electron at the n th level L_n and creates one at the k th level L_k . One may thus associate it with the inter-Landau-level transition $L_n \rightarrow L_k$, and calculate the Coulombic corrections to cyclotron resonance using the single-mode approximation. Actually, the calculation is done in a purely algebraic manner if one notes that the charge operators $R_{\mathbf{p}}^{kn}$ obey the W_∞ algebra.

The result is the following [10]: The cyclotron-resonance energy for a general $L_a \rightarrow L_b$ channel with the Landau levels filled up to $n = n_f$ is written as

$$\begin{aligned} \epsilon_{\mathbf{k}=0}^{\text{exc}} &= \epsilon_b - \epsilon_a + \Delta \epsilon_{\mathbf{k}=0}^{b \leftarrow a}, \\ \Delta \epsilon_{\mathbf{k}=0}^{b \leftarrow a} &= \sum_{\mathbf{p}} v_{\mathbf{p}} \gamma_{\mathbf{p}}^2 \left[\sum_{n \leq n_f} (|g_{-\mathbf{p}}^{an}|^2 - |g_{-\mathbf{p}}^{bn}|^2) - g_{\mathbf{p}}^{bb} g_{-\mathbf{p}}^{aa} \right]. \end{aligned} \quad (3.1)$$

Note that $n_f = 1, 0_+, -1, -2, -3$ correspond to the filling factors $\nu = 4n_f + 2 = 6, 2, -2, -6, -10$, respectively. The $\sum_{n \leq n_f} (|g_{-\mathbf{p}}^{an}|^2 - |g_{-\mathbf{p}}^{bn}|^2)$ term refers to the change in quantum fluctuations, via the $a \rightarrow b$ transition, of the filled states.

For standard QH systems this correction $\Delta \epsilon_{\mathbf{k}=0}^{b \leftarrow a}$ vanishes for each transition to the adjacent level, $L_n \rightarrow L_{n+1}$,

according to Kohn's theorem. Let us consider it for the $0 \rightarrow 1$ transition in graphene. Interestingly, it happens that $|g_{-\mathbf{p}}^{00}|^2 - |g_{\mathbf{p}}^{10}|^2 - g_{\mathbf{p}}^{11} g_{-\mathbf{p}}^{00} = 0$ also holds for graphene, with $g_{\mathbf{p}}^{00} = 1$, $g_{\mathbf{p}}^{10} = -\ell p/2$ and $g_{\mathbf{p}}^{11} = 1 - \ell^2 p^2/4$. Any nonzero shift $\Delta \epsilon_{\mathbf{k}=0}^{1 \leftarrow 0}$ therefore comes from the quantum fluctuations of the Dirac sea (valence band), and actually diverges logarithmically with the number N_L of filled Landau levels in the sea,

$$\Delta \epsilon_{\mathbf{k}=0}^{1 \leftarrow 0} = \sum_{\mathbf{p}} v_{\mathbf{p}} \gamma_{\mathbf{p}}^2 \sum_{-N_L \leq n \leq -1} (|g_{-\mathbf{p}}^{0n}|^2 - |g_{\mathbf{p}}^{1n}|^2) = V_c \mathcal{C}_N, \quad (3.2)$$

$$\mathcal{C}_N \approx (\sqrt{2}/8) (\log N_L - 1.017),$$

$$V_c \equiv \alpha/(\epsilon_b \ell) \approx (56.1/\epsilon_b) \sqrt{B[\text{T}]} \text{ meV}. \quad (3.3)$$

This divergence in \mathcal{C}_N derives from short-wavelength vacuum polarization and is present even for $B = 0$, i.e., in free space [12]. It thus does not make sense to discuss the magnitude of \mathcal{C}_N . The legitimate procedure is to renormalize v_0 by rescaling

$$v_0 = Z_v v_0^{\text{ren}} \quad (3.4)$$

and to put the reference to the cutoff into Z_v .

The renormalized velocity v_0^{ren} is defined by referring to a specific resonance. Let us take the $0 \rightarrow 1$ resonance and choose to absorb the entire $O(V_c)$ correction at some reference scale (e.g., at magnetic field B_0) into Z_v , i.e., we write

$$\epsilon_{\mathbf{k}=0}^{1 \leftarrow 0} |_{\nu=2} = \epsilon_1 + \Delta \epsilon_{\mathbf{k}=0}^{1 \leftarrow 0} = \sqrt{2} v_0^{\text{ren}} |_{B=10\text{T}} / \ell \equiv \omega_c^{\text{ren}} |_B. \quad (3.5)$$

The renormalized velocity then runs with B ,

$$v_0^{\text{ren}} |_B = v_0^{\text{ren}} |_{B_0} - \frac{\alpha}{8\epsilon_b} \log(B/B_0), \quad (3.6)$$

decreasing gradually for $B > B_0$. We denote $v_0^{\text{ren}} |_B$ as v_0^{ren} and $\omega_c^{\text{ren}} |_B$ as ω_c^{ren} for short.

The resonance energies $\epsilon_{\mathbf{k}=0}^{b \leftarrow a}$ for all other channels, as illustrated in Fig. 1 (a), are made finite by this renormalization. The resulting corrections $\propto V_c$ then make sense as genuine observable corrections. In particular, for several intraband channels one finds

$$\begin{aligned} \epsilon_{\mathbf{k}=0}^{2 \leftarrow 1} |_{\nu=6} &= \epsilon_{\mathbf{k}=0}^{-1 \leftarrow -2} |_{\nu=-6} = (\sqrt{2} - 1) \{ \omega_c^{\text{ren}} - 0.264 V_c \}, \\ \epsilon_{\mathbf{k}=0}^{3 \leftarrow 2} |_{\nu=10} &= \epsilon_{\mathbf{k}=0}^{-2 \leftarrow -3} |_{\nu=-10} \\ &= (\sqrt{3} - \sqrt{2}) \{ \omega_c^{\text{ren}} - 0.358 V_c \}. \end{aligned} \quad (3.7)$$

Cyclotron resonance in graphene is governed by the selection rule $\Delta|n| = \pm 1$, and, as a result, graphene supports interband cyclotron resonances. Some typical channels yield

$$\begin{aligned} \epsilon_{\mathbf{k}=0}^{2 \leftarrow -1} |_{\nu=-2} &= (\sqrt{2} + 1) \{ \omega_c^{\text{ren}} + 0.122 V_c \}, \\ \epsilon_{\mathbf{k}=0}^{1 \leftarrow -2} |_{\nu=-2} &= (\sqrt{2} + 1) \{ \omega_c^{\text{ren}} + 0.155 V_c \}, \\ \epsilon_{\mathbf{k}=0}^{1 \leftarrow -2} |_{\nu=-6} &= (\sqrt{2} + 1) \{ \omega_c^{\text{ren}} + 0.084 V_c \}, \\ \epsilon_{\mathbf{k}=0}^{2 \leftarrow -3} |_{\nu=-10} &= (\sqrt{2} + \sqrt{3}) \{ \omega_c^{\text{ren}} + 0.044 V_c \}. \end{aligned} \quad (3.8)$$

It is clear from this structure that cyclotron resonance is best analyzed by plotting the rescaled energies

$\epsilon_{\mathbf{k}=0}^{b \leftarrow a} / |s_b \sqrt{|b|} - s_a \sqrt{|a|}|$ as a function of \sqrt{B} or B . The Coulombic many-body effect will be seen as a variation of the characteristic velocity $v_0^{\text{ren}}[1 + O(V_c)]$ from one resonance to another, and a deviation of ω_c^{ren} from the \sqrt{B} behavior would indicate the running of v_0^{ren} with B .

Actually, experiment by Jiang *et al.* [6] did observe a small deviation of the $1 : (1 + \sqrt{2})$ ratio of $\epsilon_{\mathbf{k}=0}^{1 \leftarrow 0}$ to $\epsilon_{\mathbf{k}=0}^{2 \leftarrow -1}$ well outside of the experimental errors under magnetic fields $B = (6 \sim 18)$ T. Such data are included in Fig. 1 (b), which plots $\epsilon_{\mathbf{k}=0}^{1 \leftarrow 0}$ and $\epsilon_{\mathbf{k}=0}^{2 \leftarrow -1} / (\sqrt{2} + 1)$ as a function of \sqrt{B} . A small increase of v_0^{ren} in $\epsilon_{\mathbf{k}=0}^{2 \leftarrow -1} / (\sqrt{2} + 1)$, relative to $\epsilon_{\mathbf{k}=0}^{1 \leftarrow 0}$, is roughly consistent with Eq. (3.8) which suggests a $0.122 V_c / \omega_c^{\text{ren}} \sim 4\%$ increase in v_0^{ren} (since $V_c / \omega_c^{\text{ren}} \sim 0.3$).

This feature is more pronounced in Fig. 1 (c), which plots the same data in units of $\omega_c = \sqrt{2} v_0^{\text{ren}}|_{B=10\text{T}} / \ell \propto \sqrt{B}$. There a dotted curve represents a possible profile of the running of v_0^{ren} with B , and, especially, the $(-1 \rightarrow 2)$ data (with smaller error bars) suggests such running.

The data are thus consistent (in sign and magnitude) with the present estimate of the many-body effect. In this connection, let us note that an earlier experiment on thin epitaxial graphite [13] also observed the same pair of resonances, with apparently no deviation from the $1 : (1 + \sqrt{2})$ ratio. This measurement was done under relatively low magnetic fields $B = (0.4 \sim 4)$ T, and it could be that a small deviation, under larger error bars, simply escaped detection, apart from the potential difference between thin graphite and graphene.

More precise measurements of cyclotron resonance, especially in the high B domain, would be required to pin down the many-body effect in graphene. In this respect, the comparison between interband and intraband resonances from the *same* initial state, such as the $(-2 \rightarrow \pm 1)$ resonances and $(-3 \rightarrow \pm 2)$ resonances, would provide a clearer signal for the many-body effect. One would expect sizable variations in v_0^{ren} for such pairs,

$$\begin{aligned} \Delta R(-2 \rightarrow \pm 1) &\stackrel{\nu=-6}{\approx} 0.34 V_c / \omega_c^{\text{ren}} \sim 10\%, \\ \Delta R(-3 \rightarrow \pm 2) &\stackrel{\nu=-10}{\approx} 0.40 V_c / \omega_c^{\text{ren}} \sim 12\%. \end{aligned} \quad (3.9)$$

IV. CYCLOTRON RESONANCES IN BILAYER GRAPHENE

In bilayer graphene interlayer coupling $\gamma_1 \equiv \gamma_{A'B} \sim 0.4$ eV modifies the intralayer linear spectra to yield, in the low-energy branches $|\epsilon| < \gamma_1$, quasiparticles with a parabolic dispersion. They, in a magnetic field, support a variety of cyclotron resonances, as listed in Fig. 2 (a).

There are some other factors to be considered. Earlier Raman and IR studies [14–16] of bilayer graphene revealed a weak electron-hole asymmetry due to subleading intra- and inter-layer couplings $\Delta \sim 18$ meV and $\gamma_4 / \gamma_1 \sim 0.04$. The SMA formula (3.1) can be properly generalized to include the effect of such asymmetry parameters [10]. It turns out that not only v_0 but also γ_1 and Δ undergo infinite renormalization while γ_4 remains finite, to $O(V_c)$ at least. The renormalized excitation spectra are

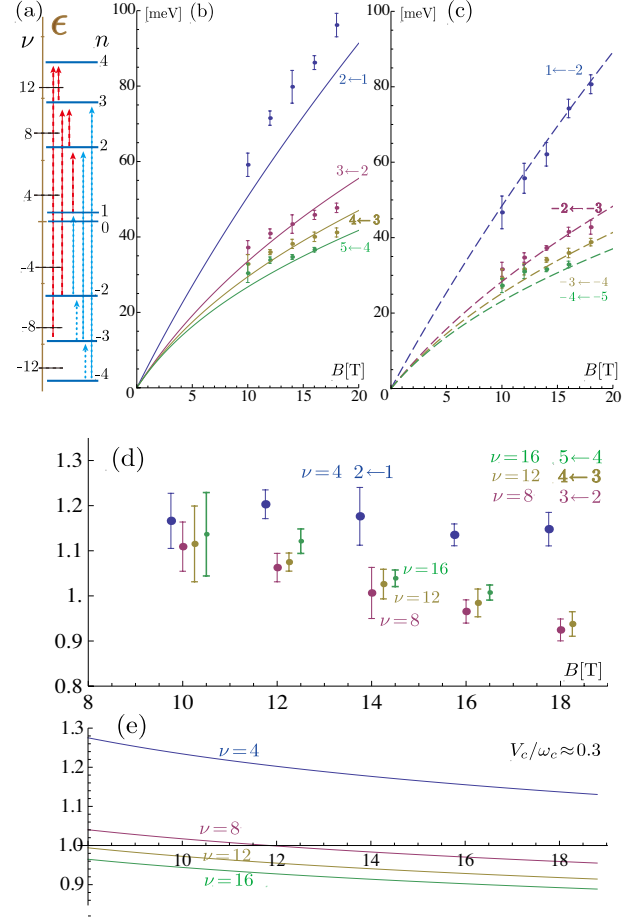


FIG. 2: (a) Cyclotron resonance in bilayer graphene. Resonance energies; (b) electron band and (c) hole band, with $v_0 = 1.1 \times 10^6$ m/s, $\gamma_1 = 404$ meV, $V_c = 0$, $\Delta = 18$ meV and $\gamma_4 / \gamma_1 = 0.04$. The experimental data are reproduced from Ref. [8]. (c) Electron data, reorganized as $\epsilon_{\mathbf{k}=0}^{b \leftarrow a} / (\eta_b - \eta_a)$ and plotted in units of $\omega_c = \sqrt{2} v_0|_{B=14\text{T}} / \ell^2$; for clarity the data points are slightly shifted in B . (d) Theoretical expectation for the running of ω_c^{ren} with B .

eventually cast in the form

$$\epsilon_{\mathbf{k}=0}^{b \leftarrow a} = (\eta_b - \eta_a) (\omega_c^{\text{ren}} + \Delta c^{ba} V_c), \quad (4.1)$$

where η_k are some given functions of $v_0^{\text{ren}} / \gamma_1^{\text{ren}}$ and Δc^{ba} are uniquely fixed as genuine quantum corrections.

The existing data on cyclotron resonance by Henriksen *et al.* [8] show an appreciable electron-hole asymmetry, and one previously had to employ different values of v_0 to fit the electron data and hole data separately. With asymmetry parameters taken into account, one can improve the theoretical fit to the data considerably, as seen from Fig. 2 (b) and (c), and apparent deviations of the $2 \leftarrow 1$ resonance suggest that the spectrum of the pseudo-zero-mode sector of degenerate $n = (0, 1)$ levels, specific to bilayer graphene, is likely to be modified from the naive one due to some other sources. Note that the data certainly suggest nontrivial features of many-body corrections, such as the running with B ; see Fig. 2 (d) and (e).

Interband cyclotron resonance was recently observed by Orlita *et al.* [9] in bilayer inclusions in multilayer epitaxial graphene on the C-face of SiC. They identify some reso-

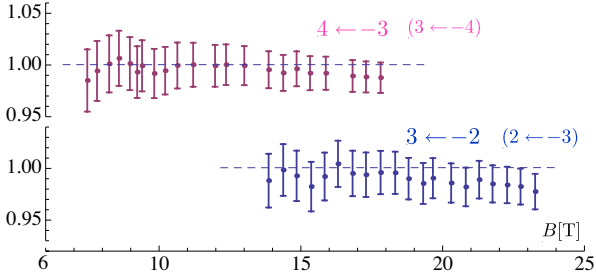


FIG. 3: Interband cyclotron resonances in bilayer inclusions in multilayer epitaxial graphene reported by Orlita *et al.* Here some data of Ref. 9 are analyzed in the same way as in Fig. 2 (d), using $v_0 = 1.02 \times 10^6$ m/s and $\gamma_1 \approx 385$ meV for zero asymmetry $\Delta = \gamma_4 = 0$.

nances and obtain, via fitting, $v_0 \approx 1.02 \times 10^6$ m/s and $\gamma_1 \approx 385$ meV, which are somewhat smaller than those for bilayer graphene. Some of their data are analyzed according to our formula in Fig. 3. The data appear to indicate slight running of v^{ren} with B , far slower than in the data of Fig. 2 on bilayer graphene. This suggests that the Coulomb

interaction could be significantly weaker (or more efficiently screened) in multilayered epitaxial graphene than in exfoliated bilayer graphene.

V. CONCLUDING REMARKS

In this paper we have studied many-body corrections to cyclotron resonance in graphene, with emphasis on the need for renormalization and its consequences. More precise measurements of cyclotron resonance are highly desired. Of particular interest are experiments that compare interband and intraband resonances from the same initial states, which would clarify the many-body effect with minimal uncertainties.

Acknowledgments

This work was supported in part by a Grant-in-Aid for Scientific Research from the Ministry of Education, Science, Sports and Culture of Japan (Grant No. 21540265).

-
- [1] D. S. L. Abergel and V. I. Fal'ko, *Phys. Rev. B* **75**, 155430 (2007)
 - [2] W. Kohn, *Phys. Rev.* **123**, 1242 (1961).
 - [3] A. Iyenga, J. Wang, H. A. Fertig and L. Brey, *Phys. Rev. B* **75**, 125430 (2007).
 - [4] Yu A. Bychkov and G. Martinez, *Phys. Rev. B* **77**, 125417 (2008).
 - [5] S. Viola Kusminskiy, D. K. Campbell and A. H. Castro Neto, *Euro. Phys. Lett.* **85**, 58005 (2009).
 - [6] Z. Jiang, E. A. Henriksen, L. C. Tung, Y.-J. Wang, M. E. Schwartz, M. Y. Han, P. Kim and H. L. Stormer, *Phys. Rev. Lett.* **98**, 197403 (2007).
 - [7] R. S. Deacon, K.-C. Chuang, R. J. Nicholas, K. S. Novoselov and A. K. Geim, *Phys. Rev. B* **76**, 081406(R) (2007).
 - [8] E. A. Henriksen, Z. Jiang, L.-C. Tung, M. E. Schwartz, M. Takita, Y.-J. Wang, P. Kim P and H. L. Stormer *Phys. Rev. Lett.* **100**, 087403 (2008).
 - [9] M. Orlita, C. Faugeras, J. Borysiuk, J. M. Baranowski, W. Strupiański, M. Sprinkle, C. Berger, W. A. de Heer, D. M. Basko, G. Martinez, and M. Potemski, *Phys. Rev. B* **83**, 125302 (2011).
 - [10] K. Shizuya, *Phys. Rev. B* **81**, 075407 (2010); *Phys. Rev. B* **84**, 075409 (2011).
 - [11] K. Shizuya, *Phys. Rev. B* **75**, 245417 (2007).
 - [12] J. González, F. Guinea and M. A. H. Vozmediano, *Nucl. Phys. B* **424** [FS], 595 (1994).
 - [13] M. L. Sadowski, G. Martinez, M. Potemski, C. Berger and H. A. de Heer, *Phys. Rev. Lett.* **97**, 266405 (2006).
 - [14] L. M. Malard, J. Nilsson, D. C. Elias, J. C. Brant, F. Plentz, E. S. Alves, A. H. Castro Neto, and M. A. Pimenta, *Phys. Rev. B* **76**, 201401(R) (2007).
 - [15] L. M. Zhang, Z. Q. Li, D. N. Basov, and M. M. Fogler, Z. Hao, and M. C. Martin, *Phys. Rev. B* **78**, 235408 (2008).
 - [16] Z. Q. Li, E. A. Henriksen, Z. Jiang, Z. Hao, M. C. Martin, P. Kim, H. L. Stormer, and D. N. Basov, *Phys. Rev. Lett.* **102**, 037403 (2009).

TRANSPORT PROPERTIES OF GRAPHENE ACROSS STRAIN-INDUCED NONUNIFORM VELOCITY PROFILES

F. M. D. Pellegrino^{1,2}, G. G. N. Angilella^{1,2,3,4*}, R. Pucci^{1,2}

¹*Dipartimento di Fisica e Astronomia, Università di Catania, Via S. Sofia, 64, I-95123 Catania, Italy*

²*CNISM, UdR Catania, Italy*

³*Scuola Superiore di Catania, Università di Catania, Via Valdisavoia, 9, I-95123 Catania, Italy*

⁴*INFN, Sezione di Catania, Italy*

* E-mail: giuseppe.angilella@ct.infn.it

ABSTRACT

We study the effect of uniaxial strain on the transmission and the conductivity across a strain-induced barrier in graphene. Here, we consider a *smooth* barrier, which should describe more realistic nonuniform strain profiles, at variance with conventional studies. Our results should afford a more accurate understanding of the transport properties in corrugated graphene, especially in view of the suggestion to design graphene-based “origami” nanodevices, where “foldings” are expected to involve several lattice spacings.

1. INTRODUCTION

Graphene is a single layer of sp^2 carbon atoms, arranged as an honeycomb lattice. Its fabrication in the laboratory [1] immediately stimulated the interest of both the experimental and theoretical communities, and many applications, which initially could only be speculated, now appear feasible. In particular, electronic quasiparticles in graphene are characterized by a band structure consisting of two bands, touching at the Fermi level in a linear, cone-like fashion at the so-called Dirac points $\pm\mathbf{K}$, and a linearly vanishing density of states (DOS) at the Fermi level [2, 3]. This implies in this novel condensed matter system the possibility of Klein tunneling across barriers [4, 5, 6, 7, 8, 9], *i.e.* perfect transmission across energy barriers, which was predicted in the context of quantum electrodynamics at relatively much larger energies.

Graphene, like most carbon compounds, is also characterized by quite remarkable mechanical properties. Despite its reduced dimensionality, graphene possesses a relatively large tensile strength and stiffness [10], with graphene sheets being capable to sustain elastic deformations as large as $\approx 20\%$ [11, 12, 13, 14, 15]. Larger strains would then induce a semimetal-to-semiconductor transition, with the opening of an energy gap [16, 17, 18, 19, 20, 21, 22]. Recently, it has been suggested that graphene-based electronic devices might be designed by suitably tailoring the electronic structure of a graphene sheet under applied strain (the so-called ‘origami’ nanoelectronics) [23]. Indeed, a considerable amount of work has been devoted to the study of the transport properties in graphene across strain-induced single and multiple barriers [24]. It has

also been suggested that strain may induce relatively high pseudo-magnetic fields [25], whose effects have actually been confirmed experimentally in graphene nanobubbles grown on top of a platinum surface [26]. Indeed, the effect of the strain-induced displacement of the Dirac points in reciprocal space can be (formally) described in terms of the coupling to a gauge field. However, applied strain also induces a variation of the Fermi velocity, v_F . In particular, uniaxial strain implies a Fermi velocity anisotropy, while an inhomogeneous strain implies a nonuniform (*i.e.* coordinate dependent) velocity profile. This can also be realized in the presence of smooth potential barriers, where it has been demonstrated that a nonuniform space variation of the underlying gate potential would result in a modulation of the Fermi velocity [27, 28, 29]. Moreover, there is considerable evidence, both experimental [30] and theoretical [27], that barrier edge effects are also important to determine the transport properties across corrugated graphene.

2. MODEL

Close to the Fermi energy and in the unstrained case, the electrons dynamics is governed by the linearized Hamiltonian

$$H = \hbar v_F \boldsymbol{\sigma} \cdot \mathbf{p}, \quad (1)$$

where $\boldsymbol{\sigma} = (\sigma_x, \sigma_y)$ is a vector of Pauli matrices, associated with the in-plane spinorial nature of the quasiparticles in graphene. Eq. (1) can also take into account intervalley processes $\mathbf{K} \leftrightarrow -\mathbf{K}$, which however can be safely neglected, at sufficiently low energies.

Applied strain is then described by means of the strain tensor [17] $\boldsymbol{\varepsilon} = \frac{1}{2}\boldsymbol{\varepsilon}[(1 - \nu)\mathbb{I} + (1 + \nu)A(\boldsymbol{\theta})]$, where $A(\boldsymbol{\theta}) = \sigma_z e^{2i\theta\sigma_y}$. Here, $\boldsymbol{\varepsilon}$ is the strain modulus, $\boldsymbol{\theta}$ the angle along which strain is applied, and $\nu = 0.14$ is the Poisson ratio for graphene [20, 31, 22, 32]. Starting from a more general, tight-binding Hamiltonian [2], and expanding to first order in the strain modulus, one obtains an anisotropic dependence on the strain angle $\boldsymbol{\theta}$, already at linear order in the impulses [32]. This can be mapped back to a linear Hamiltonian as in Eq. (1) [22], where now impulses are reckoned from the shifted Dirac points, and the Fermi velocity is anisotropic and possibly coordinate-dependent [32].

We therefore consider a smooth strain barrier, characterized by a nonuniform, continuous strain profile $\boldsymbol{\varepsilon} = \boldsymbol{\varepsilon}(\boldsymbol{\xi})$,

with

$$\varepsilon(\xi) = \frac{\varepsilon_0}{\tanh(D/4a)} \left(\frac{1}{1 + e^{-\xi/a}} - \frac{1}{1 + e^{-(\xi-D)/a}} \right), \quad (2)$$

where ξ is the coordinate along the strain direction, forming an angle θ with the crystallographic x axis. Such a strain profile is essentially flat for $|\xi - D/2| \ll a$, where $\varepsilon(\xi) \approx \varepsilon_0$, and for $|\xi - D/2| \gg a$, where $\varepsilon(\xi) \approx 0$. In the limit $a/D \rightarrow 0$, Eq. (2) tends to a sharp barrier. The linear extent a , over which the strain profile Eq. (2) varies appreciably, is naturally to be compared with the lattice step a , at the microscopic level, and with the Fermi wavelength $\lambda_F = \hbar v_F / (2\pi E)$, where E is the energy of the incoming electron. While a smooth profile can be expected on quite general grounds, the approximation of a sharp barrier is expected to hold well whenever $a \ll \lambda_F$, *i.e.* at sufficiently large incident energies. On the other hand, the details of the strain profile come into their own when $a \sim \lambda_F$. Single electron tunneling, and thus the majority of the transport properties of interest, can then be inferred by solving the stationary Dirac equation associated to Eq. (1), now including the nonuniform strain, Eq. (2) [32]. For $|\xi| \rightarrow \infty$, the solutions for the scattering problem are therefore known analytically [32] (and refs. therein). Integrating the scattering equations from large positive ξ backwards to large negative ξ , and comparing with the known analytical solution, one may extract the reflection coefficient r , relative to an incident wave with unit amplitude incoming from $\xi > 0$, as the Fourier weight with respect to its negative frequency component, whence the transmission $T(E, \phi)$ at given incidence energy E follows straightforwardly.

3. RESULTS

Fig. 1 (left panel) shows the transmission $T(E, \phi)$ as a function of the incidence angle ϕ across strain-induced sharp and smooth barriers, Eq. (2), with strain applied along the armchair direction ($\theta = \pi/2$). One observes that, upon increasing the smoothing parameter a/D , the oscillations, characteristic of Klein tunneling across energy barriers in graphene, get damped, while their envelope (lower bound) increases. The dependence of the transmission $T(E, \phi)$ on the incidence angle ϕ is only apparently asymmetric, as we are restricting to quasiparticles with momentum centred around a given Dirac cone, say $+\mathbf{K}$. Symmetry $T(E, \phi) = T(E, -\phi)$ would be restored when the effect from the neighbourhood of both Dirac cones is included. The conductivity can then be straightforwardly related to the transmission by means of the Landauer formula [33, 34], as

$$\sigma(E) = \sigma_0 D \frac{E}{\hbar v_F} \int_{-\pi/2}^{\pi/2} T(E, \phi) \cos \phi \frac{d\phi}{2\pi}, \quad (3)$$

where $\sigma_0 = 4e^2/h$ is twice the conductance quantum, and the conserved component of transmitted momentum, *i.e.* that parallel to the barrier, has been related to the incidence angle through $k_y = E / (\hbar v_F) \sin \phi$. In Eq. (3), only the propagating modes have been included in the integration. One

is then prompted to define the adimensional conductivity

$$\sigma_a(E) = \frac{\sigma(E)}{\sigma_0 D \frac{E}{\hbar v_F}}. \quad (4)$$

Fig. 1 (right panel) shows the reduced conductivity, Eq. (4), as a function of incident energy E , for tunneling across sharp and smooth barriers, Eq. (2). One observes Fabry-Pérot oscillations, whose amplitude is reduced by increasing smoothing (*i.e.*, increasing a), the barrier then tending to be a more regular function. Also, the overall increase of the transmission is reflected in an enhancement of the conductivity.

4. CONCLUSIONS

In conclusion, we have studied the effect of nonuniform strain on the conductivity across smooth strain barriers in graphene. While an increase of smoothing reduces the oscillations of the transmission as a function of the incidence angle, one finds a reduction of the Fabry-Pérot oscillations and an overall enhancement of the conductivity as a function of incidence energy. These results should help understanding the properties of corrugated graphene.

REFERENCES

- [1] K. S. Novoselov, D. Jiang, F. Schedin, T. J. Booth, V. V. Khotkevich, S. V. Morozov, A. K. Geim. *Proc. Nat. Acad. Sci.* **102**, 10451 (2005).
- [2] A. H. Castro Neto, F. Guinea, N. M. R. Peres, K. S. Novoselov, A. K. Geim. *Rev. Mod. Phys.* **81**, 000109 (2009).
- [3] D. S. L. Abergel, V. Apalkov, J. Berashevich, K. Ziegler, T. Chakraborty. *Adv. Phys.* **59**, 261 (2010).
- [4] M. I. Katsnelson, K. S. Novoselov, A. K. Geim. *Nature Phys.* **2**, 620 (2006).
- [5] J. M. Pereira, V. Mlinar, F. M. Peeters, P. Vasilopoulos. *Phys. Rev. B* **74**, 045424 (2006).
- [6] M. Barbier, P. Vasilopoulos, F. M. Peeters. *Phys. Rev. B* **80**, 205415 (2009).
- [7] M. Barbier, P. Vasilopoulos, F. M. Peeters. *Phys. Rev. B* **81**, 075438 (2010).
- [8] M. Barbier, P. Vasilopoulos, F. M. Peeters. *Phys. Rev. B* **82**, 235408 (2010).
- [9] N. M. R. Peres. *J. Phys.: Cond. Matter* **21**, 323201 (2009).
- [10] T. J. Booth, P. Blake, R. R. Nair, D. Jiang, E. W. Hill, U. Bangert, A. Bleloch, M. Gass, K. S. Novoselov, M. I. Katsnelson, A. K. Geim. *Nano Letters* **8**, 2442 (2008).
- [11] K. S. Kim, Y. Zhao, H. Jang, S. Y. Lee, J. M. Kim, K. S. Kim, J. H. Ahn, P. Kim, J. Choi, B. H. Hong. *Nature* **457**, 706 (2009).
- [12] F. Liu, P. Ming, J. Li. *Phys. Rev. B* **76**, 064120 (2007).
- [13] E. Cadelano, P. L. Palla, S. Giordano, L. Colombo. *Phys. Rev. Lett.* **102**, 235502 (2009).

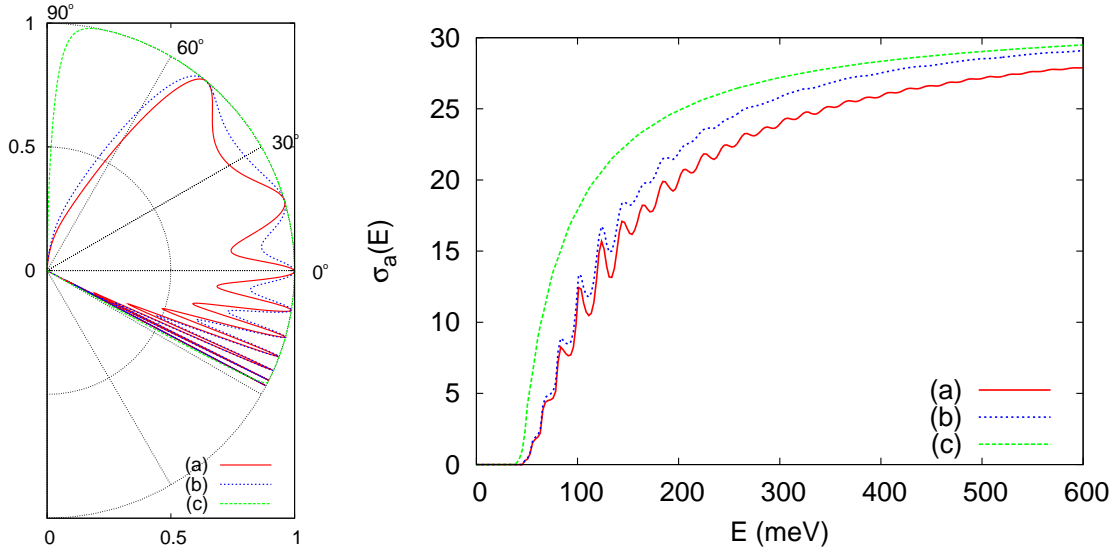


Figure 1: *Left*: Tunneling transmission vs incidence angle φ across a smooth strain barrier, with $D = 100$ nm, and incidence energy $E = 167$ meV ($\lambda_F = 0.6$ nm). *Right*: Normalized conductivity, $\sigma_a(E)$, vs incidence energy E across a smooth strain barrier, Eq. (4). In both panels, $\varepsilon_0 = 0.01$, $\theta = \pi/2$ (strain is applied in the armchair direction), while different curves refer to (a) sharp barrier, $a = 0$; (b) $a = 10^{-2}D$; (c) $a = 10^{-1}D$.

- [14] S.-M. Choi, S.-H. Jhi, Y.-W. Son. *Phys. Rev. B* **81**, 081407(R) (2010).
- [15] J.-W. Jiang, J.-S. Wang, B. Li. *Phys. Rev. B* **81**, 073405 (2010).
- [16] G. Gui, J. Li, J. Zhong. *Phys. Rev. B* **78**, 075435 (2008).
- [17] V. M. Pereira, A. H. Castro Neto, N. M. R. Peres. *Phys. Rev. B* **80**, 045401 (2009).
- [18] R. M. Ribeiro, V. M. Pereira, N. M. R. Peres, P. R. Briddon, A. H. C. Neto. *New J. Phys.* **11**, 115002 (2009).
- [19] G. Cocco, E. Cadelano, L. Colombo. *Phys. Rev. B* **81**, 241412 (2010).
- [20] F. M. D. Pellegrino, G. G. N. Angilella, R. Pucci. *Phys. Rev. B* **81**, 035411 (2010).
- [21] F. M. D. Pellegrino, G. G. N. Angilella, R. Pucci. *High Press. Res.* **29**, 569 (2009).
- [22] F. M. D. Pellegrino, G. G. N. Angilella, R. Pucci. *Phys. Rev. B* **84**, 195407 (2011).
- [23] V. M. Pereira, A. H. Castro Neto. *Phys. Rev. Lett.* **103**, 046801 (2009).
- [24] S. Gattenlöhner, W. Belzig, M. Titov. *Phys. Rev. B* **82**, 155417 (2010).
- [25] F. Guinea, M. I. Katsnelson, A. K. Geim. *Nat. Phys.* **6**, 30 (2010).
- [26] N. Levy, S. A. Burke, K. L. Meaker, M. Panlasigui, A. Zettl, F. Guinea, A. H. C. Neto, M. F. Crommie. *Science* **329**, 544 (2010).
- [27] J. Cayssol, B. Huard, D. Goldhaber-Gordon. *Phys. Rev. B* **79**, 075428 (2009).
- [28] A. Concha, Z. Tešanović. *Phys. Rev. B* **82**, 033413 (2010).
- [29] A. Raoux, M. Polini, R. Asgari, A. R. Hamilton, R. Fazio, A. H. MacDonald. *Phys. Rev. B* **81**, 073407 (2010).
- [30] E. J. H. Lee, K. Balasubramanian, R. T. Weitz, M. Burghard, K. Kern. *Nat. Nanotechnol.* **3**, 486 (2008).
- [31] F. M. D. Pellegrino, G. G. N. Angilella, R. Pucci. *Phys. Rev. B* **82**, 115434 (2010).
- [32] F. M. D. Pellegrino, G. G. N. Angilella, R. Pucci. *Phys. Rev. B* **84**, 195404 (2011).
- [33] R. Landauer. *IBM J. Res. Develop.* **1**, 223 (1957).
- [34] M. Büttiker. *Phys. Rev. Lett.* **57**, 1761 (1986).

FIRST PRINCIPLE STUDY OF BALLISTIC THERMAL CONDUCTANCE OF GRAPHENE ANTIDOT LATTICES FOR THERMOELECTRIC APPLICATIONS

H. Karamitaheri ^{1*}, M. Pourfath ¹, N. Neophytou ¹, M. Pazoki ², and H. Kosina ¹

¹ *Institute for Microelectronics, TU Wien, Vienna, Austria*

² *Department of Physics, Sharif University of Technology, Tehran, Iran*

*E-mail: karami@iue.tuwien.ac.at

ABSTRACT

In this work we present a first-principles study of lattice thermal properties of edge-hydrogen-passivated graphene antidot lattices of different dot shapes. We calculate the phononic bandstructure of antidot lattices with hexagonal, triangular and rectangular shapes. Using the Landauer transport formalism and ballistic transport considerations, we calculate the lattice thermal conductance. We show that in graphene antidot lattices with 80% fill-factor, the thermal conductance could be drastically reduced to 15%-20% of the pristine graphene value, depending on the shape of the dot. The reduction is larger for the triangular antidots because for the same fill factor, they have the longest boundary and the smallest distance between neighboring antidots. Our results could provide guidance in the design of graphene based thermal and thermoelectric devices.

1. INTRODUCTION

Thermoelectric devices convert heat into electricity and vice versa. The efficiency of thermoelectric devices depends on the ZT figure of merit defined as:

$$ZT = \frac{S^2GT}{K_{el} + K_{ph}} \quad (1)$$

where S denotes the Seebeck coefficient, G is the electrical conductance, T is the temperature, K_{el} and K_{ph} are the electrical and the lattice parts of the thermal conductance, respectively [1]. A good thermoelectric material, therefore, should simultaneously have a high Seebeck coefficient, a high electrical conductance, and a low thermal conductance. The interdependence of these parameters, however, has kept ZT low. Some of the best thermoelectric materials such as Bi_2Te_3 exhibit $ZT \sim 1$ [2], but suffer from high cost, and material abundance. Other common and inexpensive materials such as bulk silicon have a very low $ZT \approx 0.01$ [3] because of high thermal conductivity. Recently, nanostructured thermoelectric materials have been given significant attention because of the possibility of independently controlling the parameters that determine ZT and, thus, achieving high thermoelectric performance [4-6]. A large reduction in the lattice part of the thermal conductivity has been reported for nanostructures based on Si, Bi_2Te_3 ,

Pb_2Te_3 , SiGe superlattices and other materials [6-8], that resulted in significant improvements in the ZT figure of merit.

Graphene, a recently discovered form of carbon, has received significant attention over the last few years due to its excellent electrical, optical, and thermal properties [9-11]. A method to produce graphene sheets at large scale has also been reported [12]. Specifically for thermoelectrics, although the electrical conductivity of graphene is as high as that of copper [13], due to its zero bandgap it has a low Seebeck coefficient [14] and therefore a low power factor. On the other hand, several schemes for achieving a bandgap have been demonstrated [15,16], which places graphene as a potential candidate for thermoelectric applications. For this, however, its high thermal conductivity (an order of magnitude higher than that of copper [17]), needs to be significantly reduced. The high thermal conductance of graphene is mostly due to the lattice contribution, whereas the electrical contribution to the thermal conductance is minimal [17,18]. Therefore, one can design its total thermal conductance by focusing on phonon transport engineering.

Recently many theoretical studies have been performed on the thermal conductivity of graphene and graphene-based structures such as graphene nanoribbons (GNRs). It has been shown that boundaries, edge roughness, and even strain can strongly reduce the thermal conductance [19,20]. Vacancies, defects, and isotope doping could also have a strong influence [21,22].

In this work, we examine the lattice thermal properties of graphene antidot lattices with ~80% fill factor using first-principle calculations and ballistic transport considerations. We examine different shapes of antidots. Consistent with the previous works regarding different type of graphene lattice modifications, we find that the lattice thermal conductivity is significantly reduced with the introduction of antidots in the pristine lattice.

2. APPROACH

Graphene antidot lattices (GAL) are geometrical structures as shown in Fig. 1, where antidots are formed periodically in the graphene lattice [23]. The antidots can have different shapes and sizes and, thus, the antidot lattices different fill factors. Such structures, with antidot

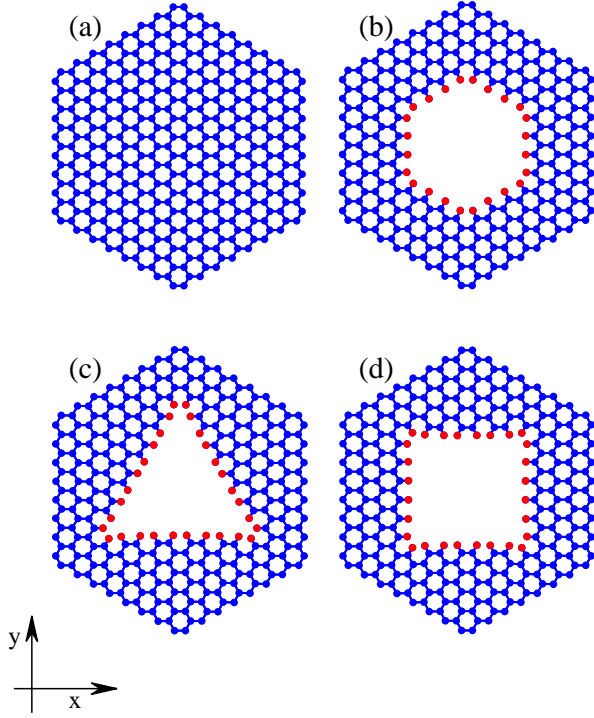


Fig. 1: Geometrical structures of different GALs. (a) Pristine graphene. (b) Hex(8,96,24). (c) IsoTri(8,90,30). (d) Rect(8,104,24). Hydrogen atoms are shown in red color. Transport assumed to be along the x-direction.

spacing below 100 nm have been recently experimentally realized [24], and have been proposed for electrical and optical applications [16,23]. Theoretical studies, also indicate that by introducing regular array of antidots in the semi-metallic graphene sheet, it is possible to achieve a direct bandgap [16]. In this paper we investigate the lattice thermal properties of GALs using first-principle calculations. The unit cell of a hydrogen-passivated GAL can be described by three parameters (L, N_C, N_H) , where L is the side length of the hexagon in the units of the graphene lattice constant ($a=2.46\text{\AA}$), N_C is the number of carbon atoms removed from the pristine supercell, and N_H is the number of hydrogen atoms that passivate the edge carbon atoms. In Fig. 1 Hex, IsoTri, and Rect represent a hexagonal, iso-triangular, and rectangular antidot in the hexagonal unit cell, respectively. We passivate all the dangling bonds at the edges of the antidots with hydrogen atoms using a carbon-hydrogen bond of 1.1\AA length [25].

To study the phononic bandstructure of hydrogen-passivated GALs the ab-initio simulation package SIESTA is employed [26]. We use a double zeta polarized basis set with a mesh cut-off 125 Ry. The general gradient approximation is used for the exchange correlation potential with a functional proposed by Perdew et al. [27]. Brillouin zone sampling was carried out by a $10\times 10\times 1$ Monkhorst-Pack grid. For structural relaxation, the positions of the atoms are changed until the force acting on each atom becomes smaller than 0.03-

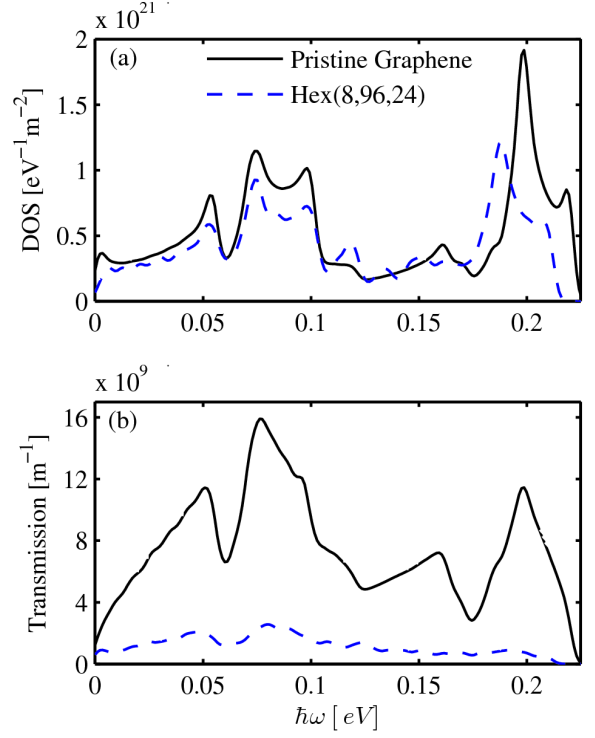


Fig. 2: Comparison between (a) density of states and (b) transmission of pristine graphene and Hex(8,96,24).

eV/\AA . Self consistency in the total energy is achieved with a tolerance of less than 10^{-4} Ry. For phonon calculations, the force constant matrix is calculated by displacing each atom 0.04 Bohr along the coordinate directions around its equilibrium position and evaluating the forces exerted by the other atoms.

Using the phononic bandstructures, the density of modes is calculated, and from this the ballistic transmission $T_{ph}(E)$ is extracted. In the ballistic limit the transmission can be extracted from the density of modes $M_{ph}(E)$ [28]:

$$T_{ph}(E)_{ballistic} = M_{ph}(E) = \sum \delta(E - \varepsilon_{ph}(k)) \Delta k_{\perp} \frac{\partial \varepsilon_{ph}(k)}{\partial k_{\parallel}} \quad (2)$$

where δ is the delta function, k_{\perp} refers to the wave vector component perpendicular to the transport direction and k_{\parallel} to the wave vector component parallel to the transport direction. Once the transmission is obtained, the transport coefficient is calculated within the framework of the ballistic Landauer theory as:

$$K_{ph} = \frac{1}{h} \int T_{ph}(\omega) \hbar \omega \frac{\partial n(\omega)}{\partial T} d(\hbar \omega) \quad (3)$$

Where $n(\omega)$ denotes the Bose-Einstein distribution function [29].

3. RESULTS AND DISCUSSION

Figure 2 compares the phonon density of states (DOS) and the transmission of the the pristine graphene (solid-

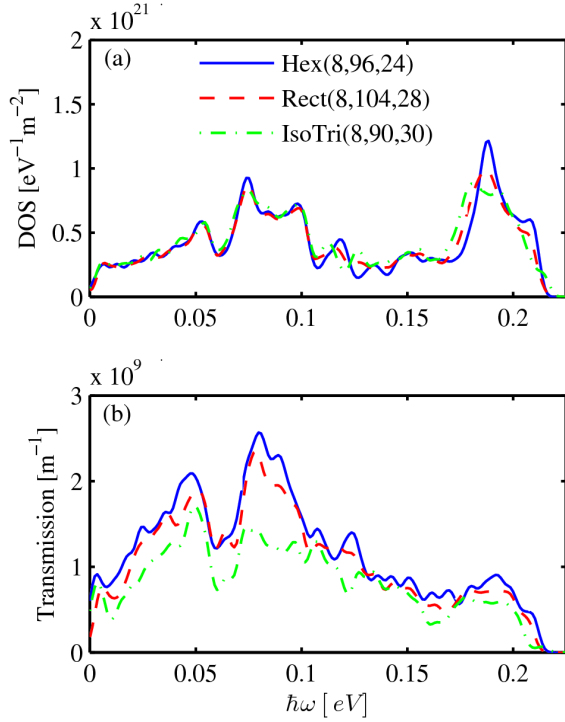


Fig. 3: Comparison between (a) phonon density of states and (b) transmission of different GALs.

black line) to those of the Hex(8,96,24) GAL (dashed-blue line). The GAL DOS in Fig. 2a is very similar to that of the pristine graphene. The phonon DOS is mostly related to the number of carbon atoms in the unit cell. Since the fill factor of the antidot lattice is $\sim 80\%$, no drastic changes are observed in the phonon DOS calculation. The transmission of the antidot lattice, on the other hand, is drastically reduced from the pristine graphene value as shown in Fig. 2b. Introduction of antidots changes the phonon group velocity and results in phonon reflections or possible localization behavior near the antidot edges, which reduces the transmission considerably. This signals a drastic change in the thermal conductance as well, as we will show later on. The important result from this observation, however, is that even small antidots, compared to the filled area of the graphene can have a large effect on the thermal properties, something which could be proven useful for the design of efficient thermoelectric devices for which low thermal conductivity is needed.

The reduction in the thermal conductance has also some dependence on the exact geometry of the antidots. The antidot shape, the number of edge atoms, the distance between neighboring antidots and the type of the edges (zigzag or armchair) have some effect on the transmission probabilities. To investigate the effect of these parameters, we compare the thermal conductance of a hexagonal, a rectangular, and a triangular GAL with similar fill-factors of 81%, 80%, and 84%, respectively. The phonon DOS and transmission probabilities are shown in Fig. 3a and 3b respectively. The three different

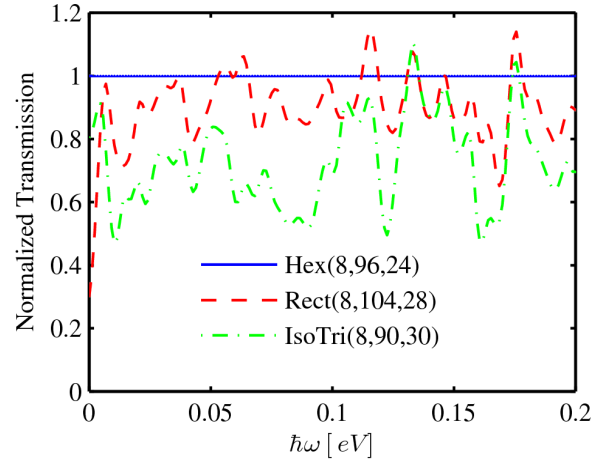


Fig. 4: Transmission of the IsoTri(8,90,30) and Rect(8,104,28) GALs normalized to the transmission of the Hex(8,96,24).

structures are labeled Hex(8,96,24) – solid/blue, Rect(8,104,28) – dashed/red, and IsoTri(8,90,30) – dashed-dot/green, respectively. The DOS in all three GALs in Fig. 3a is of similar magnitude as expected since the fill factor is nearly the same. The transmission probabilities, on the other hand, indicate some variations depending on the shape of the GALs as shown in Fig. 3b. The Hex(8,96,24) has the highest and IsoTri(8,90,30) the lowest transmission probabilities through most of the phonon energy spectrum.

The difference in the transmission, however is not large. To compare the differences in the transmission of the three different GALs, in Fig. 4 we plot the transmission probabilities of the three GALs normalized to the transmission of the hexagonal GAL, which has the highest transmission. From this figure, it is clear that the transmission of the rectangular GAL is $\sim 10\text{-}20\%$ lower than that of the hexagonal one in most of the energy spectrum. The transmission of the triangular GAL is $\sim 40\%$ lower.

There are two possible reasons why the transmission of the IsoTri(8,90,30) GAL is smaller compared to the Hex(8,96,24) GAL. The first one is geometrical in nature. The triangular GAL has a larger circumference. The triangular GAL has 30 edge atoms for each antidot, whereas the hexagonal one has 24 edge atoms. In addition, the distance between the nearest neighbor antidots in the triangular antidot case is smaller. This could be the reason behind the lowest transmission probability for the triangular antidot lattice. The second reason is related to the type of the edges that form the antidot. In a recent work, Tan et al. theoretically showed that the phonon dispersion in zigzag edge graphene nanoribbons is more dispersive compared to the phonon dispersion in armchair ribbons [30]. Phonons, therefore, tend to localize more around armchair edges. Viewing each edge in the GALs as the edge of a short ribbon, one can explain the differences between the thermal conductances. The phonon dispersion of Hex(8,96,24),

Table 1: Comparison of the thermal conductances of different GALs. The results are normalized to the thermal conductance of pristine graphene.

Structure	Normalized thermal conductance
Pristine Graphene	1
Hex(8, 96, 24)	0.2202
IsoTri(8, 90, 30)	0.1464
Rect(8, 104, 28)	0.1894

which has only zigzag boundaries is more dispersive, whereas that of the IsoTri(8,90,30) antidot which has only armchair edges is less dispersive. The transmission probability is, therefore, larger in Hex(8,96,24). The Rect(8,104,28) has both zigzag and armchair edges. Its circumference, with 28 atoms is larger than that of the hexagonal antidot but smaller than that of the triangular one. Therefore, its phonon transmission probability lies between those of the Hex(8,96,24) and IsoTri(8,90,30) structures. Although further work is needed in order to clearly identify the reasons behind these variations in the transmission, our results indicate that the geometry and the edge types would play a part in this.

The reduction in the transmission probabilities of the antidot lattices compared to pristine graphene, as well as the differences in the transmission between the different antidot shapes will result in different thermal conductances as well. The thermal conductance is calculated using the Landauer formalism in the ballistic limit as shown in Eq. 3. Table 1 summarizes the results for the thermal conductance of GALs normalized to the pristine graphene conductance. The thermal conductance of the GALs is reduced to ~20% of the original pristine graphene value, which indicates that such channel could be utilized for thermoelectric applications, where such large reductions in the thermal conductance are highly desirable.

4. CONCLUSION

The phonon density-of-states, transmission probability and ballistic thermal conductance for hydrogen-passivated graphene antidot lattices of ~80% fill factor was theoretically investigated. First principle calculations were used for the phonon bandstructure, and the ballistic Landauer approach for phonon transport calculation. We show that the ballistic thermal conductance can decrease up to ~5X by introducing antidots in the pristine graphene lattice. Geometrical parameters, such as area, circumference, and boundary edge of antidots could also be utilized as design parameters for achieving additional thermal conductance reduction optimization, although small. Among all the GALs studies in this work, the triangular antidot has the lowest thermal conductance, possibly because of its longest boundary and its smallest distance between neighboring antidots at the same fill factor compared to hexagonal or rectangular geometries.

5. ACKNOWLEDGEMENTS

This work was supported by the Austrian Climate and Energy Fund (Contract No. 825467) and the Austrian Science Fund FWF (Contract F2509).

6. REFERENCES

- [1] G. Nolas, J. Sharp, H. Goldsmid, *Thermoelectrics: Basic Principles and New Materials Developments*, Springer, 2001.
- [2] H. Goldsmid, *Introduction to Thermoelectricity*, Springer, 2010.
- [3] L. Weber, E. Gmelin, *Appl. Phys. A* **53**, 136 (1991).
- [4] A.I. Hochbaum, R. Chen, R. Delgado, W. Liang, E. Garnett, M. Najarian, A. Majumdar, P. Yang, *Nature* **451**, 163 (2008).
- [5] A. Boukai, Y. Bunimovich, J. Tahir-Kheli, J.K. Yu, W. Goddard, J. Heath, *Nature* **451**, 168 (2008).
- [6] R. Venkatasubramanian, E. Siivola, T. Colpitts, B. O'Quinn, *Nature* **413**, 597 (2001).
- [7] T.C. Harman, P.J. Taylor, M.P. Walsh, B.E. LaForge, *Science* **297**, 2229 (2002).
- [8] Z. Xiaofang, J. Zuimin, L. Jianhui, T. Xiaodong, C. Qingming, Z. Hui, Z. Pengxiang, *J. Phys. D: Appl. Phys.* **42**, 225303 (2009).
- [9] K. Novoselov, A. Geim, S. Morozov, D. Jiang, Y. Zhang, S. Dubonos, I. Grigorieva, *Science* **306**, 666 (2004).
- [10] L. Falkovsky, *IOP J. Phys.:Conf. Ser.* **129**, 012004 (2008).
- [11] A. Balandin, S. Ghosh, W. Bao, I. Calizo, D. Teweldebrhan, F. Miao, C. Lau, *Nano Lett.* **8**, 902 (2008).
- [12] K. Kim, Y. Zhao, H. Jang, S. Lee, J. Kim, K. Kim, J.H. Ahn, P. Kim, J.Y. Choi, B. Hong, *Nature* **457**, 706 (2009).
- [13] J.H. Chen, C. Jang, S. Xiao, M. Ishighami, M. Fuhrer, *Nature Nanotech.* **3**, 206 (2008).
- [14] J.H. Seol, I. Jo, A.L. Moore, L. Lindsay, Z.H. Aitkenhary, M.T. Pettes, X. Li, Z. Yao, R. Huang, D. Broido, N. Mingo, R.S. Ruoff, L. Shi, *Science* **328**, 213 (2010).
- [15] M. Han, B. Ozyilmaz, Y. Zhang, P. Kim, *Phys. Rev. Lett.* **98**, 206805 (2007).
- [16] T.G. Pedersen, C. Flindt, J. Pedersen, A.P. Jauho, N.A. Mortensen, K. Pedersen, *Phys. Rev. B* **77**, 245431 (2008).
- [17] A.A. Balandin, S. Ghosh, W. Bao, I. Calizo, D. Teweldebrhan, F. Miao, C.N. Lau, *Nano Lett.* **8**, 902 (2008).
- [18] J. Hone, M. Whitney, C. Piskoti, A. Zettl, *Phys. Rev. B* **59**, R2514 (1999).
- [19] H. Sevincli, G. Cuniberti, *Phys. Rev. B* **81**, 113401 (2010).
- [20] Z. Guo, D. Zhang, X.G. Gong, *Appl. Phys. Lett.* **95**, 163103 (2009).
- [21] Y. Ouyang, J. Guo, *Appl. Phys. Lett.* **94**, 263107 (2009).
- [22] H. Zhang, G. Lee, A.F. Fonseca, T.L. Borders, K. Cho, *Journal of Nanomaterials* **2010**, 537657 (2010).
- [23] J. Bai, X. Zhong, S. Jiang, Y. Huang, X. Duan, *Nature Nanotech.* **5**, 190 (2010).
- [24] J. Eroms, D. Weiss, *New J. Phys.* **11**, 093021 (2009).
- [25] D.W. Boukhvalov, M.I. Katsnelson, A.I. Lichtenstein, *Phys. Rev. B* **77**, 035427 (2008).
- [26] D. Sanchez-Portal, P. Ordejon, E. Artacho, J.M. Soler, *Int. J. Quantum Chem.* **65**,453 (1997).
- [27] J.P. Perdew, K. Burke, M. Ernzerhof, *Phys. Rev. Lett.* **77**, 3865 (1996).
- [28] S. Datta, *Quantum Transport: Atom to Transistor*, Cambridge University Press, Cambridge, 2005.
- [29] Y. Ouyang and J. Guo, *Appl. Phys. Lett.* **94**, 263107 (2009).
- [30] Z. Tan, J. Wang, and C. Gan, *Nano Lett.* **11**, 214 (2011).

RAMAN MONITORING OF STRAIN INDUCED EFFECTS IN MECHANICALLY DEPOSITED SINGLE LAYER GRAPHENE

Paola Russo*¹, Giuseppe Compagnini¹, Cristiano D'Andrea², Onofrio M. Maragò,² Pietro G. Gucciardi², J. -C. Valmalette^{3,4}

¹*Dipartimento di Scienze Chimiche, Università di Catania, Viale A. Doria 6 Catania 95125 Italy*

²*CNR-Istituto per i Processi Chimici-Fisici, Viale F. Stagno D'Alcontres, I-98158 Messina, Italy*

³*Université du Sud Toulon Var, BP 20132, F-83957 La Garde Cedex, France*

⁴*CNRS, IM2NP (UMR 6242), BP 20132, F-83957 La Garde Cedex, France*

* E-mail: paolarusso@gmail.com

ABSTRACT

Graphene shows remarkable electronic and optical properties which is attracting enormous interest in the materials community. In order to make graphene a real technology, a control of its properties is a must. In this respect, a crucial step for the use of graphene in device fabrication is the deposition onto suitable substrates. Till now, micromechanical cleavage of graphite produces high-quality graphene sheets. The aim of this work is to study the strain effects induced in graphene during the production. This study reveals that the deposition method randomly produces strained and unstrained graphene sheets, which can be distinguished through Raman spectroscopy and Atomic Force Microscopy (AFM).

1. INTRODUCTION

Single layer graphene, defined as a two-dimensional (2D) honeycomb lattice of carbon atoms, has stimulated a lot of interest because it exhibits exceptionally high crystal and electronic quality, making it a promising candidate for applications in many fields such as gas storage, microelectronics and photovoltaics [1, 2]. One of the most interesting properties of graphene is related to its mechanical behaviour [3]. This fact together with a controlled variation of the electronic system through the introduction of foreign species [4, 5] or induced defects [6,7] is of great importance since one atom thick graphene films represents the ultimate limit in miniaturization in the previously mentioned applications. Because graphene is a single-layer membrane, it is also amenable to external perturbations, such as mechanical deformation. Recent proposals suggest that strain, which arises when a crystal is compressed or stretched out of equilibrium, can be used to engineer graphene electronic states through the creation of a pseudo-magnetic field [8]. Strain is sometimes intentionally applied in order to improve mobility, as in the strained silicon technology, which is used in modern microelectronics. In any case the precise determination and monitoring of intentional or unintentional stress and strain are an essential prerequisite for understanding and tuning the interplay between the geometrical structure of graphene and its electronic properties. Spectroscopic and microscopic techniques such as Raman spectroscopy and Atomic

Force Microscopy (AFM) have been the main tools for the characterization of unstrained and strained graphene sheets.

In this paper we have studied several graphene layers obtained by mechanical exfoliation and we have observed that this method frequently leads to the deposition of strained sheets because of the mechanical stress induced during the deposition procedure. The stressed layers are randomly distributed onto the substrate and the strain can be partially restored by using suitable thermal annealing procedures.

2. EXPERIMENTAL SECTION

Mechanical exfoliation of a Highly Oriented Pyrolytic Graphite (HOPG) was employed to transfer single-layer graphene sheets on a Si/SiO₂ substrate with an oxide thickness of 300 nm in order to maximize the optical contrast of graphene on the substrate [9, 10].

Despite more efficient procedures have been presented in the literature [11, 12], mechanical exfoliation remains the best method in order to obtain defect free graphene layers, furthermore it leads to deposition onto the substrate surface a large number of randomly dispersed graphene islands with several thickness, from single-layers to multi-layers graphene sheets.

To provide identification of single layers, the samples were investigated with an optical microscope and then by SFM, their presence afterwards was confirmed by performing micro-Raman spectroscopy.

Dynamic SFM was carried out in air using a commercial instrument (MultimodeNanoscope IIIa, Digital Instruments, Santa Barbara, California) equipped with a phase extender apparatus and a Q-box module.

Etched-silicon probes with a pyramidal-shape tip having a nominal curvature of 10 nm and a nominal internal angle of 35° were used. During the scanning, the 125-µm-long cantilever, with a nominal spring constant in the range of 20–100 N m, oscillated at its resonance frequency (~330 kHz). Height and phase images were collected by capturing 512 x 512 points in each scan and the scan rate was maintained below 1 lines per second. Phase images have been collected to qualitatively highlight different materials or defects on the sample. During the imaging, temperature and humidity were about 293 K and 40%, respectively.

Raman spectra were acquired with excitation at 514.5 nm (Ar ion laser) and analyzed by a Jobin Yvon 450 mm focal length monochromator, equipped with a CCD camera detector cooled at 77 K. The incident laser beam was focused by a 100x objective and the laser power on the samples was kept to a minimum to avoid heating. Raman spectra at 632.8 nm wavelength were carried out with a homemade setup employing a HR460nm spectrometer, coupled to an Olympus BX microscope, and equipped with a CCD camera, LN₂ cooled at 77 K. Raman line profiles were acquired at 514.5 nm on a HR800 Raman spectrometer mounting a Physics Instruments Piezotable (model P-733.2CD) capable of 100x100 mm² scan with 0.3 nm resolution.

3. RESULTS AND DISCUSSION

Raman spectroscopy is an important, non-destructive tool to study the properties of carbon based materials [13]. For graphene, Raman spectroscopy has been successfully employed to investigate phonon properties and electron-phonon coupling, to identify the number of graphene layers and to provide information about the doping and disorder.

The typical Raman spectrum of a defect-free graphene layer shows two main features: the so-called G band appearing at 1582 cm⁻¹ and the 2D band (also called G' in some works) at 2700 cm⁻¹. When the sample presents some defects or at the edge of each layer it is also possible to detect the disorder-induced D-band at about half of the frequency of the 2D band (around 1350 cm⁻¹) [14, 15]. The G band originates from in-plane vibration of sp² carbon atoms. It is a doubly degenerate (TO and LO) phonon mode (E_{2g} symmetry) at the Brillouin zone centre and represents the only band coming from a first order Raman scattering process in defect free graphene. The 2D band originates from a two phonon double resonance Raman process, involving two TO phonons near the K point, while the D-band arises from a process involving one TO phonon and one defect. For a single layer graphene the 2D band at room temperature exhibits a single Lorentzian lineshape with a full width at half maximum (FWHM) of ~24 cm⁻¹. Moreover in single layer graphene the 2D signal is generally more intense than the G one because of a triple resonance process. All these features allow to distinguish graphene from thicker flakes [16].

In fig. 1 we report two typical Raman spectra of two deposited graphene layers obtained under similar conditions as described in the experimental section. It is important to consider that these two layers are representative of a very common situation randomly observed in our production method. Both spectra do not show any relevant D band signal at about 1350 cm⁻¹ confirming the absence of a significant number of defects, but we noticed some pronounced differences. In particular spectrum (a) exhibits the characteristic features of a single layer graphene as previously described, while spectrum (b) shows an asymmetric and broader 2D band and a different 2D/G intensity ratio.

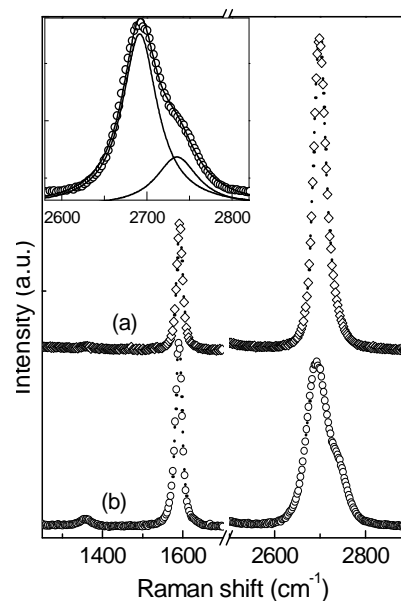


Fig.1: Raman Spectra for two typical single layer graphene obtained after mechanical exfoliation and deposition onto a SiO₂/Si substrate. The inset shows a deconvolution of the 2D band relative to spectrum (b).

Moreover the 2D band in spectrum (b) can be fitted with two distinct peaks (see inset fig.1), which we denote by 2D⁻, at 2691 cm⁻¹, and 2D⁺, at 2734 cm⁻¹ according to a notation reported in literature [17].

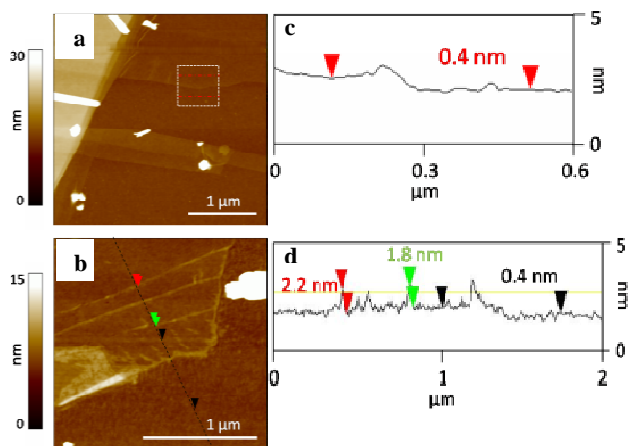


Fig. 2: Topographic (a, b) images relative to the flakes analyzed by Raman spectroscopy and reported in fig.1. Sections are also shown in c and d, showing the layer thicknesses and the height of the observed creases (bright contrast in the phase and topographic images).

Indication on the morphology and the structural parameters of the two layers analyzed can be obtained by AFM as reported in Fig. 2.

In this figure we show the topographic (a, b) as well as their section analysis (c, d). These revealed that both the analyzed sheets consist in a single layer graphene with a step height of about 0.4 nm in agreement with literature data [18]. The topographic images also showed that the morphology of the two layers is markedly different, in particular, the flake that have been previously characterized by Raman spectroscopy and reported in fig.

1 (a), appears as a flat surface, while the flake in fig. 2 (b), whose spectrum is shown in fig. 1 (b), seems to have corrugation lines like creases in a tissue. Probably these folds could induce a stress in the graphene layer and be the cause of the already discussed differences in the two Raman spectra.

Recently some research groups have reported Raman studies of the 2D mode of single layer graphene under uniaxial strain, observing an induced modification of the 2D band [17, 19]. In these works graphene layers were deposited onto flexible PDMS (polydimethylsiloxane) substrates and by bending the substrates, the graphene flakes were subjected to an uniaxial strain. This result in a 2D band shift toward lower frequencies with a remarkable response. Moreover it was observed an asymmetric peak broadening and a clear splitting in two peaks $2D^-$ and $2D^+$. This splitting increases with increasing the strain value. It was also found that the intensity ratio of the two components $2D^-$ and $2D^+$ depends on the angle between the direction of the applied strain (ϵ) and the polarization of the incident light (P) during Raman measurements. In particular the studies showed that when the polarization of the incident light is parallel to the strain direction, $2D^-$ is dominant. We collected different Raman spectra varying the angle between the direction of the strain (ϵ) and the direction of the polarization of the incident light (P). In such a case we are assuming that the strain direction is perpendicular to the folds.

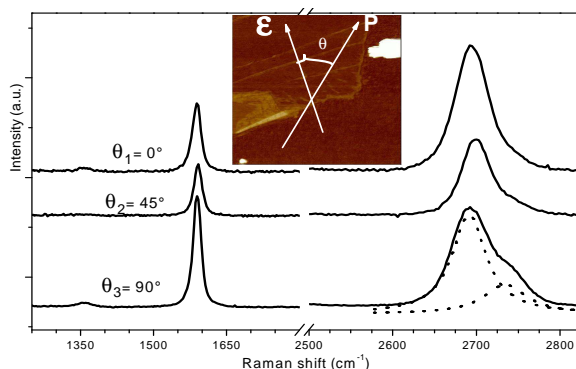


Fig.3: Evolution of the 2D modes for the single layer graphene with folds as a function of the angle (θ) between the strain direction (ϵ) and the polarization of the incident light (P).

Some of the Raman spectra obtained are shown in Fig. 3, in this case θ is the angle between the polarization of the incident light and the direction orthogonal to the observed corrugations in sample (b) as shown in the inset in Fig. 3. As expected the intensity ratio of the two peaks ($2D^-$ and $2D^+$) varies as a function of the angle between P and ϵ . Moreover it is noteworthy that the 2D band intensity at $P // \epsilon$ is smaller than the intensity at $P \perp \epsilon$, in agreement with ref. 17. For the same sample we collected Raman spectra also with the 632.8 nm wavelength, but we didn't notice any changes in the spectra.

What is remarkable is the fact that every time we deposit graphene layers onto a Si/SiO₂ substrate with the "Scotch tape" technique we randomly obtain corrugated samples.

Fig. 4 reports a sample where a step by step stacking from single layer to multilayers is present (a). There we performed some Raman spectra as indicated in (b). As we can see from the spectra labeled 1, 2, 3 and 4, the 2D band of the single layer is broad and asymmetric and we can distinguish the 2 components $2D^-$ and $2D^+$.

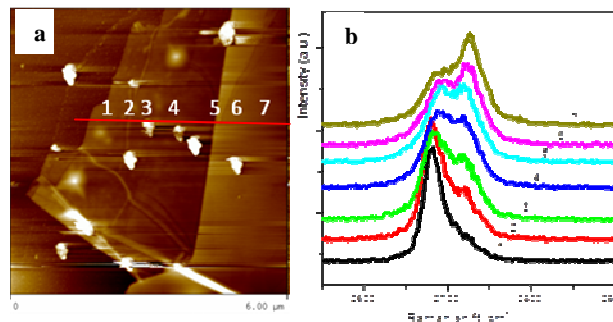


Fig.4: (a) topographic image of a sample prepared by mechanical exfoliation. It is possible to notice the presence of some folds. (b) Raman spectra collected along the sample. It is clear the splitting of 2D band in two components $2D^-$ and $2D^+$.

The three spectra indicated in fig. 4 (b) with the numbers 5,6,7 are similar to the multilayers spectra, thus confirming that we performed the analysis on the thicker layers showed in the topographic image fig.4 (a).

CONCLUSIONS

From these observations it is clear that the "Scotch tape" deposition method accidentally and randomly induces deformations on the deposited single layer graphene which can be easily observed by AFM. These corrugations results in a strain which can be measured using Raman spectroscopy as suggested in literature. The entity of such a strain, related to the $2D^+ - 2D^-$ separation, is reported in Fig. 5.

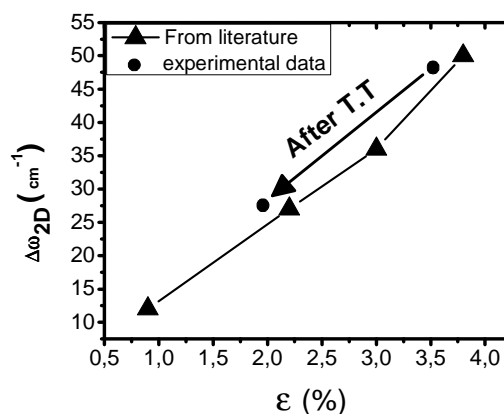


Fig.5: Change in the $2D^- - 2D^+$ distance as a function of the strain as reported in ref [17]. The figure also reports the splitting value for the corrugated sample presented in this work, before and after a thermal treatment at 300° C in vacuum.

Preliminary results have shown that thermal annealing at 300°C consistently reduce the strain value as reported in

the same Fig. 5. Further measures are underway to clarify the role of temperature in releasing the strain.

ACKNOWLEDGEMENT

The authors wish to thank Chiara Musumeci for her precious support.

REFERENCES

- [1] E. Stolyarova, D. Stolyarov, K. Bolotin, S. Ryu, L. Liu, K. T. Rim, M. Klima, M. Hybertsen, I. Pogorelsky, I. Pavlishin, K. Kusche, J. Hone, P. Kim, H. L. Stormer, V. Yakimenko and G. Flynn, *Nano Lett.*, **9**, 332, (2009).
- [2] A. K. Geim and K. S. Novoselov, *Nat. Mat.*, **6**, 183 (2007).
- [3] W. Frank, D. M. Tanenbaum, A. M. van der Zande, and P. L. McEuen, *J. Vac., Sci. Technol. B*, **25**, 2558 (2007).
- [4] G. Giovanetti, P. A. Khomyakov, G. Brocks, V. M. Karpan, J. van den Brink and P. J. Kelly, *Phys. Rev. Lett.*, **101**, 026803 (2008).
- [5] C. Coletti, C. Riedl, D. S. Lee, B. Krauss, L. Patthey, K. von Klitzing, J. H. Smet, and U. Starke, *Phys. Rev. B* **81**, 235401 (2010).
- [6] G. Compagnini, F. Giannazzo, S. Sonde, V. Raineri and E. Rimini, *Carbon*, **47**, 3201, (2009).
- [7] G. Compagnini, G. Forte, F. Giannazzo, V. Raineri, A. La Magna, I. Deretzi, *J. Mol. Struct.*, **993**, 506, (2011).
- [8] N. Levy, S. A. Burke, K. L. Meaker, M. Panlasigui, A. Zettl, F. Guinea, A. H. Castro Neto, and M. F. Cromie, *Science*, **329**, 5991,
- [9] K. S. Novoselov, D. Jiang, F. Schedin, T. J. Booth, V. V. Khotkevich, S. V. Morozov, A. K. Geim, *Proc. Natl. Acad. Sci. U.S.A.* **102**, 10451 (2005).
- [10] K. S. Novoselov, A. K. Geim, S. V. Morozov, D. Jiang, Y. Zhang, S. V. Dubonos, I. V. Grigorieva and A. A. Firsov, *Science*, **306**, 5696 (2004).
- [11] F. Cataldo, G. Compagnini, G. Patané, O. Ursini, G. Angelini, P. R. Ribic, G. Margaritondo, A. Cricenti, G. Palleschi, F. Valentini, *Carbon*, **48**, 2596, (2010)
- [12] M. Lotya, Y. Hernandez, P. J. King, R. J. Smith, V. Nicolosi, L. S. Karlsson, F. M. Blighe, S. De, Z. Wang, I. T. McGovern, G. S. Duesberg and J. N. Coleman, *J. Am. Chem. Soc.* **131**, 3611, (2009)
- [13] L. D'Urso, G. Compagnini, O. Puglisi, *Carbon*, **44**, 2093 (2006).
- [14] L. M. Malard, M. A. Pimenta, G. Dresselhaus, M. S. Dresselhaus, *Phys. Rep.* **473**, 51 (2009).
- [15] G. Compagnini and G. Baratta, *Appl. Phys. Lett.*, **61**, 1796 (1992).
- [16] A. C. Ferrari, J. C. Meyer, V. Scardaci, C. Casiraghi, M. Lazzeri, F. Mauri, S. Piscanec, D. Jiang, K. S. Novoselov, S. Roth and A. K. Geim, *Phys. Rev. Lett.*, **97**, 187401 (2006).
- [17] M. Huang, H. Yan, T. F. Heinz and J. Hone, *Nano Lett.*, **10**, 4074 (2010).
- [18] A. Hashimoto, K. Suenaga, K. Urita, T. Shimada, T. Sugai, S. Bandow, H. Shinohara and S. Iijima, *Phys. Rev. Lett.*, **94**, 045504 (2005).
- [19] O. Frank, M. Mohr, J. Maultzsch, C. Thomsen, I. Riaz, R. Jalil, K.S. Novoselov, G. Tsoukleri, J. Parthenios, K. Papagelis, L. Kavan and C. Galiotis, *ACS Nano*, **5**, 2231, (2011).

CARBON NANOSTRUCTURES FOR GAS SENSING APPLICATIONS

M. Penza

ENEA, Italian National Agency for New Technologies, Energy and Sustainable Economic Development, Technical Unit Brindisi Technologies for Materials, Brindisi, Italy

E-mail: michele.penza@enea.it

ABSTRACT

Carbon nanotubes and other carbon nanostructures have been successfully processed and engineered for advanced gas microsensors with novel functional properties. Their superior gas sensing properties can be enhanced by surface-functionalizations with metal nanoclusters (i.e., Pt, Pd, Au, Ag, Ru, etc.) and other foreign materials (metalloporphyrins, metal oxides, polymers, DNA, etc.), including functional groups attached covalently/non-covalently to their sidewalls, and nanocomposites. Here, a review will highlight some illustrative examples of carbon nanotubes for performing gas detection applications.

1. INTRODUCTION

At the current state-of-art, carbon nanotubes (CNTs) [1-14] and other carbon-based nanostructures have been successfully processed and studied for innovative gas microsensors with novel functional properties, at the level of advanced proof-of-concepts and nanoscale prototypes. Due to very high surface-to-volume ratio, hollow nanostructure, high electron mobility, great surface reactivities and high capability of gas adsorption, CNTs have been investigated as building blocks for fabricating novel devices at nanoscale such as high-performance gas sensors and nano-platforms for biosensing.

We investigate carbon nanotubes in the format of networked layers at multi-walled structure grown by RF-PECVD and CVD technology onto alumina low-cost substrates for gas sensing applications. In particular, CNTs have many distinct properties that may be exploited to develop the next generation of gas sensors with high sensitivity, broad selectivity, low limit of detection up to a ppb level, good stability, low power consumption, repeatability, wireless communication and low-cost.

The gas sensing properties of the CNTs networked layers can be enhanced by surface-functionalizations with metal nanoclusters (Pt, Pd, Au, Ag, Ru, etc.) [5,7,8,9] and other nanostructured functional materials (metalloporphyrins, semiconducting oxides, polymers, DNA, etc.), including functional groups attached covalently/non-covalently to their walls [2,4,10,11,13]. The functional carbon-nanostructures can be integrated in a wide portfolio of advanced transducers for innovative gas microsensors such as chemiresistors (CRs), Field Effect Transistors (FETs), Surface Acoustic Waves (SAWs), Quartz Crystal Microbalances (QCMs), Thin Film Bulk Acoustic Resonators (TFBARs), optical fibers, etc.

This lecture will review highlights and illustrative examples from gas sensing area to give an overview of applications of carbon-based nanostructures for advanced gas detection and chemical sensing. The final part of lecture will be devoted to some current research projects on gas sensors based on functional carbon-nanostructures and sensor-systems at ENEA in Brindisi Research Center.

2. SYNTHESIS OF CARBON NANOTUBES

Primary synthesis methods for single-walled (SWCNTs) and multi-walled carbon nanotubes (MWCNTs) at the bottom-up approach include arc-discharge, laser-ablation, chemical vapor deposition (CVD), pyrolysis, gas-phase catalytic growth from carbon monoxide (HiPco), electrochemical methods [15]. These synthesis methods provide direct growth of the carbon nanotubes onto substrates, mainly coated by catalysts. During nanotubes synthesis, impurities in the form of catalyst particles, amorphous carbon, non-tubular fullerenes, non-nanotube material are also produced. This means that a controlled method for fabrication of carbon nanostructures and nanomaterials does not exist yet. Thus, subsequent purification steps are required to separate nanotubes and to remove impurities (metals, catalysts, amorphous carbon, etc.) that could suppress the advantageous properties of the carbon nanotubes at nanoscale. Each of these synthesis techniques has its advantages and disadvantages, which are discussed in the extensive literature available on this topic [16-18].

The current state-of-the-art of CNTs fabrication focuses on the direct growth of the nanomaterial onto catalysed substrates with nano-patterned transition metals (Fe, Co, Ni, etc.). This means that CNTs bundles tend to grow perpendicularly to the catalysed surface according to a *forest-like* structure with a dense network of vertically-aligned individual nanotubes [19]. However, there is no convincing approach yet for growing dense CNTs mats parallel to the chip surface in two perpendicular directions. A controlled approach for horizontal alignment of the CNTs can be an electrical field applied to induce alignment of the CNTs rope or individual nanotube parallel to the electric field. This method has been successfully applied on silicon substrate with an external alternating-current electric field [20]. Another approach to align CNTs is to apply a surface acoustic wave to a liquid CNTs suspension. The lateral piezoelectric field of the standing wave can align the carbon nanotubes with a controlled angle with respect to

the direction of the wave propagation [21]. It is demonstrated also that the dielectrophoretic force (DEP) due to an electrical field can align and orient the carbon nanotubes for a rapid assembly to build practical nanosensors [22]. Smith *et al.* [23] produced thick films of aligned SWCNTs and ropes by filtration/deposition from suspension in strong magnetic fields.

Generally, CNTs are very often used to coat a transducer to provide new functionalities. This approach is based commonly on a CNTs suspension to be deposited onto planar surfaces, platforms or devices through various methods such as spray-coating [24], solvent-casting [25], Langmuir-Blodgett thin-film technique [26-27].

In Table 1, a comparison of processes and conventional technologies used to grow CNTs directly onto catalyst-coated substrate is reported.

Table 1. Comparison of processes and technologies used to grow directly carbon nanotubes onto substrates.

SYNTHESIS PROCESS	GROWTH TEMPERATURE	GROWTH RATE	CNTs CHARACTERISTICS
Arc-discharge	2000 - 3000°C	~ 1 mm/min (20 V-100 A)	- Few defects of pentagons/heptagons on walls - By-products of non-nanotube material - Length CNTs: 1-30 µm; Diameter CNTs: 5-30 nm - Mass production: 10 g/day (97% yield SWCNTs)
Laser-ablation	1000 - 1500°C	< 1 mm/min	- Few defects of pentagons/heptagons on walls - By-products of non-nanotube material - Length CNTs: 1-30 µm; Diameter CNTs: 5-20 nm - Mass production: 10 g/day (97% yield SWCNTs)
CVD	400 - 1100°C	~ 0.5 µm/min	- Many structural defects on walls - Minor by-products of non-nanotube material - Length CNTs: 1-50 µm; Diameter CNTs: 1-30 nm - Mass production: 50 kg/day (70-80% yield CNT)
HiPco	800 - 1200°C	~ 5 µm/min	- High-quality structural SWCNTs - Length CNTs: 1-20 µm; Diameter CNTs: 1-5 nm - Mass production: 1 kg/day (90% yield CNT)

2.1. CVD Technology for CNTs growth

This synthesis technique utilizes metal catalyst clusters in the gas phase or on substrate surfaces to decompose a carbon containing feedstock gas, such as methane (CH₄), acetylene (C₂H₂), ethylene (C₂H₄), carbon monoxide (CO), or their combination in a proper gas-mixture. The resulting carbon atoms dissolve in, or are adsorbed on, the catalyst particles and are released in the form of a nanotube starting with a buckyball-type cap when the concentration exceeds the maximum solubility. The nanotube continues to grow as long as carbon continues to be delivered at the right rate and the form of catalyst does not change. The growth temperature depends on the type of nanotube to be grown, the catalyst composition and size, and lies in the range 400 - 1100°C, lower than temperatures used in the arc-discharge or laser-ablation processes. For this reasons, it is believed that CVD nanotubes have a higher density of defects.

The advantage of CVD nanotube production is the possibility of structuring the catalyst particles and, hence,

selectively growing the nanotubes where they are required. Moreover, under the right experimental conditions, only nanotubes are fabricated and minor unwanted graphitic material.

The general nanotube growth mechanism in a CVD process involves the dissociation of hydrocarbon molecules catalyzed by the 3d transition metal (Co, Fe, Ni, etc.), and dissolution and saturation of carbon atoms in the metal nanoparticles. The precipitation of the carbon atoms from the saturated metal particle leads to the formation of the tubular carbon solids in sp² structure. The tube formation is favored over other forms of the carbon such as graphitic sheets with open edges. This is because a tube contains no dangling bonds and therefore is in a low-energy form. For MWCNTs growth, most of the CVD methods employ ethylene or acetylene as the carbon feedstock and the growth temperature is typically in the range of 550 - 750°C. Iron, nickel or cobalt nanoparticles are often used as catalyst. At high temperatures, carbon has finite solubility in these transition metals, which leads to the formation of metal-carbon solutions and therefore the previously mentioned growth mechanisms. Extensive literature on CNTs growth mechanisms including experimental and theoretical aspects has been reviewed in various reports [28-29].

CVD nanotube growth is believed to promise an enhanced control of the fabricated carbon nanotubes better than the other techniques such as arc-discharge and laser-ablation.

The choice of the carbon feedstock gas is one of the key elements to the growth of high-quality carbon nanotubes containing no defects and very-low content of amorphous carbon. It was demonstrated by H. Dai and co-workers [30] that the chemical and textural properties of the catalyst materials dictate the yield and quality of the SWCNTs by using methane as feed-gas in the CVD growth. A catalyst consisting of Fe/Mo bimetallic species supported on a sol-gel derived alumina-silica multilayer material produces individual SWCNTs and bundle of single-walled carbon nanotubes with a surface area of 200 m²/g, grown at 900°C in a quartz-tube furnace. The diameters of the SWCNTs are dispersed in the range of 0.7 - 3 nm with a peak at 1.7 nm. The yield of the nanotubes is up to a value of 45 wt.%; e.g., 1 gram of catalyst yields 0.45 gram of SWCNTs.

2.1.1. CVD-growth of CNTs at ENEA Lab

Multi-walled carbon nanotubes (MWCNTs) networked films were grown by chemical vapour deposition (CVD) technology [31] onto alumina substrates previously coated with Cobalt (Co) sputtered nanosized catalyst of nominal thickness of 7.5 nm. The substrate size was 5 mm width x 5 mm length x 0.6 mm thickness. A thermal CVD apparatus was used for growing carbon nanotubes. The substrates were placed in a quartz boat and then inserted into the center of a 1-inch diameter quartz tube reactor housed in a furnace. The tube was evacuated at a base pressure of 5 x 10⁻³ Torr by a rotative pump. Hence the substrates were heated up to 550°C in a H₂ flux of 100 sccm at a working pressure of 100 Torr. Then, acetylene

(C₂H₂) was introduced at a flow rate of 20 sccm added to H₂ at a flow rate of 80 sccm. The flow rate was controlled using two separate mass flow controllers. The CNT growth was performed with a total pressure of 100 Torr for 30 minutes. After growth, the furnace was cooled to room temperature in H₂ atmosphere. Then, a pair of metal strips of Cr/Au (20 nm/300 nm) was vacuum sputtered onto CNTs films to serve as electrical contacts for a gas sensor configured as a two-pole chemiresistor. The Cr/Au electrode sizes were 1 mm width x 5 mm length. The gap between two electrodes was 3 mm.

2.2. RF-PECVD Technology for CNTs growth

Another aspect of the CVD technique is its ability to synthesize aligned arrays of the carbon nanotubes with controlled diameter and length. The synthesis of well-aligned and straight carbon nanotubes on a variety of substrates has been accomplished by the use of plasma-enhanced chemical vapor deposition (PECVD), where the plasma is excited by a RF or DC source, or a microwave source. Ren *et al.* [32] have grown aligned carbon nanotubes onto substrates coated by nickel catalyst by using ammonia as catalytic gas and acetylene as carbon source-gas. A DC power generates the required PECVD plasma and a tungsten hot-filament assists the dissociation of the reactive gases and supply heat to the substrate for the growth of the nanotubes. M. Penza *et al.* [6] demonstrated that RF-PECVD is a valid deposition system to grow networked films onto alumina substrates differently coated by catalysts of Co and Fe to promote synthesis of dense multi-walled carbon nanotubes for enhanced gas sensing applications. A review of the CNTs synthesis by PECVD method has been proposed by M. Meyyappan *et al.* [33]. H. Dai and co-workers [34] have grown CVD-based array of aligned carbon nanotubes for studying the field emission properties.

For the catalytic growth of carbon nanotubes in the CVD technique, two models have been proposed to explain the experimental observations: the *base-growth* and *tip-growth*, which were originally developed for the catalytic growth of the carbon filament [35]. In the case of PECVD growth, the catalytic particles are usually found at the tip and explained by the *tip-growth* model. On the contrary, the *base-growth* model has been used to explain the vertically aligned carbon nanotube growth by thermal CVD using iron catalyst. However, the growth of aligned carbon nanotubes is possible through both tip-growth and base-growth models, depending on the catalyst and substrate used in the deposition method.

2.2.1. RF-PECVD-growth of CNTs at ENEA Lab

A Radio Frequency-discharge Plasma Enhanced Chemical Vapour Deposition (RF-PECVD) apparatus was used for the vertically-aligned CNTs growth. The substrates was coated by iron (Fe) catalysts as a thin film deposited by RF magnetron sputtering. The Fe clusters sizes ranged from 10 to 50 nm. The Fe-coated alumina substrates were placed in a stainless-steel reaction chamber onto a graphite heated electrode. Hence the

chamber was evacuated at a base pressure of 1×10^{-2} Torr by a rotative pump. A two-step procedure was used to synthesize a vertically-aligned CNTs film. In step 1, the Fe-coated substrates were first treated at 600°C in a H₂ plasma at a pressure of 1.5 Torr. The H₂ flow rate was fixed at 100 sccm, and the RF power (13.56 MHz) of 100 W was supplied for 5 minutes to promote the formation of catalyst particles and reduce iron oxides to metallic iron. In step 2, acetylene (C₂H₂) was introduced into chamber at a flow rate of 20 sccm mixed with a H₂ flow rate of 80 sccm. The flow rate was controlled using two separate mass flow controllers. The working pressure and RF power were fixed at 1.5 Torr and 100 W, respectively for 30 minutes. The parameters of the CNTs growth process are summarized in the Ref. [9].

3. CARBON NANOSTRUCTURES GAS SENSORS

One of the most widely studied nanomaterials is the carbon, not as we conventionally know it in the form of thin-films or bulk materials but in the form of hexagonal lattices of carbon atoms arranged in one-dimensional nanotubes. Carbon nanotubes [36] are effectively rolled sheets of graphite with a few nanometers in diameter and up to a tens or hundreds of microns in length.

The exceptional mix of the physical properties of the CNTs for instance the large surface area as high up to $1600 \text{ m}^2 \text{ g}^{-1}$, the high chemical reactivity of the caps and walls, the bandgap of semiconducting nanotubes tailored by diameter, the excellent mechanical strength but ultra-light weight, the high thermal stability, the high electron mobility, the rich electronic properties and ballistic transport characteristics, the high aspect ratio ranging from 10 to 1000, the hollow nanostructure with tube diameter of a few nanometers, make CNTs an ideal platform for many chemical micro/nano-sensor systems with capability of real applications.

Generally, a sensor is a device combining a transducer which converts a physical or chemical quantity into an electrical, optical, or other measurable quantity. For example, a chemical sensor, and in particular a gas sensor, is intended to determine the composition and concentration of the chemical stimulus inputs via an electrical signal output. Figure 1 shows a typical scheme of a gas sensor based on adsorbent CNTs as a proof-of-concept for a designed nanosensor.

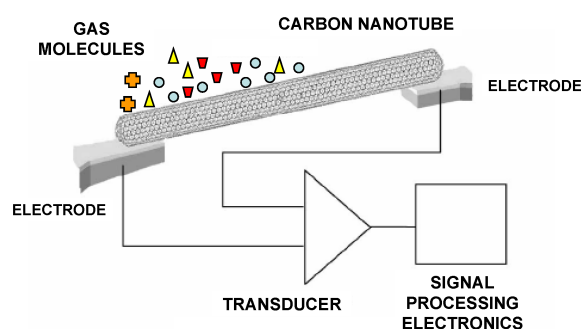


Figure 1. Scheme of a CNT-based gas sensor with advanced transducer and electronics.

3.1. Metal-modified CNTs gas sensors

The functionalization of the carbon nanotubes is a powerful strategy to improve gas sensitivity and fabricate selective nanomaterials. Functionalizing the surface of these nanostructures offers another route for expanding their chemical sensing capability. In fact, the charge exchange between an adsorbate and the carbon nanotubes changes the electron density in the nanomaterial, modifying the carrier density in the nanostructure. The surface-modifications in the nanostructures can enhance the charge transfer by applying external perturbations (electric field, radiation, thermal heating, ultrasonication), attachment of functional groups or catalytically functionalizing sidewalls of carbon nanomaterials. Recently, gas sensors based on functionalized CNTs have been proposed capable of detecting small gas concentrations with specificity. Nanoclusters of noble metals (Au, Pt, Pd, Ag, Ru, etc.) are used as decorations onto sidewalls to enhance gas sensitivity [5,7,8,9,31] of CNTs networks, operating at a sensor temperature from 20 to 250°C, to detect various gas molecules of NO₂, NH₃, H₂, CH₄, H₂S, C₆H₆, and volatile organic solvents.

3.1.1. Networked CNTs layers

M. Penza *et al.* [37] demonstrated the impact of the tailored load of Au nanoclusters functionalizing the sidewalls of the MWCNTs networks on gas sensing properties of a chemiresistor, working at a temperature ranging from 20 to 250°C. Au clusters with increasing size of 5-15 nm, 5-30 nm, and 5-60 nm enhanced gas response compared to un-modified CNTs-sensors for various reducing gases (NH₃, H₂S) and an oxidizing gas (NO₂), down up to a sub-ppm level of detection limit. Negligible responses were recorded to CO, N₂O, SO₂. Figure 2 shows Au-nanoclusters onto CNTs sidewalls and the gas sensing performance. The effect of sensor temperature on gas sensitivity is also reported. An optimal operating temperature for each Au-modified CNTs-sensor exposed to NO₂ gas has been recorded: e.g., the temperature of maximum NO₂ gas sensitivity for CNTs loaded with Au nanoclusters of 5 nm was 200°C. Good repeatability of the electrical response to 200 ppb NO₂ is also measured, at 200°C.

Moreover, a chemiresistor based on CNTs networks functionalized with sputtered Pt and Pd nanoclusters of nominal thickness of 5 nm has been fabricated by RF-PECVD technology for sub-ppm gas sensors to address chemical detection of hazardous pollutants such as NO₂. M. Penza *et al.* [5] demonstrated that the metal-functionalized CNTs-sensors provided higher sensitivity compared to un-modified CNTs for significantly enhanced gas detection of NO₂, H₂S, NH₃, CO up to a low limit of sub-ppm level. Pt- and Pd-functionalized CNTs-sensors exhibited better sensing performances compared to un-modified CNTs, and especially Pt-modified CNTs sensor was found to detect NO₂ gas in the range from 100 to 600 ppb at higher sensitivity than Pd-modified CNTs sensor, working at 200°C. These results

provide clear evidence that metal-functionalized CNTs-sensors are excellent candidates for air-pollutants sensing.

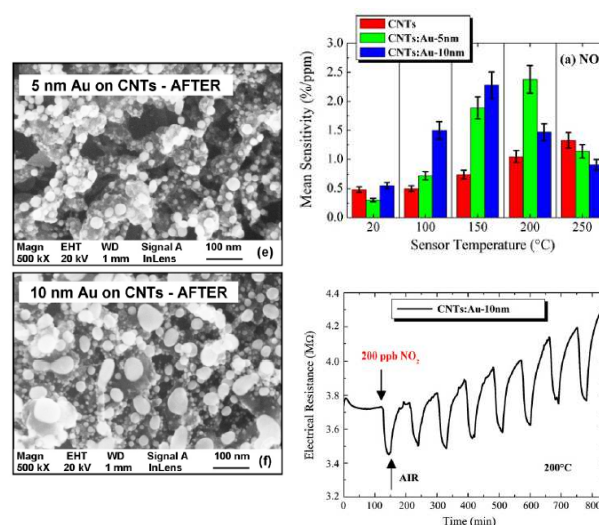


Fig. 2. SEM image of the CNTs networks with Au-clusters of loading 5 nm and 10 nm, after thermal annealing. Comparison of the mean sensitivity for three chemiresistors based on un-modified CNTs, 5 nm and 10 nm loaded-Au modified CNTs nets, versus temperature. Repeatability of the sensor response to eight pulses of 200 ppb NO₂ at 200°C. This figure is reprinted and adapted with permission from Elsevier, by M. Penza *et al.*, *Sensors Actuators B* 140 (2009) 176.

3.1.2. Vertically-aligned CNTs layers

M. Penza *et al.* [9] demonstrated vertically-aligned MWCNTs layers RF-PECVD synthesized on Fe-coated alumina substrates as *forest-like* nanostructure (see Figure 3). A miniaturized CNT-based gas sensor array was developed for monitoring landfill gas (LFG) at a temperature of 150°C. The sensor array was composed of 4 sensing elements with un-modified CNT, and CNT loaded with 5 nm nominally thick sputtered clusters of Pt, Ru and Ag. Chemical analysis of the multicomponent gas mixtures constituted of CO₂, CH₄, H₂, NH₃, CO and NO₂ was performed by array sensor responses and pattern recognition based on Principal Component Analysis (PCA). PCA results demonstrated that the metal-decorated and vertically-aligned CNT sensor array is able to discriminate the NO₂ presence in the multicomponent mixture LFG. The size of metal clusters decorating CNT top-surface varied in the range of 5-50 nm. Functional characterization based on electrical charge transfer sensing mechanisms in the metal-modified CNT-chemoresistors array demonstrated high sensitivity providing minimal sub-ppm level detection down up to 100 ppb NO₂, at 150°C.

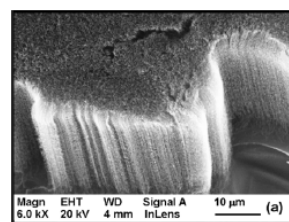


Figure 3. Vertically-aligned CNTs for gas sensors.

3.2. Metalloporphyrin-modified CNTs gas sensors

Macromolecules are used to functionalize the carbon nanotubes for enhanced gas sensing properties, even at room temperature. Particularly, metalloporphyrins (MPPs) are among the functional materials characterized by flexible and multiple molecular recognition properties. The basic porphyrin ring is an extended aromatic system formed by four pyrrolic rings linked by methynic bridges. This basic structure is turned into a metalloporphyrin when a transition metal atom (Fe, Co, Ni, Cu, Mo, Zn, Mn, etc.) replaces the two hydrogen atoms at the central core. Also, other modifications include compounds at the lateral positions. Thus, a metalloporphyrin can offer a wide variety of interaction mechanisms that can be exploited for gas sensing. Recently, M. Penza *et al.* [10,12,13] demonstrated the effect of the surface functionalization of the CNTs networked films with spray MPP layer on gas sensitivity. MPP-modified CNTs networks exhibited an increased sensitivity of the electrical resistance towards concentrations of common volatile organic compounds of alcohols, amines, aromatics, ketones, and toxic gases (NO₂, NH₃), at room temperature. The gas adsorption properties of the MPP-functionalized CNTs exhibited broad selectivity and high sensitivity. PCA analysis was performed using the gas response of a sensors array by providing a capability of the compounds recognition. These results were considered very promising for the development of arrays of CNTs-based gas nanosensors with broad selectivities for fingerprinting analysis of gaseous complex samples.

3.3. CNTs-composites gas sensors

High attention has been paid to the *composite materials* for gas sensing due to their possibility to operate at room temperature. Compared to counterpart metal oxides sensors, the CNTs-based nanocomposites work at room temperature and are easy to fabricate. Polymer composite materials consist of a polymeric matrix which acts as an insulating matrix and dispersed particles, e.g. nanotubes, of conducting materials which act as conducting path of the nanocomposite materials. The gas sensing behavior of conducting filler-matrix composite materials can be described by the volumetric change of the matrix due to adsorbed vapor and the accompanying change of the percolation-type conductivity. This type of composite material shows a drastic change in the electrical conductivity around a critical composition described as *percolation threshold*. Usually, it depends on the shape of the conducting filler. Generally, the composite with higher aspect ratio of the conducting filler shows the lower threshold and the sharper change in the conductivity around the threshold. Therefore, composite materials equipped with conducting filler of higher aspect ratio, like carbon nanotubes, are expected to show higher sensitivities at room temperature.

CNTs-composites exhibit high gas adsorption capability and are very sensitive to mass changes in the piezoelectric transducers such as SAW, QCM and TFBAR.

3.3.1. SAW and QCM sensors

M. Penza *et al.* [26,38] demonstrated that highly-sensitive microacoustic vapor sensors based on SAW 433 MHz oscillators were able to detect volatile organic compounds (VOCs) at room temperature using a nanocomposite film of HiPco single-walled carbon nanotubes (SWCNTs) embedded in a cadmium arachidate (CdA) amphiphilic organic matrix prepared by the Langmuir-Blodgett (LB) technique with a different weight SWCNTs filler-content. The structural properties and the surface morphology of the nanocomposite were examined by X-ray diffraction, transmission and scanning electron microscopy, as shown in Figure 4. HR-TEM image revealed that the pristine as-received SWCNTs were organized in tangled bundles with diameters of several tens of nanometers. They appear coated by CdA host-matrix and randomly distributed in tangled nets of nanotubular chains densely aggregated. The sensing characteristics for acoustic devices indicated that sensitivity to polar and nonpolar tested VOCs of the SWCNTs-CdA composite increased with SWCNTs filler content. In addition, a QCM 10 MHz transducer has been coated on both sides for comparison of the gas sensing properties. The results demonstrate that the SAW device is at higher sensitivity than QCM sensor due to its higher resonating frequency.

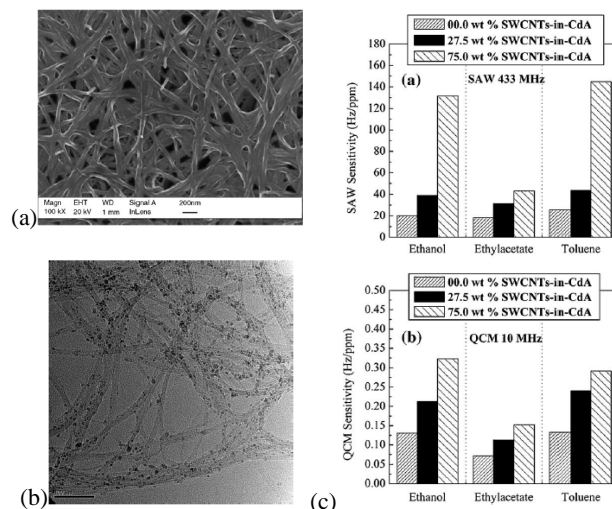


Fig. 4. (a) SEM image of the SWCNTs-CdA 27.5 wt.% LB nanocomposite film. (b) TEM image of pristine HiPco SWCNTs material used as filler in the nanocomposite. (c) Comparison of room-temperature sensitivity of nanocomposite SWCNTs-CdA LB film with different weight filler-content onto SAW 433 MHz and QCM 10 MHz transducer. This figure is reprinted and adapted with permission from Elsevier, by M. Penza *et al.*, Materials Science & Engineering C 26 (2006) 1165.

3.3.2. TFBAR sensors

M. Penza *et al.* [39] demonstrated a Thin Film Bulk Acoustic Resonator (TFBAR) based on vibrating membrane of AlN/Si₃N₄ fabricated onto silicon substrate and functionally characterized as gas sensor at resonating frequency of 1.045 GHz. This novel TFBAR-based gas sensor was functionalized by a sensing nanocomposite layer, prepared by Langmuir-Blodgett (LB) technique, of single-walled carbon nanotubes (SWCNTs) embedded in a host-matrix of organic material of cadmium arachidate.

High-performance gas detection of SWCNTs-coated TFBAR sensor was reported at room temperature. The sensing device exhibited high sensitivity (e.g. acetone: 12 kHz/ppm; ethylacetate: 17.3 kHz/ppm), fast response (within 2-3 minutes), slow reversibility (within 1 hour), good repeatability (variation $\leq 5\%$) of response towards tested organic vapors of acetone, ethylacetate, toluene.

4. CONCLUSIONS

CNTs-based gas sensors are reviewed at the state-of-art. CNTs exhibit a large surface area and outstanding structural, electrical, optical, thermal, mechanical properties, which make them exciting nanomaterials as promising candidates for the next generation of chemical sensors. The future of CNTs gas sensors looks very bright in combination to various transducers, but continued progress need to overcome the current challenges, move to the development of reliable commercial devices, and lead to a class of chemical sensor nanomaterials with superior sensitivity, reduced sizes, low-cost, stable response, selectivity and long lifetimes for a wide range of harsh environments and applications.

5. ACKNOWLEDGEMENTS

The work carried out at ENEA, *Italian National Agency for New Technologies, Energy and Sustainable Economic Development*, in the Brindisi Laboratories, was done thanks to valuable contribute by M. Alvisi, R. Rossi, D. Suriano, E. Serra, V. Pfister, G. Cassano, P. Aversa, R. Pentassuglia, D. Di Maio. This work was partially financed by three research grants from Regione Puglia Government to support the local Italian SMEs innovation.

6. REFERENCES

- [1] J. Kong, N.R. Franklin, C. Zhou, M.G. Chapline, S. Peng, K. Cho, H. Dai, *Science* **287**, 622-625 (2000).
- [2] P. G. Collins, K. Bradley, M. Ishigami, A. Zettl, *Science* **287**, 1801-1804 (2000).
- [3] P. Qi, O. Vermesh, M. Grecu, A. Javey, Q. Wang, H. Dai, *Nano Lett.* **3**, 347-351 (2003).
- [4] T. Zhang, S. Mubeen, N.V. Myung, M.A. Deshusses, *Nanotechnology* **19**, 332001 (2008).
- [5] M. Penza, R. Rossi, M. Alvisi, G. Cassano, M.A. Signore, E. Serra, R. Giorgi, *Sens. Actuators B* **135**, 289-297 (2008).
- [6] M. Penza, G. Cassano, R. Rossi, A. Rizzo, M.A. Signore, M. Alvisi, N. Lisi, E. Serra, R. Giorgi, *Appl. Phys. Lett.* **90**, 103101 (2007).
- [7] M. Penza, G. Cassano, R. Rossi, M. Alvisi, A. Rizzo, M.A. Signore, Th. Dikonimos, E. Serra, R. Giorgi, *Appl. Phys. Lett.* **90**, 173123 (2007).
- [8] A. Star, V. Joshi, S. Skarupo, D. Thomas, J.-C. P. Gabriel, *J. Phys. Chem. B* **110**, 21014-21020 (2006).
- [9] M. Penza, R. Rossi, M. Alvisi, E. Serra, *Nanotechnology* **21**, 105501 (2010).
- [10] M. Penza, R. Rossi, M. Alvisi, M.A. Signore, E. Serra, R. Paolesse, A. D'Amico, C. Di Natale, *Sensors and Actuators B* **144**, 387-394 (2010).
- [11] J. M. Schnorr, T.M. Swager, *Chemistry of Materials* **23**, 646-657 (2011).
- [12] M. Penza, M. Alvisi, R. Rossi, E. Serra, R. Paolesse, A. D'Amico, C. Di Natale, *Nanotechnology* **22**, 125502 (2011).
- [13] M. Penza, R. Rossi, M. Alvisi, D. Valerini, E. Serra, R. Paolesse, E. Martinelli, A. D'Amico, C. Di Natale, *Sensor Letters* **9**, 913-919 (2011).
- [14] Special Issue *Nanomaterials for Chemical Sensing Technologies*, in *Journal of Sensors*, Vol. 2009, M. Penza et al., Guest Eds. (Hindawi, La Vergne, TN, USA, 2009), pp. 365.
- [15] E.T. Thorstenson, Z. Ren, T.-W. Chou, *Composites Science & Technology* **61**, 1899-1912 (2001).
- [16] T.W. Ebbesen, P.M. Ajayan, *Nature* **358**, 16-19 (1992).
- [17] H. Dai, *Carbon Nanotubes: Synthesis, Structure, Properties, and Applications* **80**, eds. M. S. Dresselhaus, G. Dresselhaus, and Ph. Avouris, Chapter 3 "Nanotube Growth and Characterization," Springer-Verlag, Berlin, pp. 29-53, 2001.
- [18] A.F. Ismail, P.S. Goh, J.C. Tee, S.M. Sanip, M. Aziz, *Nano: Brief Reports and Reviews* **3**, 127-143 (2008).
- [19] S.P. Turano, J.D. Flicker, W.J. Ready, *Carbon* **46**, 723-728 (2008).
- [20] X.Q. Chen, T. Saito, H. Yamada, K. Matsushige, *Appl. Phys. Lett.* **78**, 3714-3716 (2001).
- [21] C.J. Strobl, C. Schaflein, U. Beierlein, J. Ebbecke, A. Wixforth, *Appl. Phys. Lett.* **85**, 1427-1429 (2004).
- [22] R.H.M. Chan, C.K.M. Fung, W.J. Li, *Nanotechnology* **15**, S672-S677 (2004).
- [23] B.W. Smith, Z. Benes, D.E. Luzzi, J.E. Fischer, D.A. Walters, M.J. Casavant, J. Schmidt, R.E. Smalley, *Appl. Phys. Lett.* **77**, 663-665 (2000).
- [24] M. Penza, F. Antolini, M. Vittori-Antisari, *Thin Solid Films* **472**, 246-252 (2005).
- [25] J. Li, Y. Lu, Y. Qi, M. Cinke, J. Han, M. Meyyappan, *Nano Lett.* **3**, 929-933 (2003).
- [26] M. Penza, M.A. Tagliente, P. Aversa, G. Cassano, *Chem. Phys. Lett.* **409**, 349-354 (2005).
- [27] V. Kestic, G.C. Duesberg, J. Muster, M. Burghard, S. Roth, *Chem. Mater.* **10**, 2338-2340 (1998).
- [28] H. Dai (2001) *Carbon Nanotubes: Synthesis, Structure, Properties, and Applications* **80**, eds. M. S. Dresselhaus, G. Dresselhaus, and Ph. Avouris, Chapter 3 "Nanotube Growth and Characterization," Springer-Verlag, Berlin, pp. 29-53, 2001.
- [29] O. Zhou, H. Shimoda, B. Gao, S. Oh, L. Fleming, G. Yue, *Acc. Chem. Res.* **35**, 1045-1053 (2002).
- [30] A. Cassell, J. Raymakers, J. Kong, H. Dai, *J. Phys. Chem.* **103**, 6484-6492 (1999).
- [31] M. Penza, R. Rossi, M. Alvisi, D. Suriano, E. Serra, *Thin Solid Films* **520**, 959-965 (2011).
- [32] Z.F. Ren, Z.P. Huang, J.W. Xu, J.H. Wang, P. Bush, M.P. Siegal, et. Al., *Science* **282**, 1105-1107 (1998).
- [33] M. Meyyappan, L. Delzeit, A. Cassel, D. Hash, *Plasma Sources Sci. Technol.* **12**, 205-216 (2003).
- [34] S. Fan, M.G. Chapline, N.R. Franklin, T.W. Tombler, A.M. Cassell, H. Dai, *Science* **283**, 512-514 (1999).
- [35] R.T.K. Baker, *Carbon* **27**, 315-323 (1998).
- [36] S. Iijima, *Nature* **354**, 56-58 (1991).
- [37] M. Penza, R. Rossi, M. Alvisi, G. Cassano, E. Serra, *Sens. Actuators B* **140**, 176-184 (2009).
- [38] M. Penza, M.A. Tagliente, P. Aversa, G. Cassano, L. Capodiecchi, *Materials Science and Engineering C* **26**, 1165-1170 (2006).
- [39] M. Penza, P. Aversa, G. Cassano, D. Suriano, W. Wlodarski, M. Benetti, D. Cannatà, F. Di Pietrantonio, E. Verona, *IEEE Trans. Electron Devices* **55**, 1237-1243 (2008).

SYNTHESIS, CHARACTERIZATION AND SENSING PROPERTIES OF ELECTROSPUN CNTs/POLYMER/METAL OXIDES COMPOSITES

P. Frontera^{*1}, A. Donato¹, S. Trocino¹, P. L. Antonucci¹, G. Neri²

¹*Dept. of Mechanics and Materials, University "Mediterranea" of Reggio Calabria, Italy*

²*Dept. of Industrial Chemistry and Materials Engineering, University of Messina, Italy*

*E-mail: patrizia.frontera@unirc.it

ABSTRACT

MWCNTs/polymer/metal oxide composites fibers, where polyvinyl acetate (PVAc) is the base polymer and titania (TiO₂) the metal oxide, have been prepared by the electrospinning technique. Composite samples with different MWCNTs loading were prepared and annealed in air at 600 °C. The morphological and microstructural properties of spun and annealed samples have been examined using XRD, TGA and SEM analysis. The electrical and oxygen sensing characteristics of the annealed composites have been evaluated, with the aim to study the effect of MWCNTs on the sensing behavior and develop oxygen sensors with enhanced performances.

1. INTRODUCTION

Electrospinning is a technique which offers numerous advantages for obtaining fibers with high surface area suitable for many applications [1]. Recently, fabricating metal oxide fibers through electrospinning has attracted much attention since electrospinning can generate composite polymer/metal oxide fibers with good control of fiber size and morphology. One interesting application might be the preparation of sensing layer for resistive gas sensors. Previous reports on the response of electrospun fibers of several metal oxides, such as MoO₃, SnO₂ and WO₃ to different target gases (NO₂, NH₃, CO, etc) show them capable of detecting low concentration of these analytes with high sensitivity [2]. Compared with the bulk- or film-type gas sensors, the nanofibers provide much more surface adsorption sites for gaseous species because of their high surface-to-volume ratio. This consequently yields superior sensitivity when they are used for sensing materials. Moreover, they are very promising for applications which have strict requirements on sensor size and weight, operating temperature, power consumption, and flexibility.

Recently, Yang et al. reported that the addition of low amount of nanotubes into the electrospinning solution is advantageous for making MWCNTs/PVAc/SnO₂ composite fibers with enhanced properties [3]. The addition of small quantities of carbon nanotubes to polymer and metal oxides is known to cause a dramatic increase in the electrical conductivity of the matrix host, due to a percolation behavior caused by "bridging" these phases with carbon nanotubes. Then, addition of CNTs

during the electrospinning process could help to obtain conductive composites suitable for resistive sensor devices, and operating at lower temperature than conventional sensors.

Most of the earlier work on MWCNT-filled composite fibers by electrospinning method focuses on their mechanical properties [4], while electrical properties are rarely investigated. In the light of these considerations, we initiated a study on the electrical properties of MWCNTs/polymer/metal oxides fibers prepared by the electrospinning method with the final aim to develop new composite materials for gas sensing applications. Here, the preparation and characterization of a series of MWCNTs/PVAc/TiO₂ fibers with different MWCNTs loading is reported. These composites were applied to fabricate resistive-type sensors suitable for oxygen monitoring. Because of their simpler design and manufacturing process, with potential cost reduction, resistive oxygen sensors are of great interest in many applications, such as in the automotive, food processing and biomedical field [5-7]. Recent researches are addressed to find accurate and reliable oxygen sensors for personal safety devices, to be used, for example, by workers in confined spaces such as mines, submarines, and space shuttles, and for monitoring low oxygen concentrations in the food industry.

2. EXPERIMENTAL

MWCNTs/PVAc/TiO₂ composite nanofiber were obtained by using the electrospinning apparatus described in Fig. 1.

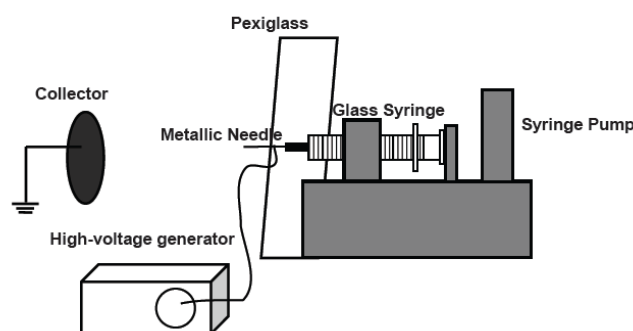


Fig. 1. Electrospinning apparatus.

The solution for electrospinning was prepared using the following procedure. First, MWCNTs (Helix Material, purity >95%, outer diameter: 40–60 nm, length: 1–2 μm) were functionalized refluxing them with concentrated HNO_3 . In particular, 100 mg MWCNTs in 200 mL of 2.5 M HNO_3 were sonicated for 30 min in a round bottom flask to completely disperse the MWCNTs into the HNO_3 solution. The mixture was then refluxed for 20 h at 110 $^\circ\text{C}$. The MWCNTs were separated by centrifugation, washed three times with water and then dispersed in DMF with Cetyltrimethylammoniumbromide (CTMABr, Aldrich) by sonication for 3 h. Poly (vinyl acetate) (PVAc, $M_n = 500,000$) was added into the solution with stirring resulting in content of 11,5% weight respect overall solution. After stirring for 1h, glacial acetic and titanium isopropoxide (TIP, 97%), respectively, were added. The solution was kept under stirring for 12 h when the dark viscous solution became homogeneous. Samples with different MWCNTs loading were prepared by varying the nanotubes/TIP ratio, in the range 0–4 wt%.

The mixture was then subjected to electrospinning using a commercial apparatus (Linari Engineering supplied) under an applied voltage of 25 kV and a flow rate of 0,35 ml/h. The nanofibers were collected on an aluminum foil placed 10 cm below the needle tip. The electrospun fibers were then calcined up to 600 $^\circ\text{C}$ for 2h with a ramping rate of 10 $^\circ\text{C}/\text{min}$.

The morphology of the samples was investigated by scanning electron microscopy (SEM), using a Jeol scanning electron microscope. X-ray diffraction analysis (XRD) was performed using a Philips X-Pert diffractometer equipped with a Cu-K α radiation. Diffraction peaks identification was performed on the basis of the JCPDS database of reference compounds. The thermogravimetric (TG) analysis was performed by using a TG/DSC NETZSCH STA 409 instrument. The analyses were carried out with a heating rate of 10 $^\circ\text{C}/\text{min}$ in static air up to 600 $^\circ\text{C}$.

The sensing device consists of an alumina substrate with Pt interdigitated electrodes. The sensing layer was deposited by screen printing. Gas sensing tests were carried out inside a stainless-steel chamber under controlled atmosphere. Mass flow controllers were used to adjust desired concentrations of target gas in dry air. The electrical resistivity measurements and sensors response were performed using the four point probe method, by means of an Agilent 34970A multimeter. Sensors response to oxygen, S , is defined as $S = R/R_0$, where R_0 is the resistance of the sensor in pure nitrogen and R the electrical resistance at different concentrations of O_2 .

3. RESULTS AND DISCUSSION

3.1 Synthesis and characterization

The thermal stability of the as spun composites was first investigated by thermogravimetric analysis (Fig. 2). TGA curves of composite materials, indicated that PVAc

is completely oxidized at the temperature of 600 $^\circ\text{C}$, while the oxidation of MWCNTs is complete only at higher temperature.

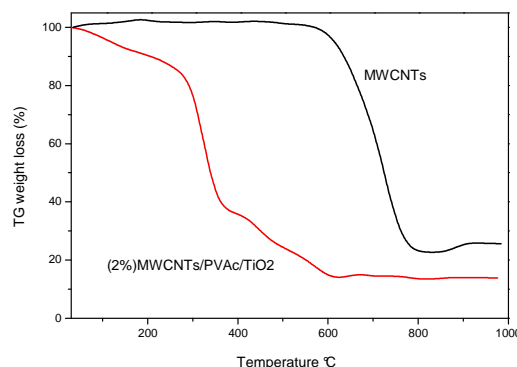


Fig.2. TGA profiles of MWCNTs and as-spun (2%)MWCNTs/PVAc/TiO₂ composite.

In according, FT-IR of the composite samples after annealing at 600 $^\circ\text{C}$ in air showed the complete combustion of the polymer matrix, as indicated by the lacking of the characteristic adsorption band of PVAc (Fig. 3).

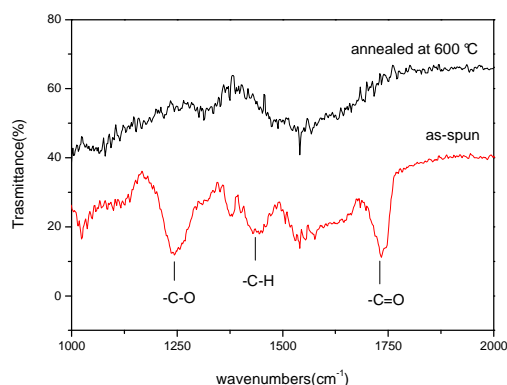


Fig. 3. FT-IR profiles of as-spun and annealed PVAc/TiO₂ composite at 600 $^\circ\text{C}$ in air.

Fig. 4 shows the morphology of the electrospun composite samples. A randomly distributed network of fibers was observed on the as spun samples (Fig. 4a). The fibers structure changed during the annealing, depending on the MWCNTs loading. On low loaded MWCNTs-composites, the fibers undergo a partial destruction (Fig. 4b), while at higher loading, they are almost completely absent (Fig. 4c). XRD analysis revealed that all of the as-spun fibers prior to calcinations were amorphous. After calcinations at 600 $^\circ\text{C}$, the crystalline anatase phase was found without contamination of other phases (Fig. 4d).

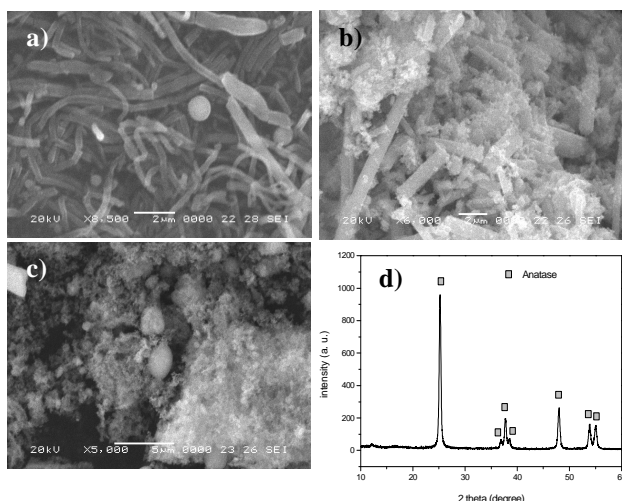


Fig.4. SEM images of: a) as-spun (0.06%)MWCNTs/PVAc/TiO₂; b)(0.06%)MWCNTs/PVAc/TiO₂ after calcination at 600 °C; c) (2%)MWCNTs/PVAc/TiO₂ after calcination at 600 °C; d) XRD of (0.06%)MWCNTs/PVAc/TiO₂ after calcination at 600 °C.

3.2 Electrical characteristics

In order to assess the potential applicability of the composites synthesized in this study to chemical sensors, their electrical characteristics and oxygen sensing properties were investigated. Because of their high surface-to-volume ratio, the electrospun fibers provide much more surface adsorption sites for gaseous species, when compared with the bulk- or film-type structures. The superior sensitivity of fibers-based sensors, has been largely reported [2, 8].

The device for the electrical and sensing measurements consists of a ceramic substrate provided with interdigitated electrodes. Initially we attempted to deposit a layer of spun MWCNTs/PVAc/TiO₂ directly onto the interdigitated electrodes. Fiber mats so deposited exhibited poor adhesion to the substrate surface and were easily removed during the successive heat treatment at high temperature. The fabrication process of the sensors was therefore changed, involving first the collection of composite fibers on an aluminium film collector. They were then detached from the collector surface, calcined at 600 °C and finally deposited on the sensor substrate by the screen printing method. In this way adhesion to the ceramic substrate was improved, allowing to fabricate the devices for the electrical and sensing tests.

The baseline resistance in air of some of the devices so fabricated is reported in Fig. 5. The high baseline resistance measured (in the mega-ohm range) was attributed to the grained microstructure and the almost insulating behavior of titania. Hence, charge-carrier pathways are constrained passing through many narrow interparticle contacts or “necks”, which contribute to high resistance values observed. Increasing the temperature the carrier mobility increases, determining a resistance decrease. It can be observed that the lower temperature at which the baseline resistance is within the measurable range decreases with the loading of MWCNTs.

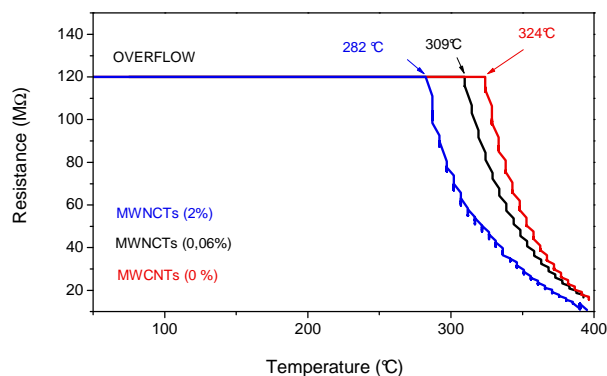


Fig. 5 Electrical resistance in air vs. temperature of electrospun MWCNTs/PVAc/TiO₂ composites as a function of the MWCNTs loading.

This finding suggests a percolation behavior caused by “bridging” of the insulating phase with carbon nanotubes. That is, at crossing points, the height of potential barrier for the conduction is strongly reduced, and conduction occur through the privileged conduction paths provided by the MWCNTs network.

3.3 Sensing tests

Preliminary oxygen sensing tests demonstrated the good performance of the composites-based sensors. In according with the n-type behaviour of the titania, it has observed an increase of the electrical resistance at the addition of O₂. The typical dynamic response of the electrospun (0.06%)MWCNTs/PVAc/TiO₂-based oxygen sensor at the temperature of 400 °C is shown in Fig. 6.

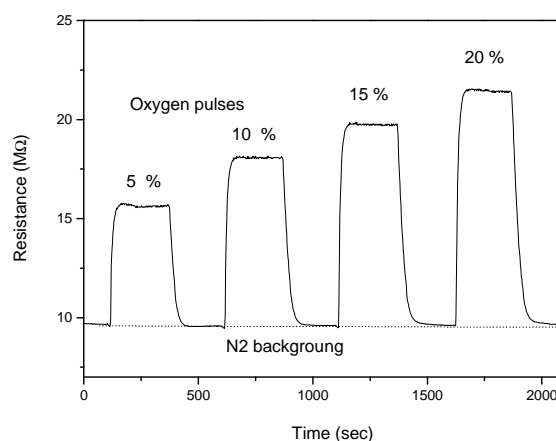


Fig. 6. Dynamic response of (0.06%)MWCNTs/PVAc/TiO₂ sensor towards oxygen at 400 °C.

At the operating temperature of 400 °C, sensors display a reversible, and reproducible response towards oxygen in nitrogen. Moreover, they show a quick response and recovery, which is an advantage for practical applications. It is worth noting also that the sensor responses were very stable and reproducible for repeated testing cycles.

Results above reported can be explained by a mechanism which combines surface phenomena and oxygen diffusion into the bulk. Briefly, immediately after the exposure to oxygen, adsorbed species at the surface compensate surface vacancies, leading to a fast increase of resistance, caused by a widening of the depleted layer at the external shell of the grains. Later, ions migrate into the bulk compensating oxygen vacancies in the material. This diffusion into the bulk is responsible for the long-term drifts observed after exposing most metal oxide films at these temperatures to changes of the oxygen concentration in nitrogen [9]. On our MWCNTs-loaded sensors, signal reaches the original values after each brief pulse, indicating a fast dynamics.

The effect of carbon nanotubes on the sensor response is reported in Fig. 7a-b. At the addition of MWCNTs, initially the response decrease. However, with a further increase of the nanotube loading, a positive effect is registered leading to a very sensitive sensor when 4 wt% of MWCNTs are present.

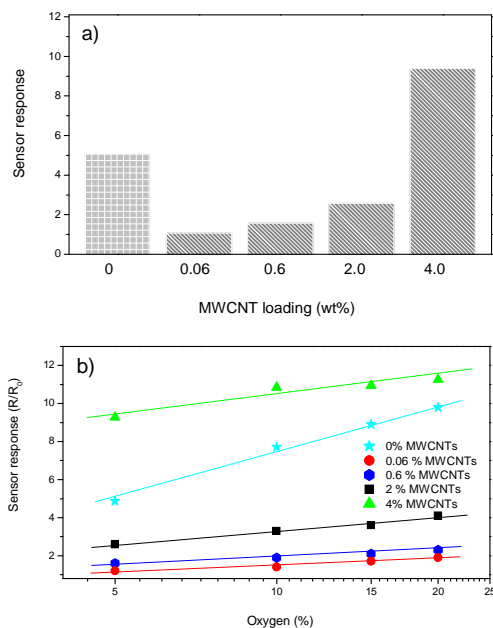


Fig. 7 a) Sensor response to 5 % of oxygen in nitrogen as a function of MWCNTs loading; b) Calibration curve for the composite samples investigated.

Fig. 7b, shows the calibration curves for the different MWCNTs-loaded samples. From the graphs it appears that the sensors with a MWCNTs loading of 4% is the most sensitive, especially at low oxygen concentrations. This result is most promising for a future development of low concentration oxygen sensors to be applied in the food industry.

On the basis of the characterization study, it seems that the MWCNTs loading play a key role in addressing the sensor features. Then, an extensive work is currently underway in order to optimize the sensing layer formulation. Other parameters are also relevant (for

example, polymer nature, annealing temperature, etc.) and will be investigated as well.

4. CONCLUSION

MWCNTs/PVAC/TiO₂ nanofibers were synthesized via an electrospinning process. Composite samples with different MWCNTs loading were prepared and annealed in air at different temperatures up to 600 °C. The sensing results obtained indicate that the methodology proposed in this work can be used for the preparation of MWCNTs/metal oxide composites with potential applications in oxygen sensors.

REFERENCES

- [1] D. Li, Y. N. Xia, *Adv. Mater.* **16**, 1151 (2004).
- [2] G. Wang, Y. Ji, X. Huang X, X. Yang, P.-I. Gouma, M. Dudley, *J. Phys. Chem. B*, **110** 23777 (2006).
- [3] A. Yang, X. Tao, R. Wang, S. Lee, C. Surya, *Applied Physics Letters* **91**, 133110 (2007).
- [4] M. M. Treacy, T. W. Ebbesen, J. M. Gibson, *Nature* **381** 678 (1996).
- [5] Y. Xu, X. Zhou, O. T. Sorensen, *Sens. Actuat. B* **65**, 2 (2000).
- [6] G. Neri, *Science of Advanced Materials* **2**, 3 (2010).
- [7] R. Ramamoorthy, P. K. Dutta, S. A. Akbar, *J. of Materials Science* **38** 4271 (2003).
- [8] I.-D. Kim, A. Rothschild, B. H. Lee, D. Y. Kim, S. M. Jo, H. L. Tuller, *Nano Lett.* **6** 2009 (2006).
- [9] F. Hernandez-Ramirez, J. D. Prades, A. Tarancon, S. Barth, O. Casals, R. Jimenez-Diaz, E. Pellicer, J. Rodriguez, J. R. Morante, M. A. Juli, S. Mathur, A. Romano-Rodriguez, *Adv. Funct. Mater.* **18**, 2990 (2008).

NO₂ SENSOR BASED ON ULTRA-THIN TITANIA COATING ON CARBON NANOFIBERS

N. Donato¹, M. Latino², G. Neri*³, D. Spadaro³, C. Marichy⁴, M.-G. Willinger^{4,5},
N. Pinna^{4,6}

¹*Dept. of Matter Physics and Electronic Engineering, University of Messina, Italy*

²*Dept. of Chemical Science and Technologies, University of Rome Tor Vergata, Italy*

³*Dept. of Industrial Chemistry and Materials Engineering, University of Messina, Italy*

⁴*Dept. of Chemistry, CICECO, University of Aveiro, 3810-193 Aveiro, Portugal*

⁵*Dept. of Inorganic Chemistry, Fritz Haber Institute of the Max Planck Society, Berlin, Germany.*

⁶*World Class University (WCU) program of Chemical Convergence for Energy & Environment (C2E2), School of Chemical and Biological Engineering, College of Engineering, Seoul National University (SNU), Seoul 151-744, Korea.*

*E-mail: neri@ingegneria.unime.it

ABSTRACT

The growth of ultra-thin and uniform TiO₂ coating on carbon nanofibers (CNFs) by a non-aqueous Atomic Layer Deposition (ALD) approach, as well as their structural characterization and electrical properties investigation, have been reported. The NO₂ gas sensing behavior of these titania-coated carbon nanofibers was studied by fabricating resistive-type sensors and measuring changes in electrical resistance with respect to concentration and time. In contrast to pure CNFs, the hybrid sensors responded to NO₂ at near room temperature, evidencing unprecedented p-type responsiveness.

1. INTRODUCTION

Increasing demands for more sensitive chemical sensors for air-quality control, environmental monitoring, healthcare, defense and security, and other applications have led to an interest in nanostructures based on semiconducting metal oxides as sensing layer in resistive sensor devices [1]. However, they operate at high temperature, which is a strong limitation for some applications. In order to enhance the sensing performances at near room temperature and consequently reduce the power consumption of the device, an attractive strategy consists in depositing the metal oxide on the surface of suitable carriers.

In this paper we describe the film growth, as well as the structural characterization and electrical properties, of ultra-thin TiO₂ coating on carbon nanofibers (CNFs). Titanium dioxide is a wide-band gap semiconductor, well-known as a stable and highly reactive photocatalyst and widely used for gas sensors [2, 3]. On the other hand, carbon nanotubes/nanofibers are characterized by a high conductivity, high aspect ratio (>1000) and tubular geometry, providing ready gas access to a large specific surface area and percolation at very low volume fractions.

Moreover, such composites can favor the dispersion and stability of titania structures at nanometer scale, enabling chemical, physical, photochemical, and surface properties quite different from those of the bulk.

TiO₂/carbon nanotubes (CNTs) hybrid composites have been already used successfully as gas sensors [4]. The sol-gel process appears as the most common technique to synthesize titania-CNTs hybrids. Early attempts focused on the dispersion of CNTs into titania films [5]. Furthermore, the sol-gel route has been also used as a simple route for the deposition of titania particles/films on the CNT walls. Typically, the thickness of the coating can be controlled by various parameters, such as the reaction time, the reaction composition, and the choice of metal precursor. To enable a more homogeneous coating, the use of titanium tetraisopropoxide was revealed more effective [6]. Upon reducing the amount of TiO₂ with respect to CNTs, Jitianu *et al.* obtained a thin but rather irregular and partial coating of TiO₂ on CNTs [7]. However, thickness control to nanometer precision is challenging.

We recently reported the preparation of ultra-thin films of metal oxides by means of a non-aqueous sol-gel Atomic Layer Deposition (ALD) approach for sensing applications [8,9]. This technique allows the conformal deposition of a metal oxide as a continuous either amorphous or crystalline film with a controlled thickness. Herein, we describe the film growth, the structural characterization and electrical properties of ultra-thin TiO₂ coating on CNFs, by this ALD approach. The sensing properties towards NO₂ have been investigated, with the aim to study the sensing properties and to develop a gas sensor operating at near room temperature.

2. EXPERIMENTAL

Titanium dioxide was deposited on functionalized carbon nanofibers (Applied Science PR-24-PS). The functionalization of the nanofibers was done by treating

them with concentrated HNO_3 at $100\text{ }^\circ\text{C}$ for 2 h. Titanium isopropoxide and acetic acid were used as metal and oxygen precursors, respectively. The deposition took place at $200\text{ }^\circ\text{C}$ in an exposure mode reactor. Metal precursor and carboxylic acid were introduced subsequently by pneumatic ALD valves from their respective reservoirs. The reservoirs were kept at 80 and $30\text{ }^\circ\text{C}$, respectively. For the deposition, pure nitrogen was used as a carrier gas at a constant flow rate of 5 sccm. In a typical experiment the valves were opened for 0.02 s for carboxylic acid and 1 s for the metal alkoxide. The residence and purging periods were 20 s and 15 s, respectively. The growth per cycle under these conditions was around 0.06 nm. The morphology of the samples were investigated by scanning electron microscopy (SEM) and transmission electron microscopy (TEM).

The sensing device consists of an alumina substrate with Pt interdigitated electrodes on one, and a Pt heater on the other side. The spacing between the Pt electrodes measures 200 microns. The active sensing layer was deposited by screen printing. Gas sensing tests were carried out inside a stainless-steel chamber under controlled atmosphere. Mass flow controllers were used to adjust desired concentrations of target gas in dry air. The electrical resistivity measurements and the sensors responses were recorded using the four point probe method, by means of an Agilent 34970A multimeter.

3. RESULTS AND DISCUSSION

3.1 Synthesis and characterization

ALD has been successfully employed for the deposition of ultra-thin titania films on various substrates [10]. As the ALD film growth is based on self-limiting surface reactions, this process enables the deposition control at the atomic scale. In particular, ALD processes have been proposed to form TiO_2 monolayer on one dimensional nanostructures, such as nanotubes [11]. For example, Gomathi *et al.* used metal chloride precursor to coat acid-treated CNTs with TiO_2 [12]. However, the as-deposited coating consisted predominantly of amorphous hydroxide species; a subsequent calcination of the samples at $350\text{ }^\circ\text{C}$ to form the oxide specie was required. Recently, by a non-hydrolytic ALD approach, the coating of carbon nanotubes/nanofibers with crystalline metal oxide films without any post-annealing at high temperature is achievable [13]. Paths required for obtaining the TiO_2 coating on the nanofiber walls are described in the followings. The CNTs/CNFs were first functionalized in order to form anchoring species (i.e. -COOH and -OH) on the surface. Then titanium isopropoxide will react with the surface carboxylic acids on CNTs/CNFs forming an interfacial Ti-carboxylate layer. The reaction will stop when all the surface carboxylic acid groups reacted with titanium precursor. Then excess precursor molecules and the byproduct are purged, and acetic acid vapor is subsequently introduced to the system. The new surface carboxylic groups formed are ready to react with titanium precursor molecules again in the latter step, where a titanium isopropoxide will react

with the surface carboxylic acids on CNTs via an ester elimination condensation step forming a TiO_2 layer. Then, one layer of TiO_2 has been grown by the completion of one cycle of chemical reactions. By repeating the latter two steps, TiO_2 layers can be deposited one per one, in a highly controlled way. SEM analysis with back scattering electron (BSE) of a sample prepared applying 65 cycles, with a theoretical TiO_2 coating 3.9 nm thick, is shown in Fig. 1. A brighter contour in the inner and outer part of the tube demonstrates the coating with a higher electronic density material. TEM indicates that the TiO_2 coating is continuous and uniform along the whole surface of the tubes, only a few nanometers thick (3-4 nm) and presents the same thickness in both the inner and outer surface. Moreover, it appears pinhole-free, likely as a result of the deposition method, which provide films chemically bonded to the substrate.

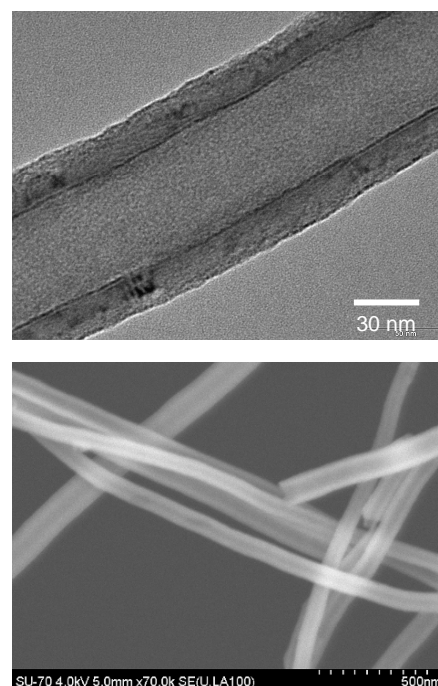


Fig. 1. SEM and HRTEM images of the TiO_2 /CNFs.

3.2 Electrical characteristics

The electrical resistance of thick films made of either CNFs or TiO_2 /CNFs composite deposited on a ceramic substrate provided with interdigitated electrodes, as a function of the operating temperature, was first examined.



Fig. 2 Schematic view of the TiO_2 /CNFs sensing layer deposited on the patterned alumina substrate.

It can be assumed that the three dimensional network of both single pure and coated fibers deposited randomly

oriented over the electrodes (see Fig. 2 for a schematic representation) is responsible of electrical paths between the adjacent Pt electrodes.

In Fig. 3 is reported the electrical resistance in air of CNFs and TiO₂/CNFs composite films *versus* the operating temperature investigated. On the one hand, the resistance of both films decreases as the temperature raises, indicating a semiconducting behavior.

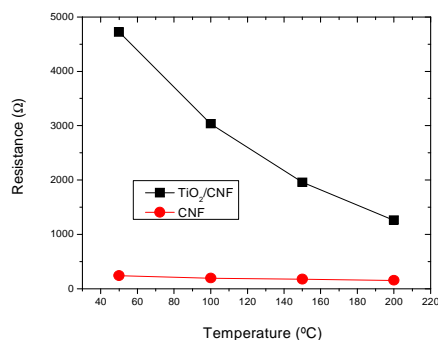


Fig. 3 Electrical resistivity in air of pure CNFs and TiO₂/CNFs films versus the operating temperature.

The resistance of the pure CNF film is in the range 50-150 ohm, as a result of the high electrical conduction of carbon nanofibers. Instead, a much higher resistance value (10³-10⁴ ohm) is measured for the TiO₂/CNFs film. On the other hand, the baseline resistance of the hybrid film is significantly lower than that registered on titania nanoparticles-based films, suggesting that the very low TiO₂ film thickness and the high conductivity of the carbon nanofiber core are responsible for the observed behaviour. Specifically, as CNFs are coaxially coated with the titania, the shell of TiO₂ should create high contact resistance at crossing points (see Fig. 2). However, due to the low TiO₂ thickness, tunneling effect can help to overcome this limitation reducing the height of potential barrier for the conduction at crossing points, whereas the CNF core provide a privileged conduction path.

3.3 Sensing tests

Preliminary tests carried out with NO₂ and O₂ as target species revealed that pulses of these gases in air decrease the electrical resistance. The sensor response to either nitrogen dioxide or oxygen, S, is defined as $S = [(R-R_g)/R] \cdot 100$ where R is the baseline resistance of the sensor and R_g the electrical resistance at different concentrations of the target gas. Fig. 4 shows the sensor response towards NO₂ as a function of the operating temperature in air. Sensing tests to NO₂ were performed at a concentration of the target gas equal to 5 ppm. While the sensing behavior of the uncoated CNF film is not affected by the target gas at any temperature, the response of the TiO₂/CNFs sensor is strongly influenced by the operating temperature. The sensor showed a detectable response starting from near ambient temperature (40 °C). The response increased with the temperature, showing a maximum in the range 100-150 °C, then decreased.

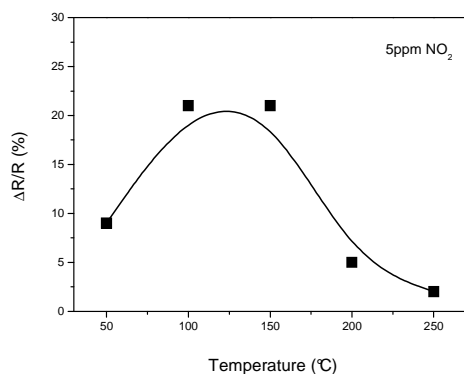


Fig. 4 Effect of the temperature on the TiO₂/CNFs sensor response towards 5 ppm of NO₂.

The dynamic response of the TiO₂/CNFs sensor to nitrogen dioxide at the temperature of 150 °C is shown in Fig. 5a. As previously mentioned, the sensor resistance decreases in the presence of NO₂.

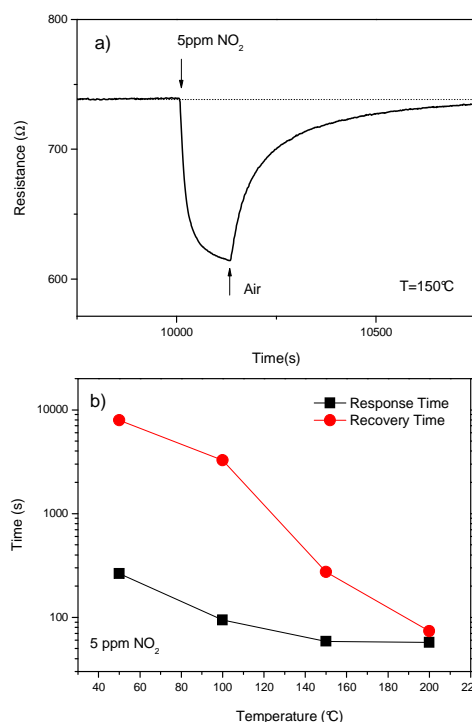


Fig. 5. a) Dynamic response of TiO₂/CNFs sensor to 5 ppm of NO₂ gas; b) Response and recovery times of the sensor as a function of the operating temperature.

The values of τ_{res} and τ_{rec} , *i.e.* the response and recovery times of the sensor, respectively, as a function of the operating temperature, are reported in Fig. 5b. One can clearly observed that both dynamic parameters of the sensor strongly decrease with the temperature. The response is faster than the recovery and, also at near room temperature, the sensor responds in less than 4 minutes.

3.4 Sensing mechanism

On the basis of the sensing results reported here, the TiO₂/CNFs material behaves as a p-type semiconductor. This indicates that upon adsorption of nitrogen dioxide molecules on titania coating, the electronic charge is transferred to the adsorbed NO₂ and this in turn causes an effective electronic charge transfer from the carbon nanotube towards the titania coating, decreasing the overall resistance of the heterostructured sensing layer.

As NO₂ behaves as an oxidizing or reducing agent, depending on the temperature and concentrations [14], this could cause a misinterpretation of the results. Therefore, to prove the p-type conductivity of the sensing layer, further experiments were performed with oxygen as target gas (Fig. 6).

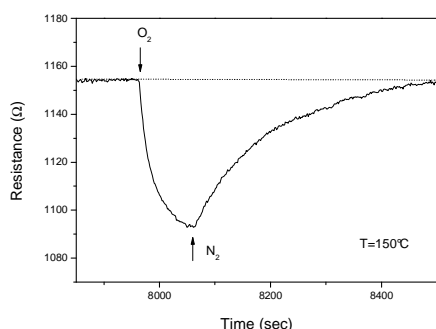


Fig. 6. Dynamic response of gas sensor to 20% O₂ in nitrogen.

The results obtained can be explained as in the case of NO₂. In order to formulate hypotheses about the behavior observed with the TiO₂/CNFs composite layer, we would first consider that pure titania films in the anatase phase are generally considered n-type semiconductors, while only few reports demonstrated a p-type behavior [15]. The presence of carbon nanotubes, seems to favor the n- to p-type transition. Bittencourt *et al.* reported that multiwalls CNTs/WO₃ films behave either as p-type or n-type semiconductors depending on the loading of carbon nanotubes dispersed into the WO₃ matrix [16]. Sanchez *et al.* found a reversed Ti_xO_y → adsorbate direction for the charge transfer in the interaction of NH₃ with TiO₂/CNTs [17], which is expected to decrease the resistance with electron-acceptor adsorbates, as observed with our TiO₂/CNFs composites in the presence of NO₂ or oxygen.

The behavior on TiO₂/CNFs hybrid composite can be also related to the very low thickness of the titania layer. A further activity is then programmed to investigate this aspect. Interestingly, previous results obtained with a SnO₂/CNFs sensor have shown that it behaved differently than TiO₂/CNFs, i.e. the response to both NO₂ and O₂ led to an increasing of the resistance [9]. In order to explain these data and clarify the sensing mechanism, further experiments are in progress.

4. CONCLUSION

Ultra-thin TiO₂ coating were grown by a non-aqueous sol-gel ALD approach on carbon nanofibers. The TiO₂ coating was very thin, uniform and pinhole-free. The

TiO₂/CNFs hybrid composite was applied to fabricate a resistive gas sensor operating at low temperature for monitoring NO₂.

The sensor developed has shown unprecedented p-type responsiveness. Hypotheses have been formulated in order to explain the appearance of p-type conductivity and the sensing behavior with NO₂ and O₂ as target gas. Based on the results obtained, further studies are planned in order to assess the influence of titania coating thickness on the sensing properties and sensor performances.

REFERENCES

- [1] G. Neri, *Science of Advanced Materials* **2**, 3 (2010).
- [2] T. Sasaki, S. Nakano, S. Yamauchi, M. Watanabe, *Chem. Mater.* **9**, 602 (1997).
- [3] T. Sasaki, S. Nakano, S. Yamauchi, M. Watanabe, *Chem. Mater.* **9**, 602 (1997).
- [4] E. Llobet, E. H. Espinosa, E. Sotter, R. Ionescu, X. Vilanova, J. Torres, A. Felten, J. J. Pireaux, X. Ke, G. Van Tendeloo, F. Renaux, Y. Paint, M. Hecq, C. Bittencourt, *Nanotechnology* **19**, 375501 (2008).
- [5] E. Llobet, E. H. Espinosa, E. Sotter, R. Ionescu, X. Vilanova, J. Torres, A. Felten, J. J. Pireaux, X. Ke, G. Van Tendeloo, F. Renaux, Y. Paint, M. Hecq, C. Bittencourt, *Nanotechnology* **19**, 375501 (2008).
- [6] H. Song, X. Qiu, F. Li, W. Zhu, L. Chen, *Electrochem. Commun.* **9**, 1416 (2007).
- [7] A. Jitianu, T. Cacciaguerra, R. Benoit, S. Delpeux, F. Beguin, S. Bonnamy, *Carbon* **42**, 1147 (2004).
- [8] M. G. Willinger, G. Neri, E. Rauwel, A. Bonavita, G. Micali, N. Pinna, *Phys. Chem. Chem. Phys.* **11**, 3615 (2009).
- [9] C. Marichy, N. Donato, M.-G. Willinger, M. Latino, D. Karpinsky, S.-H. Yu, G. Neri, N. Pinna, *Adv. Funct. Mater.* **21**, 658 (2011).
- [10] C. Marichy, A. Pucci, M.-G. Willinger, N. Pinna in *Atomic Layer Deposition of Nanostructured Materials*, N. Pinna and M. Knez (Ed.) Wiley-VCH, Chapter 14, 327 (2012).
- [11] V. R. Rai, S. Agarwal, *J. Phys. Chem. C* **113**, 12962 (2009).
- [12] A. Gomathi, S. R. C. Vivekchand, A. Govindaraj, C. N. R. Rao, *Adv. Mater.* **17**, 2757 (2005).
- [13] G. Clavel, E. Rauwel, M.-G. Willinger, N. Pinna, *J. Mater. Chem.* **19**, 454 (2009).
- [14] B. Ruhland, T. Becker, G. Muller, *Sens. Actuators B* **50**, 85 (1998).
- [15] F. Hossein-Babaei, M. Keshmiri, M. Kakavand, T. Troczynski, *Sens. Actuators B* **110**, 28 (2005).
- [16] C. Bittencourt, A. Felten, E.H. Espinosa, R. Ionescu, E. Llobet, X. Correig, J.-J. Pireaux, *Sens. Actuators B* **115**, 33 (2006).
- [17] L. Zheng, T. Xu, G. Li, Q. Yin, *Jpn. J. Appl. Phys.* **41**, 4655 (2002).
- [17] M. Sanchez, M. E. Rincon, R. A. Guirado-Lopez, *J. Phys. Chem. C*, **113**, 21635 (2009).

AN INKJET DEPOSITION SYSTEM FOR WATER-BASED SOLUTIONS OF MWCNT/PMA FOR SENSING APPLICATIONS

N. Donato*⁽¹⁾, D. Aloisio⁽¹⁾, E. Patti⁽¹⁾, G. Scolaro⁽¹⁾, G. Neri⁽²⁾, D. Spadaro⁽²⁾, S. Trocino⁽³⁾, A. Donato⁽³⁾, M. Latino^(2,4)

⁽¹⁾ Dept. of Matter Physics and Electronic Engineering, University of Messina, Italy

⁽²⁾ Dept. of Industrial Chemistry and Materials Engineering, University of Messina, Italy

⁽³⁾ Dept. of Mechanics and Materials, University "Mediterranea" of Reggio Calabria, Italy

⁽⁴⁾ Dept. of Chemical Science and Technologies, University of Rome Tor Vergata, Italy

*E-mail: ndonato@unime.it

ABSTRACT

In this work are reported efforts made about the development of an inkjet deposition system for inks based on water solutions of multiwalled carbon nanotubes (MWCNT) and poly(methacrylic acid) (PMA). The core of the deposition system consisted of an HP720 printer head, modified to allow the printing of inks on different substrate typologies. The developed system has been employed in the deposition of MWCNTs/PMA contacts on glossy papers and PET transparency sheet for flexible electronics. By varying the printing cycles (i.e. performing an overprinting) it was possible to modulate the thickness of the printed film. The deposition of Ag-doped MWCNT/PMA films on alumina-based sensor substrates was also investigated with the aim to fabricate sensor devices for practical applications.

1. INTRODUCTION

The use of inkjet printing for the deposition of conductive or semiconducting nanostructured materials is one of the turning points for low cost sensor devices development. By means of this technique it is possible to achieve regular patterns for making electrodes or sensing layers for resistive sensors in a more efficient way and avoiding the employment of expensive low-vacuum deposition systems.

On the research of conductive ink, several materials were studied including metals, conductive polymers, and metallic nanoparticle suspensions [1]. Direct writing or drop-on-demand (DOD) technology represents a new method in which conductive inks, are directly printed on the substrate using inkjet printing technology and then form conducting lines after heat treatment [2]. Viscosity and surface tension are the two most important properties of general inks. Size, dispersion and stability are also crucial for the conductive ink system, because the nozzle of the printer would be clogged with larger particles or due to the aggregation of nanoparticles. Thus, it is important to synthesize/formulate ink dispersions with the required rheological properties [3]. Previously, we used MWCNTs-based inks in the prototyping sensor

electrodes printed on glossy papers [4,5]. The aim of this work is to prepare inks based on chemically treated carbon nanotubes dispersed in a suitable aqueous polymer solution. For this scope, a stable aqueous ink of MWCNTs in a poly(methacrylic acid) (PMA) solution was used. PMA acts stabilizing the dispersion of MWCNTs in water. Furthermore, PMA does not show any toxic effects and for this reason it may be used in many applications where a bio-compatible material is required.

Stable colloidal suspensions of silver nanoparticles (AgNPs) in the cross-linked PMA solution with controlled size distribution have been also prepared through a UV irradiation controlled synthesis [6]. PMA was used to induce the Ag⁺ reduction, avoiding metal clustering. This is due to the intrinsic polymer structure and, in particular, to the steric effect of the methyl groups that favors the metal coordination to the carboxylic parts of the macromolecule.

Silver nanoparticles have been studied for their unique sensing properties, in particular by exploiting the optical properties changes in the presence of suitable analytes such as ammonia [7,8]. Here, the volatile organic vapor sensing properties of pure and AgNPs-doped MWCNT/PMA films deposited by inkjet printing were studied.

2. EXPERIMENTS

The core of the deposition system is made by a HP 720C inkjet printer, modified by mounting a home-made translation mechanics as shown in Figure 1. The printing cycling is controlled by home-made electronic board based on Atmel ATmega 16 microcontroller and a relay Array. The microcontroller board is employed to change the polarity of the DC motors of the printer, allowing the over writing and the repositioning of the samples in a more controlled way. The developed electronics employs the control signal coming from the printer to trigger the printing cycles, by means of this solution the microcontroller board is perfectly added with the printer electronics in the printing process. The inkjet printing system allows the deposition of water- or -ethanol based

inks of suspensions of nanostructured materials. The inkjet printer model was chosen by considering that the black cartridge of the HP720C is easy to fill, there is no sponge medium in it, and the printing head of the printer is on the cartridge. So by changing the cartridge it is possible to renew the printing head and its nozzles. The HP720C has an ink drop size of 33 pL and a black color resolution of 600 x 600 dpi.

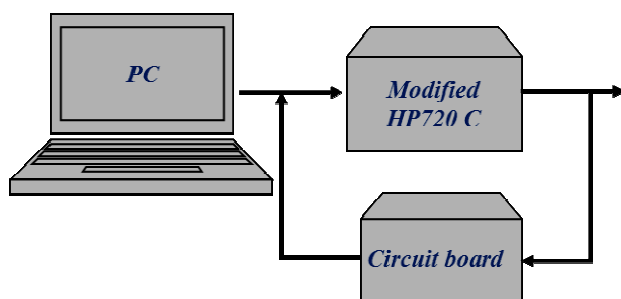
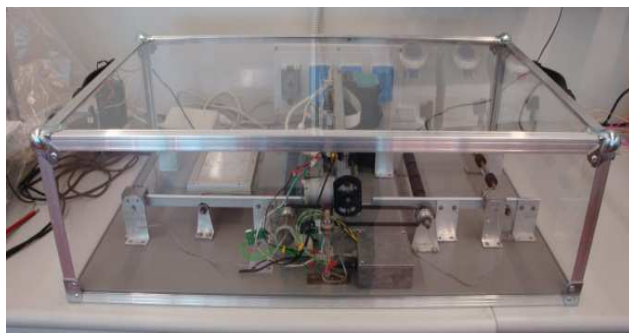


Fig.1 Picture and block diagram of the deposition system

The ink solution was prepared by first functionalizing MWCNTs by means of a typical procedure described as follows: MWCNTs were suspended in concentrated nitric acid (15 M) and refluxed for 18 hours at 110 °C to modify the MWCNTs surface, they were then rinsed with distilled H₂O until the pH of the solution was neutral, and finally they were dried at 80 °C in vacuum oven. Then MWCNTs were dispersed in the PMA (30% water solution of sodium stabilized PMA, Mw = 9500), with a weight ratio MWCNTs/PMA of about 17wt% and sonicated for four hours at 60 °C. All chemicals were used as received without further purification. Distilled water was used to set the desired dilutions.

Ag NPs/PMA colloids were prepared by a photo-induced reduction process under UV irradiation of silver nitrate (AgNO₃, 98%-pure powder, Sigma-Aldrich) in a dilute solution of PMA used as reducing and capping agent. Then, MWCNTs were dispersed in the AgNPs-PMA capped, with a weight ratio MWCNTs/AgNPs-PMA of about 17wt% and sonicated for four hours at 60 °C.

The as prepared solutions were used to fill the cartridge of the deposition system. In Fig. 2 is reported a picture showing a patterned electrodes deposited on flexible

glossy photopaper. Depositions have been also made on alumina substrates with platinum electrodes and complex devices as BAW and SAW resonators (not reported).

In order to investigate the electrical and sensing properties of the deposited inks, the fabricated prototypes were introduced in a stainless-steel test chamber for the electrical and sensing tests. The experimental bench for the electrical characterization of the sensors allowed to carry out measurements in controlled atmosphere. Electrical measurements were carried out at room temperature, under a dry synthetic air or nitrogen total stream of 50 sccm, collecting the sensors resistance data in the four point mode. Ethanol coming from a bubbler can be further diluted at a given concentration by a mass flow controller array made by Bronkhorst. The concentration of target gas was varied from 0 to 3.5 %. A multimeter data acquisition unit Agilent 34970A and Keithley 2400 source meter were used for acquiring the sensor signal. The gas response, S , is defined as $S = R_0/R$ where R_0 the baseline resistance and R is the electrical resistance of the sensor at different ethanol concentrations.

3. RESULTS

The printing on several substrates it is allowed by the facilities developed on the inkjet printing system. Specifically, it is possible to easily set the printing area and the working distance of the nozzles to follow the substrates topologies, even on packaged devices as SAW on TO39 package. The packaged devices are mounted in specific sample holders that allow the alignment and the positioning of the sample with respect the printing head, assuring the repeatable overwriting cycle, if needed.



Fig.2 Inkjet printing of MWCNT/AgNPs-PMA thin films as electrodes on flexible substrate.

In Fig. 3 are reported SEM micrographs of MWCNT/AgNPs-PMA thin films printed on glossy photo-paper. Top view image shows the network structure of the deposited carbon nanotubes embedded in the polymer matrix, forming a film about 500 nm thick (see

section view in Fig. 3). A previous TEM analysis indicated that Ag clusters in the nanometer range are presents wrapped to the PMA structure.

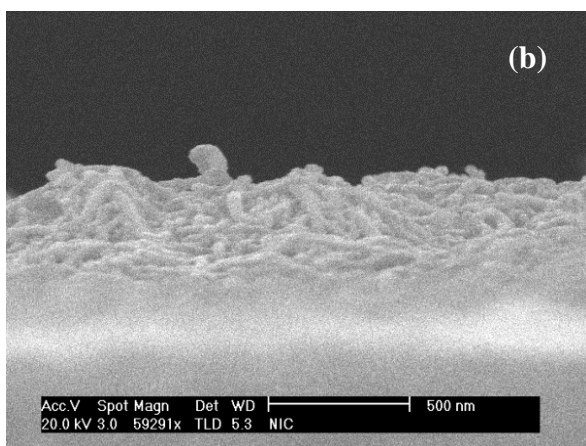
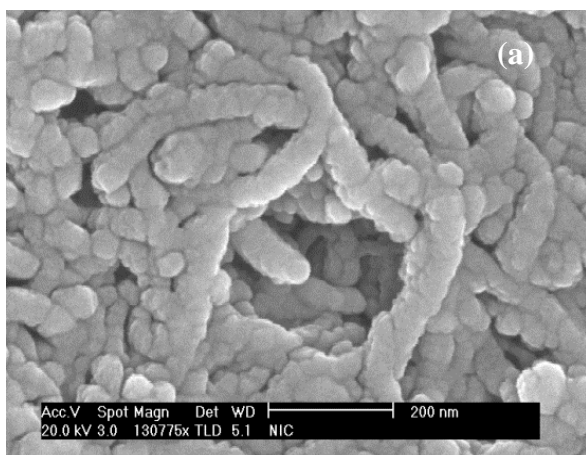


Fig.3 SEM micrographs of MWCNT/AgNPs-PMA thin films printed on flexible glossy paper substrate: top view (a) and section view (b).

A complete electrical characterization of the inks deposited on the various substrates has been then carried out. By varying the printing cycles (i.e. performing an overprinting) it was possible to modulate the thickness of the printed film.

In Fig. 4 are reported the resistance measurements performed on the AgNPs-PMA/MWCNTs sample printed on alumina substrate with 100 μ m spaced platinum electrodes. It can be noted a decreasing of the baseline resistance by increasing the number of overprinting cycles. This effect was recorded with all the substrate typologies, indicating that the phenomenon observed is related to the film itself and not conditioned by the nature of the underlying substrate.

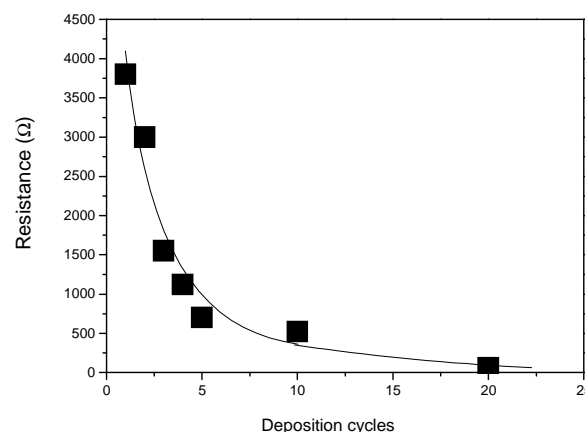


Fig.4 Baseline resistance in air of the AgNPs-PMA /MWCNTs printed sample as a function of deposition cycles

In order to characterize the electrical behavior of the printed samples, *I-V* cycling tests were performed. In Fig. 5 are reported the *I-V* cycles of AgNPs-PMA/MWCNTs sample on glossy photo paper made by 20 overprinting cycles. The linear response in all range of voltage tested indicate an ohmic behavior. Furthermore, it can be seen how increasing the temperature brings to an increasing of conductance. This electrical behavior vs. temperature is agreement with the presence of MWCNTs acting as a semiconductor.

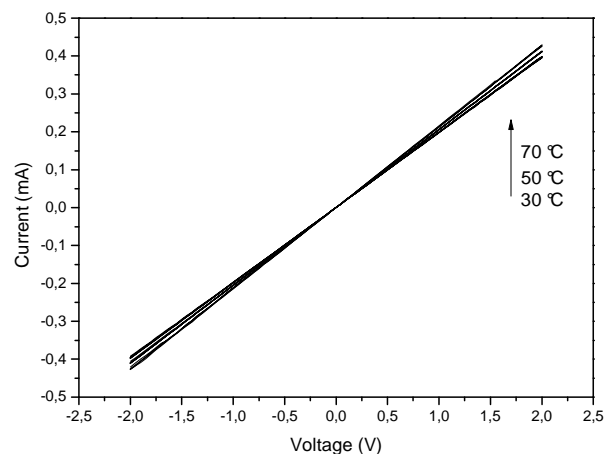


Fig.5 *I-V* plot as a function of the temperature for electrodes printed on photo paper with 20 overprinting cycles.

The sensing properties of inks prepared and deposited as sensing layer on alumina substrates were also investigated. In Fig. 6 are reported the calibration curves of the pure- and AgNPs-doped inks recorded with ethanol as target gas. It is noteworthy that, the presence of MWCNTs is essential in order to carry out the measurements, because the resistance of pure- or AgNPS-doped films is very high and not measurable with the conventional instrumentation.

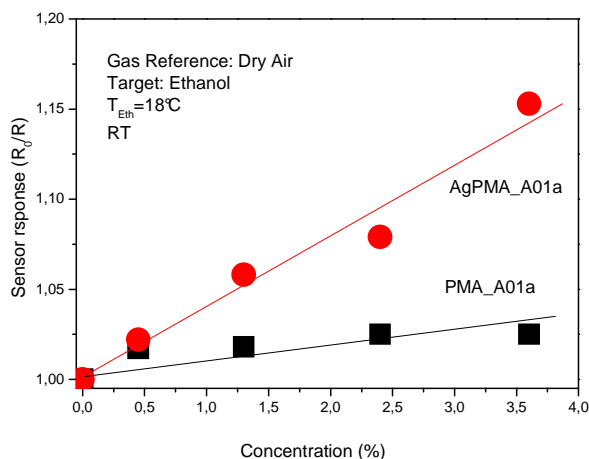


Fig.6 Comparison of the calibration curves recorded for PMA/MWCNTs and AgNPs-PMA/MWCNTs samples.

The mechanism of ethanol detection on these inks relies on the hydrogen bonding established between the $-\text{COOH}$ group on the PMA matrix and the alcoholic group. It clearly appears from our results as the presence of silver nanoparticles in the polymer further enhances the sensing properties of the film towards ethanol.

Further investigation are then in progress in order to evaluate how the size of the Ag nanoparticles and their concentration in the PMA matrix can modulate the sensing properties of the developed devices.

4. CONCLUSION

In this work were reported the experimental activities regarding the development of an inkjet deposition system for water-inks based on multiwalled carbon nanotubes dispersed in pure- and silver nanoparticles-doped poly(methacrylic acid). The core of the deposition system consisted of an HP720 printer head, modified to allow the printing of inks on different substrate typologies. The developed system has been employed both in the reproducible deposition of regular patterns for making electrodes on flexible substrates and the deposition of sensing layers. The ethanol sensing of these latter were investigated and the promoter effect of Ag nanoparticles was highlighted.

5. ACKNOWLEDGMENTS

This work was founded with MIUR PRA08-09 of University of Messina.

6. REFERENCES

- [1] P. Calvert, *Chem. Mater.*, **13** 3299 (2001).
- [2] Y-C Lu, K-S Chou, *Journal of the Chinese Institute of Chemical Engineers* **39** 673 (2008).
- [3] H-H Lee, K-S Chou, K-C Huang, *Nanotechnology* **16** 2436 (2005).
- [4] A. Arena, N. Donato, G. Saitta, *Microelectronics Journal*, **40** 887 (2009).

[5] A. Arena, N. Donato, G. Saitta, A. Bonavita, G. Rizzo, G. Neri, *Sensors and Actuators B*, **145** 488 (2010).

[6] D. Spadaro, E. Barletta, F. Barreca, G. Curro, F. Neri, *Applied Surface Science* **255** 8403 (2009).

[7] H. Guo and S. Tao, *Sens. Actuators B*, **123** 578 (2007).

[8] S. T. Dubas, V. Pimpan, *Talanta* **76** 29 (2008).

LIQUID PHASE FUNCTIONALIZATION OF CARBON NANOTUBES: MORPHOLOGY AND SURFACE MODIFICATION

C. Milone^{1*}, E. Piperopoulos¹, S.H. Abdul Rahim¹, M. Lanza², S. Santangelo³, S. Galvagno¹

¹ *Department of Industrial Chemistry and Materials Engineering, Engineering Section, University of Messina, Messina, Italy*

² *C.N.R., Institute for Chemical Physics Processes Sect. Messina, Messina, Italy*

³ *Department of Mechanics and Materials, Engineering Faculty, "Mediterranea" University, Reggio Calabria, Italy*

* E-mail: cmilone@unime.it

ABSTRACT

Functionalization of carbon nanotubes was carried out at 333 K with a mixture of HNO₃ (67 wt.%) and H₂SO₄ (98 wt.%). The influence of the nitric to sulphuric acid volume ratio on the morphology and crystalline quality of carbon nanotubes, as respectively monitored by transmission electron microscopy and Raman spectroscopy, was evaluated. The chemical composition of carbon surface upon different functionalization conditions, in terms of type and amount of oxygenated groups originated, was monitored by temperature programmed desorption. The results showed that, as H₂SO₄ concentration increases, a strong enhancement of oxygenated groups occurs, while the tubular structure is preserved.

1. INTRODUCTION

The use of carbon nanotubes (CNTs) in heterogeneous catalysis as support for noble metal and/or metal oxides [1] or as direct catalyst [2,3] is becoming larger owing to their higher stability under reaction conditions, especially in oxidation processes.

Regardless the role of CNTs in the catalytic cycle (support or direct catalyst), their surface chemistry seems to play an important role in addressing the catalytic behavior. Modification of the surface by addition of oxygenated functional groups can affect the preparation of carbon-supported catalysts, in terms of dispersion of metallic phase, due to the modification of acid-base properties and hydrophobicity [4].

Similarly, the catalytic properties of metal free CNTs are also influenced by the surface chemistry [3,5-7]; several studies, indeed, demonstrate that creation of quinones/carbonyl groups over CNTs surface improves CNT activity in the case of oxidative dehydrogenation of ethylbenzene to styrene [2], while a proper tuning of the acid properties of the surface is of relevance for the catalytic wet air oxidation and ozonation reactions [3,5-7].

In this frame, it clearly appears the importance of modification of the surface properties of CNTs and the knowledge of the concentration and distribution of the attached functional moieties for catalytic applications.

In this study, the variation of the morphology and chemical properties of the CNT surface upon liquid phase functionalization by HNO₃ and H₂SO₄ mixture at different volume ratio is investigated.

The influence of the functionalization conditions on the CNT morphology and crystalline quality are monitored by means of transmission electron microscopy (TEM) and Raman spectroscopy (RS). The type and amount of surface groups are estimated by temperature programmed desorption (TPD).

2. EXPERIMENTAL

2.1 Materials

CNTs were prepared by chemical vapor deposition of isobutane (i-C₄H₁₀) over 29 wt.% Fe catalyst supported on Al₂O₃. Details of the preparation procedure are reported elsewhere [8]. After synthesis, the carbonaceous product was separated from the catalyst through the following steps: a first treatment with a solution of NaOH (1 M) at 353 K followed by a treatment with a solution of HCl (1 M) to remove support and iron particles, respectively. The purified sample was finally washed with distilled water and dried at 353 K for 12 hrs.

Functionalization of CNTs in nitric-sulphuric acid mixture was undertaken in an ultrasonic bath at 333 K for 6hrs. 3 g of purified CNTs were weighed and added to 300 ml of acid mixture (67% HNO₃ and 98% H₂SO₄) having a proper volume ratio (3:1, 1:1 and 1:3).

After treatment, carbon material was separated by filtration through 0.2 µm filter paper, washed with water to neutral pH and dried at 353 K for 12 hrs.

Catalysts code reported in Table 1 summarizes information relative CNTs treatment. CNTs-p and CNTs-N:S stands for pristine and functionalized nanotubes, respectively. N:S indicates the nitric-sulphuric volume ratio used for the functionalization.

2.2 Characterization of CNTs

Morphology and dimensions of the CNTs were investigated by using a TEM JEOL JEM 2010, operating at 200 kV and equipped with a Gatan 794 Multi-Scan CCD camera.

Surface area, SA(m²/g), was determined by adsorption-desorption of dinitrogen at 77 K, after out-gassing (10⁻⁴ mbar) the samples at 353 K for 2 hrs, using surface area analyzers – Qsurf Series.

Raman scattering was measured, at room temperature, in the 800–3350 cm⁻¹ spectral range by using a double monochromator (Jobin Yvon Ramanor U-1000) equipped with a microscope (Olympus BX40) and a photomultiplier (Hamamatsu R943-02) operating in photon-counting mode. An Ar⁺ laser (Coherent Innova 70) operating at 2.41 eV (514.5 nm) excited Raman scattering. Light was focused onto the sample to a spot of 2 μm in diameter through the X50 microscope objective lens.

A 30 s long acquisition time was used to improve the S/N ratio. In order to reliably describe the sample bulk, several different locations of each specimen were sampled on account of the possible structural non-homogeneity.

After normalisation and averaging, background was subtracted and Lorentzian bands were used to reproduce the spectra. The integrated-intensity ratios were then calculated. Qualitative and quantitative evaluation of the functional groups introduced over CNTs surface was performed by means of TPD. Analyses were carried out using a flow reactor equipped with a quadrupole mass spectrometer (HPR 20 HIDDEN ANALYTICAL instrument). Samples (30 mg) were placed in a U-shaped quartz tube inside an electrical furnace and heated at 10 K min⁻¹ up to 1373 K using a constant flow rate of helium (30 scfm). The mass signals m/z = 28 (CO), 30 (NO), 44 (CO₂), and 64 (SO₂) were monitored during the analysis. The amounts of CO, CO₂, NO and SO₂ were calibrated at the end of each analysis with pure gases. After treatment of the acquired data, the TPD spectra of CO, CO₂, NO and SO₂ (in μmol g⁻¹ s⁻¹) were obtained.

3. RESULTS AND DISCUSSION

3.1 Morphology and crystalline quality of CNTs

Results of TEM analysis, shown in Figure 1, evidence that CNTs-p look as long carbon filaments (length ≥ 5 μm), with external diameter between 5 nm and 20 nm (Figure 1a). Higher magnification microphotographs (inset of Figure 1a) evidence that tube-walls are mainly constituted by smooth graphene-layers. Upon treatment with nitric-sulphuric mixture, the tubular structure of carbonaceous material is preserved (Figure 1b-c), regardless the relative acid volume ratio

When functionalization is carried out with the poorest sulphuric acid mixture (N:S= 3:1), no considerable modification of the side graphitic sheets occurs (inset Figure 1b). As the concentration of sulphuric acid increases, instead, side-walls appear severely degraded. A thick layer of amorphous carbon covering the tubes, evidenced by the white arrows in the inset of Figure 2c, together with an increased number of edges and steps at external sheets appears. These results undoubtedly indicate that the use of rich sulphuric acid mixtures is more harmful for CNT crystalline structure.

Table 1. Sample code, surface area and results of Raman spectra decomposition.

Code	SA (m ² /g)	I _G /I _D	L _C (nm)	I _G /I _G	I _G /I _D
CNTs-p	196	0.56	2.47	0.82	0.46
CNTs-3:1	195	0.54	2.38	0.58	0.31
CNTs-1:1	194	0.48	2.10	0.50	0.24
CNTs-1:3	172	0.47	2.07	0.49	0.23

SA values of functionalized samples, measured by N₂ adsorption and reported in Table 1, do not significantly vary with respect to that of un-treated tubes. Very close values are instead found for CNTs-p, CNTs-3:1 and CNTs-1:1, while a slight reduction, by 13%, is observed for CNTs-1:3 sample. SA lowering for the most rich sulphuric acid treated sample could be due to the strongest entanglement of carbon nanotubes, as evidenced from the comparison of Figure 1a-c, caused by the electrostatic interaction between the polar functional groups introduced that reduces the tube-tube distance and, hence, the exposed external surface area. It is indeed known that a strong CNT agglomeration occurs upon oxidative treatment [9].

Based on a stronger interaction between tubes and damaging of the tubes evidenced by TEM a larger number of functional groups should be expected on CNTs-1:3 sample. The crystalline quality of the CNTs is investigated also by means of RS.

Raman spectra (not shown for brevity) evidence that all the samples exhibit similar features: the graphite-like in-plane optical mode at 1580 cm⁻¹ (G-band); the band, at 1350 cm⁻¹, originating from lattice defects (vacancies, pentagons, heptagons or other defects and by finite size effects) that break the basic graphene-layer symmetry (D-band) [10,11]; its overtone at 2700 cm⁻¹ (G'-band) that, conversely, is detected only in nanotubes constituted by a sequence of smooth graphene sheets [12]; and the D'-mode at 1610 cm⁻¹ that, similar to the D-mode, is a disorder-activated double resonance Raman feature; the two modes respectively originate from inter- and intra-valley scattering processes [13].

After background subtraction, the spectral features are fitted to Lorentzian bands and the integrated-intensity ratios are calculated. The extent of structural defects is monitored by the G/D intensity ratio (I_G/I_D) that, for fixed excitation energy, lowers with decreasing in-plane correlation length (i.e. mean inter-defect distance). Thus, it monitors the average size of domains with graphitic order (L_C=4.4·I_G/I_D) [14]. Instead, the G'/G intensity ratio (I_G/I_G) is generally regarded as an indicator of long-range order [12]. Thus, the overall crystalline quality, which improves with increasing mean inter-defect distance and/or unundulated tube-wall number (i.e. with increasing I_G/I_D and/or I_G/I_G, respectively), is pictorially described by the G'/D intensity ratio (I_G/I_D). The results shown in Table 1 prove that acid attack increases the density of lattice defects, as signaled by the lowering of I_G/I_D, and downgrades the CNT crystalline quality,

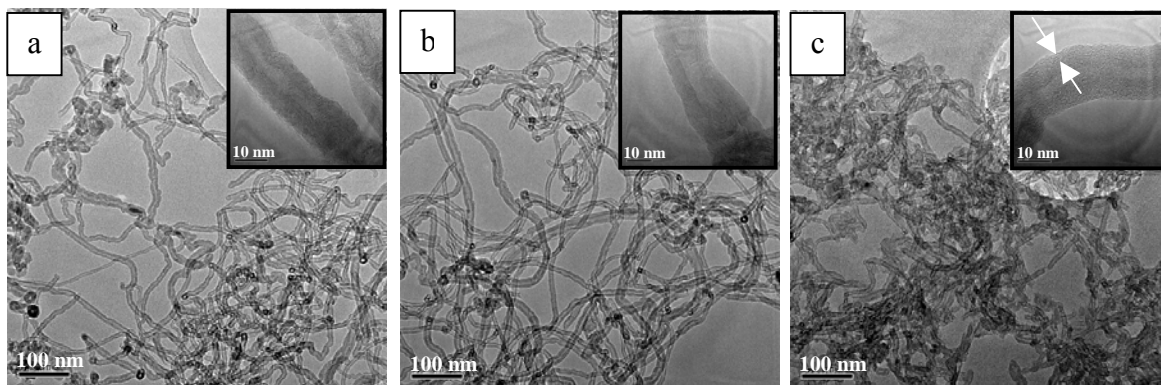


Figure 1. Morphology of CNTs as monitored by TEM. Photos refer to (a) CNTs-p, (b) CNTs-3:1 and (c) CNTs-1:3

as monitored by the lowering of the I_G/I_D . The increased amount of lattice defects present in graphene sheets causes L_C to reduce from 2.47 nm in CNTs-p to 2.38 nm in CNTs-3:1 and to 2.07 nm in CNTs-1:3, indicating that decreasing nitric-sulphuric acid volume ratio is more harmful to the CNT crystallinity. The data reported in Table 1 allow clarifying the origin of the CNT crystalline quality downgrade, i.e. the nature of structural modifications produced by the treatment. Comparing intensity ratios, it comes into view that I_G/I_G (which diminishes by even 40%) undergoes a greater variation than I_G/I_D (maximum reduction: 16%). This is because, although CNTs substantially maintain their structure after acid treatment, the number of smooth tube-walls becomes dramatically smaller.

3.2 Chemical composition of CNT surface

The surface chemical characteristics of CNTs are evaluated by means of TPD, a thermal analysis become popular for the characterization of the oxygen-containing groups on the surface of carbon materials.

In this technique, all oxygenated surface groups are thermally decomposed releasing CO and/or CO₂ at different temperature.

In general, CO₂ evolution results from removal of carboxylic acids at low temperature (423–723 K) and lactones at higher temperature (873–1073 K); carboxylic anhydrides originate both CO and CO₂ in equal amount in the range of temperature 623–923 K; from removal of phenols and quinones/carbonyl groups CO evolve at 837–1023 K and 973–1223 K, respectively [7].

CNTs-p show a broad and weak CO₂ peak in the range of temperature 400–650 K (Figure 2a) and a more intense contribution in the range 873–1073 K (Figure 2e), which fairly agree with the removal of carboxylic acid groups and lactones, respectively [7] and a sharp CO peak at ≈ 1200 K, likely arising from more energy demanding removal of quinones/carbonyl groups [7] (Figure 2e).

As effect of functionalization, CO₂ and CO evolution augments with the increasing of sulphuric acid concentration (Figures 2b-d and f-h), indicating an enhancement of functional groups introduced onto the CNT surface as the oxidative condition becomes more aggressive.

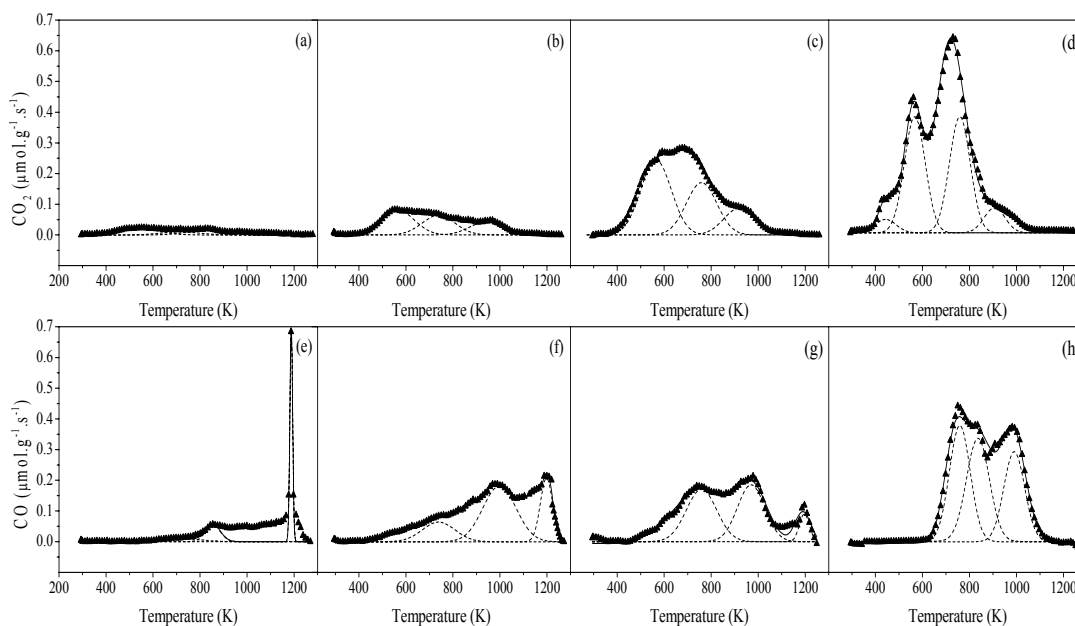


Figure 2. Results of the decomposition of CO₂ and CO TPD profiles. Data refers to: CNTs-p (a) and (e); CNTs-3:1 (b) and (f); CNTs-1:1 (c) and (g); CNTs-1:3 (d) and (h). (▲ TPD experimental data; - - - individual peaks; — sum of individual peaks)

Table 2. Results of decomposition of CO₂ and CO TPD profiles using multiple Gaussian function

Code	Carboxylic acids		Carboxylic anhydrides		Lactones		Phenols		Quinones/ carbonyls	
	T _M (K)	A (μmol/g)	T _M (K)	A (μmol/g)						
CNTs-p	535	34	716	15	832	24	855	31	1188	76
CNTs-3:1	567	102	739	82	940	56	986	201	1198	122
CNTs-1:1	565	281	759	175	918	102	970	161	1196	46
CNTs-1:3	443	33	727	307	915	40	836	297	-	-
	567	344					990	233		

The TPD results also allow the identification and quantification of the functional groups present on the materials surface by peak assignment, as described elsewhere [7].

The amount of oxygenated groups, such as carboxylic acids, carboxylic anhydrides, lactones, phenols and quinones/carbonyl groups, can be obtained by decomposition of the complex TPD profiles. A multiple Gaussian fitting function is used to reproduce each spectrum according to the method proposed by Pereira et al. [15]. The use of Gaussian function is justified by the shape of TPD peaks, which are a result of continuous random distribution of binding energies of the surface groups [16]. In the case of carboxylic anhydrides, which decompose by releasing one CO and one CO₂ molecule, in the fitting procedure it was assumed that the related CO and CO₂ peaks must have the same shape and equal magnitude.

As shown in Figure 2, the decomposition procedure fitted the data quite well for CO and CO₂ TPD profiles of the samples. Table 2 reports the assignment and the distribution of the oxygenated groups (T_M is the temperature of the component peak maximum and A is the concentration calculated by the integrated peak area).

The results show that as CNTs are treated under more aggressive conditions, i.e. with enriched sulphuric acid mixture, carboxylic acids, anhydrides and phenols functionalities progressively increase. The generation of lactones and quinones/carbonyl functionalities is not favored by the use of the oxidant acid mixture and in the case of quinones/carbonyl groups their concentration approaches to zero when the richest sulphuric acid mixture is used.

Besides oxygenated groups directly originated from the oxidation of carbon onto the surface, TPD analysis demonstrated that evolution of SO₂ also occurs for all the functionalized samples in the range of temperature 450–800 K in agreement with the decomposition of sulphonic acid groups [17].

The amount of these groups increases from 6 μmol/g for CNTs-3:1 to 182 μmol/g for CNTs-1:1, reaching the highest value (448 μmol/g) for CNTs-3:1 sample.

Nitration of carbon surface is instead negligible being the amount of NO released from all the oxidized samples in the range of temperature 400–600 K lower than 4 μmol/g.

4. CONCLUSIONS

Liquid phase functionalization of CNTs by nitric-sulphuric acid mixture leads to a strong modification of the chemical composition of the surface with a progressive enhancement of the concentration of carboxylic acids, anhydrides, phenols and sulphonic acid groups as the concentration of sulphuric acid in the reaction mixture increases. However, even under the harshest functional conditions the tubular structure is preserved.

5. REFERENCES

- [1] J.M. Tang, K. Jensen, M. Waje, W. Li, O. Larsen, K. Pauley, Z. Chen, P. Ramesh, M.E. Itkis, Y. Yan, R.C. Haddon, *J. Phys. Chem. C* **111**, 17901, (2007).
- [2] J.J. Delgado, X. Chen, J. P. Tessonier, M.E. Schuster, E. Del Rio, R. Schögl, D.S. Su, *Catal. Today*, **150**, 49, (2010).
- [3] S.Yang, X.Li, W.Zhu, J.Wang, C.Descorme, *Carbon*, **46**, 445, (2008).
- [4] P. Serp, J.L. Figueiredo, *Carbon Materials for Catalysis*, Wiley, New Jersey, 2009.
- [5] Z.Q. Liu, J. Ma, Y. H.Cui, B.P.Zhang, *Appl. Catal., B*, **92**, 301, (2009).
- [6] Z.Q. Liu, J. Ma, Y.H. Cui, L. Zhao, B.P. Zhang, *Appl. Catal., B*, **101**, 74, (2010).
- [7] J.L. Figueiredo, M.F.R. Pereira, *Catal. Today*, **150**, 2, (2010).
- [8] M.G. Donato, S. Galvagno, M. Lanza, G. Messina, C. Milone, E. Piperopoulos, A. Pistone, S. Santangelo, *J. Nanosci. Nanotechnol.*, **9**, 3815, (2009).
- [9] W. Xia, C. Jin, S. Kundu, M. A. Muhler, *Carbon*, **47**, 919, (2009).
- [10] A.C. Ferrari, J. Robertson, *Phys. Rev. B.*, **61**, 14095, (2000).
- [11] Z. Wang, X. Huang, R. Xue, L.J. Chen, *Appl. Phys.*, **84**, 227, (1998).
- [12] Y.A. Kim, T. Hayashi, K. Osawa, M.S. Dresselhaus, M. Endo, *Chem. Phys. Lett.*, **380**, 319, (2003).
- [13] M.S. Dresselhaus, G. Dresselhaus, R. Saito Jorio, *Phys. Rep.*, **409**, 47, (2005).
- [14] F. Tuinstra, J.L. Koenig, *J. Chem. Phys.* **53**, 1126, (1970).
- [15] A.G. Goncalves, J.L. Figueiredo, J.J.M. Orfão, M.F.R. Pereira, *Carbon*, **48**, 4369, (2010).
- [16] J.M. Calo, P.J. Hall *Fundamental issues in the control of carbon gasification reactivity*, Kluwer Academic Publisher, Dordrecht, 1991.
- [17] H.T. Gomes, S.M. Miranda, M.J. Sampaio, A.M. Silva, T. J.L. Faria, *Catal. Today*, **151**, 153, (2010).

SINGLE WALL CARBON NANOTUBES DEPOSITED ON STAINLESS STEEL FOIL AS COUNTER ELECTRODE FOR DYE SENSITIZED SOLAR CELLS

G. Calogero* ⁽¹⁾, O.M. Maragò ⁽¹⁾, P. G. Gucciardi ⁽¹⁾, G. Di Marco ⁽¹⁾

⁽¹⁾ CNR-IPCF, Istituto per i Processi Chimico-Fisici, Messina, Italy

* E-mail: calogero@me.cnr.it

ABSTRACT

Dye-sensitized solar cells (DSSCs) have attracted much attention due to their good light to electricity conversion efficiency, simple fabrication and low cost. The counter electrode employed for the regeneration of electrolyte is commonly constituted by a platinum film deposited on a conductive glass. Carbonaceous material, are quite attractive to replace platinum due to a higher corrosion resistance against iodine, higher catalytic activity and lower costs. We report on the implementation of stainless steel foils coated with dispersed Single Wall Carbon Nanotubes as novel, low cost and highly efficient counter electrodes for DSSCs.

1. INTRODUCTION

DSSCs (see schematic representation in Fig. 1) consist of a high porosity nanocrystalline photoanode made of TiO₂ semiconductor nanoparticles (15 to 20 nm diameter, $E_{\text{gap}} = 3.2$ eV), deposited on a transparent conducting oxide (TCO) glass support and sensitized with a self-assembled monolayer of dye molecules anchored to

the TiO₂ surface [1,2]. When illuminated, the dye molecules capture the incident photons generating electron/holes pairs. The resultant electrons, at excited states, are immediately injected (within 100 fs) into the conduction band of the TiO₂ and transported to the electron-collecting counter electrode, the cathode. Regeneration of dye molecules is accomplished by capturing electrons from a liquid electrolyte (iodide/iodine solution), sandwiched face-up on the cathode, that catalyses the reduction of tri-iodide. Currently, DSSCs cathodes are made of platinum layers deposited on transparent glass which are, in turn, coated by a conductive layer such as Fluorine doped Tin Oxide (FTO) or Indium Tin Oxide (ITO). Furthermore it tends to degrade over time when in contact with an iodide/iodine liquid electrolyte, reducing the overall efficiency of DSSCs [3]. During the last few years strong efforts have been directed towards the replacement of such elements with low cost and more versatile materials. Metal sheets or foils are flexible substrates with excellent electrical and thermal conductivities suitable to employed in the cathodes fabrication [4]. On the other hand, carbonaceous materials feature good catalytic properties,

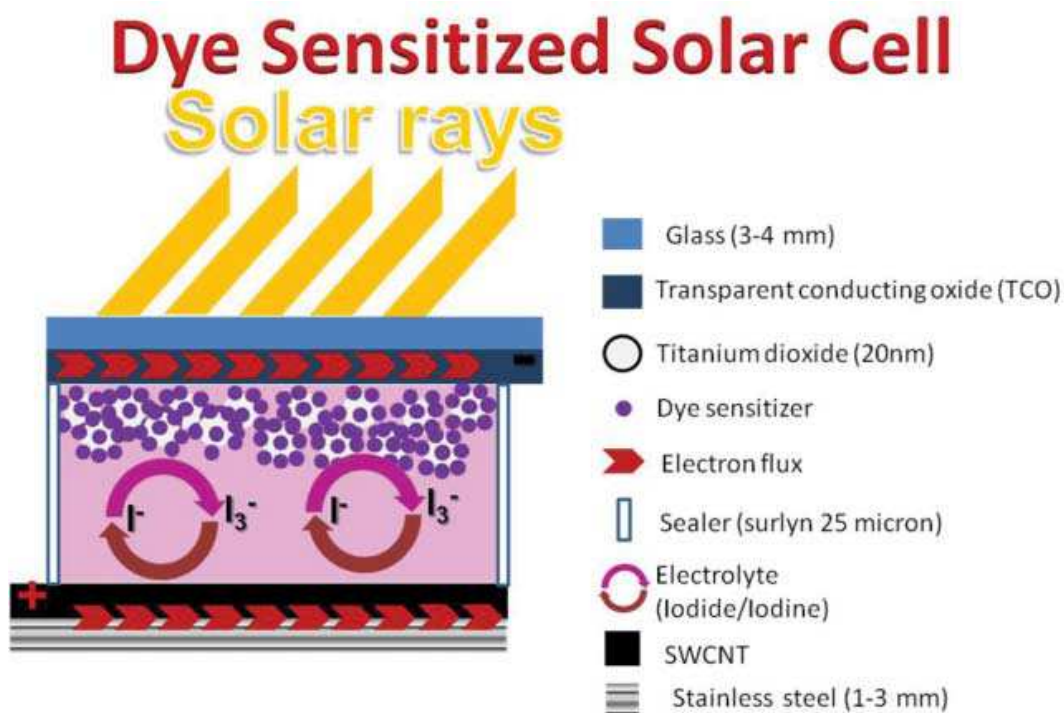


Figure 1. Section view of a DSSC with SWNT deposited on a stainless-steel substrate as counter electrode.

electronic conductivity, corrosion resistance towards iodine, high reactivity, abundance and low cost [5]. In 1996 Kay et al. [6] demonstrated the importance of the high surface area introducing carbon black powder in graphite counter electrodes to enhance its catalytic activity. Since then, other research groups have employed different carbonaceous materials such as graphite, carbon black, activated carbon, fullerene, hard carbon sphere, carbon nanotubes (CNTs) and graphene [7-15]. Single Wall Carbon Nanotubes (SWNTs) are made by rolling up a single grapheme sheet with a fullerene like end-cap[3]. Their electronic properties are described by a pair of integers (n , m), the chiral indices, that determine univocally their semiconducting or metallic nature. Multi-Wall nanotubes (MWNTs) consist of multiple concentric SWNTs with random chirality, making them metallic on average. Carbon nanotubes combine advantages such as high electrical conductivity, chemical stability and high surface area with good electrochemistry and catalytic properties making them suitable for applications in many energy conversion technologies such as catalytic counter electrode materials in DSSCs. In particular, CNTs are efficient to catalyze the tri-iodide reduction and, thus, are good candidates to replace Platinum in DSSCs [3,5]. The excellent electrical and thermal conductivity of stainless steel sheets, combined with the chemical stability and high surface area of SWNTs, make them excellent candidates as catalytic counter electrodes in DSSCs. In this study we introduce a novel cathode type in DSSCs, based on the combination of SWNTs as catalysts and stainless-steel foils as conductive substrates, comparing the solar energy conversion efficiency and other parameters connected with the current–voltage (I – V) curve of these cells with the corresponding parameters of standard cells employing Pt and FTO as catalyst and conductive substrate, respectively.

2. EXPERIMENTAL

The conductive glass plates (FTO glass, fluorine-doped SnO_2 , sheet resistance $15 \Omega/\text{cm}^2$), the Pt catalyst T/SP and the Ti_nanoxide (T) paste were purchased from Solaronix SA and used as supplied. All the solvents and chemicals employed for the experiments were reagent or spectrophotometric grade. CarboLex AP-grade SWNTs produced by arc discharge were purchased by Aldrich (part 519308, lot 05224EC). The sample purity is declared to be 50–70%. Nominal diameters and lengths range between $dt = 1.2$ – 1.5 nm and $L = 2$ – $5 \mu\text{m}$, respectively. For optical characterization, SWNTs were individualized in water–surfactant solution (Sodium cholate, Aldrich, Cat: 27,091-1), by ultrasonication followed by ultracentrifugation [5]. For cathode preparation SWNTs were dispersed in water by ultrasonication without any further pre-treatment. The stainless-steel sheets and foils were purchased from a shop specializing in metals and sized in our laboratory, the chemical composition of the metallic sheet is the following: 18–20% Cr, 8–12% Ni, 1% Si, 0.030% S,

0.045% P, 2% M_2n , 0.08% C as reported from the American Iron Steel Institute (AISI) and the metallic sheets are classified as AISI 304 (or X8 CN1910 according to UNI 4047).

The synthetic dye cis-di(thiocyanato)-bis-(2,2'-bipyridyl-4,4'-dicarboxylate) ruthenium (II), called N3, was synthesized and purified following the procedure reported in the literature [16]. A standard solution was prepared by dissolving 20 mg of the inorganic complex (N3) in 50 mL of ethanol. The photoanodes were prepared by depositing TiO_2 films on FTO conducting glass. First, two edges of the FTO glass plate were covered with four layers of adhesive tape (3M Magic) to control the thickness of the film and to mask electric contact strips. Then the TiO_2 paste was spread uniformly on the substrate by sliding a glass rod along the tape spacer. The resulting mesoscopic oxide film was 12–14 mm thick and transparent, presenting negligible light scattering. After drying the TiO_2 , the covered glass plates were sintered in air for 30 min at 450°C , cooled to about 80°C and soaked in N3 dye solution overnight. Excess dye was removed by rinsing with ethanol. The investigated counter electrodes were prepared according to the following procedures. Sample P1: the Pt catalyst T/SP paste was spread on FTO glass and heated at 450°C for 30 min. Sample P2: we used a Pt mirror (350 nm thick) obtained by thermal vapor deposition (or sputtering) of Pt onto FTO conducting glass. Sample P3: analogous to P2 except for the substrate that in this case was a thin (2 mm) stainless steel sheet. Sample C1: we drop cast bundles of Carbolex SWNTs dispersed in water onto a FTO conducting glass substrate. 2 mg of nanotubes powder were dispersed in 10 ml of water by ultrasonication at 200W for 2 h. Nanotubes were then dropped cast onto the substrate, whose temperature was set to 150°C . Sample C2: same procedure of sample C1, but exploiting a thin (2 mm) stainless-steel sheet as substrate. Current–Voltage curves were recorded by a digital Keithley 236 multimeter connected to a PC and controlled by homemade software. Sunlight irradiation was provided by a LOT-Oriel solar simulator (Model LS0100-1000, 300 W Xe Arc lamp powered by LSN251 power supply equipped with AM1.5 filter, $100\text{mW}/\text{cm}^2$).

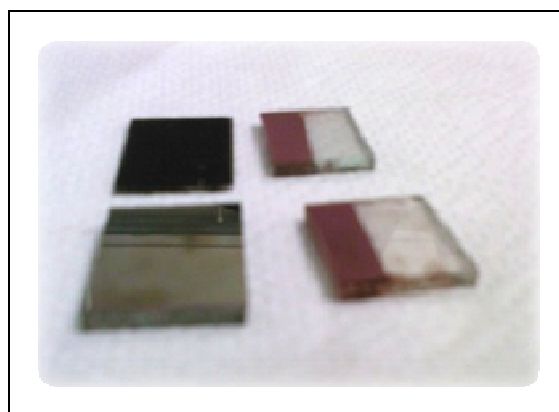


Figure 2. On the left there are the SWCNT cathode (up) and of Pt sputtered (bottom) while on the right there are the corresponding the sensitized photoanode.

3. RESULTS

For DSSC testing we selected a high corrosion resistance set of different stainless steel sheets with low Nickel content (< 12%). We did not observe any corrosion effect on the stainless steel sheets conductivity after their immersion in the electrolyte solution. This confirms that stainless-steel foils are suitable as substrates for DSSCs. In Table 1 are reported the parameters obtained by I–V measurements: fill factor (FF), open circuit voltage (Voc), short circuit current density (Jsc) and conversion energy efficiency (η). The best solar energy conversion efficiency ($\eta = 4.5\%$) was achieved with the P3 method (Pt mirror/stainless steel cathode) and it is comparable to the one reported by Fang et al. [4] using a metal sheet as counter electrode. Metallic platinum based counter electrodes (P2 and P3) act as light reflectors and highly efficient conductors, remarkably improving the efficiency of the solar cells with respect to P1, C1 and C2. The lower efficiency obtained on P2 with respect to P3 is due to the higher resistance of the FTO glass substrate. We

combining the high surface area of SWNTs with the high conductivity of the metal sheet. This result is comparable to the sample P2 and to the data reported on purified SWNTs by Suzuki et al. [11]

4. CONCLUSIONS

We demonstrated the preparation of a DSSC based on a novel stainless-steel cathode coated with commercial low cost non purified SWNTs. Measurements on 0.52 cm² test cells showed an efficiency of 3.92%. We achieved with the SWNTs based cathode on stainless steel (C2) a solar energy conversion efficiency which is higher than the one obtained with Pt-transparent/FTO counter electrodes (P1), and is comparable to the one obtained with Pt mirrors (P2 and P3). Stainless-steel foils as substrates coated with commercial low cost SWNTs are innovative, original, stable, cheap and highly efficient counter electrodes for DSSCs. Indeed the combination of SWNTs and stainless steel opens up new industrial opportunities for large area, long term stability and low cost DSSCs.

Table 1. Brownian motion of (a) a standard latex microbead (2 μ m diameter), (b) a carbon nanotube and (c) a graphene flake.

Catalyst	Substrate	Jsc (mA/cm ²)	Voc (Volt)	energy conversion %
P1	FTO on glass	11.87	0.65	2.42
C1	FTO on glass	8.20	0.65	2.5
P2	FTO on glass	8.27	0.66	3.7
C2	Stainless steel	9.21	0.66	3.92
P3	Stainless steel	10.92	0.66	4.5

argue that the difference in performance between samples P1 and P2 is because in the latter the metallic mirror acts as a light reflector. The efficiency difference between C1 vs. C2 is related to the different conductivity of the employed substrates. However, the catalytic effect of SWNTs (C1) is slightly higher than platinum in the transparent cathode (P1). Concerning the SWNTs based cathode the best value was obtained with the C2 (3.9%),

5. REFERENCES

- [1] B. O'Regan and M. Gratzel, *Nature*, **353**, 737 (1991).
- [2] C. G. Granqvist, *Sol. Energy Mater. Sol. Cells* **91**, 1529 (2007).
- [3] P. Calandra, G. Calogero, A. Sinopoli, P. G. Gucciardi, *Int. J. Photoenergy* doi:10.1155/2010/109495 (2010).

- [4] X. Fang, T. Ma, G. guan, M. Akiyama, T. Kida and E. Abe, *Thin Solid Films* **472**, 245 (2004).
- [5] G. Calogero, F. Bonaccorso, O.M. Maragò, P. G. Gucciardi, G. Di Marco, *Dalton Transaction*, **39**, 2903, (2010).
- [6] A. Kay and M. Graetzel, *Sol. Energy Mater. Sol. Cells*, **44**, 99 (1996).
- [7] X. Wang, L. Zhi and K. Mullen, *Nano Lett.*, **8**, 323 (2008).
- [8] K. Imoto, K. Takahashi, T. Yamaguchi, T. Komura, J. Nakamura and K. Murata, *Sol. Energy Mater. Sol. Cells*, **79**, 459 (2003).
- [9] Z. Huang, K. X. Liu, K. X. Li, D.M. Li, Y. H. Luo and H. Li, *Electrochem. Commun.*, **9**, 596 (2007).
- [10] K. X. Li, Z. X. Yu, Y. H. Luo, D. M. Li and Q. B. Meng, *Mater. Sci. Technol.*, **23**, 577 (2007).
- [11] K. Suzuki, M. Yamaguchi, M. Kumagai and S. Yanagida, *Chem. Lett.*, **32**, 28 (2003).
- [12] J. E. Trancik, S. C. Barton and J. Hone, *Nano Lett.*, **8(4)**, 982 (2008).
- [13] T. Hino, Y. Ogawa and N. Kuramoto, *Carbon*, **44**, 880 (2006).
- [14] W. J. Hong, Y. X. Xu, G. W. Lu, C. Li and G. Q. Shi, *Electrochem. Commun.*, **10**, 1555 (2008).
- [15] J. Chen, K. Li, Y. Luo, X. Guo, D. Li, M. Deng, S. Huang and Q. Meng, *Carbon*, **47**, 2704 (2009).
- [16] Md. K. Nazeeruddin, A. Kay, I. Rodicio, R. Humphry-Baker, E. Müller, P. Liska, N. Vlachopoulos and M. Grätzel, *J. Am. Chem. Soc.*, **115**, 6382 (1993).

NANODIAMONDS: HINTS FOR BIO-TECHNICAL APPLICATIONS

Silvia Orlanducci^{1*}, Emanuela Tamburri¹, Ilaria Cianchetta¹, Daniela Sordi¹, Maria Letizia Terranova^{1,3}, Daniele Passeri², and Marco Rossi^{2,3}

¹*Dept. of Chemical Science and Technology and MINIMALab,
University of Rome "Tor Vergata", Roma, Italy*

²*Dept. of Fundamental and Applied Sciences for Engineering and CNIS,
University of Rome "Sapienza", Roma, Italy*

³*NanoShare S.r.l., a startup company for human technologies, www.nanoshare.eu, Roma, Italy*

*E-mail: silvia.orlanducci@uniroma2.it

ABSTRACT

Thanks to its extreme chemical inertness, optical transparency, exceptional hardness and minimal toxicity, diamond is widely considered as one of the most promising and intriguing materials for a large variety of bio-applications. The recent progresses in the production of nanodiamond have now boosted the interest for its application as a multifunctional bio-technological material.

In this paper we present some relevant strategies that are being developed in our labs towards enabling nanodiamond-based bio-applications.

1. INTRODUCTION

Among the large number of nanoparticles that are being investigated for their feasibility to interact with biological entities at the nano-scale, nanodiamond crystallites are widely considered at present the more promising. It has been proven that nanodiamond is an excellent substrate for the adhesion and growth of several types of cells in vitro, and can advantageously and selectively bind various biological molecules. Therefore, the nanodiamond can be considered as an ideal surface for sensing, detecting, separating and purifying biological systems. Other remarkable application deals with the photophysical properties of systems characterized by bright photoluminescence in the extended red region and by the absence of photobleaching and photoblinking.

In our labs a variety of different strategies are being explored to prepare specific platforms based on nanodiamonds. In particular, we are developing different methodologies and testing technologies devoted to possible applications for sensing, imaging, and drug-delivery.

In such a framework we shortly describe here some under-developing synthetic strategies dealing with bio-related applications of nanodiamond are shortly described in the follow.

2. EXPERIMENTAL

The nanodiamond samples are prepared by CVD from CH₄/H₂ gas mixtures, or by self-assembling of colloidal

dispersions of nanodiamond particles produced by dynamical synthesis. In this last case specific protocols are followed to avoid re-aggregation of the primary nanoparticles. The decoration by metal nanoparticles is achieved by electrochemical methods (Au, Ag, Ni) and also by electroless procedures (Au).

The surface modifications of the diamond surfaces are obtained by surface adsorption, electrostatic linking or covalent bonding.

3. RESULTS AND DISCUSSION

Fluorescent nanodiamond (FND) is emerging as a new type of nanomaterial that holds great promise for biological applications. FND exhibits several remarkable features, including emission of bright photoluminescence in the extended red region, no photobleaching and photoblinking, and easiness of surface functionalization for specific or nonspecific binding with nucleic acids and proteins, etc. These excellent photophysical properties, together with the good biocompatibility may open up new frontier in biosensing.

A technology based on the use of metallic nanostructures that interact with fluorophores to increase their emission intensity has long been recognized since its discovery in 1980.

Typically, a 2- to 10-fold enhancement in the fluorescence intensity is observed for fluorophores with low quantum yields. A number of biotechnological applications taking advantage of this so-called metal-enhanced fluorescence (MEF) have been developed, such as, to improve the sensitivity of DNA hybridization assays.

To bring together the appealing advantages of FND and MEF in our laboratory we prepare nanometric diamonds in form of particles (Figure 1-a) and films with fluorescent properties and couple them with plasmonic metals nanoparticles for the production of interesting systems for photonic applications.

In this contest we investigated the color centers generated by N or by the insertion of semiconductive species, as Si, inside the diamond lattice that maintained their structural properties (Figure 2-b) [1].

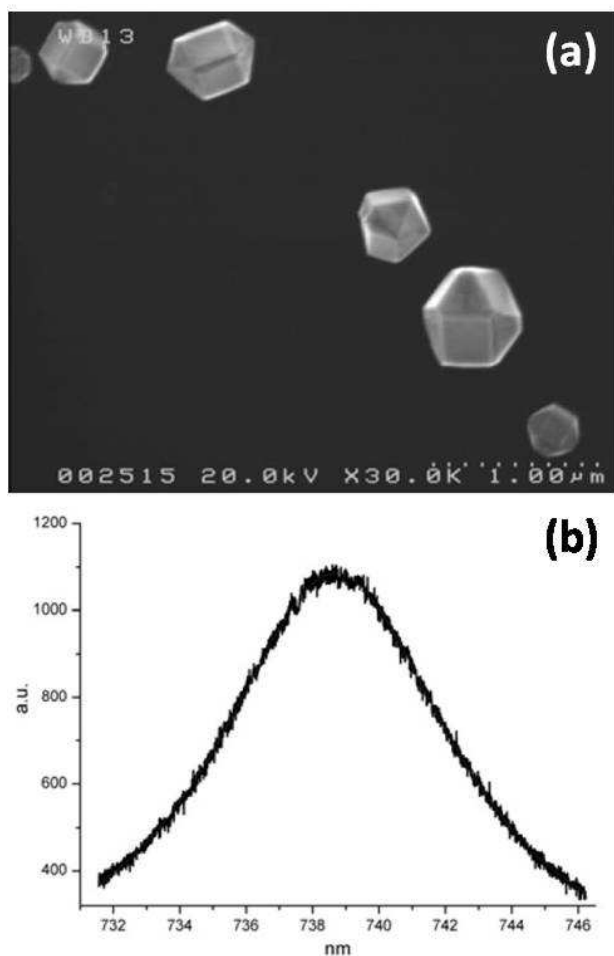


FIGURE 1: (a) FE-SEM image of nanocrystalline diamond; and (b) photoluminescence of silicon colour centre in nanocrystalline diamond

Figure 2 shows the FE-SEM images of nanodiamond particles decorated by Au nanoparticles. These hybrid samples are prepared for optical sensing of organic and bio-molecules.

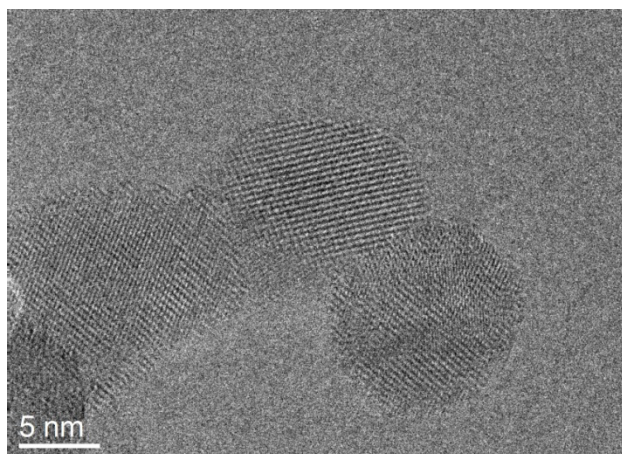


FIGURE 2: HR-TEM image of diamond nanoparticles decorated with Au particles

As regards the surface modifications of the diamond phase, the relationship between the conditions of the chemical processes inducing the various functionalizations and the optical responses is also deeply investigated (Figure 3).

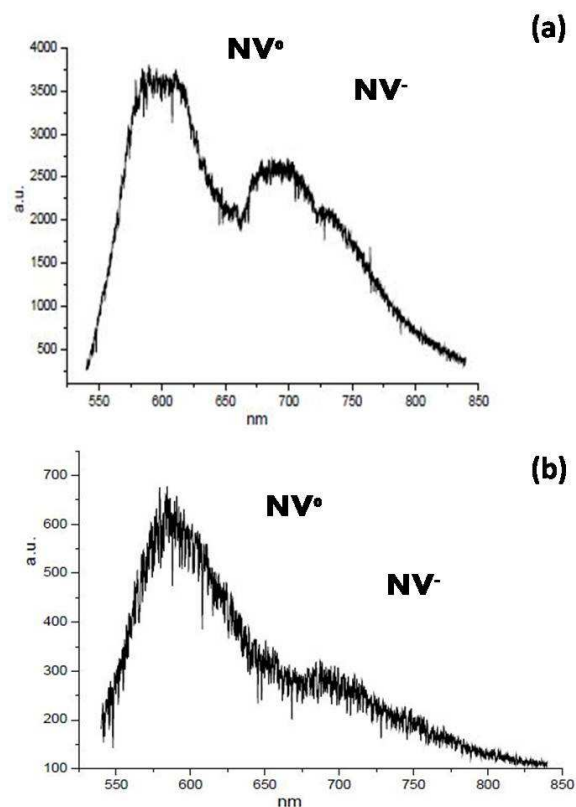


FIGURE 3: Photoluminescence of nitrogen-vacancy colour centre Silicon of nanodiamond before (a) and after (b) surface functionalization with acyl chloride.

A series of differently bonded nanodiamond-molecule systems are produced in order to test the chemical/physical interactions and to define the binding forces acting between functionalized DND surfaces and linked or adsorbed moieties. These materials represents a proof-of-principle for the development of drug-delivery systems. Moreover preparation of materials suitable in perspective for imaging is addressed by linking fluorophores to the nanodiamond surfaces (Figure 4).

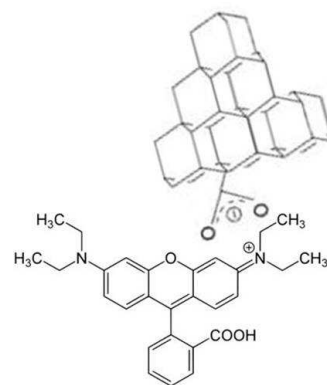


FIGURE 4: Example of a dye-nanodiamond particle conjugate

Different functionalizations of nanodiamond crystallites are under consideration for their application to diamond enhanced thickness shear mode resonator for selective bio-sensing (Figure 5).

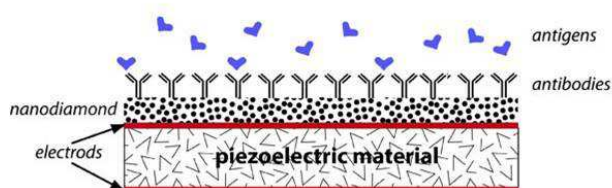


FIGURE 5: Scheme of a diamond-based enhanced thickness shear mode resonator

This kind of devices, assembled by nanoparticles or by differently shaped nanostructures obtained by diamond films nanosculpturing, can be used also for electrochemical microgravity and visco-elastic monitoring of molecule/diamond surface interactions.

Last but not least, nanocomposite layers formed by nanodiamond grains embedded in conductive polymer matrices (Figure 6) are being produced for bioelectrodes and sensors assembling [2].



FIGURE 6: TEM image of a polyaniline-nanodiamond film composite

4. CONCLUSIONS

The objective of the present research is to extend and finalize results and competences up-to-now acquired by our group in the field of carbon nanomaterials to the realization of diamond-based devices for bio-related applications.

5. REFERENCES

- [1] S. Orlanducci, V. Sessa, E. Tamburri, M.L. Terranova, M. Rossi, S. Botti, *Surf. & Coat. Tech.* **201** (2007) 9389
- [2] E. Tamburri, S. Orlanducci, V. Guglielmotti, G. Reina, Marco Rossi, M.L. Terranova, *Polymer* **52** (2011) 5001-5008

CHANGE OF MECHANICAL AND PHYSICAL PROPERTIES OF AN EPOXY RESIN INDUCED BY CARBON NANOTUBE PRESENCE

V. Brancato*¹, A.M. Visco¹, A. Pistone¹, M. Fazio¹, D. Iannazzo², A. Piperno², S. Galvagno¹

⁽¹⁾ *Industrial Chemistry and Material Engineering Department, Engineering Faculty, University of Messina, Italy*

⁽²⁾ *Dept. Farmaco-Chimico, University of Messina, 98168, Messina, Italy*

*Corresponding author. +39 90397 7286, E-mail: vbrancato@unime.it

ABSTRACT

Blends of carbon nanotubes (CNTs) and polymeric matrices became common due to their mechanical and physical properties. In particular, the epoxy resin matrix is an important thermoset polymer widely used for the manufacturing of advanced nanocomposites ranging from microelectronics to aerospace.

The uniform dispersion of the CNTs in the epoxy matrix is a crucial point since they tend to cluster or agglomerate as bundles of micrometer sizes losing all the advantages resulting from the use of a nanoscale filler. Thus, the improvement of CNT dispersion in the polymer matrix is one of the major still unsolved issues. Besides, the capability to create a strong interfacial bond between the polymeric matrix and the CNT reinforcement is another important goal to improve the ultimate mechanical or physical properties in the nanocomposite.

With this aim, in the present paper we studied the effect of improved dispersion of multi-walled CNTs in the epoxy based nanocomposites. So, pristine, carboxylic and amino functionalized multi-walled CNTs were used as nanofillers in the epoxy-based composites. Epoxy/CNTs composites were characterized by HRTEM, SEM, mechanical flexural and Izod resilience tests.

These tests were performed both on the neat materials and on the nanocomposites in order to highlight the CNTs dispersion degree in the composite and/or the presence of interfacial bonds between the CNTs and the epoxy matrix. Experimental results have shown that the presence of chemical groups have improved the CNTs dispersion in the polymeric matrix, in particular for the amino ones. As a consequence, the mechanical and physical features are higher than the neat epoxy or the epoxy filled with pristine CNTs.

1. INTRODUCTION

The development of high-quality multifunctional materials is the main interest of industrial and academic

research. In particular during the last decades, great attention was directed to the preparation of advanced nanocomposites with suitable synthetic polymers and fillers, with the purpose to obtain the best physical and mechanics features.

For example, the use of multi walled carbon nanotubes (MWCNTs) in polymer composites has attracted great attention due to their highly mechanical, thermal, and electrical properties [1-4]. They are widely used in the manufacturing of advanced nanocomposites in various applications, from microelectronic to aerospace fields.

It is well known that the carbon nanotubes/polymer composites have generally less or only slightly better resistant than the neat polymer, since the dispersion of MWCNTs and /or their adhesion with the matrix are weak [5]. The nanotubes tend to cluster or agglomerate as bundles of micrometer sizes. For this reason one of the bigger difficulties encountered during processing of MWCNT-reinforced epoxy composites is the uniform dispersion of the MWCNTs in the epoxy matrix. Yu – Huan Liao et al. [6] have conducted several experiments in order to investigate the factor that could influence the CNTs dispersion in an epoxy matrix. Their research results have indicated that solvent dilution together with sonication are an effective method for improving MWCNTs dispersion and enhancing the mechanical properties of nanocomposites. First experimental work focusing on the interfacial interaction in MWCNT/matrix was performed by Cooper et al.: they have found that an enhancement of the interaction can be achieved by a chemical modification of the MWCNTs, which could be link them directly to the matrix. A reaction between functional groups and matrix enables a stress transfer between the polymer and the CNTs. Various surface treatment techniques have been applied, such as oxidation in acid solution, dry oxidation in oxygen, anodic oxidation, amino functionalized and plasma treatments [7].

In this paper, we have studied the effects of improved dispersion and the interfacial bonding between multi-

walled CNTs (MWCNTs) and the epoxy matrix on the mechanical (flexural and impact) behavior of the epoxy based nanocomposites. With this aim, pristine, carboxylic or amino functionalized MWCNTs were used to prepare epoxy-based composites with different loading of MWCNTs. HRTEM, SEM and FTIR characterizations were performed in order to highlight a correlation among the chemical-physical properties and the mechanical properties of MWCNTs/epoxy system.

2. EXPERIMENTAL

Pristine MWCNTs were synthesized by catalytic carbon vapor deposition (CCVD) from isobutane at 600 °C using Fe/Al₂O₃ as catalyst (Fe=29 wt%) according to a previously reported procedure (purity >95%) [4]. Pristine MWCNTs were oxidized with a mixture of sulfuric acid/nitric acid (molar ratio 1:1 v/v, 98% and 69% respectively) at 60°C for 6h to obtain carboxylic MWCNTs. Ammine MWCNTs were synthesized by heating the carboxylic MWCNTs in 30 mL of neat oxalyl chloride at reflux for 48h in order to obtain the corresponding acetyl chloride MWCNTs and, finally, were conjugated with 3,6-dioxaoctamethylenediamine.

MWCNTs/epoxy nanocomposites were obtained by sonication for 2h of pristine, oxide and amino functionalized MWCNTs (0,4% wt) in an epoxy system containing DGEBA and DGEBF in ratio of 2:1 (Ampreg 26, supplied by Gurit) at 60°C, to make the resin less viscous (Fig.1a,b).

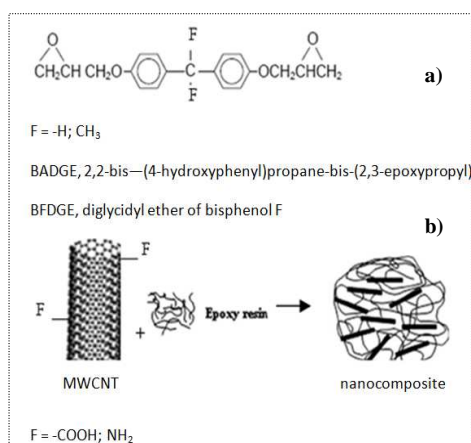


Figure 1: (a) Chemical formulation of the epoxy resin employed; (b) Scheme of formation of the nanocomposites with differently functionalized MWCNTs

Then ethanol was added at the mixture that was sonicated in an ultrasonic bath for 1h at the same temperature. Then the remaining ethanol was pulled out from the mixture putting it under magnetic stirring at 80°C for 2h; finally the hardener was added into the mixture in the ratio 33,3:100 by weight and post cured at 50°C for 96h.

The morphology of MWCNTs was analyzed using an HRTEM JEOL JEM 2010 analytical transmission electron microscope (LaB₆ electron gun) operating at 200 kV and equipped with a Gatan 794 Multi-Scan CCD camera for digital imaging. HRTEM samples were prepared by placing a drop of the MWCNTs dispersed in isopropanol on holey-carbon coated copper grids. The formation of the functional groups on MWCNTs was verified by Fourier transform infrared spectrophotometer (FTIR, ThermoNicolet Nexus 5700) scanning small amounts of MWCNTs pressed into a pellet with potassium bromide (KBr). The investigated wave length range was between from 500 to 4000 cm⁻¹, with a resolution of 4 cm⁻¹.

Scanning electron microscope JEOL, JSM 5600 LV was used to carry out morphological investigations of the fracture surfaces. For these tests the resin samples were coated in vacuum with a very thin gold film to make them electrically conductive. The electron acceleration voltage was of 10 kV and the photo magnification was of 100x.

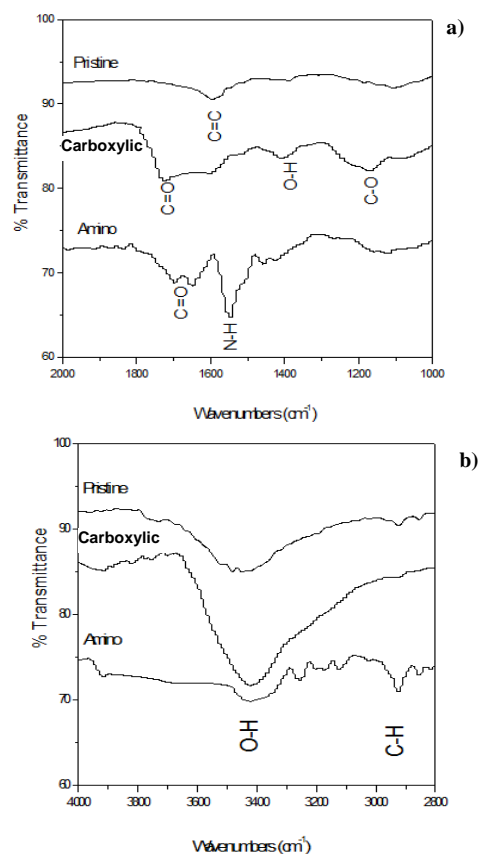


Figure 2: FTIR spectra of pristine, carboxylic and amino MWCNTs in the 1000-2000 cm⁻¹ (a) and in the 2800-4000 cm⁻¹ (b) wave length range.

Mechanical flexural tests were carried out at 25°C by a universal testing machine LLOYD LR 10K, with a crosshead speed of 1,25 mm/min (ASTM D - 790). Izod resilience test was carried out by a CEAST RESIL

IMPACTOR equipped with a 25J slug (ASTM D - 256 – 10 international protocol). Samples have same geometry for both mechanical tests: 12.7 mm x 64 mm and 4.2 mm thickness. The notch for the impact test, 2.5 mm deepness, was performed by a CEAST NOTCHVIS with a angle of cut of 45°.

3. RESULTS AND DISCUSSION

FT-IR analyses

FT-IR analyses allowed to obtain qualitative confirmation regarding the occurred functionalization of MWCNTs. The weak and broad signals usually obtained in the FT-IR spectra of carbon nanotubes did not allow to perform a deep quantitative investigation, but surely gave useful informations about the different kinds of functional groups formed on MWCNTs surface.

Fig. 2 a,b shows the FT-IR spectra of pristine and functionalized MWCNTs. For the pristine MWCNTs the IR spectrum shows important absorption bands at 1595 cm^{-1} (assigned to conjugated C=C stretching and associated with the vibration of carbon skeleton), at 3450 cm^{-1} and at 1120 cm^{-1} (corresponding to the presence of O-H groups due to atmospheric moisture or bland oxidation occurred during the purification step). Figure also shows that after the oxidation treatments new peaks arose with signals at 1720 cm^{-1} and 1180 cm^{-1} (assigned to stretching vibrations of C=O and C-O groups present in carboxylic acids) and at 1400 cm^{-1} , due to O-H bond in carboxylic group. The results indicate that carboxylic groups have been attached to the MWCNTs.

The FTIR spectrum of the amino MWCNTs sample shows the appearance of new peak at 1650 cm^{-1} , which corresponds to amide carbonyl (C=O) stretch. Furthermore, the presence of band at 2920 cm^{-1} (representing the stretching of methylene group (-CH₂-) of ethoxyethanamine moiety molecules) and the band at 1540 cm^{-1} (corresponding to N-H bending) suggests the presence of amide functional groups (-CONH-) on MWCNTs. These FT-IR spectra data confirm the coupling reaction between the 3,6 dioxaoctamethylenediamine and oxidized MWCNTs.

TEM analyses

The structure and morphology of the treated MWCNTs was investigated using HRTEM analyses. **Fig. 3** shows low and high magnification TEM image of the pristine and amino MWCNTs. The as-synthesized MWCNTs are held together into bundles due to Van der Waals forces. The TEM images of pristine MWCNTs (**fig. 3a**) shows that the nanotubes are entangled and randomly oriented; their outer surface is smooth with a diameter and a length of ~30 nm and 10-20 μm, respectively (**fig. 3c**).

The amino MWCNTs are well dispersed and most of the nanotubes are shortened (length of MWCNTs ~ 5 μm) (**Fig. 3b**). The magnified TEM image amino MWCNTs shows that the outer surface is rougher compared to the pristine one as a result of the functionalization treatment. However, TEM images confirm that the functionalization treatments do not involve significant damages to MWCNTs structure.

The TEM of the oxidized MWCNTs exhibited an intermediate situation among these upper described of the pristine and the amino MWCNTs.

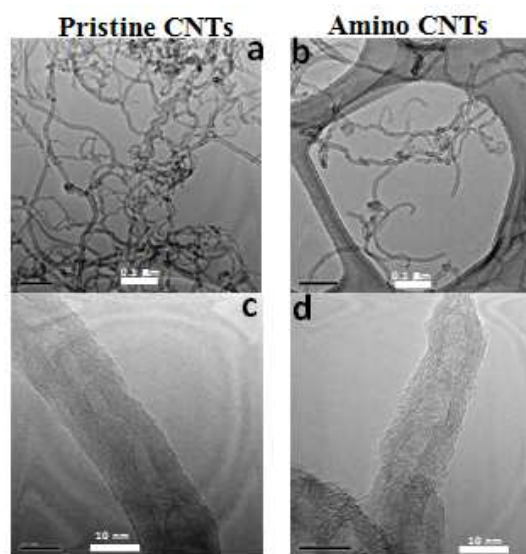


Figure 3: Low (a-b) and high magnification (c-d) TEM images of pristine (sx) and amino (dx) MWCNTs.

SEM analyses

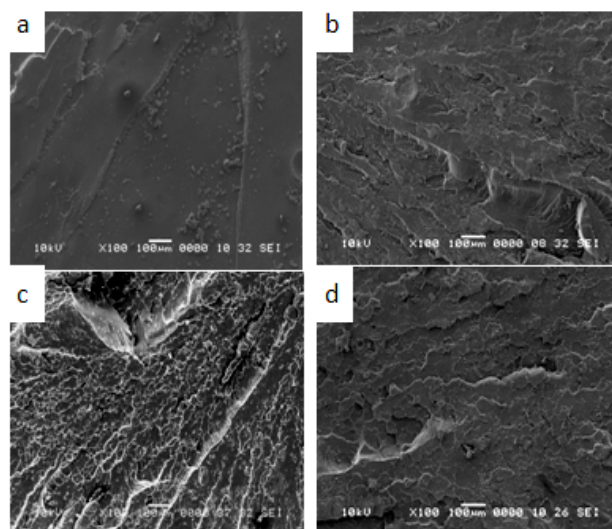


Figure 4: Fracture surfaces of neat resin (a), of nanocomposites filled with pristine (b) carboxylic (c) and amino (d) functionalized MWCNTs.

The SEM images of **fig.4** show the morphology of the fracture surfaces of the investigated samples.

In particular, **fig.4a** shows that of the neat resin: it appears smooth, due to the brittle behaviour. The other images show the modification of the surface morphology induced by the presence of the CNTs (**Fig. 4b**) and by the functional group presence (oxidized, **Fig. 4c**, and amino, **Fig. 4d**). The surfaces exhibit a progressive loss of brittle behaviour and an improvement of ductile behaviour in the order: pristine < carboxylic < amino.

Mechanical tests

Fig. 5 shows the flexural curves ($\sigma - \epsilon$) of the different kinds of nanocomposites. The mechanical results highlighted that the surface modified MWCNTs improves the mechanical features of neat epoxy matrix in the order: amino > carboxylic > pristine.

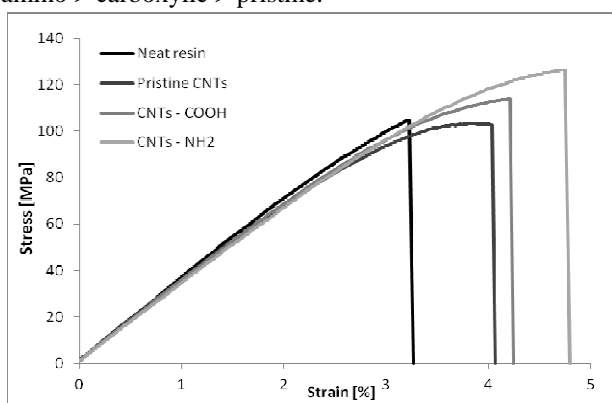


Figure 5: $\sigma - \epsilon$ curves of epoxy based nanocomposites containing pristine, carboxylic and amine functionalized MWCNTs.

The nanocomposites containing the amino or carboxylic MWCNTs exhibit higher stress (**Fig. 5**). This behavior is in agreement with the morphologic results, upper described. Comparing the pristine MWCNTs with the amine functionalized MWCNTs, these latter have better enhancement effect on the matrix. This indicates that the interfacial bonding enables an effective stress transfer between the epoxy matrix and the amino MWCNTs.

This better behavior is also confirmed by the resilience test (**Fig. 6**). Resilience improves in the order: pristine < carboxylic < amino.

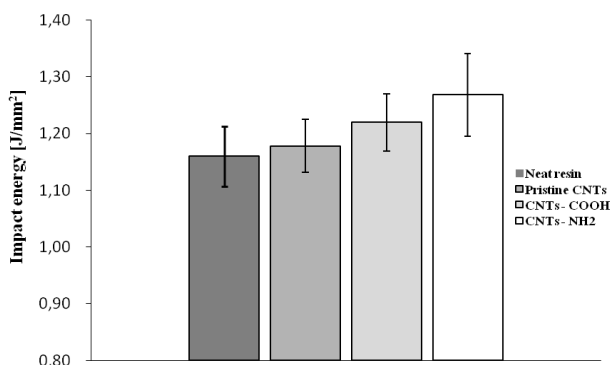


Figure 6: Resilience of epoxy based nanocomposites containing pristine, carboxylic and amino functionalized MWCNTs.

4. CONCLUSIONS

In conclusion, in this work we studied nanocomposites made by epoxy resin and different kinds of carbon nanotubes: pristine, carboxylic and amino functionalized MWCNTs.

The effect of functionalization was characterized through FT - IR and TEM. The analyses have confirmed that carboxylic groups or amino functional groups have been attached to the MWCNTs. In particular, from the observation with the transmission electronic microscope it is verified that the functionalization treatments do not involve significant damages to the CNTs structure.

Three point flexure and Izod impact tests were carried out on the samples to determinate the mechanical features. The analyses highlighted that the carbon nanotubes improve the mechanical resistance of the neat epoxy resin moving from pristine to the amino functionalized CNTs. SEM investigation of the fracture surface of the nanocomposites showed evidence of improvement in the dispersion and interfacial interaction of MWCNTs in the matrix. With the addition of functionalized CNTs the surfaces exhibit a progressive loss of brittle behaviour by improvement in mechanical properties.

5. REFERENCES

- [1] Z. Spitalsky, D. Tasis, K. Papagelis, C. Galiotis, *Progress in Polymer Science*, **35**, 357–401, 2010.
- [2] L. Guadagno, B. De Vivo, A. Di Bartolomeo, P. Lamberti, A. Sorrentino, V. Tucci, L. Vertuccio, V. Vittoria, *Carbon*, **49(6)**, 1919-1930, 2011.
- [3] J. A. Kim, D. G. Seong, T. J. Kang, J. R. Youn., *Carbon*, **44(10)**, 1898-1905, 2006
- [4] A. Arena, N. Donato, G. Saitta, S. Galvagno, C. Milone, A. Pistone, *Microelectronics Journal*, **39**, 1659–1662, 2008.
- [5] Z. Yaping, Z. Aibo, C. Qinghua, Z. Jiaoxia, N. Rongchang, *Materials Science & Engineering A* **435 - 436** (2006) 145 - 149
- [6] Y.-H. Liao, O. Marietta-Tondin, Z. Liang, C. Zhang, B. Wang, *Materials Science & Engineering A*, **385** (2004) 175 - 181.
- [7] F.H. Gojny, K. Schulte, *Compos. Sci. Technol.* **64** (2004) 2303–2308.

EXPERIMENTAL AND CALCULATED OPTICAL PROPERTIES OF POLYYNES AND CUMULENES CHAINS PREPARED BY LASER ABLATION IN LIQUIDS

G. Forte¹, L. D'Urso^{2*}, E. Fazio³, S. Patanè³, F. Neri³, O. Puglisi², G. Compagnini²

¹ *Dipartimento di Scienze del Farmaco, Università di Catania, Viale A. Doria 6, 95125 Catania*

² *Dipartimento di Scienze Chimiche, Università di Catania, Viale A. Doria 6, 95125 Catania*

³ *Dipartimento di Fisica della Materia e Ingegneria Elettronica, Università di Messina, Viale F. Stagno d'Alcontres 31, 98166 Messina*

* E-mail: gforte@unict.it

ABSTRACT

A mixture of polyynes chains of different length have been prepared by laser ablation, in various solvents, starting from graphite rods. Colloidal solutions are characterized by the UV-vis spectroscopy technique. The comparison between the DFT calculated UV-vis spectra of colloids with experimental one clearly indicates that polyynes are the dominant species produced by the ablation process. The optical limiting properties were investigated by the Z-scan method, using a nanosecond pulsed laser. The effect of the carbon chain length distribution, the solvent polarity and acidity was taken into account to explain the nature of the optical limiting behaviour.

1. INTRODUCTION

Polyynes represent a unique class of organic compounds; they consist in sp-hybridized carbon chains, and are perhaps the simplest and yet most intriguing of conjugated organic oligomers. These one dimensional (1D) materials deserve special attention as they are considered simple models to build linear molecular conductors due to their high π bond conjugation, optical transparency and non-linear optical properties. To date, formidable synthetic obstacles have been surpassed and polyynes are successfully synthesized and their long-term stability was checked [1]. Pulsed laser ablation in a confining liquid is a one step-down procedure to synthesize significant quantities of controlled carbon based materials dispersed in different solvents. In this frame, here we discuss about the influence of different solvents with increasing polarity on the synthesis of polyynes (LCC) starting from graphite rods. In order to identify the species which contribute to the linear optical properties, DFT calculations were performed to both polyynic series (HC_{2n}H , $3 \leq n \leq 6$) and cumulenic series ($\text{H}_2\text{C}_{2n}\text{H}_2$, $3 \leq n \leq 6$) in the different solvents, and monocyano HC_{2n+1}N ($3 \leq n \leq 5$) and dicyano NC_{2n}N ($4 \leq n \leq 5$) series in acetonitrile. Therefore, UV-Vis results were correlated with the nonlinear optical response of produced carbon species. Moreover the effect of the solvent polarity and acidity was taken into account to explain the nature of the optical limiting behaviour.

2. MATERIAL AND METHODS

2.1. Experimental

Pulsed laser ablation was performed in water, acetonitrile, methanol and cyclohexane. The target consists in a graphite rod (99.99% of purity). The ablation was carried out at room temperature and using the 532 nm pulse from a Nd:YAG laser; each pulse with a power density of 0.5 J/cm^2 with a repetition rate of 10 Hz. The typical irradiation times of 20 min. A Perkin-Elmer LAMBDA 2 spectrophotometer was used to perform the absorbance measurements in the 190-900 nm range. To study the non-linear optical properties of the samples we performed Z-scan measurements [2] using a pulsed Nd:YAG laser ($\lambda = 532 \text{ nm}$, 5 ns pulse duration, 10 Hz repetition rate). After the nonlinear optical limiting measurements, the optical absorbance characterization has been again performed in order to test the LCC photo-stability.

2.2. First Principle Approach

The equilibrium geometry of cumulene $\text{H}_2\text{C}_{2n}\text{H}_2$ ($3 \leq n \leq 6$) and polyynes HC_{2n}H ($3 < n < 6$), monocyano HC_{2n+1}N ($3 \leq n \leq 5$) and dicyano NC_{2n}N ($4 \leq n \leq 5$) chains were calculated, in different solvents, e.g. water, methanol, acetonitrile and cyclohexane, using the Becke's three parameters exchange functional supplemented with the Lee-Yang-Parr correlation functional, B3LYP [3-4]. The conductor-like Polarizable Continuum Model (CPCM) [5] was adopted for calculating the solvent effect. Ultraviolet-Visible (UV-vis) spectra were investigated by using the single excitation configuration interaction (CIS) whose results are in good agreement with experimental data. Eventually, geometry optimization and UV-vis spectra were performed by using the 6-311+** basis set, while D95 (d) basis set was adopted to evaluate atomic charges.

3. RESULTS AND DISCUSSION

3.1. Linear optical properties

In Fig.1 (a,b) are reported the absorption spectra before and after every Z-scan analysis of the LCCs obtained in water and cyclohexane. Spectra show electronic

transitions of carbon chains located between 190 and 300 nm. As reported in previous works [6] laser ablation in water lead to carbon chains $C_{2n}H_2$ with mainly $n = 3-4$ (see **Fig. 1a**). Longer chains with $n = 6$ and $n = 4$ (C_6H_2 and C_8H_2) produce signals at 200-207 nm and 216-226 nm, respectively. Methanol (spectra not shown here) and cyclohexane solution mainly gives longer polyynes chains (from C_6H_2 to $C_{12}H_2$), (see **Fig. 1b**) with the same chain length distribution and similar degradation behaviour during Z-scan analysis.

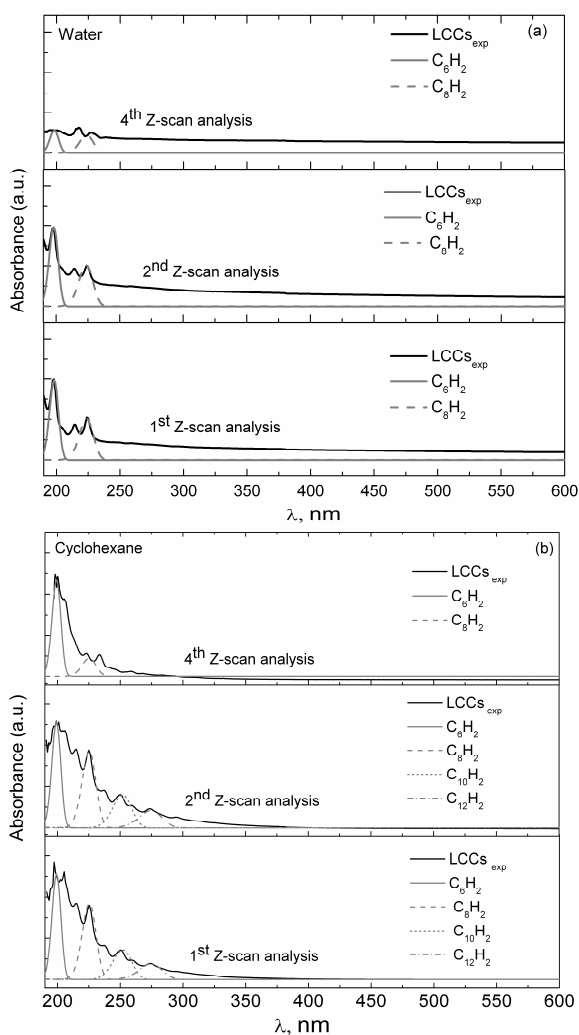


Fig.1. Experimental and calculated UV-vis absorption spectra of LCCs produced in water (a) and cyclohexane (b), before and after Z- scan analysis. (experimental data are reported in black continuous line)

It is necessary to point out that nonlinear optical measurements require that samples are exposed to prolonged high density 532 nm irradiations, as a consequence the UV-vis LCC features little by little disappear. In addition we found that the degradation behavior depends on the employed solvent. After degradation it resulted that cyclohexane and methanol-based samples are mainly populated by the C_6H_2 chains instead water-based sample suffers a gradual decreasing in intensity of the overall polyynes peaks together with a light red shift. This behaviour can be ascribed to the degradation products resulting from chain interactions

that tend to evolve toward sp^2 -like structures. Moreover, when laser ablation is carried out in acetonitrile, in addition to H-terminated polyynes, monocyano and dicyano carbon chains are also present in solution as already reported by Cataldo [7]. In this case, for peak assignments and for the relative concentration calculation, were also considered the electronic transitions of $NC_{2n+1}H$ ($n = 3,4,5$) and $NC_{2n}N$ ($n = 3,4$). The LCC in acetonitrile follows a different behavior: after repeated Z-scan measures the absorbance features of shorter chain molecules disappeared and only the fingerprint of $C_{12}H_2$ and $C_{14}H_2$ were detected. All the produced systems fully degrade after 4-5 cycles of Z-scan measures. We evaluate the relative amount of the different species by fitting the most intense observed peaks and assuming the same extinction coefficient for the calculated and experimental spectra. As reported in **Table 1**, the results are in good agreement with the literature data [7].

Solvents	C_6H_2 %	C_8H_2 %	$C_{10}H_2$ %	$C_{12}H_2$ %	$C_{14}H_2$ %
Cyclohexane	65	24	8	3	-
Methanol	66	23	7.5	3.5	-
Water	75	23	traces	traces	-
Acetonitrile	-	8	9	13	23

Tab.1. Relative abundance of the observed polyynes series in the different solvents, obtained by fitting the most intense peaks and assuming the same extinction coefficient for the calculated and experimental spectra.

3.2. First principle calculations

All the calculations were carried out respectively in water, methanol, acetonitrile and cyclohexane but no significant difference is observed among the polar solvents. Therefore we will henceforth report the data in methanol (M, polar solvent, 1.70 debye) and cyclohexane (C, apolar solvent) in order to evidence the effect of polarity solvents on LCCs electronic transitions. Atomic charges, evaluated by means of B3LYP/D95(d), are symmetrically distributed in all the analyzed systems. It was found that the polar solvent increases the negative charge along the chain leaving a more marked positive charge onto hydrogen atoms. The net charge tends to become neutral in the central region of the molecules with increasing of the chain length. In cumulenes the net positive charge of hydrogen atoms is mainly balanced by the next carbon atom while in polyynes the two carbon atoms next to hydrogen are principally involved in the charge balance. The Density of States for polyynes and cumulenes is reported in **Fig. 2**. The gap HOMO-LUMO decreases when the carbon chain length become longer (**Fig.2 a,b**). The comparison between polyynes and cumulenes (**Fig.2 c**) show that, in the latter, states move closer near the HOMO suggesting a higher electron delocalization for this structures. Such features is confirmed by bond lengths, here not reported, which tend to become equal in

cumulenes, as the number of carbons increase. Calculated values for the main electronic transitions of $D_{\infty h}$ polyynes (${}^1\Sigma_u^+ \leftarrow X^1\Sigma_g^+$) and D_{2h} cumulenes (${}^1B_{1u} \leftarrow X^1A_{1g}$) are reported in **Table 2** together with the oscillator strength. Calculated UV-vis spectra in methanol and cyclohexane show a slightly difference in wavelength absorption values. Peaks in cumulenes occur at lower frequency with respect to polyynes because the energy levels are closer in the former, see **Table 2**. Such finding is confirmed by the lower gap values calculated in cumulenes. From comparison with experimental data, see **Fig. 1**, it results that $HC_{2n}H$ ($3 \leq n \leq 6$) are the species mainly present in solution. The trend of the peaks calculated for polyynes is in strong agreement with the experimental data; such values, in fact, differ by a constant from the experimental ones.

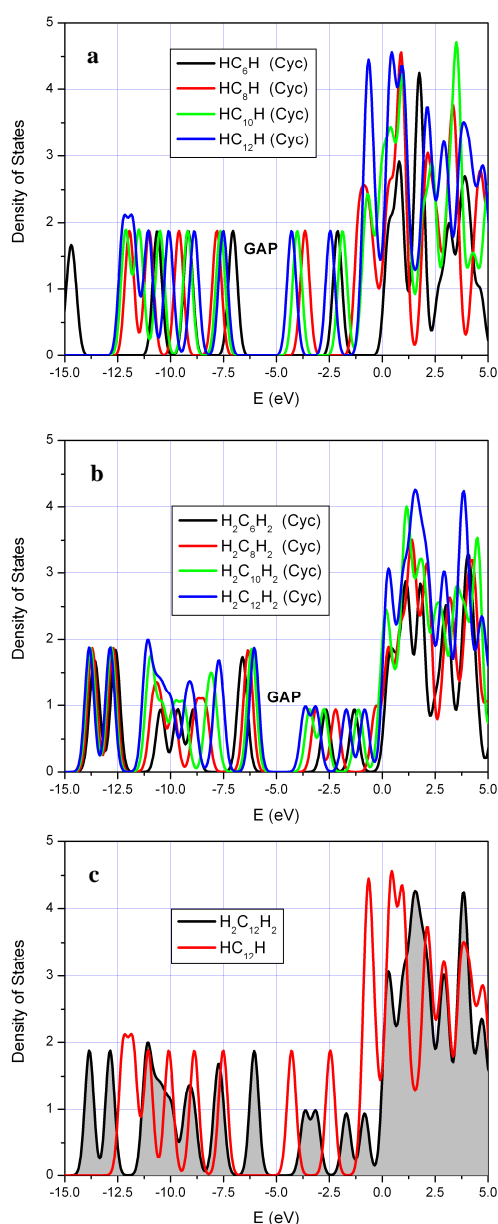


Fig.2. Density of States (DOS) are reported for polyynes (a) and cumulenes (b). and their comparison in reported in (c)

UV-vis spectra of monocyano and dicyano carbon chains are also evaluated in acetonitrile since the presence of such species has been detected in this solvent.

For these compounds, calculated absorption wavelengths are partially in agreement with experimental values

(a)	λ	f_{calc}	(b)	λ	f_{calc}
C_6H_2 (C)	193.8	4.2	C_6H_2 (C)	313.3	1.9
C_6H_2 (M)	186.7	4.3	C_6H_2 (M)	297.8	1.7
C_8H_2 (C)	222.1	5.7	C_8H_2 (C)	371.0	2.6
C_8H_2 (M)	213.6	5.8	C_8H_2 (M)	352.4	2.3
$C_{10}H_2$ (C)	248.5	6.9	$C_{10}H_2$ (C)	426.4	3.5
$C_{10}H_2$ (M)	238.9	7.1	$C_{10}H_2$ (M)	401.9	3.0
$C_{12}H_2$ (C)	248.4	8.1	$C_{12}H_2$ (C)	478.4	4.5
$C_{12}H_2$ (M)	272.5	8.0	$C_{12}H_2$ (M)	453.6	4.0

reported by Scemama et al. [8], while differ from the data reported by Cataldo [7].

Table 2. Wavelengths (nm) and oscillator strengths of a) the first (${}^1\Sigma_u^+ \leftarrow X^1\Sigma_g^+$) transitions in the $HC_{2n}H$ series in methanol (M) and cyclohexane (C) and b) the first (${}^1B_{1u} \leftarrow X^1A_{1g}$) transitions in the $HC_{2n}H$ series in methanol (M) and cyclohexane (C)

3.3. Z-scan analysis

The optical limiting efficiency of the samples was investigated by means of Z-scan measurements. The nonlinear mechanism is activated at a fluence of 0.6 J/cm^2 , 0.2 J/cm^2 and 0.1 J/cm^2 , respectively for the samples prepared in water/acetonitrile, methanol and cyclohexane. To exclude any contribution to the optical limiting performance due to the solvents, we measured their transmittance and find that it remains unchanged around 1. A direct correlation seems possible among the chain length, the solvent polarity and the nonlinear threshold. The LCC/methanol solution has the longer chain and the lower nonlinear threshold. LCCs in water and acetonitrile showed the same threshold fluence. The acetonitrile solution is populated by longer polyyne chains, therefore we expected a threshold value comparable to those obtained for LCC prepared in methanol and cyclohexane, populated by longer chains. However, also the presence of monocyano and dicyano polyynes and the highest acetonitrile polarity strongly affect the nonlinear response. **Fig. 3** shows the normalized transmittance curves as a function of polyynes sample position in the open and closed/open aperture, respectively. The LCCs prepared in water, methanol and acetonitrile, show a saturable absorption (SA) and self-defocusing effects.

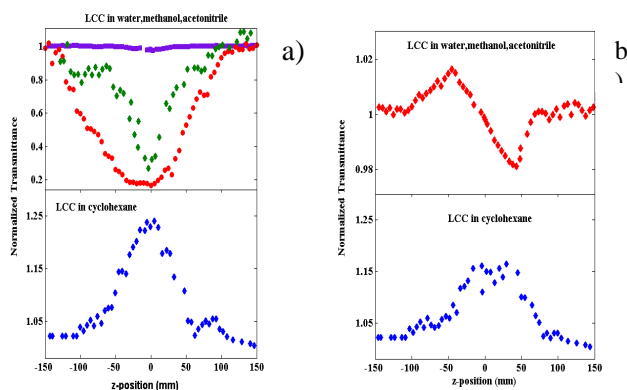


Fig. 3. Normalized transmittance as a function of sample position in (a) open and (b) a closed/open aperture configuration.

Being the measured n_2 value negative, we can conclude that the effect may be easily explained as a local heating due to conversion the energy absorbed by the polyyne into heat and a local increasing of the liquid temperature which, in turn, induces a local density reduction with a refractive index change. The LCC solutions prepared in cyclohexane show an increased transmittance indicating a saturable absorption (SA) mechanism, both in open and closed/open aperture configuration. In the focus region, the high energy density is able to promote the formation of carbon chain anions, C^{2n-} [9]. These species absorb in the 400-800 nm wavelength range and cannot be observed in the UV/VIS optical measurement because of their very short lifetime, barely limited to the time of the laser action. The same effect cannot be observed in the samples produced in a polar solvent. In this case, the negative species are promptly neutralized by a proton transfer due to the acidity of polar solvent and, therefore, the saturable absorption phenomena cannot take place. The nonlinear refraction index n_2 and the nonlinear absorption coefficient β (which, in turn, gives the real and the imaginary part of the susceptibility $\chi^{(3)}$) were estimated from the Z-scan data. On the overall, emerges that the resulting $\chi^{(3)}$ values increases from 3×10^{-11} esu for LCCs in polar solvents to 1.0×10^{-10} esu for LCCs in cyclohexane. These values are comparable to ones reported for single wall carbon nanotubes [10], which are considered good optical limiting materials. Moreover, after several irradiation, the optical limiting behaviour is still activated, as shown in **Fig 4**. The Z-scan data remain almost unchanged even if the normalized transmittance values are reduced as well as the overall absorbance ones. This indicates a relatively good photostability of all the samples under prolonged nanosecond laser irradiation. The transmittance decreasing behaviour is obviously ascribed to the decreased LCC concentration, independently on the sp^2 degradation products present in solution

4. CONCLUSIONS

In summary, linear carbon chains were successfully produced by laser ablation in liquid and their linear and Nonlinear optical properties were univocally captured by UV-vis and Z-scan measures as function of solvents at

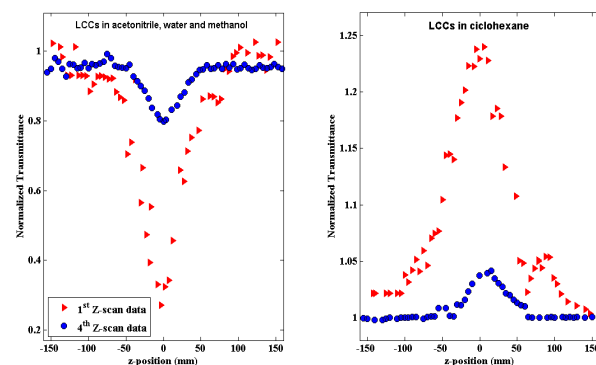


Fig. 4. Normalized transmittance as a function of sample position in the open aperture, after repeated measurements.

different polarity. A systematic analysis of the DFT computed structural and electronic response of both polyyne and cumulenic model molecules as a function of the solvents with different polarity was also carried out. The comparison between the calculated UV-vis spectra with experimental one clearly indicates that polynes with different chain length are the dominant species produced by the ablation process. On the overall, we demonstrated that both solvents with different polarity and chain length distributions have a driving role in the nonlinear optical response. Regarding the nonlinear mechanisms, a change from RSA to SA was observed as function of both solvent polarity and acidity.

5. REFERENCES

- [1] J. F. Xu, M. Xiao, R. Czerw; *Chem. Phys. Lett.* 389 (2004) 247-250.
- [2] E. Fazio, F. Neri, S. Patanè, L. D'Urso, G. Compagnini; *Carbon* 49 (2011) 306-310.
- [3] C. Lee, W. Yang, R.G. Parr; *Phys. Rev. B* 37 (1988) 785-789.
- [4] A.D. Becke; *J. Chem. Phys.* 98 (1993) 5648.
- [5] M. Cossi, N. Rega, G. Scalmani, V. Barone; *J. Comp. Chem.*, 24 (2003) 669-681.
- [6] G. Compagnini, V. Mita, R.S. Cataliotti, L. D'Urso, O. Puglisi; *Carbon* 45 (2007) 2445-2458
- [7] F. Cataldo; *Tetrahedron* 60 (2004) 4265-4274.
- [8] A. Scemama, P. Chaquin, M.C. Gazeau, Y. Bénilan; *Chem. Phys. Lett.* 361, (2002) 520-524.
- [9] P. Freivogel, M. Grutter, D. Forney and J.P. Mayer; *J. Chem. Phys.* 107 (1997), 4468-4472
- [10] J. Seo, S. Ma, Q. Yang, L. Creekmore, R. Battle, M. Tabibi, S. Jung, and M. Namkung, *J Phys: Conf Ser* 38 (2006) 37-40.

INFLUENCE OF THE MICROSTRUCTURE OF CARBON NANOTUBES ON THE CATALYTIC WET AIR OXIDATION OF *P*-COUMARIC ACID

E. Fazio¹, E. Piperopoulos², S.H. Abdul Rahim², M. Lanza³, S. Santangelo⁴,
G. Mondio¹, F. Neri¹, C. Milone^{2*}

¹ Dept. of Matter Physics and Electronic Engineering, University of Messina, Italy

² Dept. of Mechanics and Materials, University "Mediterranea" of Reggio Calabria, Italy

³ CNR, Inst. for Chemical Physical Processes, Messina Section, Italy

⁴ Dept. of Industrial Chemistry and Materials Engineering, University of Messina, Italy

* E-mail: cmilone@ingegneria.unime.it

ABSTRACT

Chemical composition, bonding configurations and threefold- to fourfold-coordinated carbon bonding ratio of pristine and annealed MWCNTs are investigated by means of X-ray photoemission and reflection electron energy loss spectroscopy in view of their use as catalysts towards the degradation of *p*-coumaric acid. Preliminary results of their catalytic efficiency are also reported.

1. INTRODUCTION

The incessant and rapid increment of human population causes a continuous increase of fresh water demand for industrial and domestic activities, thus calling for the development of technologies to be used for the treatment of wastewater and recycling. Olive mill water (OMW) is an agro-industrial waste featured by a high organic content [1]. The presence of polyphenols at high concentration leads to a serious concern for OMW direct biological treatment. Among the manifold oxidation processes proposed for the abatement of bio-recalcitrant phenolic compounds present in OMW, the catalytic ones allow working under milder oxidation conditions (pressure, temperature). Recently, we have demonstrated that multi-walled C nanotubes (MWCNTs) are efficient catalysts for the catalytic wet air oxidation (CWAO) of *p*-coumaric acid [2], a molecule whose chemical structure is closely related to that of bio-recalcitrant polyphenolic fraction present in the olive oil processing waste water, with better performances than the widely used activated carbon [3]. Here, we report on the characterization of pristine and annealed MWCNTs catalysts by means of X-ray photoemission spectroscopy (XPS) and reflection electron energy loss spectroscopy (REELS). Our aims are to monitor the composition of the carbon-based materials, to study the specific bonding configurations and to infer information about the change of the threefold/fourfold carbon coordination ratio. Preliminary results of the measurements of the catalytic efficiency of pristine and annealed MWCNTs towards the degradation of *p*-coumaric acid (PCA) are also reported.

2. EXPERIMENTAL

MWCNTs were prepared by catalytic route. Chemical vapour deposition (CVD) of isobutane ($i\text{-C}_4\text{H}_{10}$) was carried out over Al_2O_3 supported Fe catalyst (iron loading: 29 wt %). Catalyst (0.5 g) was placed in a quartz boat inside a quartz tube located in a horizontal electric furnace. It was reduced at 500 °C under a 1:1 H_2+He 120 sccm flow; after 1 h, the temperature was raised to 600 °C, and then the helium was replaced by isobutane. Synthesis reaction was carried out under a 1:1 $i\text{-C}_4\text{H}_{10}+\text{H}_2$ 120 sccm flow for 2 h.

After synthesis, raw products were cooled to room temperature (RT) under inert (He) atmosphere and subsequently treated with a solution of NaOH (1 M) at 80 °C to remove alumina support and with a solution of HCl (1 M) to eliminate residual iron particles.

Purified sample were finally washed with distilled water and dried at 80 °C for 12 h. A part of it was annealed in inert (He) environment at 950 °C for 2 h.

Chemical composition and mass density of pristine and thermally treated MWCNTs (*p*-CNTs and *t*-CNTs, respectively) were investigated by means of XPS and REELS using a VG ESCALAB vacuum system.

The Al $K\alpha$ radiation (1486.6 eV) of a conventional twin anode Al/Mg $K\alpha$ was used as a source for the XPS measurements. Excited photoelectrons were analysed by means of a VG Scientific CLAM 100 hemispherical analyser.

REELS measurements were carried out using a VG LEG61 electron gun. The primary electron energy was 2.0 keV; the incidence angle was always about 40° from the normal to the sample surface. The gun current was about 10 mA, while the pass energy of the analyser was set at 20 eV. The acceptance angle β of the analyser was approximately 3°. Under these conditions, the overall energy resolution, as determined from the shape (FWHM) of the elastic peak of the REELS spectrum, was approximately 0.6 eV. During measurements, the analysis-chamber pressure was in the 10^{-7} Pa range.

The crystalline arrangement was investigated by measuring Raman scattering excited at 2.41 eV.

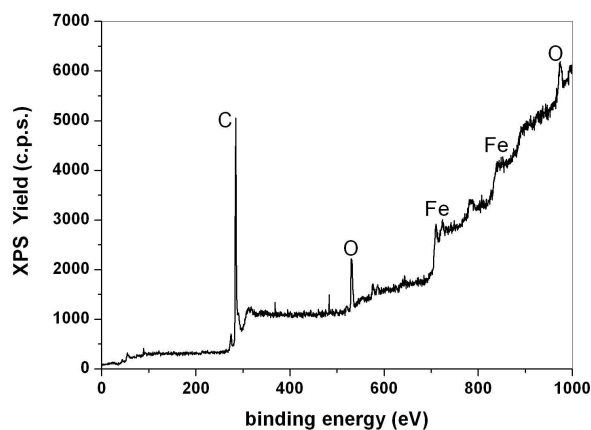


Fig. 1. XPS spectrum of the pristine MWCNT sample.

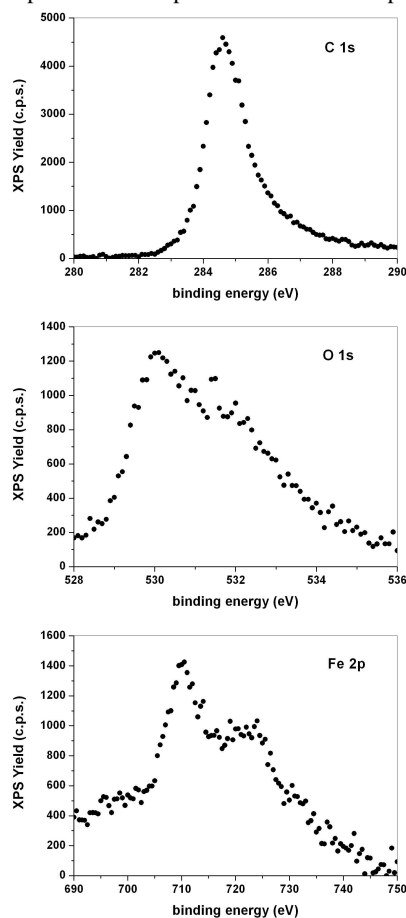


Fig. 2. C 1s, O 1s and Fe 2p XPS spectra of pristine sample.

3. RESULTS AND DISCUSSION

3.1. XPS analysis

Figure 1 shows the wide-scan spectrum for the pristine MWCNT sample. The spectrum of the treated one looks quite similar.

Figure 2 displays the C1s, O1s and Fe2p high-resolution XPS spectra of the pristine sample. The core line of C1s peak is located at 284.5 ± 0.1 eV, as in the case of the C bulk material. The O1s structure exhibits two distinct components centred approximately at 530.2 ± 0.1 eV and 531.9 ± 0.1 eV, ascribed to C-O and O-H bonds,

Tab. 1. Results of XPS and REELS analyses.

		p-CNTs	t-CNTs
From XPS	x_C (%)	91.1	88.0
	x_O (%)	6.3	8.9
	x_{Fe} (%)	2.6	3.1
From REELS	E_p (eV)	23.30	24.07
	E_π (eV)	4.9	4.9
	n_{val} (cm ⁻³)	$3.94 \cdot 10^{23}$	$4.20 \cdot 10^{23}$
	ρ (g cm ⁻³)	1.765	1.818
	N_C (atoms cm ⁻³)	$8.96 \cdot 10^{22}$	$9.24 \cdot 10^{22}$
	[C-C sp ²] (%)	0.632	0.592
	[C-C sp ³] (%)	0.368	0.408

respectively. The characteristic components $2p_{3/2}$ and $2p_{1/2}$, located respectively at 710 ± 0.1 eV and 725 ± 0.1 eV, are detected in the Fe2p structure.

From the area of the above peaks, by using proper sensitivity factors, the concentration of each element can be inferred. The composition of p-CNTs and t-CNTs correspondingly obtained is reported in Tab. 1.

After carbon, oxygen is the most abundant chemical species in both the samples. Moreover, traces of iron (nanoparticles encapsulated by carbonaceous layers or sucked into the tube channel during CNT extrusion and, hence, escaped to the post-growth purification step [4]) are detected, in agreement with results of previous analyses [2].

As expected, annealing at 950°C introduces some changes in the chemical composition of the MWCNTs.

Temperature-programmed analysis carried out on the pristine sample [5] has evidenced the presence of several groups (carboxylic acids, carboxylic anhydrides, lactones, phenols and quinones/carbonyl groups), likely anchored at the defect sites on its surface. Their detachment reflects onto an upshift of the Raman G-band from 1576.6 cm^{-1} in p-CNTs to 1579.5 cm^{-1} in t-CNTs (spectra not shown for brevity). The smaller atomic concentration of C in t-CNTs (88% vs 91%) is consistent with the thermal decomposition of these surface functionalities.

Of course, lowering of the C concentration in t-CNTs reflects on increased relative weight of the encapsulated iron (Tab. 1).

Although the O concentration should decrease too owing to the detachment of oxygenated surface groups, an increase is observed. Inertness of the environment, upon which annealing is performed, rules out the occurrence of iron oxidation during the process. Thus, the only possibility is that the increased relative weight of the oxygen, contained in carbon-coated (previously oxidised) iron-nanoparticles, masks the expected decrease. This hypothesis is fairly compatible with the presence, formerly detected [4], of C-encapsulated Fe_2O_3 nanoparticles within the purified reaction products.

3.2. REELS analysis

In its simplest description, the REELS spectrum can be considered as a linear combination of the bulk and surface contributions, $Im(-1/\epsilon)$ and $Im(-1/(\epsilon+1))$, expressed in terms of the complex dielectric constant ϵ of the analysed material [6].

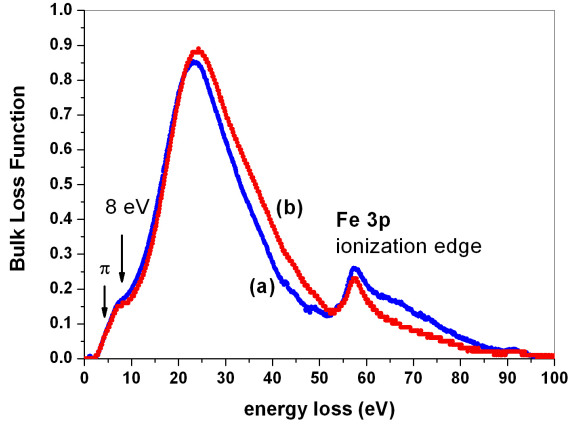


Fig. 3. Bulk loss functions of (a) p-CNTs and (b) t-CNTs, as derived from REELS at a primary energy of 2.0 keV.

In particular, when the wavelength λ_{el} of the impinging electrons is much lower than their mean free path Λ in the solid, the surface contribution may be considered negligible and the measured spectrum can be considered as built up exclusively by the bulk response. In present case, being $\Lambda \approx 49 \text{ \AA}$ and λ_{el} of the order of 0.27 \AA , this condition is satisfied. Consistently, the intensity ratio between surface- and bulk-contribution is evaluated to be about 1.4%.

Figure 3 displays the bulk loss functions (BLFs), deduced by the REELS spectra measured in p-CNTs and t-CNTs for a momentum transfer of 0.132 \AA^{-1} . The main feature is the plasmon peak, due to collective excitations of valence electrons. It is centred at about 23.30 eV in case of the pristine sample and at slightly higher E_p (24.07 eV) in the BLF of the annealed one. The small plasmon peak upshift in t-CNTs is due to the increased density of valence electrons.

The slight slope variation, visible on the lower-energy side of the peak (at $\sim 4.9 \text{ eV}$), corresponds to the carbon π resonance. In addition, a weak bump ascribable to Fe is detected at 8.0 eV. Arrows point these features in Fig. 3. Moreover, in both the samples, a strong peak, centred around 57 eV, is detected in correspondence of the Fe3p ionization edge [7]. Its presence suggests that the line-shape of the π and $\pi + \sigma$ plasmon resonances is probably affected by Fe contributions, even if they are limited by the low percentage of this metal (not exceeding 3.1%).

In any case, present results seem to be in a good agreement with those reported for distant small diameter single-walled carbon nanotubes and small momentum transfers [8,9].

3.2.1. Valence electron density

After having properly subtracted the elastic peak and the secondary electron background [10], intrinsic properties of the sample can be deduced from the BLF. In particular, under the free electron approximation, known the main plasmon position E_p , the valence electron density n_{val} , can be estimated using the Drude formula,

$$n_{val} = mE_p^2 / 4\pi e^2 = 7.25 \cdot 10^{20} E_p^2 (\text{eV}) \cdot$$

Values of n_{val} obtained for p-CNTs and t-CNTs are reported in Tab. 1.

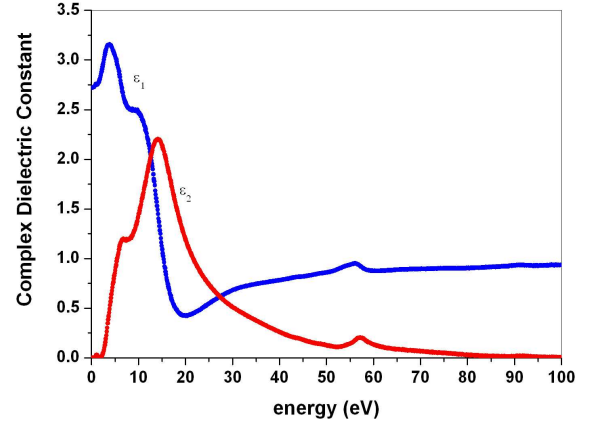


Fig. 4. The real (ϵ_1) and imaginary (ϵ_2) parts of the complex dielectric constant ϵ of t-CNTs as deduced from the BLF of Fig. 3.

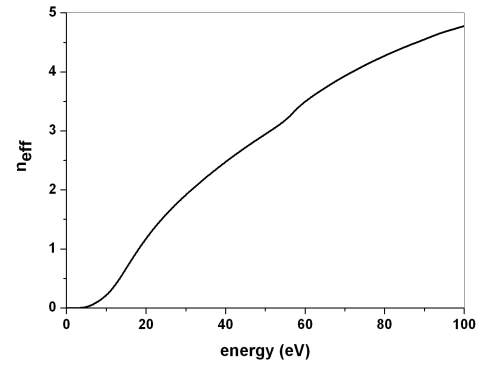


Fig. 5. The effective number n_{eff} of electrons involved in interband transitions vs the energy values.

3.2.2. Dielectric constant and effective electron number

Furthermore, the dielectric constant of the investigated samples has been deduced from the experimental BLF spectrum, assumed to be coincident with $Im(-1/\epsilon)$.

After the evaluation of $Re(-1/\epsilon)$ via a Kramers-Kronig transform, the values of the complex dielectric constant ϵ have been extracted. Results are shown in Fig. 4.

From the values of the dielectric constant, the effective number n_{eff} of electrons involved in interband transitions is then inferred (Fig. 5).

For pure carbon such a number tends to saturate at 4 electrons (C total valence electrons) at high energies (60–100 eV). In present case, the saturation approaches higher values since n_{eff} is affected by contributions of O and Fe electrons.

3.2.3. Mass density and carbon bonding fractions

Following the procedures described in Ref. [6], from results of XPS and REELS analyses the mass density of the material, as well as the differently hybridised C bonding fractions, can be evaluated.

Taking into account the chemical composition of the samples, as resulting from XPS analysis, their mass density (ρ) is estimated by using the following relationship

$$\rho = n_{val} (x_C P_C + x_O P_O + x_{Fe} P_{Fe}) / N_A (x_C n_C + x_O n_O + x_{Fe} n_{Fe}),$$

where n_{val} represents the valence electron density, x_i denote the percentage concentrations of the three atoms, P_i

indicate their atomic weight, n_i stands for the number of valence electrons per atom and N_A is the Avogadro number. The values of ρ obtained, reported in Tab. 1, are consistent with the different valence electron density of the two samples.

The fraction $[Csp^2]$ of threefold coordinated C atoms is determined from the energy position (about 4.9 eV) of the π plasmon, as already reported by other authors [8,9]), via the Drude relationship, considering a static screening factor (0.280) on π electrons due to the remaining σ ones [6]. Then, the fraction $[Csp^3]$ of fourfold coordinated C atoms straight results from the condition $[Csp^3]+[Csp^2]=1$. The values of $[Csp^3]$ and $[Csp^2]$ obtained are reported in Tab. 1.

From the analysis it is evident that, after the annealing process, the sp^3 carbon phase slightly increases at expenses of the sp^2 one.

This change is probably due to the relative increase of dangling bonds/pyramidal anchor sites left behind by the decomposition of surface functionalities upon annealing. This hypothesis is supported by the indications emerging from Raman analysis. The intensity of the D-band intensifies relative to the G-band, signalling the increase of the defect density in the graphitic tube walls (the D/G intensity ratio increases from 1.78 in p-CNTs to 1.83 in t-CNTs). This is not surprising because, as known [11], MWCNT graphitisation by annealing, involving lattice defect healing, starts at 1500 °C and completes at much higher temperatures (≥ 2200 °C).

3.3. Degradation of p-coumaric acid

CWAO of PCA is carried out in an autoclave (Parr model 4560) at 80 °C, in air, at a pressure of 2 MPa. PCA aqueous solution with a concentration 4.5 mM, corresponding to the maximum solubility of PCA in water at 25 °C, is used. The amount of catalyst (p-CNTs or t-CNTs) is 0.5 g. The residence time is fixed at 5 hrs. Further experimental details on CWAO of PCA can be found elsewhere [2].

The catalyst efficiency toward the removal of the organic carbon is evaluated by measuring the total organic carbon (TOC) content in the solution by means of a TOC analyser (Shimadzu 5050).

Pristine MWCNTs show higher efficiency towards organic carbon removal. In fact, $\Delta TOC(\%)$ obtained after 5 hrs with p-CNTs catalyst is 85.3%, while it lowers to 66.0% over the annealed sample.

This result proves that the elimination from the catalyst surface of the carbonyl type groups (whose role, in the catalytic activity of carbon materials, is due to their capability to generate oxygenated radicals [3]) reduces, by ~23%, the capacity of the catalyst to degrade organic compounds.

The residual degradation capacity of t-CNTs catalyst might be related to the (intrinsic) curvature of graphene

sheets. In fact, curvature would force the (triply coordinated) atoms to deviate from their preferential trigonal planar sp^2 bonding configurations and to acquire some pyramidal sp^3 character with partial occupancy of the fourth sp^3 orbital. Due to this constrain, greater electronic localisation and, hence, negative region and lower ionisation energies are computationally predicted [12], which makes these sites the most favoured ones for attack by electrophiles, such as oxygen.

4. CONCLUSIONS

Pristine and annealed MWCNTs are evaluated as catalysts towards the degradation of PCA. Preliminary results on TOC removal show that the catalytic efficiency lowers after thermal treatment.

The results of XPS, REELS and Raman analyses, carried in order to clarify the origin of the different performance, evidence a decrease of the C content in t-CNTs, consistent with the elimination of the surface groups involved in the catalytic activity, and a slight increase of the sp^3 carbon phase at expenses of the sp^2 one, likely responsible for the catalytic activity of the annealed sample.

Acknowledgements

We wish to thank Dr. G. Faggio (Dept. of Mechanics and Materials, Univ. "Mediterranea" of Reggio Calabria, Italy), who kindly performed Raman scattering measurements.

5. REFERENCES

- [1] A. El Hadrami, M. Belaqqiz, M. El Hassni, S. Hanifi, A. Abbad, R. Capasso, L. Gianfreda, I. El Hadrami, *J. Agron.* **3**, 247 (2004).
- [2] C. Milone, A.R. Shahul Hameed, E. Piperopoulos, S. Santangelo, M. Lanza, S. Galvagno, *Ind. Eng. Chem. Res.* **50**, 9043 (2011).
- [3] F. Stüber, J. Font, C. Bengoa, A. Eftaxias, A. Fortuny, A. Fabregat, *Topics in Catalysis* **33**, 3 (2005).
- [4] S. Santangelo, G. Messina, M.G. Donato, M. Lanza, C. Milone, A. Pistone, *J. Appl. Phys.* **100**, 104311 (2006).
- [5] C. Milone, E. Piperopoulos, S.H. Abdul Rahim, M. Lanza, S. Santangelo, S. Galvagno, "Liquid phase functionalization of MWCNTs: morphology and surface modification", present volume.
- [6] A. M. Mezzasalma, G. Mondio, F. Neri, S. Trusso, *Appl. Phys. Lett.* **78**, 326 (2001).
- [7] M. Novak, R.J. Bereczky, Z.M. Zhang, Z.J. Ding, J. Toth, D. Varga, K. Tokesi, *Surf. Interface Anal.* **40**, 522 (2008).
- [8] A.G. Marinopoulos, L. Wirtz, A. Marini, V. Olevano, A. Rubio, L. Reining, *Appl. Phys. A* **78**, 1157 (2004).
- [9] M. Knupfer, T. Pichler, M.S. Golden, J. Fink, A. Rinzler, R.E. Smalley, *Carbon* **37**, 733 (1999).
- [10] S. Tougaard, J. Kraer, *Phys. Rev. B* **43**, 1651 (1991).
- [11] J. Chen, J.Y. Shan, T. Tsukada, F. Munekane, A. Kuno, M. Matsuo, T. Hayashi, Y.A. Kim, M. Endo, *Carbon* **45**, 274 (2007).
- [12] P. Politzer, P. Lane, M.C. Concha, J.S. Murray, *Microelectron. Eng.* **81**, 485 (2005).

TOWARDS THE CONTROL OF STRUCTURAL PROPERTIES OF CNTS PRODUCED BY ARC DISCHARGE IN LIQUID ENVIRONMENTS

S. Scalese^{1*}, V. Scuderi¹

¹ *Consiglio Nazionale delle Ricerche - Istituto per la Microelettronica e Microsistemi, Strada VIII n. 5, Zona Industriale, I-95121 Catania (Italy)*

*E-mail: silvia.scalese@imm.cnr.it

ABSTRACT

Carbon nanotubes (CNTs) can be produced by several techniques, each of them owns its pros and cons. Among them arc discharge in liquids allows to obtain very good structural quality, even though it is still poorly understood as concerns the process itself and the role of the discharge parameters on the controlled formation of different kinds of nanostructures. The control of the properties of the produced materials requires a systematic study of the arcing process and the role of discharge parameters. We have investigated the formation and the morphology of the C deposit on the cathode, after arc discharge between two graphite electrodes immersed in liquid nitrogen. The deposit consists of disordered carbon structures at the bottom and on the external part of the deposit, forming like a bowl, and a core of randomly oriented multiwall carbon nanotubes (MWCNTs), aggregated in several pillars. In particular, as concerns the MWCNTs, we have observed that a suitable choice of the discharge parameters allows to achieve a good control on their structural properties (innermost and outermost diameter, number of walls, formation of linear C-chains, etc.). A comparison between nanostructures produced by arc discharge in liquid nitrogen and de-ionized water is shown.

1. INTRODUCTION

Arc discharge in gas environment is commonly used for the synthesis of carbon nanotubes (CNTs), even though the process itself is not fully characterized and the role of the discharge parameters on the formation of different kinds of nanostructures is not well defined, especially in the case of arc discharge in liquid. A morphological analysis of the carbon deposit formed on the cathode can give some useful indications in order to understand what happens during arcing and how the formation of different structures and their spatial distribution are influenced by the process and the plasma conditions. Such analysis was reported in the case of arc discharge in gaseous environments [1,2] some years ago and a qualitative explanation of the structural differences between the core and the shell of the deposit was given.

In this paper we have investigated the case of C deposit obtained by arc discharge in liquid nitrogen (LN₂), and correlated our experimental results to experimental parameters. In particular, we have shown [3-5] that

parameters such as electrode size, discharge current values, applied voltage and liquid environment greatly influence the structural quality of the nanotubes (e.g., presence of carbonaceous impurities, innermost tube diameter, number of walls) and a proper combination of these parameters allows to control the synthesis of CNTs and/or CNT-linear C chain hybrid systems [6,7].

2. EXPERIMENTAL

The discharge apparatus is formed by two high purity (99.99%) graphite rods, used as anode and cathode, submerged in LN₂ to create an inert ambient and connected to a DC power supply. Several samples were produced changing the electrode diameter between 5 and 10 mm and, for each case, the current has been varied between 15 and 80 A, keeping the voltage at 25 V.

For another set of samples the arc discharge is performed by supplying a voltage between 15-45 V, limiting the maximum current value to 80 A. Other details are given elsewhere [3-5].

The structural characterization of the samples was performed by scanning electron microscopy (SEM), transmission electron microscopy (TEM) and Raman spectroscopy.

3. RESULTS AND DISCUSSION

A morphological analysis of the C deposit forming on the cathode was performed as a function of voltage and current values used for the arc discharge. We observed the presence of two different regions: a kind of bowl consisting mainly of disordered C structures, appearing in the colder regions of the cathode surface (Fig. 1a); the other one made of CNTs, forming in the hotter region of the cathode surface and well packed into pillars (Fig. 1b). The pillars at higher magnification show to be formed by carbon nanotubes randomly oriented, as reported in Fig.1c. Size and sharpness of the pillars, as well as the CNT structure, depend on the voltage applied to start the electric arc [4,5]. Fig. 1d and Fig. 1e show typical nanotubes obtained applying a voltage of 25V and 45V respectively. A statistical distribution study of the diameter size obtained by TEM analysis are reported elsewhere [8]. They suggest that amount of CNTs with innermost diameter smaller than 1 nm decreases from 63% to 23.5%, as the voltage is increased from 25V up to 45V. At the same time, the number of CNTs with

outermost tube diameter between 5 nm and 10 nm rises from 33.3% for a voltage of 25V to 56%, for a discharge voltage of 45V.

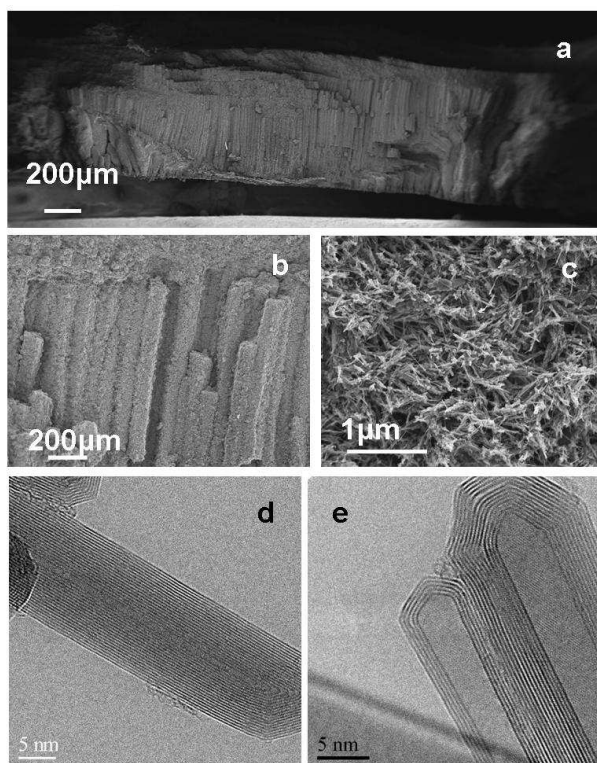


Fig.1: SEM images of (a) a typical C deposit cross section obtained for an applied voltage of 25V and a discharge current of 80A, (b) higher magnification of the core of the deposit formed by pillars, (c) CNTs randomly oriented inside the pillars. TEM images of characteristic nanotubes obtained for an applied voltage of (d) 25V and (e) 45V.

So, if we compare the two samples, we observe that CNTs produced at 45V have, on average, larger innermost tube diameters and smaller outermost tube diameters, that means fewer walls than the ones produced at 25V, as shown in Fig. 1d-e.

However, the kind and the quality of CNTs produced inside the pillars not only depend on the applied voltage, but they are strongly influenced by electrode size and discharge current values. We prepared different samples for different couples of electrodes changing the size between 5 and 10mm and the discharge current between 15-80A. The results achieved by Raman spectroscopy can be summarize in the graph reported in Fig. 2a. An increase in the electrode size and/or in the discharge current determines a better quality of the nanotubes as shown by the reduction of the I_D/I_G ratio in the Raman spectra. This trend is evident also in SEM images showing how, for a fixed current value (e.g. 50A), the use of a small electrodes (5mm diameter each other) leads to the formation of nanotubes with a bamboo-like structures and a big amount of impurities (amorphous C structures), Fig. 2b.

The use of electrodes with larger diameter (10mm) determines the formation of high quality nanotubes with

smaller diameters and lower amount of impurities (Fig. 2c).

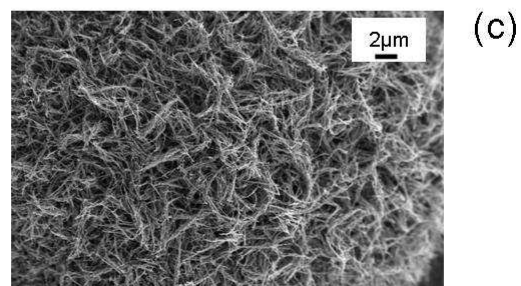
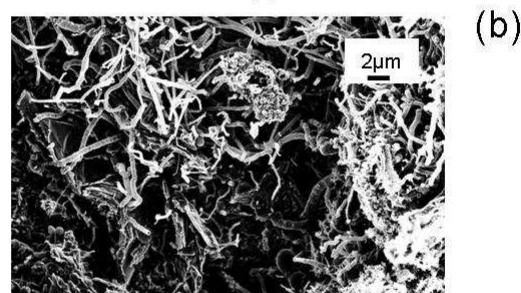
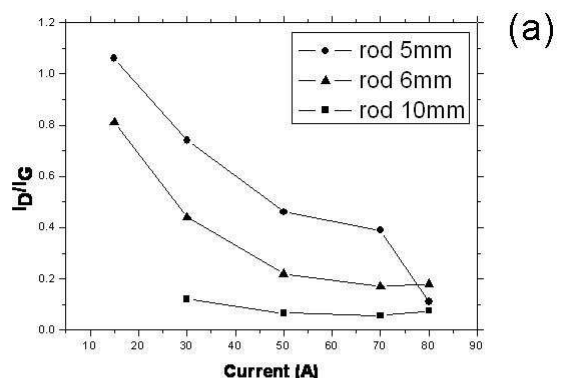


Fig. 2: (a) Trend of I_D/I_G ratio versus the discharge current values, for different electrode couples. SEM images of the sample obtained applying a voltage of 25V and a current of 50A at two rods with a diameter of (b) 5mm and (c) 10mm.

The experimental results obtained are in good agreement with the theoretical model proposed by Gamaly et al. [9] about the growth of carbon nanostructures by arc discharge.

Then, an accurate choice of the experimental parameters and geometrical configuration allows to obtain a deposit formed mainly by carbon nanotubes with specific mean characteristics. In particular experimental conditions, reported elsewhere [6,7], it is also possible to obtain hybrid systems formed by linear C chains inside CNTs. The high quality of the structures and the presence of high amount of nanotubes with an innermost diameter smaller than 1 nm has allowed us to observe radial breathing modes (RBM) in Raman spectra also for MWCNTs, due to the vibration modes of innermost tubes. The correlation between one RBM feature loss and the L-band, never observed before in the literature,

permits to point out the formation of linear C chains in CNTs having a diameter of 0.7 nm, so that the distance between the atoms in the chain and the inner wall is equal to the distance between two graphite planes, as expected [6].

Another feature extremely important is the choice of the liquid in which arc discharge takes place. The use of de-ionised water (DI-H₂O) instead of LN₂ as liquid environment for arc discharge, causes the formation of different structures. In particular, a SEM characterization of the C deposit, not reported here, allows us to observe, besides tangled MWCNTs and other smaller carbon nanostructures, the presence of several graphene layers that are not produced in such large amount when arcing is conducted in liquid nitrogen. In particular MWCNTs appear bent, tipped and/or with the external walls opened. TEM observations, reported in Fig. 3, confirm the large rate of nanotubes containing several defects (mainly pentagon and heptagon defects) [10] responsible for the CNT bending, the non-simultaneous capping of the different tubes belonging to the same MWCNT, and the existence of graphene layers.

We believe that hydrogen and oxygen atoms present in water play an important role in the formation of defects in nanotubes. In particular the formation of graphene layers can be due to hydrogen atoms that contribute to the saturation of dangling carbon bonds on the borders of graphitic planes, and prevent their rolling and the formation of closed structures [11].

4. CONCLUSION

C deposits produced by arc discharge in liquids are formed by a core of randomly oriented CNTs inside a disordered C bowl.

The structural quality of CNTs produced in this way is greatly influenced by experimental parameters such as electrode size, discharge current values, applied voltage.

In particular: higher structural order is observed for CNTs produced at higher current and/or higher voltage values; the electrode size influences the stability of the arcing process, and therefore the total amount of ordered structures; innermost tube diameter and number of walls change for CNTs produced at different applied voltages. It is also possible to obtain hybrid systems formed by linear carbon chains inside CNTs.

The choice of the liquid environment is crucial for the control of defects in CNTs and the formation of new kinds of low-dimensional C structures, like graphene layers.

5. ACKNOWLEDGEMENTS

The authors thank M. Italia for technical assistance, C. Bongiorno for TEM analyses and the group of G. Compagnini for Raman analyses.

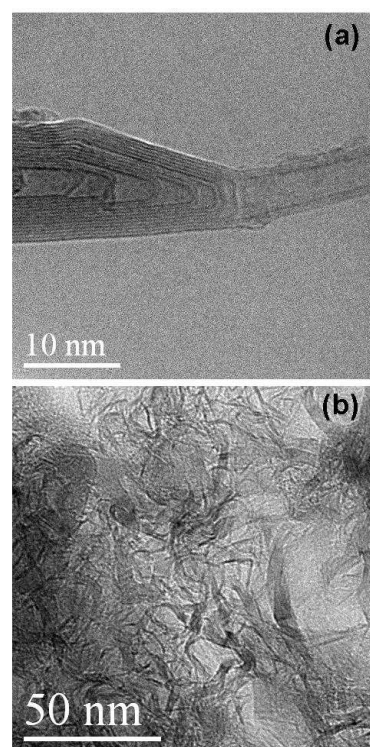


Fig. 3: TEM images of C deposit obtained by arc discharge in de-ionised water: (a) nanotube containing several defects and (b) graphene layers

6. REFERENCES

- [1] P.M. Ajayan, P. Redlich, M. Rühle, *J. Mat. Res.* **12**, 244 (1997).
- [2] N.S. Koprinarov, M.A. Konstantinova, G.V. Pchelarov, M.V. Marinov, *J. Cryst. Grow.* **171**, 111 (1997).
- [3] S. Bagiante, S. Scalese, V. Scuderi, L. D'Urso, E. Messina, G. Compagnini, V. Privitera, *Phys Stat Sol B* **247**, 884 (2010).
- [4] S. Scalese, V. Scuderi, S. Bagiante, S. Gibilisco, G. Faraci, V. Privitera, *J App Phys* **108**, 064305 (2010).
- [5] S. Scalese, V. Scuderi, S. Bagiante, S. Gibilisco, G. Faraci, N. Piluso, F. La Via, V. Privitera, *Phys.E* (2011), doi: 10.1016/j.phise.2011.08.004
- [6] V. Scuderi, S. Scalese, S. Bagiante, G. Compagnini, L. D'Urso, V. Privitera, *Carbon* **47**, 2134 (2009).
- [7] S. Scalese, V. Scuderi, S. Bagiante, F. Simone, P. Russo, L. D'Urso, G. Compagnini, V. Privitera, *J Appl Phys* **107**, 014304 (2010).
- [8] S. Scalese, V. Scuderi, S. Bagiante, I. Deretzis, A. La Magna, C. Bongiorno, G. Compagnini, S. Gibilisco, N. Piluso, V. Privitera, Accept for publication in *J Ram Spec.*
- [9] E.G. Gamaly, T.W. Ebbesen, *Phys Rev B* **52**, 2083 (1995).
- [10] S. Iijima, T. Ichihashi, Y. Ando, *Nature* **356**, 776 (1992).
- [11] V. Scuderi, C. Bongiorno, S. Scalese, submitted to *Carbon*.

TEMPERATURE CHARACTERIZATION OF THE SHEET RESISTANCE OF MWCNTS/PDDAC BASED SENSITIVE FILMS

N. Donato^{1*}, D. Aloisio¹, D. Spadaro², M. Latino^{2,3}, A. Giberti⁴ and C. Malagù⁴

¹Dept. of Matter Physics and Electronic Engineering, University of Messina, Italy

²Dept. of Industrial Chemistry and Materials Engineering, University of Messina, Italy

³Dept. of Chemical Science and Technologies, University of Rome Tor Vergata, Italy

⁴Dept. of Physics, University of Ferrara, Italy

*E-mail: ndonato@unime.it

ABSTRACT

The development of nanostructured materials opened new frontiers in the realization of sensors employed in many fields and applications. Thin and thick films of sensitive materials are widely employed in the productions of resistive or capacitive sensors. In this work, it is reported about the electrical characterization versus temperature of MWCNTS/PDDAC based sensitive film and about the development of a low cost measurement setup for the temperature characterization of the sheet resistance of sensitive films. The system is an useful aid to understand the behaviour of sensing materials working at low operating temperatures up to 100 °C and for the development and characterization of sensors working at room temperature, without any needing of integrated heaters. Here are reported experimental results regarding humidity sensing films fabricated by rubber stamp printing on a glossy paper substrate of an ink based on multiwalled carbon nanotubes (MWCNTs) and dispersed in a solution of PDDAC (poly(diallyldimethylammonium chloride)).

1. INTRODUCTION

The impact of sensors in the everyday life is well consolidated, the growing of market of such devices brings new challenges in developing new materials and technologies for the fabrication of low cost and low power consumption devices. Nanomaterials are widely employed in the development of gas sensors, they can be used in several configurations spanning from thin films [1] to nanowires for sensor arrays[2].

Since their discovery by Iijima [3] carbon nanotubes (CNTs) have emerged among innovative materials because of the variety of technological applications they find, spanning from flexible energy storage devices [4] to sensors [5]. For practical uses, self standing structures or films based on CNTs can be obtained by direct growth on suitable substrates, using high-temperature chemical vapour deposition. Other approaches are based on liquid phase deposition of surface functionalized CNTs. Surface functionalization has the effect to improve wettability and dispersion stability, when CNTs are dispersed in solvent with the aid of surfactants or polymers [6]. Recent applications in biosensing, use screen-printed CNTs

electrodes consisting of carbon nanotubes added to binders, and dispersed into suitable polymer hosts [7]. In such a contest the development of characterization systems is a key issue in understanding material properties and in the optimization of sensing films for sensors. In this work, it is reported the development of a low cost measurement setup for the temperature characterization of the sheet resistance of sensitive films. The system is an useful aid to understand the behaviour of sensing materials working at low operating temperatures up to 100 °C and for the development and characterization of sensors working at room temperature, without any needing of integrated heaters. Here are reported preliminary characterization of thin films obtained by rubber stamp printing on a glossy paper of a conductive ink developed by dispersing high purity multi walled carbon nanotubes into aqueous solutions of PDDAC (poly(diallyldimethylammonium chloride)).

2. EXPERIMENTAL

The four probe technique is a well-known method for the characterization of the sheet resistance of semiconductors, but it can be employed in the electrical characterization of films composed of different materials with sensing properties[8]. The developed system is an all in line four probe characterization setup, the sheet resistance is measured by reading voltage and current as described in Figure 1 and by deembedding the sample shape and dimensions by means of correction factors.

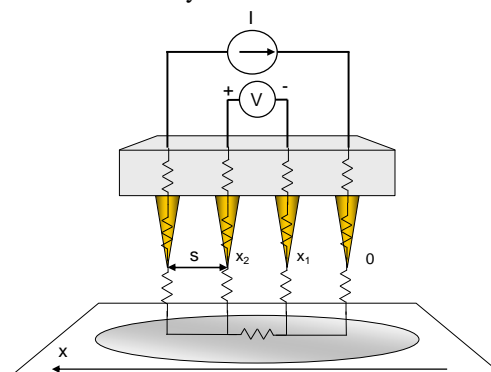


Fig. 1. Scheme of "all in line four probes" measurement set-up.

By using the four-point probe method, the semiconductor sheet resistance can be calculated:

$$R_s = F \frac{V}{I}$$

where V is the voltage reading from the voltmeter, I is the current carried by the two current carrying probes, and F is a correction factor. This factor can be computed taking into account the dimensions of the sample under test (for a squared sample the dimension of a side) and the probe spacing (i.e. the distance between a probe and the closest one). For collinear or in-line probes with equal probe spacing, the correction factor F can be written as a product of three separate correction factors:

$F = F_1 F_2 F_3$ deembedding the finite sample thickness, the finite lateral sample dimensions, and the placement of the probes with finite distances from the sample edges, respectively. For very thin samples with the probes being far from the sample edge $F_2 = F_3 \cong 1$, and the expression of the semiconductor sheet resistance can be written as: $R_s = \frac{\pi V}{\ln 2 I}$.

The probes used in this work have a spacing of 1mm and a contact area of 1mm^2 , they are realized by parts of surface mounting device (SMD) connectors and can be contacted with calibrated screws to modulate the contact pressure on the sample. The software is able to compute the right correction factor just by inserting the dimensions and the shape of the sample under test.

In Figure 2 is reported the block diagram of the measurement system, the main part of the thermal chuck is composed of two stacked Peltier cells. By means of this apparatus it is possible to perform measurements in a temperature range spanning from $-20\text{ }^\circ\text{C}$ to $120\text{ }^\circ\text{C}$ with a resolution of $0.2\text{ }^\circ\text{C}$.

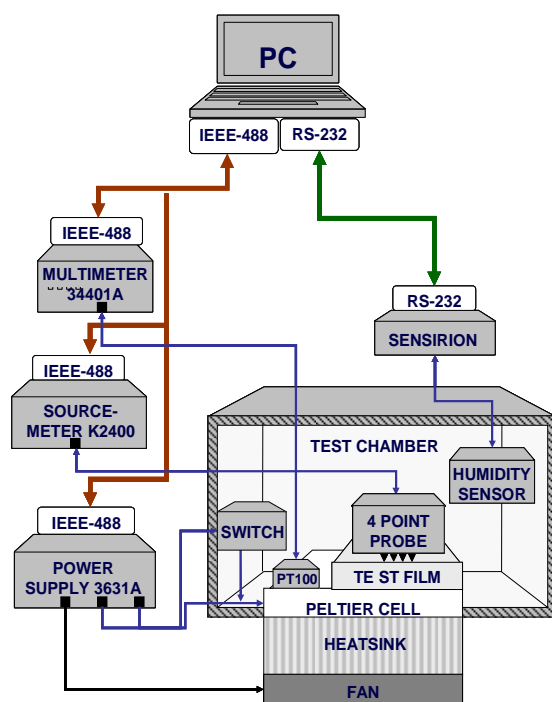


Fig. 2. Block diagram of the realized system

The temperature is monitored by a PT100 Platinum resistance sensor and settled by means of an Agilent 3631 power supply; an automated switch can change the supply polarity to the Peltier cells changing the hot/cold configuration of the side in thermal contact with the sample and consequently achieving a more efficient and fast temperature stabilization. The feedback is developed by a PID (Proportional Integrative Derivative) algorithm, both the control and the measurement procedures were developed with Agilent Vee development tool and IEEE 488.2 protocol. The software is able to handle two Keithley source meters (2400 and 6487) for medium and high resistance value measurements. A CMOS calibrated sensor (SHT21 by Sensirion), able to measure and record both the temperature and the relative humidity, is used to check the environmental conditions into the measurement chamber where is placed the thermal chuck with the sample holder.

3. RESULTS AND DISCUSSION

The samples under test are made of substrates of glossy paper with rubber stamp printed films of an ink developed by dispersing high purity MWCNTs (Baytubes C150HP supplied by Bayer) into aqueous solutions of PDDAC (poly(diallyldimethylammonium chloride)). They were prepared in 10×10 mm squared shapes and contacted as described in the previous section. The electrical characterization of the developed samples was performed using a Keithley 2400 source meter.

Figure 3 shows the dependence of the sheet resistance of the sensitive film versus temperature and humidity values; at a fixed temperature value an increasing of humidity brings to a consequent increasing of the sheet resistance, while at a fixed humidity value an increasing of temperature brings a decreasing of sheet resistance.

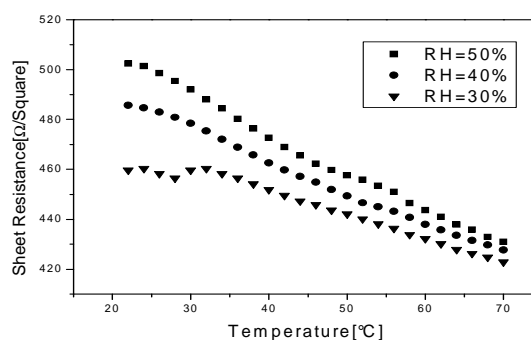


Fig. 3. Characterization of the sheet resistance vs humidity and temperature.

When the temperature is fixed, an increase in RH represents an increase of water vapour partial pressure (absolute humidity). This leads to an increase in the sheet resistance due to the increased adsorption rate of water molecules at surface. To explain the above results we would recall the ability of the hydrophilic poly(diallyldimethylammonium chloride) and/or carbon nanotubes to adsorb water molecules when exposed to humidity [9, 10].

At fixed RH instead, two effects are involved, i.e., the increasing temperature and the increase in water vapour partial pressure. As observed in Fig.3, the increase in temperature brings to a decrease in the sheet resistance, as expected in a semiconductor. This means that the effect of increasing resistance due to water vapour partial pressure increase is dominated by the usual temperature effect on a semiconductor. To better investigate the contributions of both effects (humidity and temperature) in figure 4 are reported sheet resistance measurements of a more resistive sample at two different operating conditions.

Figure 4 (a) describes the behaviour of the sheet resistance vs. temperature, the level of humidity and the temperature in the test chamber was monitored by means of a SensirionSHT21 MOS sensor. The effect of the temperature was investigated at values ranging from -15 °C to 80 °C. Considering the small variation of the humidity, the decreasing of sheet resistance can be mainly related to sensor temperature conditions. In figure 4 (b) are reported measurements of the sheet resistance vs relative humidity at 25 °C, by maintaining the temperature value constant by means of the PID control.

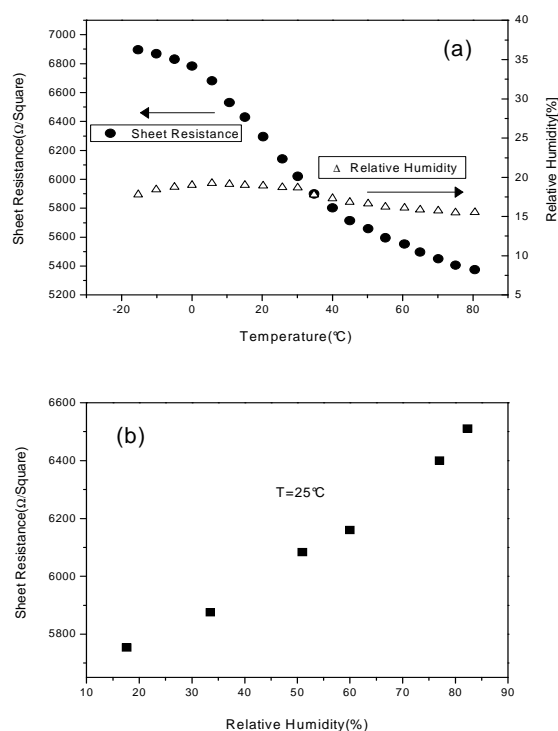


Fig. 4. Characterization of both effects: (a) sheet resistance vs. temperature with humidity monitoring, (b) sheet resistance vs. relative humidity at 25 °C.

Results obtained show that the sheet resistance increases with the increasing of relative humidity. In order to understand the observed behaviour we carried out a preliminary investigation on the PDDAC+carbon nanotubes sensing layer deposited on alumina substrates with interdigitated platinum electrodes utilized in previous work [11]. The sample were insert in a test chamber under controlled flux conditions. The characterization system allows to set the operating

temperature of the substrate and to control the composition of the test atmosphere by means of a mass flow controller array and a bubbler. In figure 5 it can be seen the temperature dependence of the measured sample resistance at dry air conditions. In figure 6 it can be seen the increasing of the resistance value at different pulses of humidity, temperature value is kept constant. Results obtained are in good agreement, that is the presence of humidity increases the bulk resistance of the sensing layer.

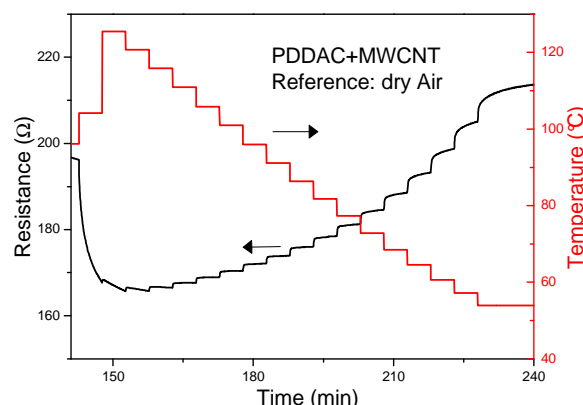


Fig. 5. Resistance vs. temperature characterization at dry air conditions.

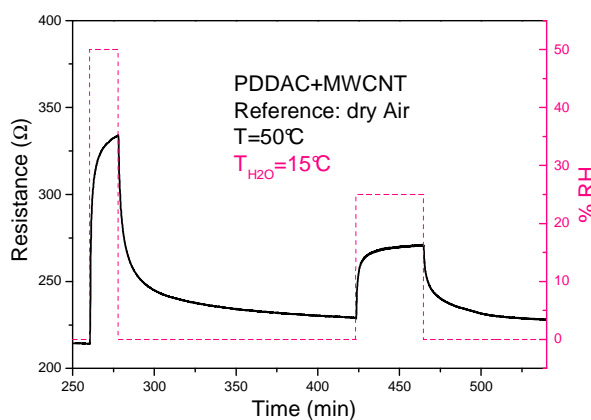


Fig. 6. Increasing of resistance in presence of humidity pulses at constant temperature values.

This behaviour can be attributed to the presence of carbon nanotubes in the sensing layer formulation. However, work is in progress in order to better understand the properties and conduction phenomena associated with the studied sensing system.

4. CONCLUSIONS

Here is reported the development of a compact and low cost setup for the electrical characterization versus temperature of thin films with sensing properties. The realized software can perform several electrical measurements (IV cycling, two port IV characterization, electrical hysteresis measurements) including the sheet resistance deembedding, the effects of the shape and

dimension of the sample under test in a full automatic way.

The characterization system is able to reproduce the whole temperature operating range of a sensor, even in critical ambient conditions, and it can be employed in the optimization of sensing materials. The preliminary results of the characterization of films of PDDAC + MWCNTs on glossy paper are quite promising for the development of disposable flexible sensors.

5. ACKNOWLEDGMENTS

This work was founded with MIUR PRA08-09 of University of Messina.

6. REFERENCES

- [1] R. Nohria, R. K. Khillan, Yi Su, R. Dikshit, Y. Lvov, K. Varahramyan, *Sensors and Actuators B: Chemical*, Vol. 114, Issue 1, 218-222, 2006.
- [2] M. Yuna, N. V. Myunga, R. P. Vasquez, J. Wang, H. Monbouquette, *Nanofabrication Technologies. Proceedings of the SPIE*, Volume 5220, pp. 37-45 (2003)
- [3] S. Iijima, *Nature*, 354 (1991) 56.
- [4] V. L. Pushparaj, M. M. Shaijumon, Ashavani Kumar, SaravanababuMurugesan, LijieCi, Robert Vajtai, Robert J. Linhardt, OmkaramNalamasu, Pulickel M. Ajayan, *Proceedings of the National Academy of Sciences of the United State of America* 104 (2007) 13574.
- [5] NirajSinha, Jiazhi Ma, and John T. W. Yeow, *Journal of Nanoscience and Nanotechnology*, Vol.6, 573-590, 2006.
- [6] XL Xie, YW Mai, XP Zhou *Materials Science & Engineering R* 19(2005) 89.
- [7] S. Sánchez , M. Pumera, E. Fàbregas, *Biosensors and Bioelectronics* 23 (2007) 332.
- [8] Liu Pengyi, Chen Junfang, Sun Wangdian, *Plasma Science & Technology* Vo1.6, No.2, Apr. 2004
- [9] L. L. Miller, J. S. Bankers, A. J. Schmidt and D. C. Boyd, *J. Phys. Org. Chem.* 13: 808-815, 2000.
- [10] Wei Fen Jiang, Shun Hua Xiao, Chun YueFeng, Hua Yang Li, XinJian Li *Sensors and Actuators B* 125 (2007) 651-655.
- [11] Neri G, Bonavita A, Galvagno S, N. Donato, A. Caddemi, *Sensors Actuators B*, 111 (2005) 71-77

RAMAN OPTICAL TRAPPING OF CARBON NANOTUBES AND GRAPHENE

M. G. Donato*⁽¹⁾, P. G. Gucciardi⁽¹⁾, S. Vasi^(1,2), M. Monaca^(1,2), R. Sayed^(1,3),
G. Calogero⁽¹⁾, P.H. Jones⁽⁴⁾, O.M. Maragò⁽¹⁾

⁽¹⁾ *CNR-IPCF, Istituto per i Processi Chimico-Fisici, Messina, Italy*

⁽²⁾ *Dipartimento di Fisica della Materia e Ingegneria Elettronica,
Università di Messina, Messina, Italy*

⁽³⁾ *Dottorato di Ricerca in Fisica, Università di Messina, Messina, Italy*

⁽⁴⁾ *Department of Physics and Astronomy, University College of London, London, UK.*

* E-mail: donato@me.cnr.it

ABSTRACT

Raman optical trapping of single-walled carbon nanotubes (SWNT) and graphene is discussed. We demonstrate the use of Raman and photoluminescence tweezers to study the properties of SWNT bundles and graphene directly in liquid, overcoming the re-aggregation phenomena taking place on dried samples. In addition, the Brownian motion of such nanostructures in the optical trap is reconstructed.

In this work, we report on recent results on optical and Raman trapping of carbon nanotubes and graphene [2,5]. We show how optical trapping can be used to obtain information on the Brownian motion of nanotube bundles and graphene flakes [2, 5]. Raman tweezers have been used to gain information on bundle composition (by means of Raman signature of each chirality). Moreover, Raman optical trapping have been used to highlight the different structural properties of graphene flakes obtained by Density Gradient Ultracentrifugation (DGU).

1. INTRODUCTION

Optical trapping is emerging as an outstanding tool for the contactless manipulation of micro- and nano-sized objects [1-7]. This phenomenon is based on the exchange of momentum between a focused light beam and a particle. If the beam is tightly focussed and the index of refraction of the particle is higher than that of the surrounding medium, a driving force compelling the particle towards the beam focus arises. A wealth of applications has been reported since the first pioneering work of A. Ashkin, ranging from cellular and molecular biology to condensed matter studies and even optoelectronics [8].

Raman tweezers are a clever evolution of optical trapping, where the light collected from the trapped particle is analysed to obtain its Raman spectrum. This is a very appealing application especially with regards to the study of single-walled carbon nanotubes (SWNTs) and graphene flakes. In fact, as grown carbon nanotubes experience aggregation phenomena that cause the formation of nanotubes bundles, independently of their electronic (metallic/semiconducting character) or structural (chirality) properties.

Aiming at sorting on the basis of their characteristics, SWNTs have been dispersed in aqueous environment with the aid of surfactants [9], but their Raman spectra must be recorded on drop-cast samples, and re-aggregation phenomena cannot be avoided. A similar problem must be faced also for graphene obtained by liquid-phase exfoliation [5]. In this framework, Raman tweezers are a viable route to study nanotubes and flakes directly in liquid, avoiding re-aggregation phenomena.

2. EXPERIMENTAL

Optical trapping setups have as central element an inverted microscope and a high numerical aperture objective (100x oil immersion, NA=1.3). The trapping laser beam (830 nm) is expanded by a telescope to overfill the back aperture of the objective in order to have a diffraction limited spot. The sample is loaded in a micro-chamber (approx. 80 microliters) and protected by a coverslip in order to minimize aging. To study the Brownian motion, the interference pattern in the back focal plane of the microscope condenser is imaged by means of a lens on a Quadrant PhotoDiode (QPD), which is a position detector. In this way, the fluctuations of the position of the trapped particle are obtained as voltage signals. In the case of spherical particles, the tracking signals are proportional to the center-of-mass displacements, whereas in the case of linear and planar structures the tracking signals encompass both translational and angular displacements.

In the Raman tweezers set-up (Fig. 1) the light scattered by the trapped particle is collected in a back-scattering configuration and spectrally analyzed by means of a monochromator (Triax 190). The 633 nm laser line of an HeNe laser is used as trapping and exciting wavelength. For the Raman signal detection, an avalanche photodiode is used.

SWNT samples are prepared using purified HiPCO or CoMoCAT single-wall nanotubes dispersed in water with the aid of surfactants such as sodium dodecyl benzene sulfonate (SDBS) or sodium taurodeoxycholate (TDC). Solutions are ultrasonicated and filtered to ensure removal of residual catalyst particles, amorphous carbon and big bundles.

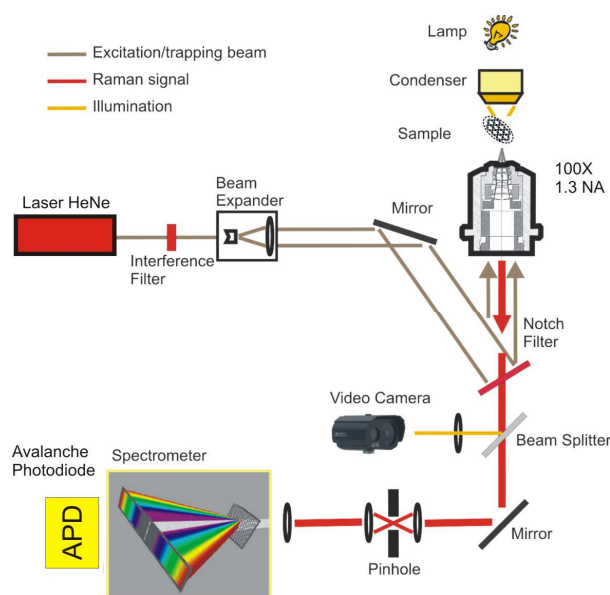


Figure 1. Raman tweezers set-up.

Graphene samples have been obtained by liquid phase exfoliation [5] of graphite powder in deionized water and a surfactant (sodium deoxycholate dihydroxy bile salt, SDC). In contrast to linear chain surfactants, *i.e.* SDBS, the flat structure of SDC disperses graphene more efficiently. The graphite-water-surfactant dispersion is mild ultrasonicated for 120 min in a low power bath sonicator and pre-ultracentrifuged to remove thicker graphitic flakes. After these steps, the supernatant is extracted and used for the DGU. In this procedure, objects having different densities float also at different heights in the ultracentrifuge cell, so they can be extracted with a fractionation method. In our case [5] the surfactant coverage of graphene flakes is exploited for the separation of graphene flakes with respect the number of layers, because the density of the graphene-surfactant complex increases with the number of graphene layers.

3. RESULTS

Figure 3 shows some of the results obtained by optical trapping of CNT bundles. Fig.3a and b show, respectively, a free floating and an optically trapped CNT bundle dispersed in a water/TDC solution. When trapped, the bundle orients itself in the beam propagation direction. Figure 3c shows the three main features of single-walled CNT: the radial breathing modes (RBM) in the 150-320 cm^{-1} region, the D and G bands (1320 and 1590 cm^{-1}) region and the 2D peak at 2620 cm^{-1} . The G band shape indicates that the trapped bundle is mainly constituted of semiconducting SWNTs, whereas the RBM region shows the presence of nanotubes having different diameters d ($\omega_{\text{RBM}} \sim 1/d$), whose chirality is shown in Figure 3d. Moreover (see Figure 4), the trapping and subsequent photoluminescence analysis of several bundles show a different chirality fractional composition of each bundle. Such information is obviously not achievable in drop-cast samples nor in standard

photoluminescence measurements, which give information on the average bundle population present in the liquid.

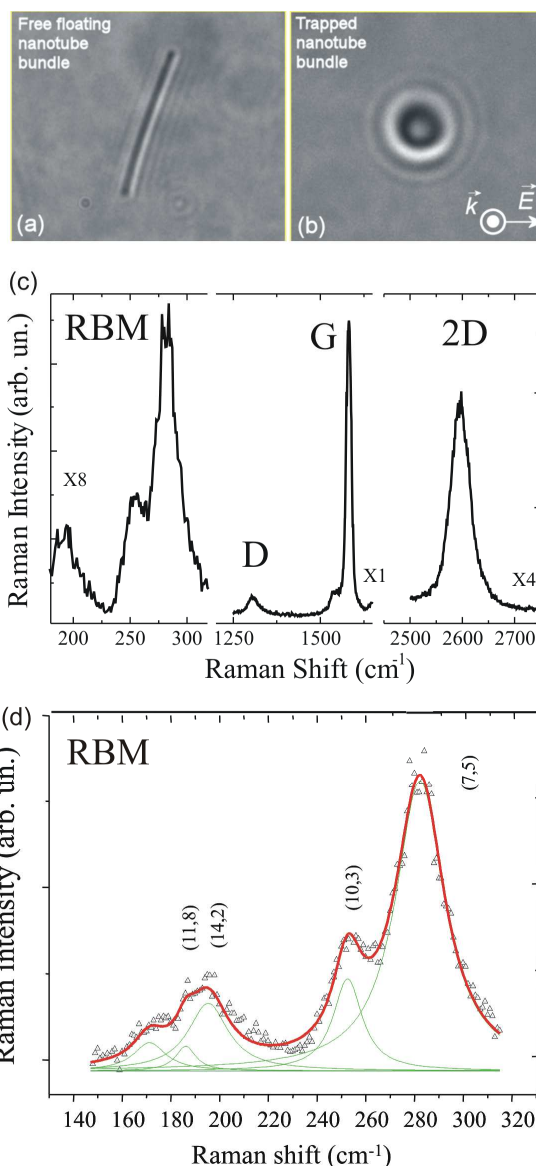


Figure 3. Optical trapping of SWNT bundles. Micrographs of free (a) and trapped (b) SWNT bundle. (c) Characteristic Raman spectral features of trapped SWNT. (d) Zoom of the radial breathing mode region in the Raman spectrum of a trapped SWNT bundle. The different chiralities present in the sample are also indicated.

In Figure 5, the micrographs of a free floating and trapped graphene flake and its Raman spectrum are shown [5]. Besides the well-known D and G peaks, which are commonly observed in sp^2 -carbon based materials, several other peaks are observed. Among these, the 2D peak (second order of D peak) is particularly interesting, because it is a single band in monolayer graphene, whereas it splits in four components in bilayer graphene, reflecting the evolution of band structure [10]. Thus, its shape and, in particular, its full width at half maximum (FWHM) is a useful indicator of the single-layer nature of a trapped graphene flake.

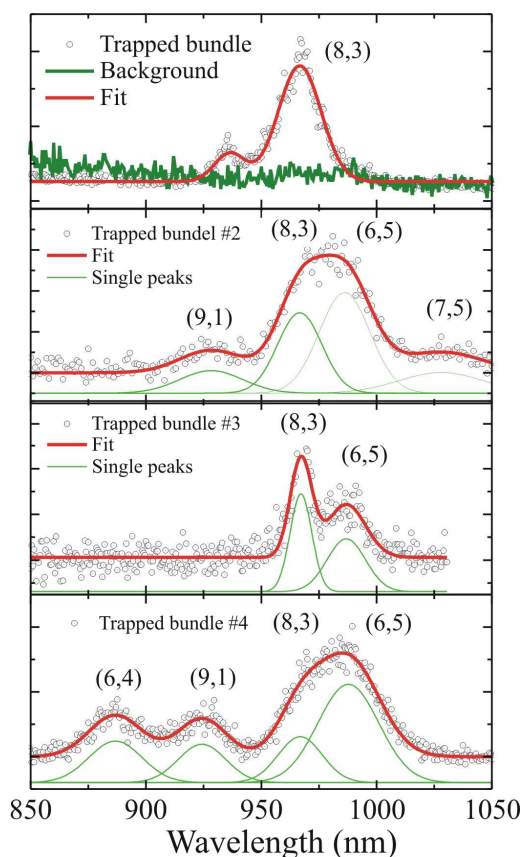


Figure 4. Photoluminescence spectra of several trapped CNT bundles. The different chiralities are also indicated.

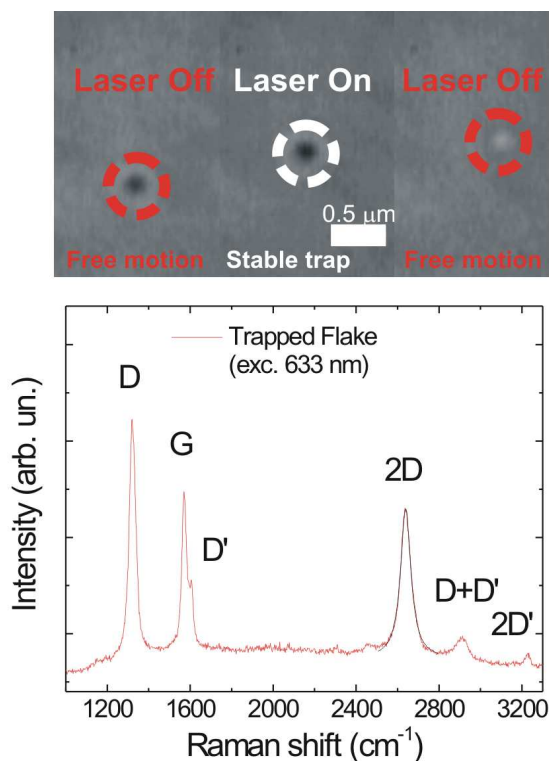


Figure 5. (Top) Optical trapping of a graphene flake in water/SDC solution. (Bottom) Raman spectrum of a trapped graphene flake. Typical Raman features are also indicated.

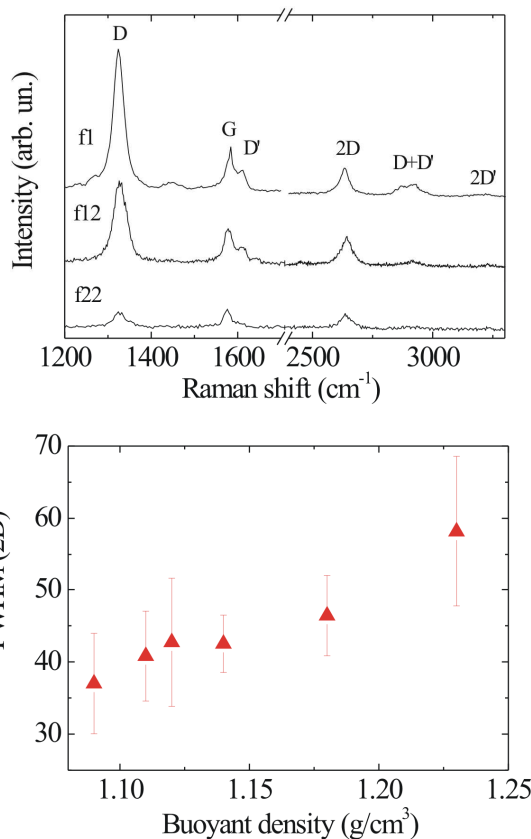


Figure 6. (Top) Raman spectra measured on trapped flakes belonging to fractions having increasing density. The FWHM of their 2D peak is compared (bottom) to the corresponding parameter obtained from Raman spectra of drop-cast samples deposited on SiO₂ substrate.

Aiming at improving the single-layer yield of liquid phase production of graphene, the DGU separation has been used. In Figure 6, the Raman spectra obtained on different fractions, going from low density (f1=1.09 g/cm³) to high density (f22=1.23 g/cm³), are shown.

It is worth noting as the average 2D peak FWHM measured on trapped flakes (Fig. 6, bottom) are always lower (about 40%) than those measured on drop-cast samples, supporting the idea that the latter suffer from re-aggregation phenomena that hinder the study of individualized graphene flakes. Moreover, the decreasing FWHM of 2D peak at lower buoyant density is consistent also with a higher concentration of single-layer flakes in these samples, confirming that DGU has a beneficial effect on the individuation of single layer graphene flakes.

Finally, the reconstruction of the Brownian motion of a trapped carbon nanotube and graphene flake in comparison with the Brownian motion of spherical microbeads is shown in Figure 7 [5]. The role of the different dimensionality clearly emerges from the dynamics of such particles in the optical trap. Such measurements show that optical trapping provides an ideal framework for both spectroscopic and mechanical probing of individualized nanostructures such as carbon nanotubes and graphene flakes.

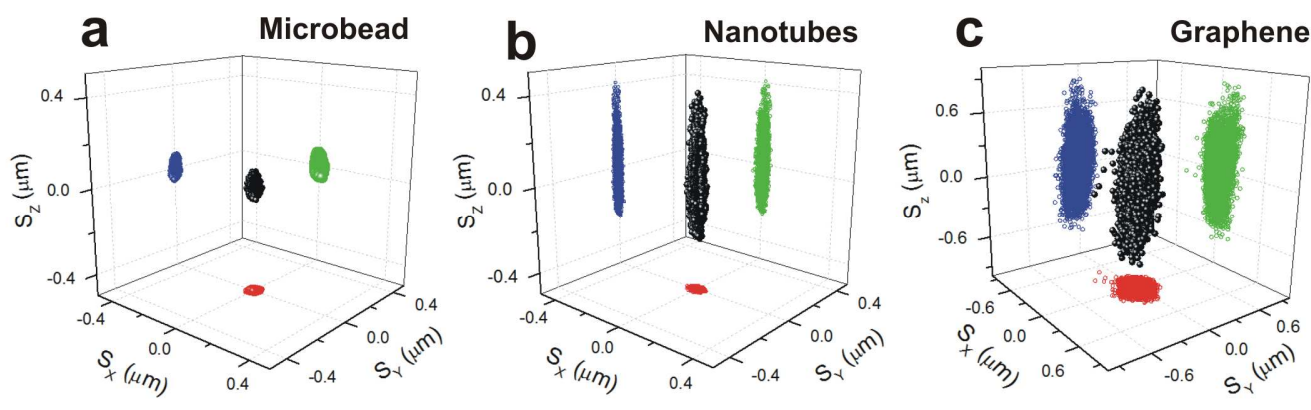


Figure 7. Brownian motion of (a) a standard latex microbead (2 μm diameter), (b) a carbon nanotube and (c) a graphene flake.

4. CONCLUSIONS

Optical trapping offers a unique opportunity to trap, manipulate, probe and characterize individual nanostructures such as carbon nanotubes and graphene. The combination with Raman and photoluminescence spectroscopy allows on one hand the spectroscopic investigation of individual nanostructures and, on the other, the improvement of their production processes and dispersion. Further developments of the technique, involving radially and azimuthally polarized laser beams [11, 12], are currently under investigation.

11. REFERENCES

- [1] O.M. Maragò, P.G. Gucciardi, F. Bonaccorso, G. Calogero, V. Scardaci, A.G. Rozhin, A.C. Ferrari, P.H. Jones, R. Saija, F. Borghese, P. Denti, M.A. Iatì, *Physica E* **40**, 2347 (2008).
- [2] O.M. Maragò, P.H. Jones, F. Bonaccorso, V. Scardaci, P.G. Gucciardi, A.G. Rozhin, A.C. Ferrari, *Nano Lett.* **8**, 3211 (2008).
- [3] P.H. Jones, F. Palmisano, F. Bonaccorso, P.G. Gucciardi, G. Calogero, A.C. Ferrari, O. M. Maragò, *ACS Nano* **3** 3077 (2009).
- [4] A.A.R. Neves, A. Camposeo, S. Pagliara, R. Saija, F. Borghese, P. Denti, M.A. Iatì, R. Cingolani, O.M. Maragò, D. Pisignano, *Opt. Express* **18**, 822 (2010).
- [5] O.M. Maragò, F. Bonaccorso, R. Saija, G. Privitera, P.G. Gucciardi, M. A. Iatì, G. Calogero, P.H. Jones, F. Borghese, Paolo Denti, V. Nicolosi, A.C. Ferrari, *ACS Nano* **4**, 7515 (2010).
- [6] O.M. Maragò, P.H. Jones, P.G. Gucciardi, *Photonic Force Microscopy: From Femtonewton Force Sensing to Ultra-Sensitive Spectroscopy*, in "Scanning Probe Microscopy in Nanoscience and Nanotechnology", ed. B. Bushan, Springer-Verlag, Berlin, Heidelberg, 2010.
- [7] E. Messina, E. Cavallaro, A. Cacciola, M. A. Iatì, P.G. Gucciardi, F. Borghese, P. Denti, R. Saija, G. Compagnini, M. Meneghetti, V. Amendola, O. M. Marago', *ACS Nano* **5**, 905 (2011)
- [8] Focus issue on Optical Manipulation, *Nature Photonics* **5**, 315-378 (2011)
- [9] F. Bonaccorso, T. Hasan, P. H. Tan, C. Sciascia, G. Privitera, G. Di Marco, P. G. Gucciardi, and A. C. Ferrari, *J. Phys. Chem. C* **114**, 17267 (2010)

[10] A. Ferrari, J.C. Meyer, V. Scardaci, C. Casiraghi, M. Lazzeri, F. Mauri, S. Piscanec, D. Jiang, K. S. Novoselov, S. Roth, A. K. Geim, *Phys. Rev. Lett.* **97**, 187401 (2007)

[11] P. H. Jones, M. Rashid, M. Makita, O. M. Maragò *Opt. Lett.* **34**, 2560 (2009)

[12] M. Rashid, O. M. Marago, P. H. Jones, *Journal of Optics A-Pure and Applied Optics* **11**, 065204 (2009)

SYNTHESIS OF GRAPHENE NANORIBBONS AND OTHER CARBON NANOSTRUCTURES

Franco Cataldo^{1,2*}

¹*Actinium Chemical Research srl, Via Casilina 1626/A, 00133 Rome, Italy*

²*Università di Tor Vergata, Via della Ricerca Scientifica, 00133 Rome, Italy*

*E-mail: franco.cataldo@fastwebnet.it

ABSTRACT

The recent research work of Actinium laboratory will be reviewed. In particular will be reviewed the synthesis of graphene nanoribbons by oxidation of single wall and multiwall carbon nanotubes. Graphene nanoribbons prepared also by arcing graphite electrodes in oleum (fuming sulphuric acids) or by neutron bombardment of graphite followed by sonication. It will be shown also the bottom-up approach used for the synthesis of very large PAHs on the way to graphene nanoribbons. Concerning other carbon nanostructures, topological defects of graphene sheets will be shortly reviewed and compared with recent amazing experimental observations. The topic of carbon nanostructures will involve also the recent achievements in the synthesis of diarylpolyynes

As appendix, it will be presented the effects of MWCNTs on the mechanical properties of a cured rubber composite.

1. INTRODUCTION

Since the discovery of the easy access to graphene from graphite by mechanical exfoliation of a graphite crystal, a number of papers and reviews have been published on the subject leading also to the awarding of the Nobel prize to Geim and Novoselov in 2010 [1-5].

Graphene is a single layer of carbon atoms arranged in condensed hexagonal rings. Such carbon atoms layers are stacked in an orderly way in graphite and are kept together by weak Van der Waals forces. By adequate treatments ranging from simple mechanical treatments to physical intercalation of molecules between the graphene layers to chemical synthesis, it is possible to prepare exfoliated graphene sheets and graphene nanoribbons. A similar approach works also with carbon nanotubes both single and multiwall, which can be chemically unzipped under oxidative or intercalation treatments.

2. OXIDATIVE UNZIPPING OF MWCNT AND SWCNT

The successful oxidative unzipping of MWCNT [6] was also studied and reproduced in our laboratory [7]. MWCNT were oxidized with KMnO_4 in acid conditions leading to graphene nanoribbons which were identified by various techniques including the transmission electron microscopy. The resulting nanoribbons were in an oxidized state and thermally unstable and when heated

decompose explosively at 152°C in the TGA leaving a reduced and finely divided soot. Such a thermal behaviour was already reported in literature for certain samples of graphite oxide which also decompose explosively under a thermal treatment.

An original achievement was the oxidation of SWCNT using a mixture of nitric and sulphuric acid leading to graphene nanoribbons which were thoroughly studied by infrared and Raman spectroscopy as well as with XPS and HRTEM analysis and AFM [8].

3. GRAPHITE EXFOLIATION BY ARCING IN OLEUM

Graphite can be swelled in oleum (fuming sulphuric acid) very slowly, requiring a number of hours. We have found that graphite rods can be swelled and then exfoliated in oleum in a couple of minutes by arcing graphite electrodes in that medium [9]. The morphology of the swelled and exfoliated graphite was studied by TEM analysis and the dispersion of swelled graphite particles in oleum by electronic absorption spectroscopy. The cathode and anode materials after arcing in oleum were recovered and studied by TGA showing the formation of residual compounds of graphite bisulphate. The uptake of bisulphate was significantly higher by the graphite from the anode material rather than the anode, reaching a composition of $\text{C}_{96}^+\text{HSO}_4^-$.

4. THE BOTTOM-UP APPROACH TOWARD GRAPHENE: FROM CORONENE TO DICORONYLENE AND BEYOND

We can define the typical synthetic routes to graphene nanoribbons as a top-down approach starting from complex precursors having already a layered or graphene-based structure.

The bottom-up approach instead involves the use of simple building blocks, for example, simple polycyclic aromatic hydrocarbons (PAHs) which are linked together to form larger “graphene” fragments with the potential advantage to control the dimension of such sheets. For example heating coronene in a sealed glass ampoule at 550-580°C leads to its dimerization to dicoronylene (see Fig. 1) [10]. Depending from the reaction conditions, the formation of dicoronylene may be accompanied by the formation of other higher oligomers of coronene (trimers, tetramers) but it is possible to achieve also the complete

carbonization of the sample. Indeed, typically the formation of dicoronylene is accompanied by the formation of a dark carbonaceous material [10].

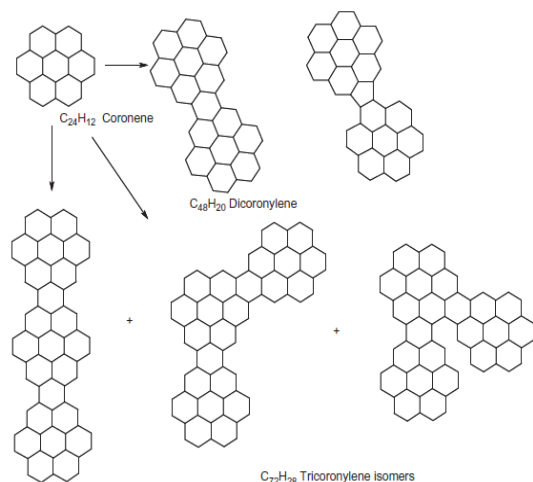


Fig. 1 – Scheme of coronene dimerization and oligomerization [10,11]

Consequently, it is reasonable to assume that coronene can be used as a “building block” to produce very large PAHs which indeed are already a fraction of a graphene sheet (see Fig. 2).

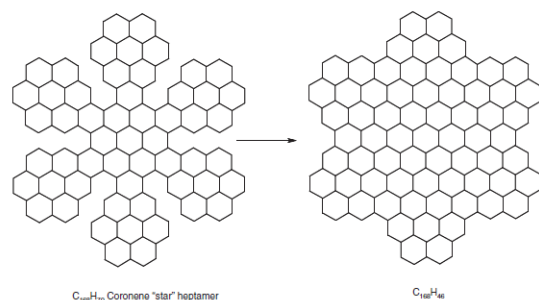


Fig. 2 – Possible structures formed by using coronene as a “building block” on the road toward graphene.

In addition to the thermal treatment of coronene, we have applied the Scholl reaction to coronene obtaining once again the dicoronylene [11]. However, the Scholl reaction requires the use of a catalyst and lower temperatures than the previous case where coronene was dimerized thermally. The use of a catalyst leads not only to the canonical dicoronylene shown in Fig. 1 with a hexagonal bridge linking two coronene units but also to another dicoronylene isomer with a pentagonal bridge linking the two coronene units (see Fig. 1) [11]. Typically the molar ratio of the canonical dicoronylene and its pentagonal isomer is 80%/20% respectively [11]. The pentagonal isomer is instead completely absent in the high temperature thermal dimerization of coronene. In further work in the attempt to produce a coronene trimer [12,13] we succeeded in the synthesis of an higher coronene oligomer, presumably a para-trimer shown in Fig. 1 whose structure was deduced on the basis of the electronic absorption spectrum in trichlorobenzene and from its radical cation spectrum in oleum [12,13].

In our studies on the bottom-up approach toward graphene nanoribbons, we have also used the Scholl reaction in the successful synthesis of quaterrylene from perylene and hexabenzocoronene from hexaphenylbenzene (see Fig. 3) [11,12].

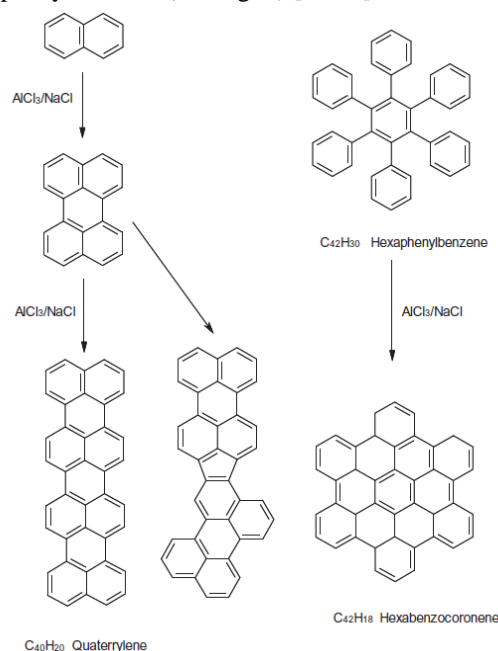


Fig. 3 – Synthesis of quaterrylene and hexabenzocoronene using the Scholl reaction

It is interesting to note that also in the case of quaterrylene two isomers are obtained simultaneously through the Scholl reaction: the canonical hexagonally bridged dimer of perylene and the “non-alternant” pentagonally bridged dimer of perylene (Fig. 3).

5. NEUTRON BOMBARDMENT OF GRAPHITE AND EXFOLIATION BY SONICATION

An original approach regarding the access to graphene nanoribbons may involve the neutron irradiation of graphite. Recently we have adopted such approach [14] displacing the carbon atoms of the graphene sheets of graphite with neutron bombardment. The displaced carbon atoms leave vacancies on the graphene sheets and are collocated between the graphene layers as Frenkel defects, causing an increase of the interlayer spacing. The neutron-bombarded graphite can be easily exfoliated by sonication while of course this is not the case for pristine virgin graphite sample [14].

6. FULLERENE-LIKE STRUCTURES IN CARBON MATERIALS LIKE CARBON BLACK

Some years ago, we have proposed that the fullerene-like defects are quite common defects in graphene sheets especially in turbostratic materials known as carbon black and such defects may play a key role in the reinforcing interactions between any polymer matrix and the carbon black fillers [15]. Recent works have shown that fullerene-like structures (intended not only as a

pentagonal defect in a graphene sheet but intended as any kind of defect e.g. heptagonal, octagonal defects as well as any other kind of vacancy or interstitial defect) are quite common in radiation treated graphite and other carbon materials [16,17] and now it is more reasonable to accept the idea that these defects must be present in carbon black. Consequently, this concept may lead to the design of new carbon blacks having an enhanced interaction with polymer matrix and an enhanced reinforcing effect [18].

7. ABOUT DIPHENYLPOLYINES AND DINAPHTHYLPOLYINES

The synthesis of diphenylpolyynes and dinaphthylpolyynes was successfully achieved using an original approach combining the adoption of the dangerous and explosive diiodoacetylene with the Cadiot-Chodkiewicz reaction conditions [19,20].

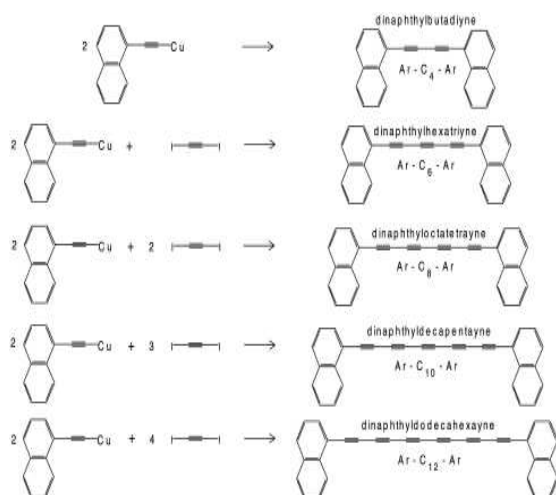


Fig. 4 - Synthesis scheme of dinaphthylpolyynes using diiodoacetylene and the Cadiot-Chodkiewicz reaction [19,20].

A mixture of polyynes phenyl- or naphthyl- terminated have been synthesized, separated by HPLC and identified by their peculiar electronic absorption spectra. In comparison to the hydrogen-terminated polyynes and the cyano-terminated polyynes the phenyl and naphthyl terminated polyynes are much more stable in air and can be even isolated from their solutions without any secondary crosslinking reaction which is well known to occur with common hydrogen-terminated polyynes [19,20].

8. REINFORCING EFFECT OF MWCNT IN A RUBBER MATRIX: AN APPLICATIVE ASPECT

The last part of the lecture deals with an applicative aspect of the new carbon materials. In particular we are focusing on the reinforcing effect exerted by MWCNT on a natural rubber-based polymer matrix [21]. The work shows that MWCNT have a very strong stiffening effect on the polymer matrix combined with a strong increase in the mechanical hysteresis. The increase in the viscosity of the polymer matrix upon the addition of MWCNT at

different levels can be modelled using a modified Einstein-Guth equation including terms which regard the aspect ratio of the filler [21].

11. REFERENCES

- [1] Novoselov KS, Geim AK, Morozov SV, Jiang D, Zhang Y, Dubonos SV et al. *Science* **306**, 666 (2004)
- [2] Novoselov KS, Jiang D, Schedin F, Booth TJ, Khotkevich VV, Morozov SV et al. *Proc. Nat. Acad. Sci.* **102**, 10451 (2005).
- [3] Geim AK, Novoselov KS. *Nature Mater.* **6**, 183 (2007).
- [4] Geim AK. *Science* **324**, 1530 (2009).
- [5] Prezhdo, O., Kamat, P.V., Schatz, G.C., *J. Phys. Chem. C*, **115**, 3195 (2011).
- [6] Konyshin, N. et al. *Nature* **458**, 872 (2009).
- [7] Cataldo, F., Compagnini, G. et al. *Fullerenes Nanotubes Carbon Nanostructures* **18**, 261 (2010).
- [8] Cataldo, F., Compagnini, G. et al. *Carbon* **48**, 2596 (2010).
- [9] Cataldo, F. et al. *Fullerenes Nanotubes Carbon Nanostructures* **20**, 152 (2012).
- [10] Talyzin, A., Cataldo, F. et al. *J. Phys. Chem. C* **115**, 13207 (2011).
- [11] Cataldo, F. et al. *Fullerenes Nanotubes Carbon Nanostructures* **19**, 713 (2011).
- [12] Cataldo, F. et al. *Spectrochim. Acta* **A77**, 998 (2010).
- [13] Cataldo, F. et al. *Polycyclic Aromatic Hydrocarbons*, submitted for publication.
- [14] Cataldo, F. et al. *Fullerenes Nanotubes Carbon Nanostructures* **20**, in press (2012).
- [15] Cataldo, F. *Carbon* **40**, 157 (2002).
- [16] Hashimoto, A. et al. *Nature* **430**, 870 (2004).
- [17] Banhard et al. *ACS Nano* **5**, 26 (2011).
- [18] Cataldo F. et al. *Fullerenes Nanotubes Carbon Nanostructures* **11**, 395 (2003).
- [19] Cataldo, F. et al. *J. Macromol. Sci.* **A47**, 739 (2010).
- [20] Cataldo, F. et al. *J. Phys. Chem. B* **114**, 14834 (2011).
- [21] Cataldo F. et al. *Fullerenes Nanotubes Carbon Nanostructures* **17**, 38 (2009).

TAGUCHI-OPTIMISED PRODUCTION OF MWCNT-BASED NANOCOMPOSITES BY CATALYTIC ROUTE

S. Santangelo^{1*}, G. Messina¹, G. Faggio¹, E. Piperopoulos², M. Lanza³, C. Milone²

¹ Dept. of Mechanics and Materials, Univ. "Mediterranea", Reggio Calabria, Italy

² Dept. of Industrial Chemistry and Materials Engineering, Univ. of Messina, Messina, Italy

³ CNR, Inst. for Chemical Physical Processes, Messina Section, Messina, Italy

* E-mail: saveria.santangelo@unirc.it

ABSTRACT

The production of multi-walled C nanotubes (MWCNTs) and MWCNT-based nanohybrids by chemical vapour deposition (CVD) of isobutane is optimised by Taguchi's robust design method. Processing conditions (calcination at 450–750°C and reduction at 500–700°C) and support material (Al₂O₃, MgO or Na⁺-K10) of the Fe-catalyst and synthesis temperature (500–700°C) are assumed to be factors controlling yield (Y_C) of the catalytic process and graphitisation degree of the grown MWCNTs, as measured by the average crystallite size (L_C) inferred from Raman spectroscopy. Poor Y_C ($<9g_{MWCNTs}/g_{Fe}$) and small L_C (~15nm) are obtained, on average, in CVD experiments before optimisation. An outstanding improvement is achieved ($Y_C \cong 51g_{MWCNTs}/g_{Fe}$ and $L_C \cong 45nm$) upon optimised conditions.

1. INTRODUCTION

MWCNTs and MWCNT-based nanocomposites are promising materials for applications in manifold advanced technology fields [1–3].

The capacity of the worldwide nanotube industrial production (estimated in hundreds of tonnes/year and seeing CVD as the dominant technique [4]) is continuously increasing. Current forecasts assign a 25% annual growth rate to nanotubes. Indeed, a real race among competitors is in progress with frequent announcements by the industrial companies of larger and larger new investments aimed at boosting their production capacity in this very profitable sector.

The reasons for CVD being the most used method of producing nanotubes on large scale are low set-up cost, easy of scale-up and high production yield. Besides bulky yields, obtainment of highly crystallised MWCNTs is a crucial task of producers. This calls for the optimisation of the manifold parameters involved in the CVD synthesis process.

Taguchi's robust design method is a powerful and efficient tool for multifactor process optimisation [5], which has been extensively applied in the most diverse fields.

In this work, it is for the *first time* applied to the optimisation of production of MWCNTs and MWCNT-based nanohybrids by iron-catalysed CVD of *i*-C₄H₁₀. In order to maximise yield of the catalytic process and graphitisation

degree of the grown MWCNTs, a small number (nine) of suitably designed CVD experiments are performed. By analyzing the results obtained, the influence on Y_C and L_C is ranked of support material (M_S), calcination- (T_C) and reduction-temperatures (T_R) of the catalyst and synthesis temperature (T_S). The parameter settings predicted to give optimal results in terms of Y_C and L_C are critically examined, eventually adjusted, and finally tested by conducting new CVD experiments.

2. EXPERIMENTAL DETAILS

2.1. Design of Experiments (DoE)

T_C , T_R , T_S and M_S were assumed to be the four factors mostly controlling the issue of the process in terms of catalytic yield and graphitisation degree of the grown MWCNTs. The reason for this assumption is that the choice of support and of catalyst processing conditions (M_S , T_C and T_R) determines number, size and dispersion of Fe-nanoparticles available for nanotube growth, while reaction conditions (T_S for given gas-flowing setup) essentially rule the rates of supply, diffusion and precipitation of carbon.

Once chosen suited variation ranges, each control factor was varied at three levels as shown in Tab. 1 and the effect of these variations was investigated. Accordingly, a $L_9(3^4)$ Taguchi matrix design was selected and nine CVD experiments were carried out under the conditions listed in Tab. 2. Two syntheses were further conducted to verify the Taguchi-derived/adjusted optimum processing conditions for the selected outputs (Tab. 2).

2.2. Catalysts: Preparation and Characterization

Iron catalysts were prepared by wetting grains of Al₂O₃ (Süd Chemie), MgO (Sigma-Aldrich, nanopowders) and Na⁺-K10 with an aqueous solution of Fe(NO₃)₃·9H₂O (Fluka, 98–100%) having an amount of iron salt suitably calculated to obtain a nominal metal content of 15wt%. Na⁺-K10 was previously obtained by dispersing 10g of as-purchased K10 clay (Aldrich) in 300ml of 1M solution of NaCl to enable the ion-exchange reaction. After calcination in air at T_C , catalysts were reduced for 2h upon 60sccm H₂ flow at T_R .

X-ray diffraction measurements (XRD, APD 2000 Ital Structures), conducted using CuK α radiation source, ascertained the presence of metallic iron in all the reduced

Control factors	Levels
-----------------	--------

	1	2	3
T_C (°C)	450	600	750
T_R (°C)	500	600	700
T_S (°C)	500	600	700
M_S	Al ₂ O ₃	MgO	Na ⁺ -K10

catalysts. The mean Fe-particle size (d_{Fe}) was estimated from the peak of Fe⁰ at 2-theta=44.7° by applying the Scherrer equation. Results obtained are reported in Tab. 2.

Further details on catalyst preparation and characterization can be found elsewhere [3,6,7].

2.3. Nanohybrids: Synthesis, Purification and Analysis

MWCNT-based nanocomposites were synthesized by direct CVD growth of MWCNTs on the selected supports. For this purpose, 0.5g of reduced catalyst, placed in a quartz boat inside the quartz reactor, was heated upon 120sccm 1:1 H₂+He flow. As T_S was reached, He was replaced with *i*-C₄H₁₀ keeping constant flow ratio and total flow rate. Reaction in *i*-C₄H₁₀+H₂ ambient was allowed for 2h.

After cooling down to room temperature (RT) upon 60sccm He flow, raw hybrid products were weighed for catalytic yield evaluation and subsequently purified by acid treatment before being subjected to routine diagnostic analyses. A solution at 12% of HF at RT removed clay support, while 1M solution of NaOH at 80°C was used for Al₂O₃ removal. A solution at 37% of HCl at RT was able to eliminate both MgO support and residual Fe-particles.

The process selectivity was monitored by means of scanning electron microscopy (SEM, JEOL JSM-5600LV at 20kV). The presence of hollow cavity inside filaments was investigated by transmission electron microscopy

(TEM, JEOL JEM-2010 at 200kV).

The crystalline quality was evaluated by measuring Raman scattering. An Ar⁺ laser (Coherent Innova 70) operating at 2.41eV provided excitation. Spectra were recorded using a microscope (Olympus BX40) coupled to double monochromator (Jobin Yvon Ramanor U-1000) and photomultiplier (Hamamatsu R943-02) operating in photon-counting mode. In order to obtain sufficient S/N ratio and prevent annealing effects, 30s acquisition time and low laser-power (3mW at the sample surface) were used. Spectra were averaged, normalised and analysed using a commercially available spectroscopic analysis software package. Lorentzian bands, superimposed to a constant background, were used to fit the spectra.

Further technical details, concerning measurements performed and instrumentation utilised, can be found elsewhere [3,6,7].

3. RESULTS OF TRIAL CVD EXPERIMENTS

Results obtained in Taguchi-designed trial experiments (#1–9) are summarised in Tab. 2. Varying T_C , T_R , T_S and M_S produces very large changes in catalytic yield (0.7–34.6g_{MWCNTs}/g_{Fe}).

SEM analysis (not shown for brevity) evidences strong differences also in the process selectivity. No or very few filamentous structures are observed at the lowest T_S (samples #1, 6 and 8) and at the highest T_R (samples #3 and 9). Scarce amount of non-tubular structures is obtained only in experiment #7. In the remaining cases (samples #2, 4 and 5) tubes and flakes-like formations (FLFs) coexist. TEM (not shown for brevity) reveals that the filamentous structures observed by SEM are MWCNTs. MWCNTs exhibit diverse size and crystallinity-degrees. The outer tube diameters vary in the range 10–70nm, as an effect of the changes of d_{Fe} (Tab. 2).

Measured Raman spectra of the purified carbonaceous products are shown in Fig. 1a. Regardless the levels of

Table 1. Experimental settings of Taguchi-designed trial experiments (#1–9) and results obtained in terms of catalytic yield (Y_C) and graphitisation degree of the grown MWCNTs, as measured by the mean crystallite size (L_C) inferred from intensity ratio of D/G Raman peaks (I_D/I_G). The mean size of Fe-nanoparticles (d_{Fe}), as determined by the variation of T_C , T_R and M_S is also reported. Experimental settings of test experiments (#10–11) are also listed, together with results correspondingly obtained.

Experiment number	Control factors				System response			
					Catalysts		Carbonaceous products	
Trial	T_C (°C)	T_R (°C)	T_S (°C)	M_S	d_{Fe} (nm)	Y_C (g _{MWCNTs} /g _{Fe})	I_D/I_G	L_C (nm)
#1	450	500	500	Al ₂ O ₃	13.7	6.33	1.47	11.29
#2	450	600	600	MgO	32.1	4.65	1.40	11.86
#3	450	700	700	Na ⁺ -K10	26.8	5.37	0.56	29.64
#4	600	500	600	Na ⁺ -K10	12.7	9.77	1.24	13.39
#5	600	600	700	Al ₂ O ₃	16.4	34.55	1.25	13.28
#6	600	700	500	MgO	34.8	0.73	1.27	13.07
#7	750	500	700	MgO	29.9	9.71	0.97	17.11
#8	750	600	500	Na ⁺ -K10	17.0	0.87	1.55	10.71
#9	750	700	600	Al ₂ O ₃	23.1	5.79	1.62	10.24
Test	T_C (°C)	T_R (°C)	T_S (°C)	M_S	d_{Fe} (nm)	Y_C (g _{MWCNTs} /g _{Fe})	I_D/I_G	L_C (nm)
#10	450	500	700	Al ₂ O ₃	13.7	50.69	1.56	10.64
#11	450	500	700	Na ⁺ -K10	22.4	10.67	0.37	44.87

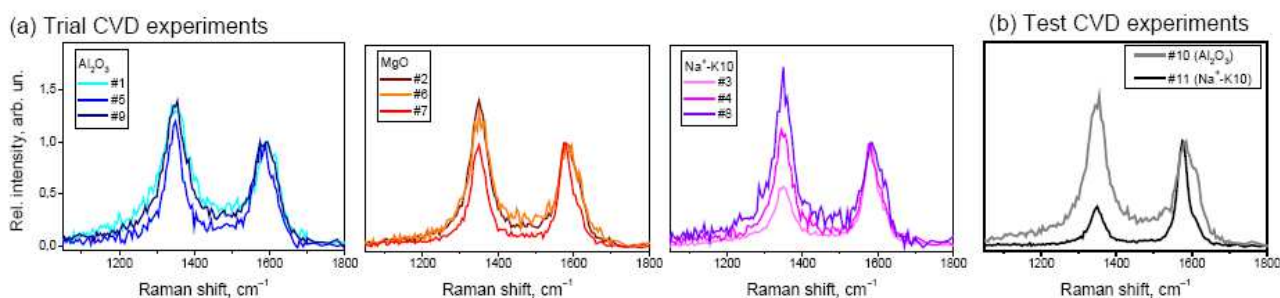


Fig. 1 Raman spectra of the pure carbonaceous products synthesised in trial (#1–9) and test (#10–11) CVD experiments. Spectra are normalized to the G-peak intensity. The same vertical scale is used for an easier comparison.

T_C , T_R , T_S and M_S selected, the spectra exhibit similar features. The fingerprint of the graphitic crystalline arrangement (G-peak at 1580cm^{-1} , arising the stretching of all C=C pairs) is detected, together with the “disorder” peak (D-peak at 1350cm^{-1} , rendered Raman-active by any kind of lattice defects relaxing the selection rules through the breaking of the basic symmetry of graphene-layers) [7,8].

The intensity ratio of D/G Raman peaks (I_D/I_G), giving a measure of the relative amount of ill-organized to defect-free graphitic sheets, is currently utilised to estimate the average size of graphitic crystallites in nanotubes and nanographites via the empirical law $L_C = 560 \cdot (I_D/I_G)^{-1} \cdot E_L^{-4}$, where $E_L = 2.41\text{eV}$ is the laser visible excitation energy [9,10]. The values of L_C here obtained (10.2–29.6nm) are reported in Tab. 2.

4. RESPONSE ANALYSIS

In order to rank the influence of M_S , T_C , T_R and T_S on Y_C and I_D/I_G (i.e. L_C), the responses obtained in CVD experiments #1–9 were analysed. This was accomplished by calculating mean squared deviation (MSD) of the data and corresponding signal/noise ratio (S/N , i.e. response variability) as follows

$$S/N(\text{dB}) = -10\log_{10}(\text{MSD}).$$

The response graphs of S/N ratio for “larger-is-better” analysis of Y_C and for “smaller-is-better” analysis of I_D/I_G are shown in Figs. 2a and 2b. They were obtained by setting $\text{MSD} = \sum_k (1/Y_k)^2/n$ and $\text{MSD} = \sum_k (Y_k)^2/n$ in the former and latter case (n and Y_k being the number of levels investigated and the k^{th} value of the chosen output [5,11,12], respectively).

The influence of each factor on Y_C and I_D/I_G , calculated as $I_k = 100 \cdot \Delta_k / \sum_k \Delta_k$ (Δ_k and $\sum_k \Delta_k$ being the S/N variations due to the changes of the k^{th} factor and of all the factors) is shown in Figs. 2c and 2d. T_S was found to be the parameter having the greatest influence on both Y_C and I_D/I_G . Instead, T_C and T_R were the least influential one in the two cases, respectively.

5. OPTIMISED CVD EXPERIMENTS

Since the highest S/N ratio indicates the optimal level of each control factor [11,12], from graphs of Figs. 2a

and 2b the conditions predicted to give maximum Y_C and minimum I_D/I_G (i.e. maximum L_C) can be inferred.

Within the ranges of M_S , T_C , T_R and T_S considered, it is expected that operating CVD at 700°C , over $\text{Fe}/\text{Al}_2\text{O}_3$ catalysts calcined at 450°C and reduced at 500°C , provides maximum catalytic yield, whereas graphitisation degree of the grown MWCNTs, as measured by L_C , should be maximum operating CVD at the 700°C , over $\text{Fe}/\text{Na}^+\text{-K10}$ catalysts calcined at 450°C and reduced at 700°C . Actually, the latter experimental setting corresponds to experiment #3, which indeed gives the largest L_C value ($\sim 30\text{nm}$) among those of set #1–9.

Configuration predicted to improve yield is *straight* tested (experiment #10). Instead, configuration predicted to maximise MWCNT graphitisation degree is slightly *adjusted* trying to improve Y_C obtainable on $\text{Fe}/\text{Na}^+\text{-K10}$ catalysts without significant loss of L_C . Since T_R has the smallest influence on I_D/I_G (Fig. 2d), experiment #11 is carried out by setting T_R at 500°C . This temperature gives similar S/N ratio as 700°C (Fig. 2b) and is expected to lead to smaller d_{Fe} for fixed T_C [13]. The reason of this choice is that the comparison between results obtained on the remaining catalysts at $T_S = 700^\circ\text{C}$ (experiments #5 and #7) demonstrates that Y_C increases as d_{Fe} decreases as an effect of the changes in T_C and/or T_R .

Results obtained in the new experiments are reported in Tab. 2. As can be seen, they confirm predictions and expectations.

SEM analysis (Figs. 3a–3b) shows that after optimisation the growth process becomes highly selective towards nanotubes. 51g of MWCNTs per gram of Fe are produced in experiment #10, with large bettering with respect to initial Y_C values (Tab. 2). Raman analysis (Fig. 1b) proves that the improvement in crystallisation degree of MWCNTs achieved in experiment #11 is really outstanding ($L_C \approx 45\text{nm}$). This is because, as evidenced by TEM analysis (Fig. 3c), upon optimised conditions, smooth and straight MWCNTs form over $\text{Fe}/\text{Na}^+\text{-K10}$ catalyst, constituted by perfectly ordered graphene sheets. It is worthwhile noticing that crystallisation degree of these MWCNTs largely exceeds that of samples reported as the best crystallized *ever* grown over clay-based catalysts (I_D/I_G is only 0.37 against 0.74–0.99 [14]).

Besides, as expected, d_{Fe} obtained at $T_R = 500^\circ\text{C}$ is smaller than at 700°C and, hence, higher metal dispersion, larger surface available for MWCNT growth and greater

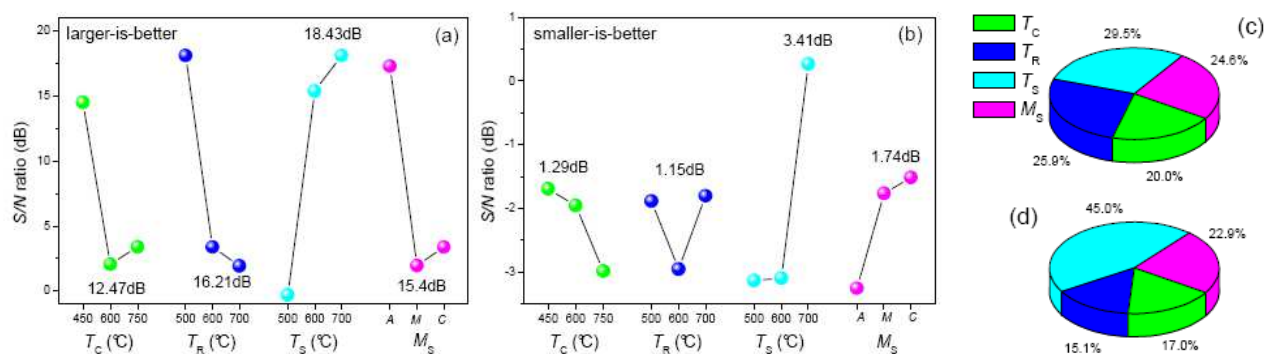


Fig. 2 Response graphs of S/N ratio for “larger-is-better” analysis of Y_C (a) and “smaller-is-better” analysis of I_D/I_G (b). A, M and C respectively denote alumina, magnesia and clay supports. In each graph, the variations of S/N , associated to the changes of the control-factors, are also reported. The influence of T_C , T_R , T_S and M_S on Y_C (c) and I_D/I_G (d) is also shown.

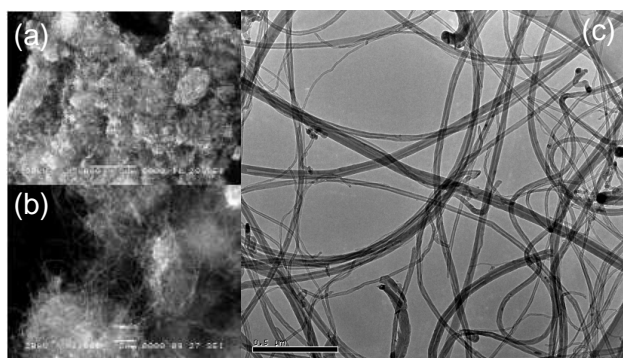


Fig. 3 SEM images of samples #10 (a) and #11 (b) and TEM image of sample #11 (c).

yield are achieved (compare d_{Fe} and Y_C values relative to sample #3 and #11 in Tab. 2).

6. FURTHER REMARKS AND CONCLUSION

Above results well match current assessments on the MWCNT growth [15–19]. C-atoms adsorbed on the free iron surface diffuse to the growth point, either through the Fe-nanoparticle or over its surface [17,18], forming graphitic monolayers. As the C/Fe solid solution is supersaturated, they extrude off the catalyst as the growing nanotube [15,17]. The growth is hampered both in case of high C diffusion-rate (CDR) and low C supply-rate (CSR), as well as in the opposite case [16]. The optimal condition for selectively growing large amounts of well graphitised MWCNTs is obtained when CSR equals CDR [16], which requires accurately balancing all the control factors.

Depending on the M_S specifics (e.g. surface area, thermal stability...), different number, size and dispersion of Fe-nanoparticles available for MWCNT growth are obtained by using the same T_C and T_R . Upon fixed T_S , this leads to different Y_C , since an optimal size range, relative to C supply, exists [19].

At $T_S=700^\circ\text{C}$, growth rate benefits from the smaller d_{Fe} obtained for $T_C=450^\circ\text{C}$ and $T_R=500^\circ\text{C}$ over $\text{Fe}/\text{Al}_2\text{O}_3$ (~14nm). Conversely, the growth rate lowering associated to the larger d_{Fe} obtained over $\text{Fe}/\text{Na}^+-\text{K10}$ (~22nm) positively reflects on the MWCNT graphitisation degree.

6. REFERENCES

- [1] *Carbon nanotubes: synthesis, structure, properties and applications*. M.S. Dresselhaus *et al.* Eds., (Topics in Applied Physics, vol.80. Springer-Verlag, Berlin, 2001).
- [2] M. Terrones, *Annu. Rev. Mater. Res.* **33**, 419 (2003).
- [3] S. Santangelo, G. Gorrasi, R. DiLieto, S. DePasquale, G. Patimo, E. Piperopoulos, M. Lanza, G. Faggio, F. Mauriello, G. Messina, C. Milone, *Appl. Clay Sci.* **53**, 188 (2011).
- [4] WTEC Study Report on International Assessment of Research and Development of Carbon Nanotube Manufacturing and Applications, World Technology Evaluation Center Inc., USA (2007).
- [5] G. Taguchi, Y. Yokoyama, Y. Wu, *Taguchi Methods/Design of Experiments* (American Supplier Institute Press, Tokyo, Japan, 1993).
- [6] S. Santangelo, G. Messina, M.G. Donato, M. Lanza, C. Milone, A. Pistone, *J. Appl. Phys.* **100**, 104311 (2006).
- [7] S. Santangelo, G. Messina, G. Faggio, M. Lanza, C. Milone, *J. Raman Spectrosc.* **42**, 593 (2011).
- [8] M.S. Dresselhaus, G. Dresselhaus, R. Saito and A. Jorio, *Phys. Rep.* **409**, 47 (2005).
- [9] L. G. Cançado, K. Takai, T. Enoki, M. Endo, Y.A. Kim, H. Mizusaki, A. Jorio, L.N. Coelho, R. Magalhães-Paniago, M.A. Pimenta, *Appl. Phys. Lett.* **88**, 163106 (2006).
- [10] M.A. Pimenta, A.P. Gomes, C. Fantini, L.G. Cançado, P. T. Araujo, I.O. Maciel, A.P. Santos, C.A. Furtado, V.S.T. Peressinotto, F. Plentz, A. Jorio, *Physica E* **37**, 88 (2007).
- [11] S. Porro, S. Musso, M. Giorcelli, A. Chiodoni, A. Tagliaferro, *Physica E* **37**, 16 (2007).
- [12] S.H. Hu, Y.C. Chen, C.C. Hwang, C.H. Peng, D.C. Gong, *J. Mater. Sci.* **45**, 5309 (2010).
- [13] C. Milone, M. Dhanagopal, S. Santangelo, M. Lanza, S. Galvagno, G. Messina, *Ind. Eng. Chem. Res.* **49**, 3242 (2010).
- [14] T. Tsoufis, L. Jankovic, D. Gournis, P. N. Trikalitis, T. Bakas, *Mat. Sci. Eng. B* **152**, 44 (2008).
- [15] C. Ducati, I. Alexandou, M. Chhowalla, G.A. Amaratunga and J. Robertson, *J. Appl. Phys.* **92**, 3299 (2002).
- [16] Z.Y. Juang, I.P. Chien, J.F. Lai, T.S. Lai, C.H. Tsai, *Diamond Relat. Mater.* **13**, 1203 (2004).
- [17] J. Robertson, *Materials Today* **10**, 36 (2007).
- [18] C.T. Wirth, C. Zhang, G. Zhong, S. Hofmann, J. Robertson, *ACS Nano* **3**, 3560 (2009).
- [19] C.N.R. Rao, B.C. Satishkumar, A. Govindaraj, M. Nath, *ChemPhysChem* **2**, 78 (2001).

USE OF THE ELECTRIC FIELDS FOR THE MANIPULATION OF MWCNTs.

V. Scuderi ^{(1)*}, A. La Magna ⁽¹⁾, A. Pistone ⁽²⁾, N. Donato ⁽³⁾, G. Neri ⁽³⁾ and S. Scalese ⁽¹⁾

⁽¹⁾*CNR-IMM, Strada VIII n.5, I-95121 Catania, Italy*

⁽²⁾*Dept. of Matter Physics and Electronic Engineering, University of Messina, Italy*

⁽³⁾*Dept. of Industrial Chemistry and Materials Engineering, University of Messina, Italy*

*E-mail: viviana.scuderi@imm.cnr.it

ABSTRACT

Carbon nanotubes (CNTs) have aroused great interest due to their exceptional properties like high current-carrying capacity, high thermal conductivity and reduced charge carrier scattering, that are very attractive for solving the technological hurdles that the semiconductor industry is facing as the circuit scaling continues. The use of both individual nanotubes and CNT networks have been explored, depending on the specific applications [1].

The physical properties depend on the density of CNT layers and the density itself guides the specific application, from flexible electronics to chemical and biological sensors; from optically transparent electrodes to nanoporous electrodes for energy storages [2].

Different approaches have been proposed [3-9] to manipulate CNTs and, in particular, to form conductive networks by means of post-synthesis deposition methods. Electrophoretic deposition (EPD) [10] is one of these methods, and is a very simple technique that offers the possibility to form patterned coatings of substrates.

In particular, our results obtained using CNTs produced by arc discharge and chemical vapour deposition show that a suitable choice of the experimental conditions allows to deposit CNT networks on both conducting and insulating substrates.

1. INTRODUCTION

In the last years the synthesis of nanosized C based materials and the study of their electrical and structural properties have received great attention due to the huge field of applications in technology and microelectronics. In particular, carbon nanotubes show interesting mechanical, electrical and optical properties [11], that depend on the technique used for the synthesis. In recent years, many works have been directed towards manipulating CNTs because microelectronics and sensing applications require the capability to produce CNT networks or ordered arrays [1]. Today, different approaches are used: nanotubes dispersion through surfactants [12] and polymers [13], or direct dispersion of pristine or functionalized CNT in organic solvent and water [14]; coating methods [15]; inkjet printing [16]; film transfer [17]; additive and subtractive patterning methods [18]. An alternative approach is electrophoretic deposition (EPD), that represents a very effective method for its simplicity and cheap equipment required, and

offers the possibility to form coatings with complex shape patterns [10].

In this work we investigate a new aspect of EPD, the possibility to adapt this technique not only for deposition on metallic structures but also in a insulating substrate.

2. EXPERIMENTAL

In our experiments, two different kinds of nanotubes were used: (i) CNTs produced by arc discharge in liquid nitrogen and oxidized in H₂O₂ at 30% for 2h in a ultrasonic bath; (ii) CNTs produced by CVD and oxidised in a concentrate HNO₃ and H₂SO₄ solution (1:1 volume ratio) at 60 °C, for 6h in a ultrasonic bath. The oxidation processes produce a different amount of surface charges, lower in the first case, higher in the second one.

Two acetone suspensions with a concentration lower than 1mg/ml were prepared. The choice to use a dilute solution allows to have a better control on the deposition rate and allows to get rid of the presence of residual materials on the sample surface due to the immersion in the solution. In this way the effect of the electric fields is the prevalent process determining the nanotube deposition.

The electrophoretic deposition was made by supplying a constant DC voltage in the range 5-30 V between two electrodes, for times between 3 and 20 min. The cathode is a Mo foil 5 mm wide and 0.25 mm thick and the anode is a SiO₂/Si substrate. In particular, we have used three different kinds of anodes: 700 nm thick SiO₂/Si with or without a metallic pattern on the substrate surface and 80 nm thick SiO₂/Si. The electrodes were positioned parallel each other at a distance of 2.5 mm.

The structural characterization of the samples was performed by scanning electron microscopy (SEM).

3. RESULTS AND DISCUSSION

In a EPD process, generally two electrodes are immersed in a solution containing charged particles. By applying a voltage to the electrodes a migration of the negative (positive) ions to the anode (cathode) is observed.

Oxidative treatment of CNTs have two effects: removal of impurities and introduction of phenolic, carboxylic and lactonic groups on the surface of the tubes. In particular, the presence of carboxylic groups determines a negative surface charge on the CNTs dispersed in solution [19], allowing the deposition on the anode.

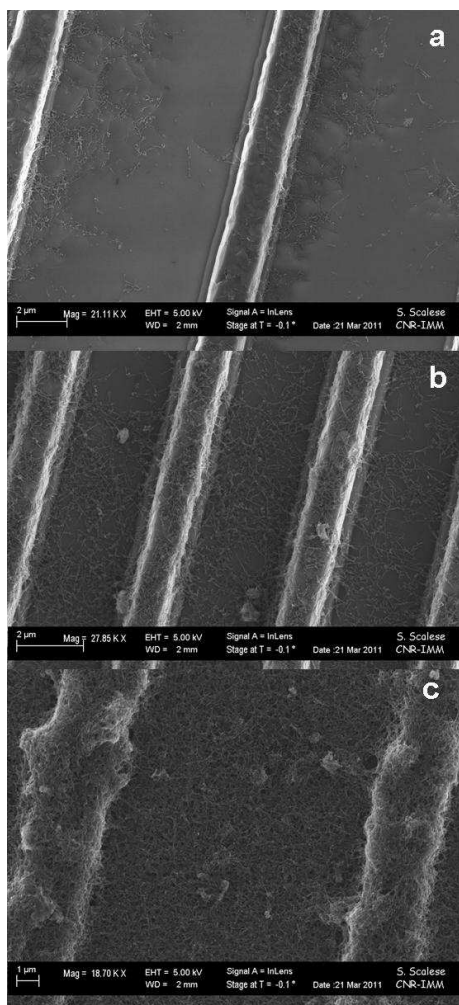


Fig.1: SEM images of metallic strips on a SiO₂ substrate after EPD, (a) and (b) groups of strips with different dimension, space and CNT density; (c) high CNT density.

EPD can therefore be used in order to deposit dense CNT layers or networks for CNTs-FET application. In this work we have studied the effects of electric field for different substrates. In Fig. 1 we report a SEM images of the surface of the sample SiO₂ sample, 700nm thick, with metallic pattern, after EPD using a solution containing CNTs with low surface charge (type (i), described in the Experimental section). In particular the sample is formed by two sets of ten Al strips, connected to a metallic pad. The pattern contains Al strips with different size and distance from each other. CNTs are deposited not only on the metallic strips but also between them.

In Fig.2a we report a simulation of the electric field between two electrodes, according to the experimental conditions. Numerical calculations based on the Poisson equation are performed using the Finite Element Method in a very large box reproducing the whole system, where different materials are considered by means of the proper dielectric properties (null field is imposed in the metal stripes regions). The simulation shows that on the sample surface the electric field is more intense in the proximity of an isolated strip. In the case of a set of strips it is more intense near the outer strip. The red and yellows arrows

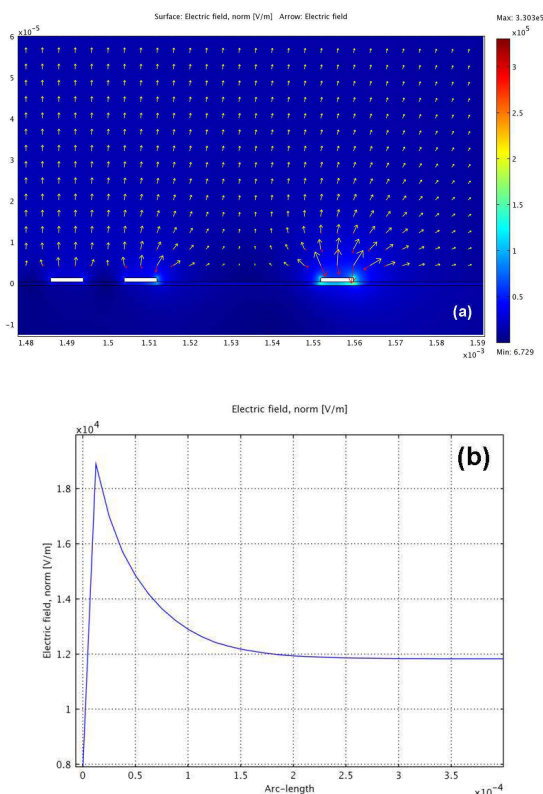


Fig.2: (a) Simulation of the electric field between an anode, patterned with strips of different dimensions and distance, and a metallic cathode. Red arrows are proportional to the electric field intensity, yellow ones to the dielectrophoretic force. The distance between the electrodes is of 2.5 mm. (b) Electric field intensity between the electrodes.

indicate the intensity and the direction of the electric field and dielectrophoretic force respectively. Inside the cell, the electric field is very intense near the surface of the anode and then it decreases to a constant value (Fig. 2b). Fig. 1a-1b show that the possibility to connect two conductive strips by a uniform CNT network depends on dimension and distance of the strips in agreement with electric field simulations. Then, a right choice of the pattern on the substrate allows to optimize the deposition. The thickness of the deposited film depends on solution concentration, electric field, electrophoretic mobility and process time [20].

EPD has also been used to deposit CNT thin films on an insulating substrate [21]. But in this case, metallic film was deposited on substrate and it was etched away after the CNT deposition. Residual of metallic particles however can be found between the insulating substrate and the nanotubes.

Here, we have investigated another opportunity. The voltage is applied between the Mo foil (cathode) and the the back side of the Si substrate (anode). On the front side of the anode an insulating SiO₂ layer is present. The effect of the electric field on the charged nanotubes present in solution is reduced by the presence of an additive dielectric layer. Therefore, in order to deposit the charged nanoparticles on the insulating surface it is necessary

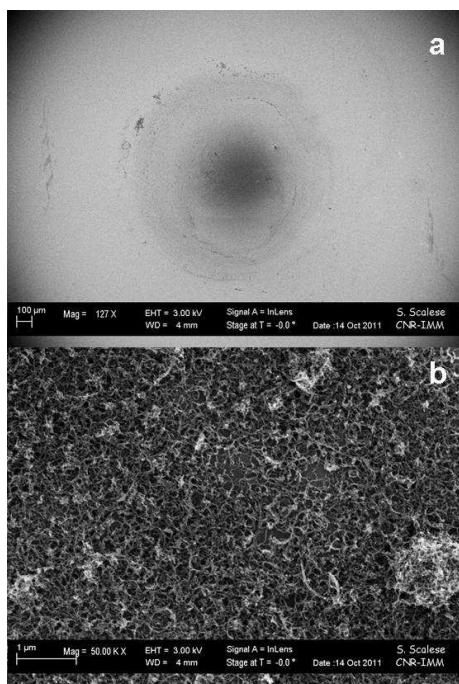


Fig.3: SEM images of (a) 80 nm thick SiO₂ layer on a Si substrate after EPD using (ii) type CNTs; (b) higher magnification of the deposit.

either an increase of the electric field intensity or an increase of the nanoparticle (nanotube) surface charge. In Fig. 3a we report the SEM image of a 80 nm thick SiO₂ layer on a Si substrate, after CNT deposition using a solution containing CNTs with high surface charge (type (ii)), applying 5V voltage for 5 minutes. During the deposition the sample surface was covered with an insulating mica mask, with a opened circle window (diameter=2mm) in order to limit the deposition in the central part of the sample. After deposition, the mask can be removed and on the sample surface the deposited area is visible due to a different contrast in the SEM image. In this circular area a uniform nanotube film was deposited, as shown in Fig. 3b. The same experiment using a CNT solution with low surface charge, do not allow to deposit CNTs on the surface of the sample, independently of the applied voltage in the range 5-30V. The oxidation treatment in H₂O₂ creates a surface charge on the nanotubes not sufficient to move the CNTs towards the anode in the presence of the insulating surface layer.

Increasing the thickness of the oxide to 700 nm, and repeating the EPD process with the solution containing CNTs with high surface charge and applying again a voltage of 5V for 5 minutes, no deposition takes place. An increase of the voltage up to 10 V is needed to compensate the increase in the thickness of the insulating layer and to observe a CNT deposition on this sample, as shown in Fig.4. The simple EPD method can therefore be used also to deposit nanoparticles on insulating layers. In particular deposition of a CNT conductive layer directly on an insulating layer without the use of sacrificial metallic layers that have to be removed afterwards can avoid the presence of metallic contamination. This can be very useful if electrical properties of pure CNTs have to be studied.

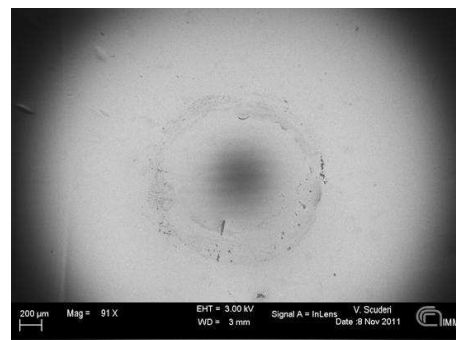


Fig.4: SEM image of 700 nm thick SiO₂ layer on a Si substrate after EPD using (ii) type CNTs, applying a voltage of 10V.

4. CONCLUSION

EPD deposition is a very simple technique to obtain uniform CNT films deposited on a metallic substrate. We have shown that it is possible to obtain CNT networks between metallic strips, forming structures useful for sensing applications. The CNT layers exhibit good macroscopic homogeneity that depend on solution concentration, applied voltage, surface charge, process time and kind of substrate.

The CNT surface charge, produced by oxidation treatment, is fundamental to move CNTs towards the anode. Then a correct choice of the applied voltage and the CNT surface charge allows to deposit directly on insulating substrate without intermediate metallic layer.

11. REFERENCES

- [1] O. Zhou, H. Shimoda, B. Gao, S. Oh, L. Flaming, G. Yue, *Accounts Chem Res* **35** 1045 (2002)
- [2] L. Hu, D.S. Hecht, G.Grüner, *Chem Rev* **110** 5790 (2010)
- [3] M.F. Islam, E. Rojas, D.M. Berjey, A.T. Johnson, A.G. Yodh, *Nano Lett* **3** 269 (2003).
- [4] K.F. Fu, Y.P.J. Sun, *Nanosci Nanotechnol* **3** 351 (2003)
- [5] Z.H. Chen, X. Du, M.H. Du, C.D. Rancken, H.P. Cheng, A.G. Rinzler, *Nano Lett* **3** 1245 (2003)
- [6] V. Krstic, G.S. Duesberg, J. Muster, M. Burghard, S. Roth, *Chem Mater* **10** 2338 (1998)
- [7] X. Zhao, B.T.T. Chu, B. Ballesteros, W.L. Wang, C. Johnston, J.M. Sykes, P.S. grant, *Nanotech* **20** 065605 (2009)
- [8] Q. Cao, S.H. Hur, Z.T. Zhu, Y.G. Sun, C.J. Wang, M.A. Meilt, M. Shim, J.A. Rogers, *Adv Mater* **18** 304 (2006)
- [9] L. Hu, D.S. Hecht, G.Grüner, *Chem Rev* **110** 5790 (2010)
- [10] A.R. Boccaccini et al, *Carbon* **44** 3149 (2006)
- [11] R.H. Baughman et al, *Science* **297** 787 (2002).
- [12] M.F. Islam, E. Rojas, D.M. Berjey, A.T. Johnson, A.G. Yodh, *Nano Lett* **3** 269 (2003).
- [13] K.F. Fu, Y.P.J. Sun, *Nanosci Nanotechnol* **3** 351 (2003)
- [14] Z.H. Chen, X. Du, M.H. Du, C.D. Rancken, H.P. Cheng, A.G. Rinzler, *Nano Lett* **3** 1245 (2003)
- [15] V. Krstic, G.S. Duesberg, J. Muster, M. Burghard, S. Roth, *Chem Mater* **10** 2338 (1998)
- [16] X. Zhao, B.T.T. Chu, B. Ballesteros, W.L. Wang, C. Johnston, J.M. Sykes, P.S. grant, *Nanotech* **20** 065605 (2009)
- [17] Q. Cao, S.H. Hur, Z.T. Zhu, Y.G. Sun, C.J. Wang, M.A. Meilt, M. Shim, J.A. Rogers, *Adv Mater* **18** 304 (2006)
- [18] L. Hu, D.S. Hecht, G.Grüner, *Chem Rev* **110** 5790 (2010)
- [19] B.J.C. Thomas, A.R. Boccaccini, M.S.P. Shaffer, *J Am Ceram Soc* **88** 980 (2005)

- [20] J. Cho, K. Konopka, K. Roźniatowski, E. García-Lecina, M.S.P. Shaffer, A.R. Boccaccini, *Carbon* **47** 58 (2009)
- [21] M.D. Lima, M.J. de Andrade, C.P. Bergmann, S.J. Roth, *J Mater Chem* **18** 776 (2008)

SHAPING OF DIAMONDS IN 1-D NANOSTRUCTURES AND OTHER STRATEGIES FOR FABRICATION OF LOW-DIMENSIONAL DIAMOND-BASED COMPONENTS

Maria Letizia Terranova^{1,3}, Valeria Guglielmotti^{1,3}, Silvia Orlanducci¹, Vito Sessa¹, Emanuela Tamburri¹, Francesco Toschi^{1,3}, and Marco Rossi^{2,3}

¹*Dept. of Chemical Science and Technology and MINIMALab,
University of Rome "Tor Vergata", Roma, Italy*

²*Dept. of Fundamental and Applied Sciences for Engineering and CNIS,
University of Rome "Sapienza", Roma, Italy*

³*NanoShare S.r.l., a startup company for human technologies, www.nanoshare.eu, Roma, Italy*

*E-mail: marialetizia.terranova@roma2.infn.it

ABSTRACT

The shaping of low-dimensional diamond materials into desired geometries, and the correlated required capability to modify and control the topography of diamond-based systems at the nanoscale, are really challenging and complex tasks, of relevant technological interest. Indeed, ordered arrays of diamond nanowires/nanocylinders are required for the fabrication of advanced photonic and electronic devices, such as stable and robust electron emitters (cold cathodes) able to work in different, and also hostile, environments.

In the present paper we describe some recent methodologies settled in our laboratories for the tailoring of diamond 1-D nanostructures.

1. INTRODUCTION

The outstanding properties, both intrinsic or induced, of diamond materials make them ideal candidates to play a major role in advanced electronic and optoelectronic technologies, for fabrication of sensors, multichip modules and emitting or photoemitting systems. For many applications, however, a nanometric control of the morphological features in terms of size, shape and orientation of the diamond units is strongly required.

The objective of our researches is to define methodologies for the tailoring of nanosized diamond materials and their shaping in specific nanoarchitectures. Presently we are developing procedures for the fabrication of elongated diamond 1D structures (nanorods, nanowhiskers, nanopillars, etc) starting from a variety of diamond-based materials.

Two main methodologies are used to achieve the controlled sculpturing of diamond.

The first is a multiscale fabrication process that allows us to produce a variety of self-standing aggregates, up to the mesoscale, with pre-definite shapes starting from colloidal suspensions of ultrananocrystalline diamond powders.

The second process relies on the many new possibilities offered by recent advances in plasma sources and in

particular by the use of a purpose-designed dual-mode MW-RF reactor. The room temperature H-etching processes occurring in the reactor enable the controlled and reproducible fabrication of 1-D nanostructures.

2. EXPERIMENTAL

Surface assisted self-assembling of ultrananocrystalline diamond is obtained starting from colloidal suspension of diamond nanoparticles [1]. For these experiments we use detonation ultrananocrystalline diamond (primary size: 4-5 nm) produced and preliminary de-agglutinated by the Federal Research and Production Center ALTAI (Russia) (Fig.1).

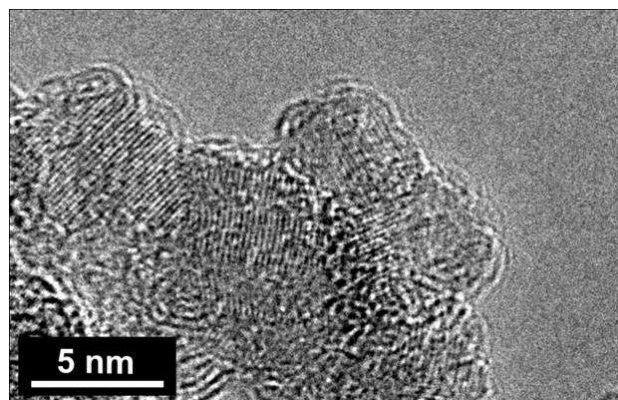


FIGURE 1: HR-TEM image of diamond particles

In our laboratories the received material is further treated following already settled protocols in order to obstruct the re-agglutination processes typical of this class of nanodiamonds. Such nanodiamond assemblies, as well as polycrystalline or B-doped single-crystal diamond plates are used as starting material for the production of diamond nanowires and nanowhiskers. These nanostructures are fabricated by means of the H-induced etching of the diamond phase, accomplished in a Plasma Assisted Chemical Vapour Deposition (PACVD) reactor, where the gas phase is activated by a dual-mode MW/RF plasma.

3. RESULTS AND DISCUSSION

Differently shaped nanodiamond assemblies (segments, slices) can be selectively obtained by a solution phase method using slurries containing different amounts of dispersed nanodiamonds (Fig.2) [2].

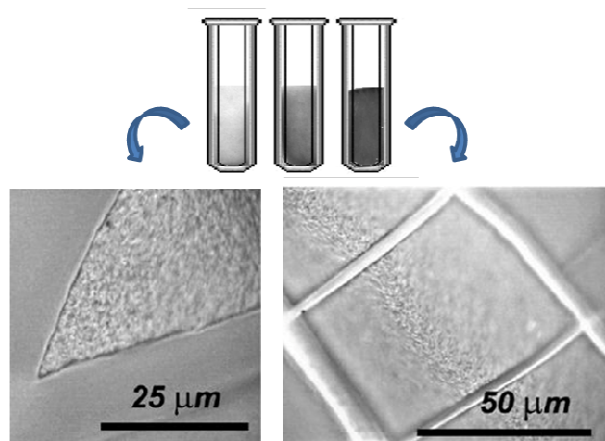


FIGURE 2: Colloidal stable dispersions containing different typologies of nanodiamond particles and self-assembled microstructures obtained from the colloidal suspension.

The nanodiamond assemblies can be also used as templates for diamond growth by CVD. In this case the coating process preserves the architecture of the pristine templates with the formation of a high uniform deposit on all the structures. The coatings are characterized by high phase purity as indicated by Raman and X-ray diffraction characterizations [3].

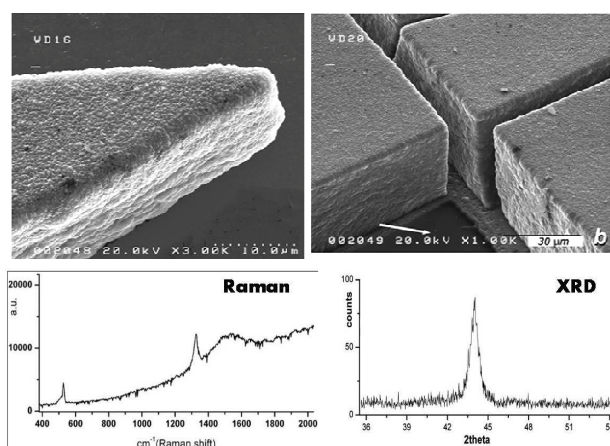


FIGURE 3: FE-SEM images (above) and Raman and X-ray diffraction (below) of CVD diamond films grown on self-assembled 3-D nanodiamond structures

Fig. 4 shows FE-SEM images acquired before and after the etching treatment of such close-packed flat layers. It can be noted as the etching provoked the generation, in the outermost diamond sheets, of a very complex structure shaped like an array of vertically aligned whiskers resulting from the erosion at the nanoscale of the pristine deposit [4].

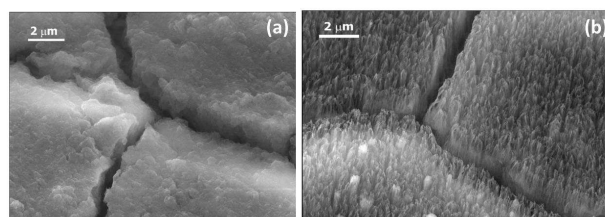


FIGURE 4: FE-SEM images of a self-assembled 3-D nanodiamond structure acquired (a) before and (b) after the etching treatment.

Nanocolumns and nanopillars are instead obtained starting from polycrystalline diamond films prepared by CVD (Fig. 5).

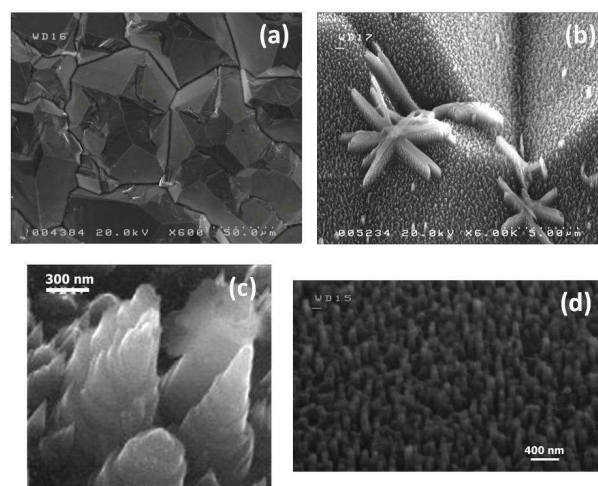


FIGURE 5: FE-SEM images of polycrystalline diamond film acquired (a) before and (b) after the etching treatment; (c) and (d) magnifications of the deposit.

The structural characterizations performed on a series of samples indicate that the etching process induced by H ions does not modify the lattice parameters of the diamond phase, that still retains its outstanding properties (Fig.6) [3].

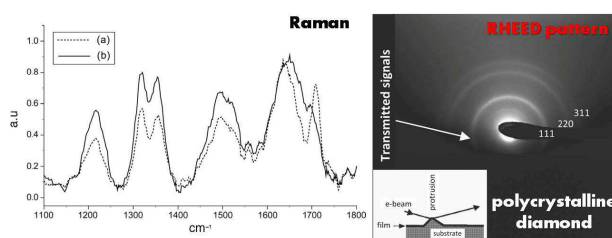


FIGURE 6: Typical Raman spectra and RHEED pattern of diamond systems subject to etching treatments.

It is worthnoting that the I/V measurements of plasma-treated diamond samples evidenced that the H-induced etching process substantially lowersthe resistivity of the material. Moreover, Field Emission measurements indicate that the elongated nanocrystalline diamond deposits are very efficient electron emitters in terms of reproducibility, current stability under medium vacuum and lack of arcing (Fi. 7). These nanostructures are highly

recommended for the assembling of cold cathodes when a material enduring harsh operation conditions is required.

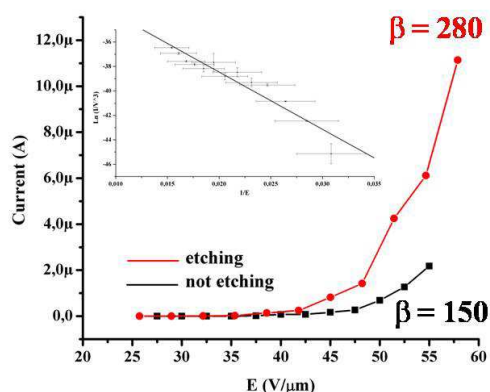


FIGURE 7: Typical I/V data and Fowler-Nordheim plot of the Field Emission characterizations carried out before and after the etching process on a diamond sample.

4. CONCLUSIONS

The entire class of nanosized diamond represents nowadays one of the most promising and exciting field of research, not only for challenging technological applications, but also for investigation of the aggregation/etching mechanisms that lead to specific nanoarchitectures with different dimensionalities.

The room temperature H-etching processes occurring in our MW-RF reactor enable the reproducible fabrication of a series of tailored diamond-based devices, where the location and the shaping of the diamond deposits can be easily controlled.

These low-dimensional diamond structures represent not only a viable alternative for easy and low-cost manufacturing of diamond micro-and nano-components for the next-generation devices, but also for different and advanced applications in the field of bioscience (as biosensing and biolabeling) where inert materials and specifically shaped surfaces are needed.

5. REFERENCES

- [1] V.Y. Dolmatov, *Russian Chemical Reviews* **70** (2011) pp. 607-626
- [2] M.L. Terranova, D. Manno, M. Rossi, A. Serra, E. Filippo, S. Orlanducci, E. Tamburri, *Crystal Growth & Design* **9** (2009) 1245
- [3] M.L. Terranova, S. Orlanducci, E. Tamburri, V. Guglielmotti, F. Toschi, D. Hampai, M. Rossi, *Nanotechnology* **19** (2008) 415601
- [4] S. Orlanducci, F. Toschi, V. Guglielmotti, E. Tamburri, M. L. Terranova, M. Rossi, *Nanosci. Nanotechnol. Lett.* **3** (2011) 83

Self-Assembling of Graphitic Nanoplatelets

R. Matassa^{1*}, S. Orlanducci², V. Guglielmotti², D. Sordi², E. Tamburri², M. L. Terranova²,
D. Passeri¹, and M. Rossi^{1,3}

¹Dept. of Fundamental and Applied Sciences for Engineering,
University of Rome "Sapienza", Via A. Scarpa 16, 00161, Rome, Italy.

²Dept. of Chemical Science and Technology-MINASlab,
University of Rome "Tor Vergata", Via della ricerca scientifica, 00133 Rome, Italy.

³Center for Nanotechnology Applied to Engineering of Sapienza (CNIS),
University of Rome "Sapienza", P.le A.Moro 5, 00185 Rome, Italy.

* E-mail: roberto.matassa@uniroma1.it

ABSTRACT

Low dimensional carbon based materials are strictly dependent from the intrinsic property of self-assembling. Three simple and fast methods to unzip Single Wall Carbon Nanotubes (SWCNTs) have provided different structural organization of graphite layers, observed by electron microscopy investigations. Our structural studies reveal the presence of a deviation from perfect crystal of the graphite aggregations, called turbostratic graphite, because of the presence of rotational and/or translational stacking faults of its hexagonal basal planes. Furthermore, one more different crystallographic phase of graphite with an orthorhombic cell and symmetry Cmma has been experimentally detected by Selected Area Electron Diffraction (SAED) analysis.

INTRODUCTION

Chemical approaches and self-assembling processes may produce graphitic nanostructures with desired shape and dimension for fundamental and practical application. One of the most feasible methods to produce graphitic layered materials is by CNT unzipping, which is a processes intentionally used to control the self-assembling aggregation of nanoribbons graphitized.

The interesting properties of low-dimensional carbon based materials have led to the exploration of numerous applications such as electronic applications due to the potential use that these light, stiff and flexible materials can offer for designing building block components in nanoelectromechanical systems (NEMS). Moreover, there have been numerous investigations on the potential use of such materials as conducting channel in CMOS transistors. Unzipping process of CNTs produces 2D nanostructures, reported in the literature as nanostrips [1], nanoplatelets [2] and also as graphene nanoribbons (GNR) [3], that are of great interest, in particular for the nature of edge dislocations and the appearance of defective dangling bonds in carbon networks. The electronic structure of such nanostructures depends

sensitively on the crystallographic orientation of the edges.

EXPERIMENTAL

The graphitic nanoplatelets were obtained from disruption of Single Wall Carbon Nanotubes (SWCNTs) by using high-shear mixing and/or treatments in sulfonitric mixtures either at room or high temperatures. Depending on the process procedures, different kinds of re-organization are found to occur, as evidenced by

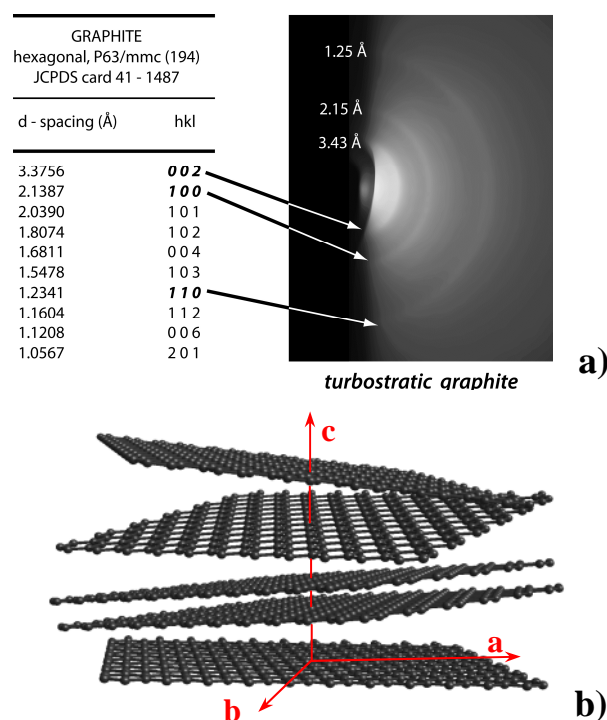


Figure 1. a) crystal structural parameters and experimental diffraction pattern of unzipped SWCNTs graphitized. b) structural model of the graphene planes in a turbostratic stacked arrangement not perfectly oriented along the c-axis.

different and complementary electron diffraction and microscopy techniques.

The adopted disruption methodology allows indeed to obtain samples characterized by very different interactions between proximal units.

Here, we focus our investigation on the structural characterization of self-assembling graphitic layers that it has been and it is a long-standing scientific problem. Unlike crystalline system, where long-range ordering is established by periodic stacking of fundamental building blocks, known as unit cells, rolled open SWCNTs process produces graphitic flakes, having no long-range translational or orientational order, although some degrees of short- and medium-range order do exist. We used transmission electron microscopy (TEM), selected area electron diffraction (SAED), scanning electron microscopy (SEM), and Reflection High Energy Electron Diffraction (RHEED) to image graphitic structures

produced from SWCNTs [4]. The samples were deposited by drop casting on a Si substrate for SEM and RHEED analyses and by dipping, for a very short time, holey carbon grids in the sulfonitric mixture for TEM and SAED analysis.

RESULTS AND DISCUSSIONS

RHEED technique conditions have been used to probe the samples achieved from SWCNTs unzipping by high-shear mixing method (Fig. 1). The electron diffraction pattern (EDP) evidences that the number of rings detected is much lower than the expected for graphite. No diffraction lines were observed from the planes hkl with $l \neq 0$, with the exception of (002) planes having a slightly broadened ring. Diffraction broadening of the (002) ring and absence of the second-order diffraction (004)

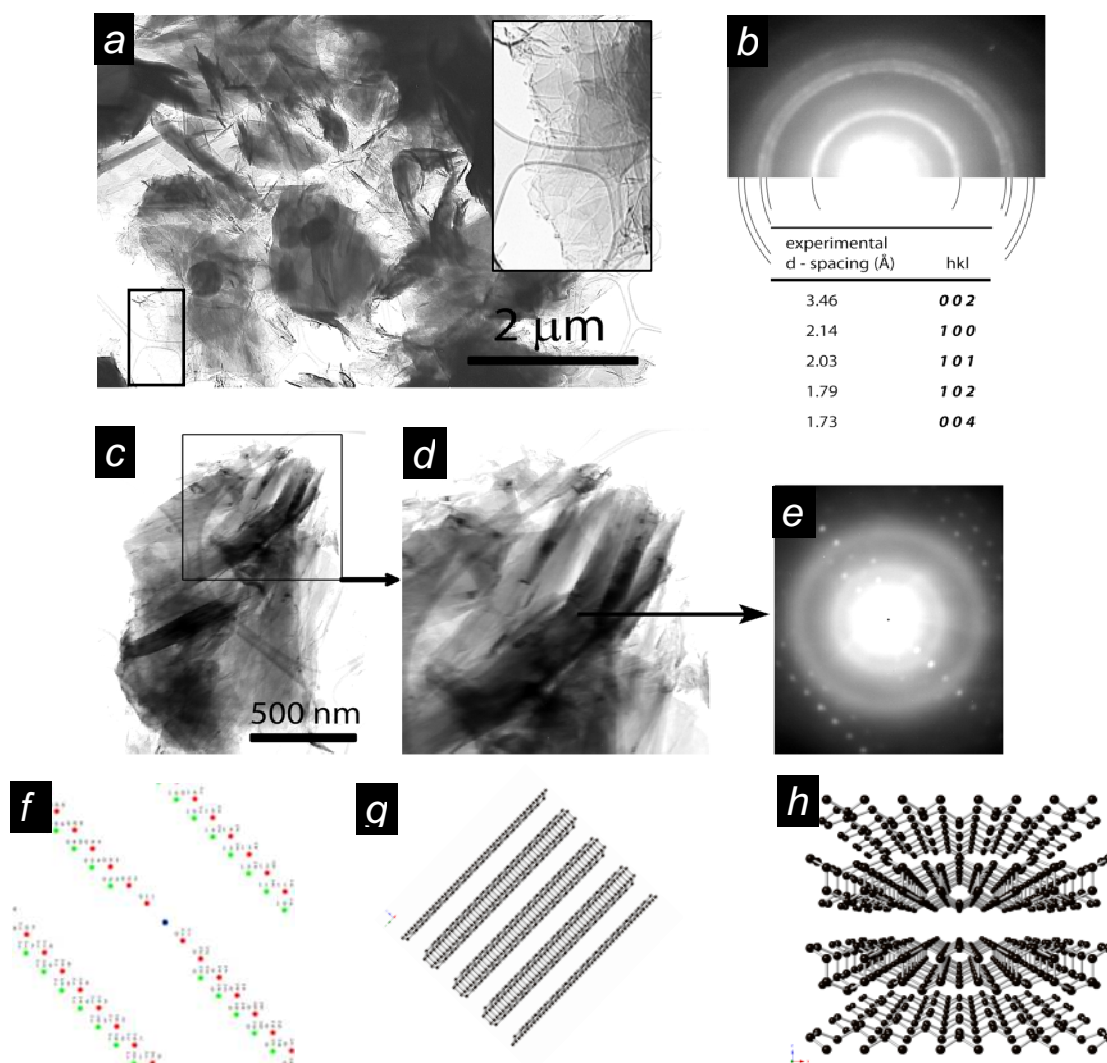


Figure 2.

a) TEM image of unzipped SWCNTs after sulfonitric mixture treatment at room temperature, and b) corresponding ED pattern. c) and d) bright field TEM image of a folding graphene layers. e) electron diffraction pattern taken from image a). f) theoretical electron diffraction pattern into reciprocal space and g) corresponding structural model of orthorhombic graphite with the electron beam along [9-11] zone axis into real space. h) perspective structural model of bilayer graphite stacking along the c crystallographic axis.

graphite ring, let us to consider a loss of periodicity along the c -axis crystallographic direction of the hexagonal lattice (Fig. 1a). The deviations from perfect single crystal is probably conditioned (i) by an interlayers distance not perfectly constant between the hexagonal planes, (ii) by rotational and/or translational stacking faults of the hexagonal basal planes, and (iii) by bending of layers planes.

From the experimental RHEED patterns, the measured interplanar distance of the basal planes has been determined to have a value of about 0.343 ± 0.003 nm. This value is larger than the interplanar distance along the c -axis of the graphite, but it is similar to the disordered form called “turbostratic graphite” [5-7], schematically drawn in Fig. 1b.

SWCNTs sample were rolled open using sulfonitric mixtures at room temperature. TEM bright field image observation shows self-aggregation of graphite nanoribbons with anisotropic bending layers on the edges depending on the extension area of the flakes graphitized (Fig. 2a). Inset exhibits evident boundary lines between nanoribbons of graphite, forming a nano-mosaic arrangement with single pieces of several shapes because of the different etching directions of the unzipped process. Transmission electron microscopy also reveals the formation of high-contrast platelets, probably due to the graphene layers stacking self-aggregation, that can be rationalized in terms of a minimization of the pristine surface energy (Figs. 2c,d).

Mesoscale EDP of these self-assembled platelets, obtained from RHEED analysis, evidences the presence of polycrystalline material with $P63/mmc$ hexagonal symmetry (Fig. 2b). The analysis of the fine structure is characterized by perfect superposition of diffraction spots coming from different crystallites randomly oriented. Since the RHEED resolution in the reciprocal space is better than in the case of SAED method in transmission conditions, accurate observation displayed one more internal weak ring pattern closer to the direct beam. The diffraction ring measures a distance spacing of about 5.65 Å, indicating the existence of anomalous different carbon phase because of the self-assembling evolution of graphite nanoribbons.

Selected Area-ED analysis probed on wrinkles and folded area display evidences of the presence of highly ordered (single-crystal) flakes with a relatively large (some thousands of nm^2) surface (Fig. 2e). Single-crystal, belongs to the diffraction spots pattern, has been characterized by EDP simulation. At the start of this study, we believe a hexagonal superstructure existed in the sample and we tried to determine it according to the EDP. The large discrepancy of the position of the diffraction spots between the experimental and theoretical patterns led us to attempt another phase of graphite with an orthorhombic cell and symmetry $Cmma$ (amcsd 0013979) (Fig. 2f). The ideal crystal-structure, oriented with $[9-11]$ zone axis, has the same lattice parameters (Fig. 2g) proposed by J. Fayos et al. [8], except the c stacking lattice parameter increased of 0.2 Å. Furthermore, this phase of graphite is recognized by the higher intensity peak of the interplanar spacing of $d_{002} = 5.64$ Å, that it has been observed and measured into

previously EDP (Fig. 2b). The crystal packing is constituted of graphite bilayers covalently bounded with the hexagonal benzene deformed into a chair conformational shape and the bilayers are shifted and

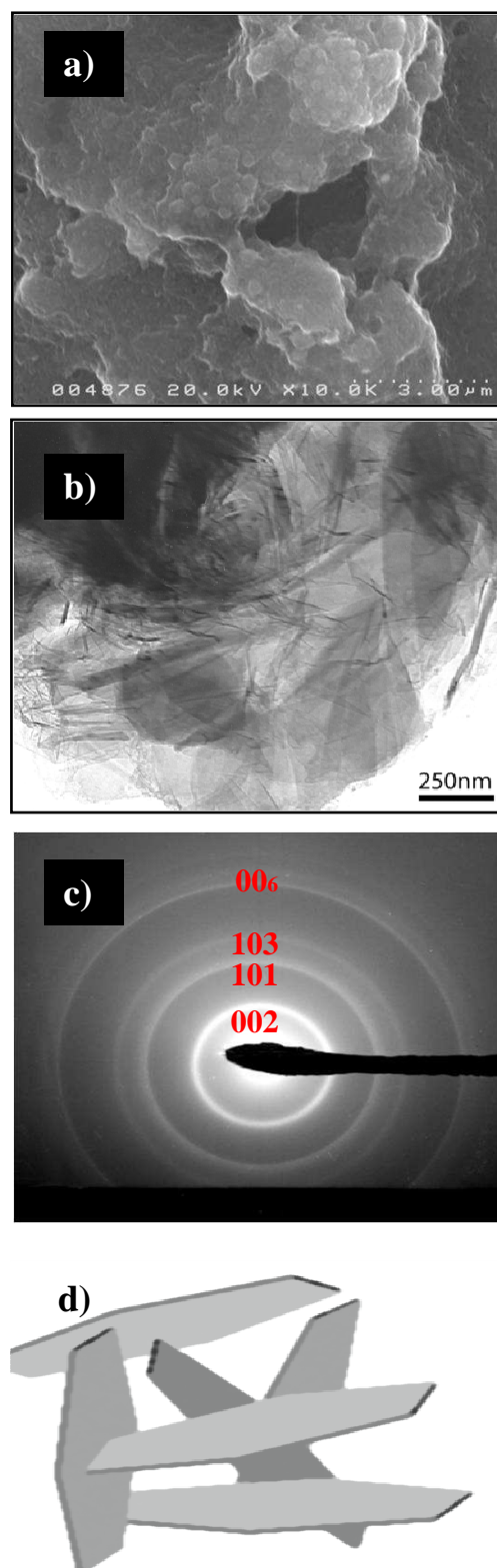


Figure 3.

- a) SEM image of unzipped SWCNTs after sulfonitric mixture treatment at high temperature,
 b) bright field TEM image of a folded graphene layers and multilayer turbostratic graphite.
 c) electron diffraction pattern taken from image a), d) 3D dimensional model of graphite layers randomly orientated.

with an inter-biplanar distances of about 3.20 Å (Fig. 2h). Two experimental broad rings overlapping the single-crystal diffraction spots have an interplanar spacing of a very large distances of $d_{002} \sim 3.42$ Å and of $d_{103} \sim 1.56$ Å, corresponding to the presence of graphite with real missed orientations and increased interplanar distance of the hexagonal graphene layers. In addition, we examined the state of the reassembled unzipped SWCNTs obtained after sulfonitric mixtures treatment with the same above procedures, but at high temperature. SEM studies show compact graphite powder with particles clustered on a roughly surface, without evidence of the typical graphite platelets aggregations (Fig. 3a). TEM analysis probed on a large nano-area shows a high degree of nanotube opening in multilayers nanoribbons and forming graphite platelets turbostratically stacked with several edges scrolled up or folded slightly (Fig. 3b).

The use of thermal treatment in annealing steps show smooth surfaces of graphitic clusters compared to the room temperature treatment. This treatment leads more uniform graphite layers, decreasing the formation/size of wrinkles around the step edges and defect line of graphite nanoribbons and increasing the growth surface of the graphite islands.

Structural characterization has been performed by RHEED analysis on a relatively large thickness of the platelet-clusters. EDP shown in Fig. 3c undoubtedly confirms the presence of polycrystalline graphite, with lattice parameters practically coincident with those ones of 'reference' graphite reported in Fig. 1a. Hypothetical 3D-view of a disordered self-assembling of graphitic nanoribbons is sketched in Fig. 3d.

As a result of the thermal-stress induced process, the bilayer of orthorhombic graphite phases was regarded as a structural phase transition into the classical hexagonal graphite phase, during annealing and recrystallization treatments

Overall, the analysis of the EDPs indicates that the platelets are 'expanded' graphite, with a larger interplanar distance between successive graphene layers and coherent slightly reduced interplanar distances for the transversal planes. It is worth to noticing that the signal of un-processed SWCNTs has not been detected into any electron diffraction pattern collected with the appearances of equatorial oscillation or lines, or short diffraction lines located in the vertical or horizontal direction, or diffraction lines with arc shapes.

In all examined samples we were able to detect the different layer form of conventional graphite and bilayers of orthorhombic graphite. One most important finding is derived from the electron diffraction technique by reflection and transmission methods. The last case study clearly confirms that EDPs are very sensitive to small variations in periodic structure or lattice imperfection and to investigate phase transition phenomena. In order to resolve the fundamental problem of how is thick the bi-dimensional structures, TEM analysis of the flake-edges must be coupled with electron diffraction pattern studies.

The results show that the assembly processes can be tailored by modulating the disruption treatments and choosing a suitable dispersion medium, in order to produce selectively different forms of self-assembling, from polycrystalline aggregates to highly self-oriented mosaic-like structures, evidencing the possibility to achieve single-crystal platelets. It is expected that the identification of cooperative mechanisms acting in such systems could help in opening innovative crystallization pathways and give a relevant contribution for nanotechnologies.

REFERENCES

- [1] S. Wohlthat, J.R. Reimers, and N.S. Hush, *Phys. Rev. B*, 81 (2010) 195125.
- [2] L. Bin, Z. Wei-Hong, *J. Mat. Science* 46 (2011) 5595.
- [3] M. Terrones, *Nature*, 458 (2009) 854.
- [4] M. Rossi, D. Manno, S. Orlanducci, A. Serra, M. L. Terranova, *Electron diffraction analysis of carbon-based nanomaterials*, in *Encyclopedia of Nanoscience and Nanotechnology*, edited by H.S. Nalwa, American Scientific Publisher, 2011, Volume 13, pages 375-425.
- [5] Z.Q. Li, C.J. Lu, Z.P. Xia, Y. Zhou, and Z. Luo, *Carbon* 45 (2007) 1686.
- [6] M. Rossi, M.L. Terranova, S. Piccirillo, V. Sessa, and D. Manno, *Chem. Phys. Lett.* 402 (2005) 340.
- [7] M.L. Terranova, M. Rossi, V. Sessa, and G. Vitali, *Solid State Comm.* 91 (2004) 55.
- [8] J. Fayos, *J. Solid State Chem.*, 148 (1999) 278.

CONCLUSIONS

DEPOSITION OF CARBON NANOWALLS AT THE ELECTRODES DURING ELECTRICAL-FIELD-ASSISTED LASER ABLATION IN WATER

M. Sinatra^{1*}, G.C. Messina¹, P. Russo¹, G. Compagnini¹, O. Puglisi¹, S. Scalese²

¹*Dipartimento di Scienze Chimiche, Università di Catania, Viale A.Doria 6, I-95125 Catania, Italy*

²*CNR-IMM, Strada VIII n.5, I- 95121 Catania, Italy*

*E-mail: sinatramarco@gmail.com

ABSTRACT

Laser ablation in liquid is emerging as a simple and reproducible way to generate a large number of nanometric structures. This method assisted by electric field allows to obtain the deposition of carbon nanostructures at the electrodes during the ablation of carbon target in water. In this work we report the first observation of the germination and growth of carbon nanowalls at the electrode's surface during Electrical-field-assisted Laser Ablation in Liquids (ELAL). The samples were characterized by scanning electron microscopy (SEM), transmission electron microscopy (TEM), Raman spectroscopy and X-Ray photoelectron spectroscopy.

1. INTRODUCTION

The discovery of graphene has stimulated enormous interest on 2D carbon nanostructure in view of their extraordinary properties and potential applications [1]. In this frame, a challenge has always been to identify a high yield production which can give graphene or graphene-like structures without collateral structural damage coupled with the possibility to manipulate the layers, individually or collectively, in order to have a particular arrangement and position for given applications [2].

Alternative to single layer graphenes, the so called carbon nanowalls (CNWs) has been discovered and synthesized by Plasma-Enhanced Chemical Vapour Deposition in a variety of different configurations [3]. They consist of aligned graphene sheets trading on a substrate with large surface areas and sharp edges. The thickness of the CNWs ranges from a few nm to some tens of nm. CNWs are expected to be good catalyst support structures for fuel cells, electron field emitters and negative electrodes for lithium ion batteries. Moreover its has been recently observed that CNWs amplify the signals during surface-enhanced Raman experiments [4] and promise high toxicity against bacteria [5].

So far, research groups have explored different synthesis methods of CNWs essentially based on plasma-enhanced chemical vapour deposition approaches.

Electrical-field-assisted Laser Ablation in Liquids (ELAL) has been recently proposed as a new approach to controllably fabricate oxide micro- and nanoparticles

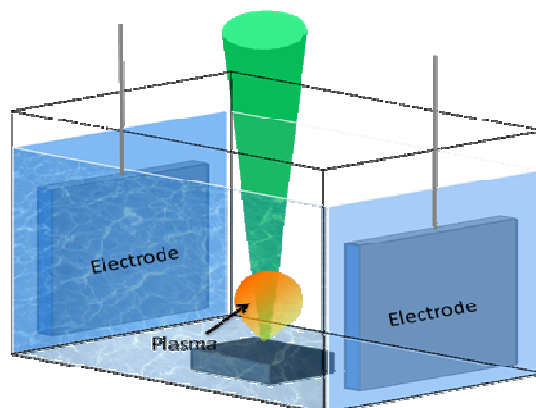


Fig.1 Schematic of experimental setup used to produce CNWs

with various shapes which has been collected from the colloidal suspensions [6].

In this work we demonstrated that during the ELAL process, CNWs are deposited on the electrode's surface. The samples are characterized by scanning electron microscopy (SEM), transmission electron microscopy (TEM), Raman spectroscopy and X-Ray photoelectron spectroscopy.

2. MATERIALS AND METHODS

In our experiments we have used a Nd:YAG laser beam (5 nsec pulse duration, 532 nm radiation wavelength, 10 Hz repetition rate) focused onto a polycrystalline graphite target (5 J/cm²) which has been previously fixed at the bottom of a flask and submerged by a few centimetres of Millipore grade distilled water. Details such a procedure is reported elsewhere [7]. During the ablation two HOPG electrodes have been immersed in the liquid in such a way to face their basal planes (see Fig.1).

The two electrodes have been charged by applying a 30 V potential and, between them, the plume has been left to develop during the ablation.

3. RESULTS AND DISCUSSION

After the synthesis the samples were characterized by SEM and TEM analysis. Fig.2 shows some electron microscopy images (SEM and TEM) taken on the positive electrode, after 20 min. and 2 hours ablation. These images are related to the HOPG surface facing the

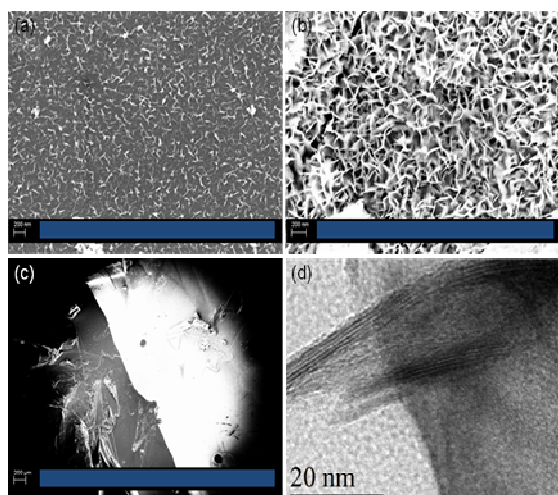


Fig.2 (a) SEM image of CNWs after 20 min. of PLA, (b) SEM image of CNWs after 2 h of PLA, (c) SEM image of the borderline of immersion for the positive electrode, (d) TEM image of CNWs.

ignited plasma plume and reveal that the electrode is uniformly covered by nanowalls (Fig.2a). By increasing the ablation time, the deposit continues to grow. In particular Fig.2b reports the situation after 2 h ablation. The carbon foils, just geminated after 20 min, are now more evident and form a uniform forest on top of the HOPG surfaces. This uniformity has been also evidenced at low magnification in Fig.2c. Here the borderline of immersion for the positive electrode is clearly observed since the bright area represents the CNWs deposit. Finally, Fig.2d displays a high resolution TEM image of the walls showing the stacking of few high quality graphene layers.

The chemical state and the structure of the nano-walls have been investigated by X-ray Photoelectron Spectroscopy (XPS) and Raman spectroscopy. The results are reported in Fig.3.

The C1s and O1s XPS spectra are shown in Fig.3 A and B. Curve fitting of the C1s and O1s spectra was performed using a Gaussian-Lorentzian peak shape after performing a Shirley background correction. The binding energy of the C–C is assigned at 284–284.5 eV and chemical shifts of +1 and +2 are typically assigned to C–OH and C=O functional groups respectively [5]. These data reveals that CNWs are mostly reduced with negligible oxidation. Moreover the analysis of O1s region indicates the presence of adsorbed H₂O, probably trapped inside the walls.

The structure of the deposit is well represented by the Raman spectrum reported in Fig.4 This has been compared with a spectrum on bare HOPG. As already reported by Kurita et al. [8], the Raman spectra of CNWs exhibit G and D bands at 1580 and 1350 cm⁻¹ with a bandwidth relatively narrow, even when the I_D/I_G intensity ratio is significantly high. This feature is distinguished from those of typical graphite like carbons and suggests that the nanowalls are composed of small crystallites with a large degree of graphitization.

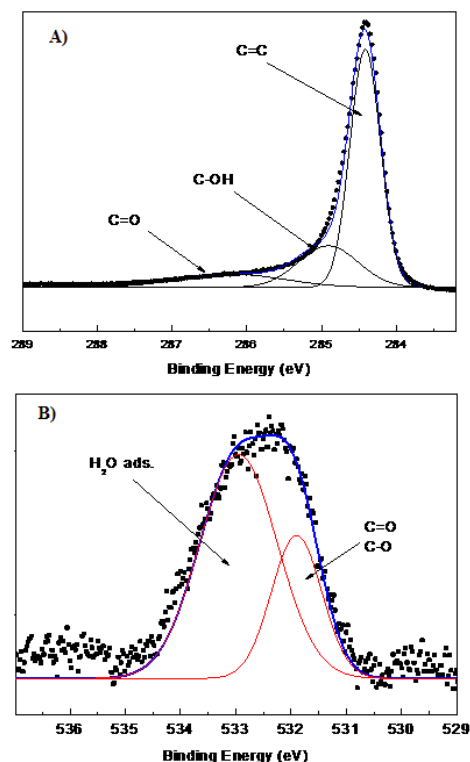


Fig.3 A) C1s XPS spectra obtained on the deposit of the CNWs after 2h of PLA, B) O1s XPS spectra obtained on the deposit of the CNWs after 2h of PLA

3.1 Mechanism of formation

We want now comment on the possible mechanism of formation and deposition of the CNWs in such an electric-field assisted laser ablation in water which can be also useful for general considerations on the growth of CNWs using different deposition methods.

We start considering that the formation of exotic carbon species during the ablation of a graphite target in a liquid environment has been extensively reported by many authors in the last few years.

When the ablation is conducted in water the main species detected are hydrogen capped polyynes [9] while ablation in organic solvents leads also to the observation of polyynes together with polycyclic aromatic hydrocarbons and related structure [10].

As a matter of fact polyyne chains (generally stable only for few hours) are considered as precursors of a large number of carbon nanomaterials such as fullerenes and nanotubes. Moreover it is well known that nanoparticles and nanostructures produced by laser ablation in liquids are electronically charged either because of their generation or because of salvation processes which gives to the particles a certain z-potential [11]. For instance it has been reported that oxidized CNT colloids are negatively charged and are attracted by the positive electrode. It is then plausible that negatively charged polyynes migrate at the anode and start to build up a complex structure such as that observed by electron microscopy.

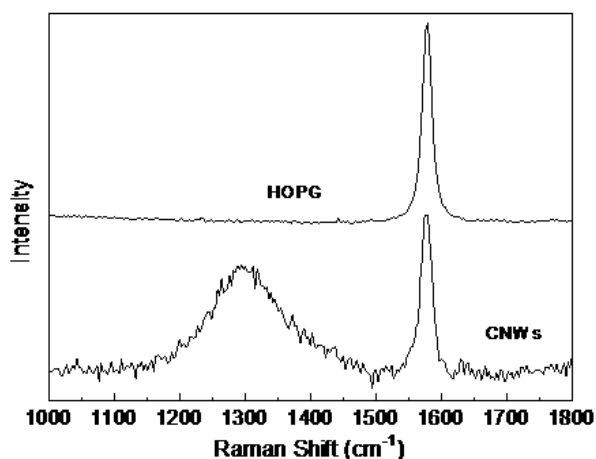


Fig.4 Raman Spectra obtained on the CNWs. The figure also reports the spectra relative to HOPG.

As in the case of nanotubes growth during arc discharge, a key parameter is the presence of an electric field associated to the plasma. This has been widely discussed by Wu et al. [12], following Plasma Enhanced Chemical Vapour Deposition experiments. In those cases the presence of a plasma coupled with a CVD process enables the formation of carbon radicals similar to those which are assumed to initiate the growth of either polyynes and carbon nanotubes during laser ablation and arc discharge experiments [13]. We are actually investigating on the role of the electric field strength and geometry on such a kind of experiments.

4. CONCLUSION

In summary we have combined the production of carbon units at the atomic/molecular level and the transport efficiency typical of electrophoretic experiments in a unique manner in order to obtain CNW material under atmospheric conditions. Here we demonstrate that the exotic carbon species formed during the ablation are able to reach the electrodes and form an uniform foils carpet.

5. REFERENCES

- [1] A.K. Geim, K.S. Novoselov, *Nat Mater*; **6**, 183 (2007).
- [2] G. Compagnini, F. Giannazzo, S. Sonde, V. Raineri, E. Rimini, *Carbon* **47**, 3201 (2009).
- [3] W. Yihong, Y. Bingjun, Z. Baoyu, S. Han, S. Zexiang, F. Yuanping, *J Mater Chem*, **14**, 469 (2004).
- [4] C. Sekhar Rout, A. Kumar, T.S. Fisher, *Nanotech* **22**, 395704 (2011).
- [5] O. Akhavan, E. Ghaderi, *ACS Nano* **4**, 5731 (2010).
- [7] G. Compagnini, A.A. Scalisi, O. Puglisi, C. Spinella, *J Mater Res* **19**, 2795 (2004).
- [8] S. Kurita, A. Yoshimura, H. Kawamoto, T. Uchida, K. Kojima, M. Tachibana, et al., *J Appl Phys* **97**, 104320 (2005).
- [9] G. Compagnini, V. Mita, R.S. Cataliotti, L. D'Urso, O. Puglisi, *Carbon* **45**, 2456 (2007).
- [10] F. Cataldo, *Carbon* **42**, 129 (2004).
- [11] J.P. Sylvestre, A.V. Kabashin, E. Sacher, M. Meunier, J.H.T. Luong, *J am chem soc* **126**, 7176 (2004).

[12] W. Yihong, Y. Bingjun, *Nano lett* **2**, 355 (2002).

[13] V. Scuderi, S. Scalese, S. Bagiante, G. Compagnini, L. D'Urso, V. Privitera, *Carbon* **47**, 2134 (2009).

ORGANIC MOLECULES ENCAPSULATED IN SINGLE WALL CARBON NANOTUBES – CHALLENGES FOR THEORETICAL MODELING

M. Kertesz^{1*}, T. Yumura²

¹ Department of Chemistry, Georgetown University, Washington, DC 20057, USA

² Department of Chemistry and Materials Technology, Kyoto Institute of Technology, Matsugasaki,

Sakyo-ku, Kyoto, 606-8585, Japan

*E-mail: Kertesz@georgetown.edu

ABSTRACT

We review recent computational results on carbon chains and carotene molecules encapsulated in carbon nanotubes and chemically attached molecules to carbon nanotubes. Modeling reproduces relevant resonant Raman frequencies and provide geometric and conformational information on the encapsulates. Chemically attached molecules induce relaxations in the carbon nanotube structure that can be interpreted using Clar VB models. Site preferences for a second chemically attached addend are found.

1. INTRODUCTION

Guest molecules encapsulated in carbon nanotubes and molecules chemically attached to carbon nanotubes display a number of fascinating properties with unique challenges for theoretical modeling. These environments provide unique nano-spaces for the study of molecules and their interactions with nanotubes. The structures of single wall carbon nanotubes (SWCNTs) are well known. The effects of encapsulation range from weak van der Waals (vdW) interactions through small amount of charge transfer (CT) to covalent bond formation between host and guests. The talk provided an overview of quantum mechanical (QM) and combined force field QM computations in modeling these complex systems [1].

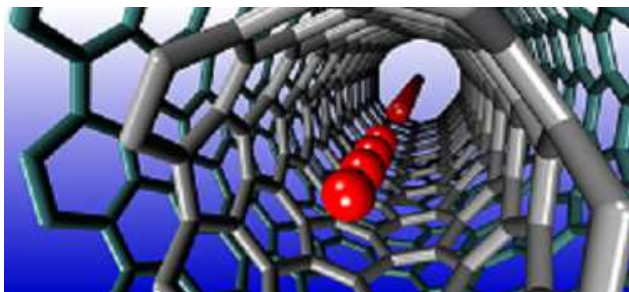


Fig. 1. Illustration of a carbon chain (in red) inside a double wall carbon nanotube. Two segments are shown before they are joined.

Two kinds of problems are reviewed: Guest molecules encapsulated within the nanotubes and molecules attached covalently to the tube. The two problems are sufficiently different to require different approaches.

2. GUEST CHAIN MOLECULES

As guest molecules two kinds were discussed: linear carbon chains and carotene molecules inside carbon nanotubes. The guest carbon chain molecules undergo strong Peierls distortion leading to a large bond length alternation, large band gap, and characteristic Raman bands.[2] Fig. 2. illustrates the Peierls distortion for an infinite linear carbon chain.

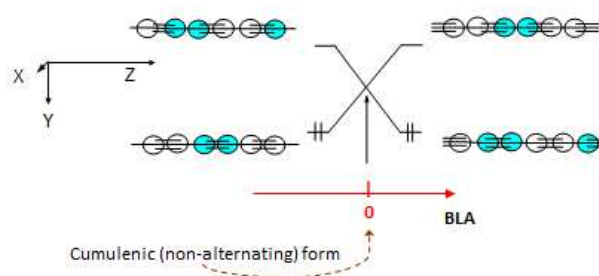


Fig. 2. Schematic illustration of the energy of a linear carbon chain as a function of bond length alternation, BLA. BLA is defined as the difference between the longer (single) and shorter (triple) bonds. The orbitals are also indicated for the distorted (alternating) form. The energy of the highest occupied orbital decreases when $|BLA|$ increases from 0 (the non-alternating form) which drive the Peierls distortion toward an alternating form. The π -orbitals are oriented perpendicular to the chain (Z-) axis leading to a degenerate pair of π -orbitals and π -bands.

Key experimental information on these encapsulated systems comes from high-resolution transmission electron microscopy and resonant Raman spectroscopy.[3] We reviewed the results of recent quantum mechanical (QM) modeling from our laboratory and others on obtaining structural information on carbon chain molecules in SWCNTs. The main conclusion of these modeling studies is that there is a good agreement between the main Raman band frequency and polarization by assuming that the chains are long (>100 carbon atoms) consistent with the HRSTM observations.[3] Also, the main Raman bands are resonantly enhanced at the laser energy is close to the bandgap of the carbon chain. This in turn enforces the consistency of the picture that very long chains are incorporated into the nanotube. Another conclusion relates to the properties of the very long carbon chains

themselves. Long carbon chains assume a bond alternating geometry consistent with the Peierls distortion picture [4]. (Fig. 2.)

The Raman active band around 1850 cm^{-1} could in principle correspond to short carbon chains. However, the investigation of the potential energy surface inside the confined quasi one dimensional spaces of nanotubes shows that aggregation of these chains is highly exothermic proceeding via a barrier that can be overcome at the high temperatures of the synthesis. Fig. 3. shows that aggregation is energetically favorable at all chain lengths considered [4].

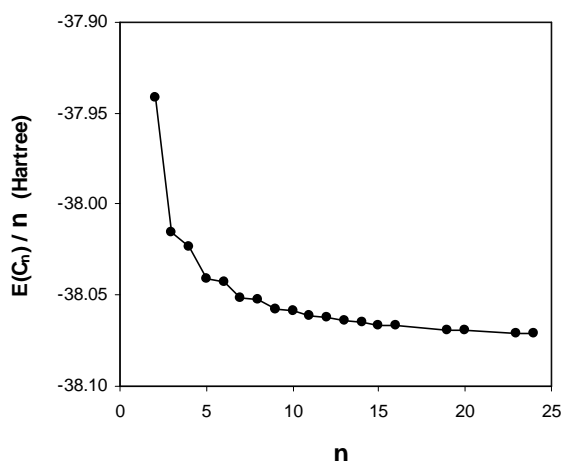


Fig. 3 Calculated total energy per carbon of linear C_n clusters. B3LYP/6-31G*

Second, careful extrapolation of the Raman active optical mode that corresponds to the CC stretching mode that alternates throughout the chain (called also the amplitude mode) has been predicted to occur at $1870\text{--}1877\text{ cm}^{-1}$ [5]. These calculations were based on a special form of force constant scaling and on quantum mechanical calculations at the B3LYP level. This is as good as any vibrational frequency prediction can be done and it is much better than ordinary DFT predictions that cover the following values (name of computer code followed by the DFT employed) (S. Yang, unpublished):

PWSCF (LDA)	1393 cm^{-1}
VASP (LDA)	1422 cm^{-1}
Gaussian 98 (GGA, PBE)	1277 cm^{-1}
PWSCF (GGA, PBE)	1256 cm^{-1}

None of these methods provide anything even close to the experiment. However, based on the $1870\text{--}1877\text{ cm}^{-1}$ frequency values we concluded that the model of alternating long carbon chains inside the nanotube is confirmed by the Raman spectroscopy.

Remaining challenge is to quantitatively interpret the small frequency shifts of this band as it has been observed under different experimental circumstances.[3, 6-8]

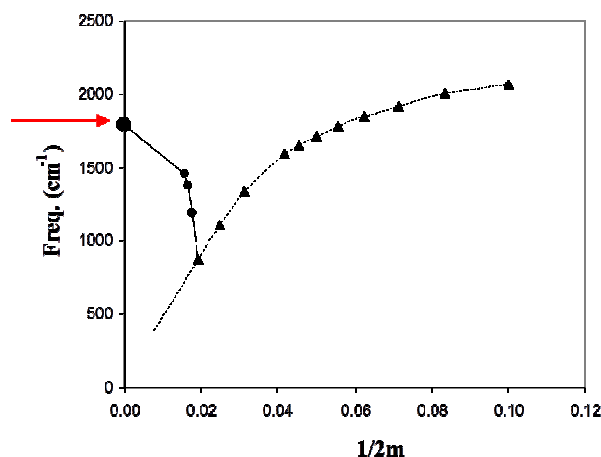


Fig. 3. The longitudinal optical mode frequencies of C_{2m} clusters as a function of $1/2m$ (B3LYP/6-31G*). The lines are to guide the eye. The filled circle on the vertical axis represents the LO mode frequency of infinite polyynic at 1870 cm^{-1} from our scaled calculations. The triangles on the right of the intersecting trends have cumulenic structures (non-alternating or mildly alternating) while the points on the left represent strongly alternating polyynic structures. Arrow indicates the frequency extrapolated to infinite chain length.

Likely these shifts are related to individualities of the encapsulating nanotubes and small charge transfers [5] that occur between the tube and the encapsulate. Fig. 4. illustrates the Raman shifts estimated by periodic commensurate DFT modeling. The red arrow indicates that a downshift of about 40 cm^{-1} is consistent with a charge transfer of only $0.01\text{ e/unit cell} = 0.005\text{ e/carbon atom}$. Such a small charge transfer can be obtained when the tube and chain are treated together [9].

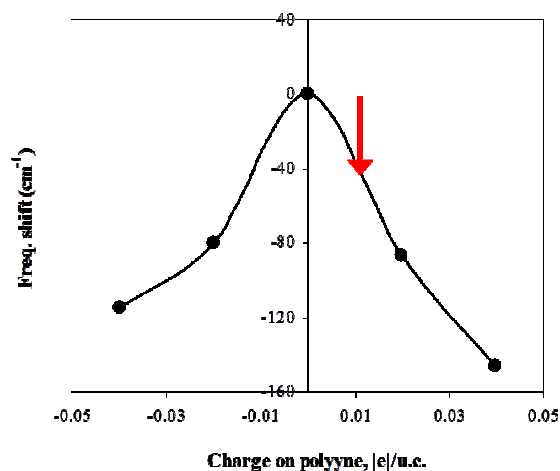


Fig. 4. Raman shift of the optical CC stretching mode in an infinite carbon chain as a function of charge transfer.

Another key argument is that the intensity of the Raman band grows very rapidly as a function of the carbon chain size [9a]. Hence the spectra should be dominated by the long chains even if some shorter chains are present. It is also possible that the finite chains have a somewhat lower frequency than the infinite chains. However, line widths

in the experiments do not indicate a wide distribution [3, 6-8].

A combination of experimental Raman spectroscopy data with force field and QM modeling can unravel the conformation of *carotene molecules* inside carbon nanotubes. [10] The process obtaining this information includes developing two surfaces: one is the potential energy surface of the encapsulate (carotene) and the other is the deviation of the predicted and experimental frequencies as a function of conformation of an isolated carotene molecule [11]. The process of minimization of the latter produced two conformations that are also low energy in terms of the total energy of the system. The success of the modeling indicated that the separate treatment of the vibrational spectra of carotene is justified. Accordingly, the main effect of the encapsulation is to impose a conformation that is not the lowest energy for the isolated carotene. However, when we estimated the van der Waals interaction between the tube and the encapsulate, we found that there is a significant driving force toward the conformations that attach the carotene to the inner wall of the tube. The estimated van der Waals interactions more than compensate for the loss of conformational energy of the encapsulate leading to an overall energy gain of the order of 10 kcal/mol. Thus:

- Conformational information can be obtained for encapsulated molecule using a combination of Raman data and modeling that includes QM and MM elements.
- vdW interactions drive to conformations that are not the lowest energy for the molecule that is not in the constrained environment of the inside of the tube.

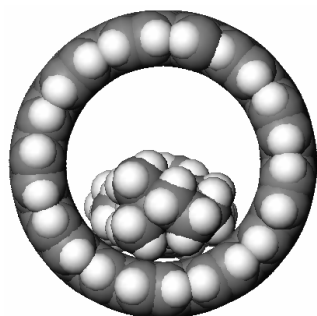


Fig. 5. One of two low energy conformation of a carotene molecule inside a single wall carbon nanotube.

3. CHEMICAL FUNCTIONALIZATION

A variety of SWCT covalent functionalizations were also reviewed: inner (endo-) and outer (exo-) additions, additions into bonds that are at various orientations with respect to the tube axis [12]. A variety of QM methods are being applied in the literature to this problem [1].

Clar valence bond (VB) representations of pristine and functionalized carbon nanotubes can provide useful insights into the substitution patterns and the respective relaxation of the carbon nanotubes. This observation is particularly useful when analyzing the effects and substitutional preferences of multiple substitutions which also show a “collective effect” in the sense that there are preferential locations for a second substitution. Various methodologies have been used by various groups; a statistics of the recent literature [13-24] is presented below [1]. Number of papers in the different overlapping categories are in parentheses:

DFT	(26)	ONIOM	(6)
Periodic	(15)	Clusters	(16)
Periodic and clusters	(3)	Chiralities other than (m,m) or (m,0)	(3)
Semi empirical	(2)	Green function	(2)
Size	30 – 130 carbons		
Substituents	O, CH ₂ , CH ₃ , SiH ₂ , phenyl, C-C ₅₉ , C(NO ₂) ₂ , COOH, CH ₂ N ₂ , NH, CH ₃ , C ₂ H ₄ , C ₃ H ₆ , C ₄ H ₈ , etc.		

These calculations provided a variety of insights into the reactivities of carbon nanotubes. Here we focus on one aspect. Certain reactions lead to the breaking and interruption of the π -conjugated network of the carbon nanotube. Functionalization with carbenes is particularly interesting. The molecular analogy with the substituted 1,6-methano[10]annulenes [25] illustrates the problem, as shown in Fig. 6. Two stable forms exist: the ‘localized’ form with 8 π -electrons and a σ -bond connecting the substitution sites, and an “aromatic” form with 10 π -electrons in which such a connection has been severed. Fig. 6. shows a few substituents and the respective $d_{1,6}$ distances.

Substituted carbon nanotubes display both types of situations according to the quantum mechanical DFT calculations.

The reason that this is important is because in the aromatic form the number of π -electrons remains the same as before the substitution. Consequently, the perturbation relative to the unsubstituted system is less severe. Applying this idea to carbon nanotubes, one expects that the aromatic form retains its high conductivity. This expectation was verified by Marzari et al. in their DFT calculations [17,21].

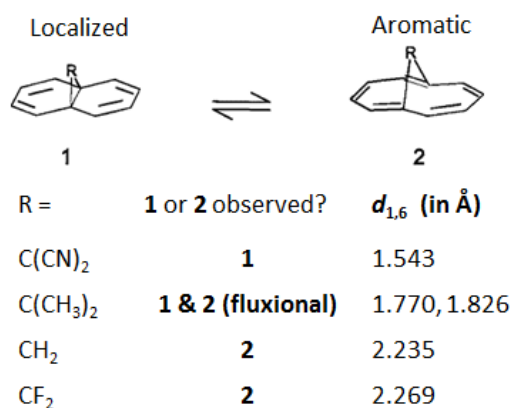


Fig. 6. Selected 1,6-methano[10]annulenes with various substituents and the respective $d_{1,6}$ distances. Short $d_{1,6}$ corresponds structure 1 while long corresponds to 2. An intermediate case designated as “fluxional” exists when the potential energy surface has two nearly equivalent minima.

Considering four cases: endo- and exohedral carbene substitutions and substitutions at bonds that are orthogonal (O) and “slanted” (S) relative to the tube axis for the (5,5) carbon nanotube we found that only the exohedral substitution at an orthogonal site retains then number of π -electrons but break the σ -bond. All others retain the σ -bond at the substitution site and the two π -electrons are used to form the new CC single bonds thereby leading to defect structures that is a strong scattering center for the conduction π -electrons. As the dexterity of experimentalists increases in controlling substitutions of carbon nanotubes, these local defects will likely play an important role in affecting the properties of functionalized nanotubes.

Finally, we discuss a collective effect observed in our DFT modeling of doubly substituted carbon nanotubes. When the separation of the two substituents is large, the stabilization energy is additive: there is no interaction between the two substituents. However, at shorter distances some sites are particularly preferred. Most striking is site S₁ (see Fig. 7.) where the additional stabilization is calculated at 25 kcal/mol [18]. A few other sites, such as O₁, O₂, and O₃ also show extra stabilization but only at about 5 kcal/mol. The interpretation of these results is aided by the use of Clar VB representations. These substitutional preferences have an electronic origin in addition to the trivial effect due to steric crowding [18, 20, 24]. These effects should be exploitable for patterned substitutions.

We thank the U.S. National Science Foundation for its support of this research (Grant CHE-1006702). The work is based on collaborations with Prof. Takashi Yumura (Kyoto TU, Japan), Paul Horn (currently at UC Berkeley,

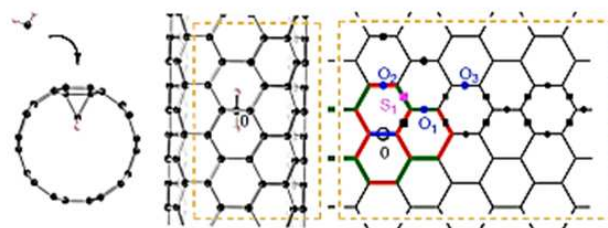


Fig. 7. The addition of a second exohedral carbene to a functionalized carbon nanotube with the first endohedral carbene. The first site is orthogonal (O) to the tube axis. The second substitution occurs at both O and S (slanted) sites.

US), Prof. J. Kurti (Budapest U., Hungary), Dr. S. Yang (Argonne National Lab.), Dr. V. Zolyomi (Lancaster U, UK).

4. REFERENCES

- [1] T. Yumura, M. Kertesz, In: *Practical Aspects of Computational Chemistry: II*, Springer V., Ed. J. Leszczynski, M. K. Shukla (2012).
- [2] A.J. Heeger, *Rev. Mod. Phys.* **60**, 781 (1988).
- [3] X. Zhao et al. *Phys. Rev. Lett.* **90**, 187401 (2003).
- [4] S. Yang, M. Kertesz *J. Phys. Chem. A*, **110**, 9771 (2006).
- [5] S. Yang, M. Kertesz, V. Zolyomi, J. Kurti. *J. Phys. Chem. A.*, **111**, 2434 (2007).
- [6] M. Jinno, et al. *Chem. Phys. Lett.*, **418**, 109, (2006).
- [7] Cazzanelli, E. et al. *Phys. Rev. B*, **75**, 121405 (2007). **2007**: 1850-1860 cm⁻¹.
- [8] Scuderi, V. et al. *Carbon*, **47**, 2134, (2009): 1846 cm⁻¹, 1863 cm⁻¹ and P7 this meeting.
- [9] Á. Ruzsnyák., V. Zolyomi, J. Kurti, S. Yang, M. Kertesz, *Phys. Rev. B*. **72**, Art. nu. 155420 (2005).
- [9a] Yang, S.; Kertesz, M. *J. Phys. Chem. A*. **112**, 146 (2008).
- [10] K. Yanagi, Y. Miyata, H. Kataura, *Adv. Mater.* **18**, 437, (2006).
- [11] P. Horn, M. Kertesz *J. Phys. Chem. C*, **114**, 12139 (2010).
- [12] G.Y. Sun, J. Kurti, M. Kertesz, R.H. Baughman, *J. Phys. Chem. B* **107**, 6924 (2003).
- [13] T. Yumura et al. *J. Phys. Chem. C*, **113**, 14184 (2009).
- [14] T. Yumura, S. Bandow, K. Yoshizawa, S. Iijima, *J. Phys. Chem. B* **108**, 11426 (2004).
- [15] J.J. Zhao, Z.F. Chen, Z. Zhou, H. Park, P.v.R. Schleyer, J.P. Lu, *Chem. Phys. Chem.* **6**, 598 (2005).
- [16] H.F. Bettinger, *Chem Eur. J.* **12**, 4372 (2006).
- [17] S. Lee, N. Marzari, *Phys. Rev. Lett.* **97**, 116801 (2006).
- [18] T. Yumura, M. Kertesz, *Chem. Mater.* **19**, 1028 (2007)
- [19] T. Yumura, M. Kertesz, S. Iijima, *Chem. Phys. Lett.* **444**, 155 (2007).
- [20] J.L. Ormsby, B.T. King, *J. Org. Chem.* **72**, 4035 (2007).
- [21] Y.S. Lee, N. Marzari, *J. Phys. Chem. C*, **112**, 4480 (2008).
- [22] E. Zurek, C.J. Pickard, J. Autschbach, *J. Phys. Chem. C*, **112**, 9267 (2008).
- [23] T. Yumura, M. Kertesz, *J. Phys. Chem. C* **113**, 14184 (2009).
- [24] T. Yumura, *Phys. Chem. Chem. Phys.* **13**, 337 (2011).
- [25] C.H. Choi, M. Kertesz, *J. Phys. Chem. A*, **102**, 3429, (1998).

AB INITIO PREDICTIONS OF COVALENT AND METALLIC INTERCALATIONS OF EPITAXIAL GRAPHENE SYSTEMS ON SiC SUBSTRATES

I. Deretzis^{*}, A. La Magna

CNR-IMM, Z.I. VIII Strada 5, 95121 Catania, Italy

^{*}E-mail: ioannis.deretzis@imm.cnr.it

ABSTRACT

We study within a density functional theory framework the electronic properties of hydrogen, germanium and lithium-intercalated epitaxial graphene systems grown on the (0001) surface of SiC substrates. A particular structural characteristic of all these systems is that when the intercalating element diffuses into the graphene/SiC interface, the first, strongly-bound graphitic layer that grows on the SiC surface gets detached from it, forming a quasi-freestanding graphene film. However, the chemical and electrostatic interactions remain distinct for each intercalating element. Hence, we find that covalently-intercalated epitaxial graphene is subject to a sublattice symmetry-breaking electronic interference that perturbs the Dirac point. Moreover, in terms of effective doping, H-intercalation leaves a neutral interface while the presence of Ge dangling bonds slightly shifts the Fermi level above the Dirac cone. On the other hand, the origin of the high *n*-type doping in the case of Li-intercalation lies in a non-uniform redistribution of Li charges. Results bring to discussion the versatility of substrate engineering in tailoring the physical properties of epitaxial graphene on SiC.

1. INTRODUCTION

During the last years, epitaxial graphene growth on SiC substrates has emerged as one of the principal technologies for a controlled synthesis of high quality graphene films [1], being only limited by the size of the originating SiC wafer. The process is based on the evaporation of the Si surface atoms from SiC by thermal annealing up to temperatures that range within 1200-2000°C. The remaining C surface atoms bind to form energetically favored thin graphite films. By fine tuning the growth parameters (e.g. temperature, pressure, etc.), growth of single graphene layers is possible directly on a semi-insulating substrate. The combination of large scales and high quality, in conjunction with the absence of post-growth material transfer processes make epitaxial graphene an ideal candidate for post-Si carbon-based nanoelectronics.

The electronic and transport properties of epitaxial graphene strongly depend on the polarization of the SiC surface. Hence, Si-face epitaxial graphene is characterized by the formation of a first carbon-rich interface layer (buffer layer) with a $(6\sqrt{3}\times 6\sqrt{3})R30^\circ$ surface reconstruction that acts as a precursor for the

overlying graphene films. The electronic interactions in the interface impose significant electron doping and have a negative influence in the conduction properties of the heterosystem with respect to the SiO₂-deposited case (e.g. in terms of reduced mean-free paths [2]). Typical graphene-like characteristics (e.g. the fractional quantum hall effect) are recovered by the application of a gate voltage that lowers the Fermi level around the Dirac point or by the decoupling of the buffer layer from the substrate via intercalation with functional adatoms [3-5]. On the other hand, electrical measurements of C-face epitaxial graphene films have shown higher mobilities with respect to the (0001) case and the typical half-integer quantum hall effect at low temperatures [6,7]. Ideally, the use of C-face epitaxial graphene for the fabrication of nanodevices could outscore the respective Si-face one [8]. However, growth on the C-face results faster and less controllable than its Si-face counterpart and graphene monolayers are too difficult to be obtained. Hence, Si-face growth acquires a particular importance and a post-processing intercalation treatment with functional elements can partially resolve the problem of the active interface, by means of passivation and detachment of the buffer layer from the substrate. The aim of this extended abstract is to investigate the fundamental structural and electronic properties of H, Li and Ge-intercalated epitaxial graphene structures from a theoretical perspective and discuss the results with respect to recent experimental findings.

2. METHODOLOGY

We perform Density Functional Theory (DFT) calculations using the SIESTA code [9] within the Perdew-Burke-Ernzerhof [10] flavor of the generalized gradient approximation. Structurally, we build a 4H-SiC substrate with four SiC bilayers, passivated with H at the bottom of the slab, over which an ideal graphene layer stands. We choose the computationally affordable $(\sqrt{3}\times\sqrt{3})R30^\circ$ model that can reproduce some basic attributes of the graphene/SiC interface when compared to the actual $(6\sqrt{3}\times 6\sqrt{3})R30^\circ$ reconstruction [11]. We use the following mixed set of basis parameters that fulfill the convergence criterion: a double- ζ (DZ) localized basis set of Sankey-type pseudoatomic orbitals for C and H and a respective double- ζ plus polarization (DZP) set for Si, Ge and Li. We post-process the SIESTA electronic Hamiltonian in order to calculate the single contributions of the localized atomic orbitals in the total band structure of the system. The ionic cores are statically modeled with

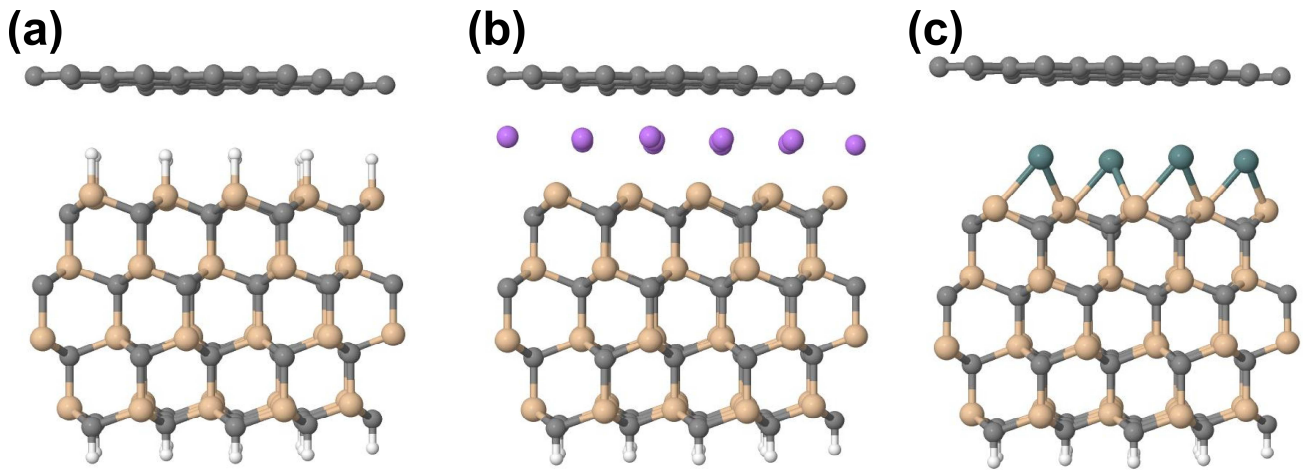


Figure 1: Relaxed intercalated epitaxial graphene structures grown on 4H-SiC(0001) in the case of (a) hydrogen, (b) lithium and (c) germanium intercalation. The minimum energy configuration for the intercalated elements are on top of the Si surface atoms for hydrogen, at the hollow positions of the first SiC bilayer for lithium and at the T4 position for germanium.

norm-conserving Troulier-Martins pseudopotentials [12] that have been tested to reproduce the main band structure properties of SiC and graphene. The electronic density is minimized at momentum space with a $7 \times 7 \times 1$ Monkhorst-Pack grid, while a 400 Ry cutoff energy has been imposed for real-space integrals. Structures relax until forces are less than 0.04 eV/\AA . We model three different systems, i.e. hydrogen, lithium and germanium-intercalated epitaxial graphene considering a full and uniform coverage of the substrate by the intercalated compound in the form of a monolayer.

3. STRUCTURAL AND ELECTRONIC PROPERTIES OF INTERCALATED EPITAXIAL GRAPHENE SYSTEMS

The SiC(0001)- $(\sqrt{3} \times \sqrt{3})R30^\circ$ cell contains three substrate atoms per atomic plain, over which eight graphene atoms are positioned, corresponding to an 8%-stretched (2×2) graphene supercell. In an absence of an intercalated element, structural relaxation gives rise to a zero-order buffer layer, whose properties have been extensively studied in the literature [11]. Hydrogen has been the first element experimentally used to passivate this interface. Here, we model H-intercalated epitaxial graphene with a geometrical configuration that assigns a single H atom on top of each Si atom of the substrate's surface. This geometry gives rise to the calculated minimum energy configuration and has been experimentally confirmed by infrared absorption spectroscopy [2]. Upon relaxation, H atoms covalently bind with the interface Si atoms and restore the ideal sp^3 hybridization of the substrate. As a result, the structurally disordered buffer layer turns into a flat graphene sheet with a distance of 2.39 \AA from the H-interface layer and 3.92 \AA from the substrate Si atoms [Fig. 1(a)]. The electronic band structure of this system shows the (2×2) folded graphene bands and confirms the minimal interaction with the SiC substrate [Fig. 2(a)]. However a small perturbation appears at the Dirac point that opens a small band gap. It is interesting to discuss the origin of this interference: it can be attributed to a

sublattice symmetry breaking effect due to a non-uniform coupling with the substrate and, in this case, it is an artifact of the small computational cell. In fact, calculations in intercalated systems (in contrast with non-intercalated ones where the manifestation of this effect is stronger) have shown that these gaps tend to disappear with the use of larger cells and are not to be measured in experimental conditions [13]. A further orbital-resolved analysis of the electronic structure shows that the Dirac point lies $\sim 0.3 \text{ eV}$ above the valence band of the SiC substrate. The designation of the charge neutrality point of the intercalated system falls exactly on the position of the Dirac cone and shows that H-intercalated graphene should be ideally neutral.

We thereon model Li-intercalated epitaxial graphene systems, considering a similar to hydrogen complete coverage of the SiC substrate (i.e. an 1 monolayer (ML) coverage). Structurally, also in this case the buffer layer relaxes into a flat graphene sheet with a vertical distance of 2.37 \AA from the Li-adlayer and 4.41 \AA from the Si atoms of the substrate [Fig. 1(b)]. However, as a first difference with respect to the hydrogen case, we find that the minimum-energy configuration for the relaxation of Li atoms is at the hollow positions of the first substrate bilayer, confirming the prevalence of metallic-type bonds between the Li adatoms and the substrate.

The electronic band structure obtained by this system [Fig. 2(b)] shows some highly-concentrated bands throughout the hole region of the spectrum that are difficult to interpret. In this sense an orbital-resolved analysis is necessary for the determination of the local contributions in the total electronic structure. Considering therefore the contribution of the $2p_z$ orbitals originating from the graphene layer, we obtain a band structure that is equal to that of ideal graphene for a large energy range around the Dirac point. This result denotes that the detachment from the substrate also in the case of Li-intercalation is almost complete, while unlike the H-intercalated case we do not obtain any interference at the Dirac point due to a better screening of the substrate from the Li cores. The important aspect though is that the graphene sheet is highly electron-doped for $\sim 1.3 \text{ eV}$,

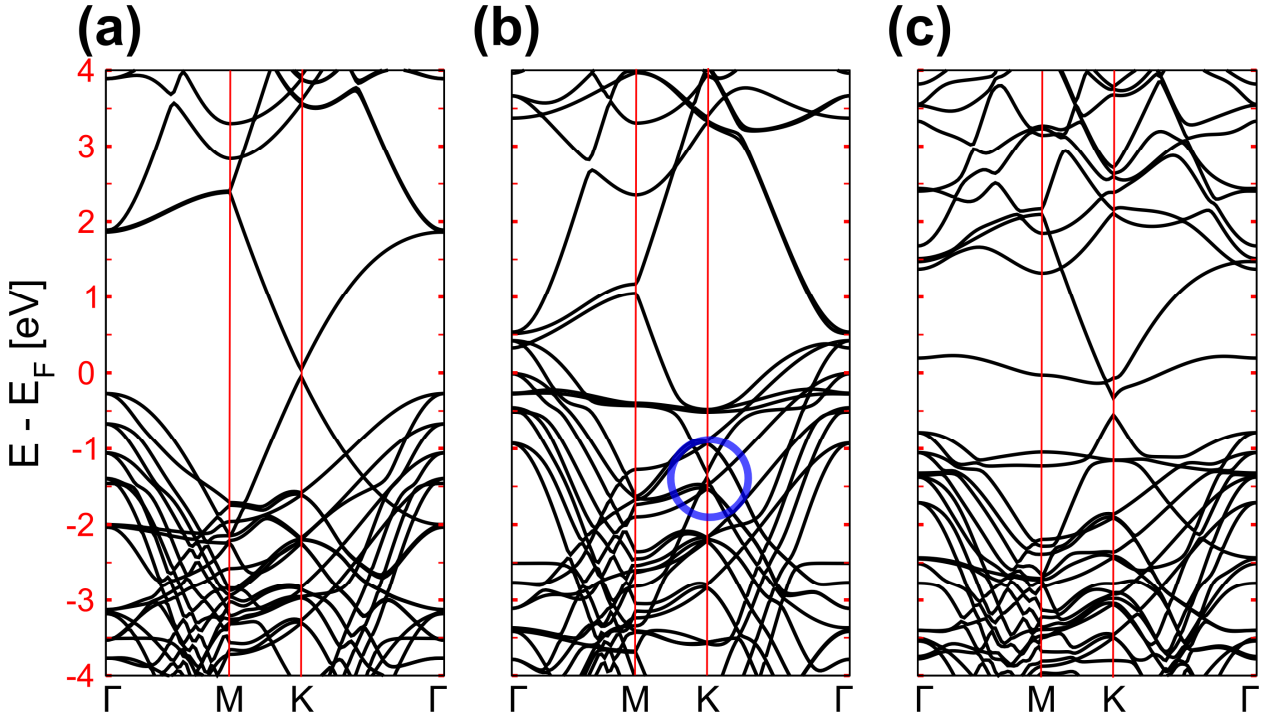


Figure 2: Electronic band structure of the intercalated 4H-SiC epitaxial graphene system in the case of (a) hydrogen, (b) lithium and (c) germanium intercalation. The blue circle indicates the position of the Dirac cone in the case of lithium intercalation.

resulting in a good agreement between theory and experiment also in this case (see the angle-resolved photoemission measurements of Ref. [4]). The origin of such high effective doping lies in the delocalization of the valence electrons of the Li atoms towards the substrate. A careful analysis of the difference in the pseudoatomic charge density $\Delta\rho$ shows that an important increase of the electronic charge takes place between the first bilayer of the SiC substrate and the Li adlayer, originating from the positions of the Li ionic cores. This non-uniform charge redistribution gives rise to a shift of the graphene bands within the valence band region of the SiC substrate, making the whole system electrically active at the vicinity of the Dirac point.

Finally, we also model Ge-intercalated epitaxial graphene [14]. In the simplest case of Ge chemisorption, a single Ge adatom occupies one of the high-symmetry positions of the SiC(0001) surface (corresponding to an 1/3 ML of coverage). Simulations have shown that out of all high-symmetry surface positions, the T4 configuration is the most stable one, having a 0.38 eV lower energy with respect to the H3 case. The top position results energetically unfavorable. In both T4 and H3 positions the Ge atom maintains a pure sp^3 -hybridization and passivates all three surface Si dangling bonds [Fig. 1(c)]. Considering that the energy offered to the system upon annealing (from ~ 600 - 920°C) can break transition barriers between T4 and H3 sites, we have studied both cases, noticing that the qualitative features of the two reconstructions hardly change. From now on discussion focuses on the T4 results. Upon relaxation, geometrically the graphene layer gets detached from the substrate and recovers planarity, maintaining a 3.45 \AA distance from the

Ge-adlayer and 5.38 \AA from the Si surface atoms. It has to be noted here that Ge intercalation gives rise to the biggest vertical distance between graphene and the substrate with respect to the previously studied elements. Detachment is also electronic, as the charge density is almost zero at the Ge-adlayer/graphene interface. Here, The system prefers to maintain a Ge dangling bond perpendicular to the graphene plain rather than form Ge-graphene bonds. This aspect reflects the weakness of the Ge-C bond with respect to the C-C one and indicates that the energy loss in the case of the breaking of the sp^2 planarity of the graphene sheet is higher than the gain from the formation of a covalent Ge-C bond. The adsorption energy of graphene on the Ge-covered SiC surface is only 19meV per C atom, justifying the term “quasi-freestanding”. The band structure of the system is characterized by the presence of the typical Dirac cone which lies within the SiC bandgap [Fig. 2(c)]. Interestingly though, the system is electron-doped with the Fermi level lying $\sim 0.2 \text{ eV}$ above the Dirac point, in good agreement with the experiment [5]. The orbital-resolved analysis here shows that this doping is the outcome of a Fermi level pinning effect by the Ge dangling-bond states (with a prevalent contribution of the Ge- $4p_z$ pseudoatomic orbitals) that give rise to the quasi-flat band that disperses around the Fermi level [Fig. 2(c)]. A last issue that has a purely computational origin is the presence of a secondary band gap between the π and π^* graphene bands, similarly to the H-intercalated case. Also in this case, the increase of the computational supercell is expected to average out the electrostatic differences induced by the substrate on the two interpenetrating graphene sublattices and minimize this gap [13].

4. CONCLUSIONS

In this extended abstract we have presented within a DFT framework the electronic structure properties of the H/Li/Ge-intercalated interfaces between graphene and the Si-face of SiC. We saw that although in all three heterostructures the first strongly-bound carbon-rich buffer layer is detached from the substrate, different electronic properties distinguish each system: in the case of covalent intercalations (with H or Ge) we observed a minimal perturbation at the Dirac point as a consequence of substrate-induced sublattice symmetry-breaking interference. In terms of doping, H-intercalation was the only one to leave the graphene sheet undoped. Ge-intercalation gave rise to a moderate electron-doping due to the presence of Ge dangling-bond states at the interface and a respective Fermi-level-pinning effect. Contrary, in the case of Li-intercalation we obtained a highly *n*-doped ideal graphene band structure, as a consequence of a non-uniform charge redistribution. A critical comparison between these three examples unfolds the potentiality of substrate engineering in epitaxial graphene structures. Intercalation processes are complex and a number of parameters (e.g. annealing temperature, presence of terraces on the SiC surface, etc.) could influence the time evolution and uniformity of the various growth stages. Towards this direction important effort has to be dedicated on the process-based simulation, which in conjunction with the total energy electronic and quantum transport part could provide a better insight on the physical properties of these chemically modified materials.

REFERENCES

- [1] C. Dimitrakopoulos *et al.*, *J. Vac. Sci. Technol. B* **28**, 985 (2010)
- [2] F. Speck, J. Jobst, F. Fromm, M. Ostler, D. Waldmann, M. Hundhausen, H. B. Weber, and T. Seyller, *Appl. Phys. Lett.* **99**, 122106 (2011).
- [3] C. Riedl, C. Coletti, T. Iwasaki, A. A. Zakharov, and U. Starke, *Phys. Rev. Lett.* **103**, 246804 (2009)
- [4] C. Virojanadara, S. Watcharinyanon, A. A. Zakharov, and L. I. Johansson, *Phys. Rev. B* **82**, 205402 (2010)
- [5] K. V. Emtsev, A. A. Zakharov, C. Coletti, S. Forti, and U. Starke, *Phys. Rev. B* **84**, 125423 (2011)
- [6] X. Wu, Y. Hu, M. Ruan, N. K. Madiomanana, J. Hankinson, M. Sprinkle, C. Berger, and W. A. de Heer, *Appl. Phys. Lett.* **95**, 223108 (2009)
- [7] N. Camara, B. Jouault, A. Caboni, B. Jabakhanji, W. Desrat, E. Pausas, C. Consejo, N. Mestres, P. Godignon, and J. Camassel, *Appl. Phys. Lett.* **97**, 093107 (2010)
- [8] I. Deretzis and A. La Magna, *Appl. Phys. Lett.* **98**, 023113 (2011)
- [9] J. M. Soler, E. Artacho, J. D. Gale, A. García, J. Junquera, P. Ordejón, and D. Sánchez-Portal, *J. Phys. Condens. Matter* **14**, 2745 (2002)
- [10] J. P. Perdew, K. Burke, and M. Ernzerhof, *Phys. Rev. Lett.* **77**, 3865 (1996)
- [11] I. Deretzis and A. La Magna, *Appl. Phys. Lett.* **95**, 063111 (2009)
- [12] N. Troullier and J. L. Martins, *Phys. Rev. B* **43**, 1993 (1991)
- [13] I. Deretzis and A. La Magna, *Phys. Rev. B* **84**, 235426 (2011)
- [14] I. Deretzis and A. La Magna, *Appl. Phys. Express* **4**, 125101 (2011)

Appendix 1: Information about the location

The second edition of the Workshop on Carbon-based low-dimensional Materials was held on December 5-7, 2011 in Catania (Italy), in the picture gallery (“Pinacoteca”) of the Diocesan Museum of Catania, situated in the ancient seminar (“Seminario dei Chierici”) of the Cathedral, in the heart of the old town.

Catania, with its 350,000 inhabitants, is the second largest city of Sicily, situated on the east coast of the Island and overshadowed by the Etna Mount, the biggest European volcano still active today, which Catania is 28 Km away from. Typical of the province of Catania is the Timpa, a stretch of coast constituted by lavic cliffs between Catania and Riposto, that offers you a beautiful view. The 17th century was particularly catastrophic for Catania. First (1669), following Etna’s eruption, a devastating lava river flowed into the city; few decades later (1693), an earthquake razed it to the ground. It followed a sumptuous reconstruction, the main protagonist being the architect Giovanni Battista Vaccarini (1702-1768) who designed the most prestigious buildings. The baroque covered nearly every ruined specimen of the past ages, that is hidden, with the exception of few remnants – below the new buildings and the city heart.

Catania is among Italian hottest cities with a summer temperature that can exceed 40° C. For general sightseeing, the periods October through December and March through June are recommended. Winter is a good time to come to Sicily if the focus of your visit is history and culture and you want to avoid the crowds.



Fig.1: Map of Sicily



Fig.2: Entrance of Museo Diocesano, location of the Workshop

CARBOMAT2011

WORKSHOP ON CARBON-BASED LOW DIMENSIONAL MATERIALS

December 5th-7th 2011 Catania (Italy)

PURPOSE

This Workshop aims to bring together researchers coming from multidisciplinary areas (physicists, chemists, biologists, engineers) and having complementary skills in order to present, from different points of view, state-of-the-art research findings in the field of nano-sized carbon based materials (nanotubes, fullerenes, linear chains, graphene, etc.). The unique and tunable properties of carbon-based nanomaterials allow the development of new technologies in a broad range of applications: nanoelectronics, environmental and biological sensors, renewable energy technologies, antimicrobial agents, membranes, and so on. For all these kinds of applications, a key role is played by the interactions between C nano-materials and a suite of elements, chemical groups, metals, antibodies, DNA molecules, enzymes, etc.

The main topics of the Workshop are: synthetic functionalization, characterization, theoretical modelling and applications of low-dimensional carbon structures. Moreover, in this edition, a special session will be focused on the interactions of carbon nanostructures with chemical groups and functional molecules, and to the use of such systems for innovative sensors.

IMPORTANT DATES

Call for papers: **July 14th, 2011**

Short abstract submission deadline: **July 15th, 2011**

Notice of abstract acceptance: **July 30th, 2011**

Final program: **September 16th, 2011**

Deadline for early registration (reduced fee): **September 20, 2011**

Extended-abstract submission deadline: **December 7th, 2011**

TOPICS

- Nanotubes, fullerenes, linear chains, graphene...
- Synthesis and characterization
- Interactions with chemical groups and functional molecules
- Theoretical modelling
- Sensors based on carbon nanostructures
- Other Applications (nanoelectronics, photovoltaic, ...)

CHAIRS

Silvia Iudice
Antonio La Magna

SCIENTIFIC COMMITTEE

Giuseppe Augello (ISI-CR)
Giuseppe Caporaso (ISI-CR)
Isabella DeVinna (CRN-ISM)
Filippo Giannini (CRN-ISM)
Antonio La Magna (CRN-ISM)
Giovanni Mei (ISI-ME)
Silvia Iudice (CRN-ISM)
Verena Stodter (CRN-ISM)

ORGANIZING COMMITTEE

Marta Italia
Giordana Leanza
Antonio Marino
Aldo Iannace

LOCATION

Diocesan Museum
P.zza Duomo - Via Etna 8
95124 Catania

SPONSORS

ADCA
ASSING
SIGMA-ALDRICH

National Research Council of Italy



Fig.3: Flyer of the Workshop

Appendix 2: List of Participants

Aloisio Davide - *University of Messina (Italy)*
Angilella Giuseppe - *Università di Catania (Italy)*
Brancato Vincenza - *University of Messina (Italy)*
Cadelano Emiliano - *CNR-IOM SLACS, Cagliari (Italy)*
Calogero Giuseppe - *CNR-IPCF, Messina (Italy)*
Campbell Eleanor - *Edinburgh University (UK)*
Casartelli Marina - *Università di Milano (Italy)*
Cataldo Franco - *Actinium Chem. Res. srl, Roma (Italy)*
Compagnini Giuseppe - *Università di Catania (Italy)*
D'Agata Salvatore - *Università di Catania (Italy)*
Deretzis Ioannis - *CNR-IMM Catania (Italy)*
Di Grazia Francesco - *CNR-IMM Catania (Italy)*
Donato Andrea - *Univ. "Mediterranea" di Reggio Calabria (Italy)*
Donato Maria Grazia - *CNR-IPCF Messina (Italy)*
Donato Nicola - *University of Messina (Italy)*
Faggio Giuliana - *Univ. "Mediterranea" of Reggio Calabria (Italy)*
Falko Vladimir - *Lancaster University (UK)*
Fazio Enza - *University of Messina (Italy)*
Forte Giuseppe - *Università di Catania (Italy)*
Frontera Patrizia - *Univ. "Mediterranea" di Reggio Calabria (Italy)*
Garofalo Ettore – *ASSING S.p.A (Italy)*
Giannazzo Filippo - *CNR-IMM Catania (Italy)*
Giordano Michele - *IMCB-CNR Portici (NA), Italy*
Giuffrida Manuela - *Sigma-Aldrich (Italy)*
Italia Markus - *CNR-IMM Catania (Italy)*
Karamitaheri Hossein - *Sharif Univ. of Technol., Tehran (Iran) & TU Wien (Austria)*
Kertesz Miklos - *Georgetown University (USA)*
La Magna Antonino - *CNR-IMM Catania (Italy)*
Lamedica Giulio – *ASSING S.p.A (Italy)*
Latino Mariangela - *Univ. Messina & Univ. "Tor Vergata" Roma (Italy)*
Lazzeri Michele - *IMPMC Paris (France)*
Leanza Giovanna - *CNR-IMM Catania (Italy)*

Marino Antonio - *CNR-IMM Catania (Italy)*
Matassa Roberto - *Univ. "La Sapienza" Roma (Italy)*
Messina Giacomo - *Univ. "Mediterranea" di Reggio Calabria (Italy)*
Milone Candida - *University of Messina (Italy)*
Morandi Vittorio - *CNR-IMM Bologna (Italy)*
Neri Giovanni - *University of Messina (Italy)*
Ortolani Luca - *CNR-IMM Bologna (Italy)*
Ottaviano Luca - *Università dell'Aquila (Italy)*
Patti Emilio - *University of Messina (Italy)*
Pellegrino Francesco M. D. - *Università di Catania (Italy)*
Penza Michele - *ENEA Brindisi (Italy)*
Piperopoulos Elpida - *University of Messina (Italy)*
Pistone Alessandro - *University of Messina (Italy)*
Prato Maurizio – *Università di Trieste (Italy)*
Ravesi Sebastiano - *ST Microelectronics Catania (Italy)*
Rizzoli Rita - *CNR-IMM Bologna (Italy)*
Russo Paola - *Università di Catania (Italy)*
Santangelo Saveria - *Univ. "Mediterranea" di Reggio Calabria (Italy)*
Scalese Silvia - *CNR-IMM Catania (Italy)*
Scolaro Giuseppe - *University of Messina (Italy)*
Scuderi Viviana - *CNR-IMM Catania (Italy)*
Shahul Hameed Abdul Rahim - *University of Messina (Italy)*
Shizuya Ken-ichi - *Kyoto University (Japan)*
Sinatra Marco Giovanni - *Università di Catania (Italy)*
Spada Aldo – *CNR-IMM Catania (Italy)*
Spadaro Donatella - *University of Messina (Italy)*
Spartà Noemi - *ST Microelectronics Catania (Italy)*
Trocino Stefano - *Univ. "Mediterranea" di Reggio Calabria (Italy)*
Veronese Giulio Paolo - *CNR-IMM Bologna (Italy)*
Zara Fabio - *ST Microelectronics Catania (Italy)*

Furthermore, we were very happy to host several students from *Università di Catania* and *Università di Messina*, who attended the Workshop with great enthusiasm:

Agati Marta (Catania)
Buscema Marzia (Catania)
Cacciato Giuseppe (Catania)
Carnemolla Enrico (Catania)
Caruso Giuseppe Mario (Catania)
Cocina Federica (Catania)
Cusumano Davide (Catania)
Di Geronimo Giulia (Catania)
Di Prima Giorgia (Catania)
Ferro Valentina (Catania)
Fioravanti Valeria (Catania)
Gentile Antonio (Messina)
Licciardello Salvatore (Catania)
Lo Faro Maria Josè (Catania)
Longo Graziella (Catania)
Malara Angela (Messina)
Mantarro Carmelo (Messina)
Raciti Rosario (Catania)
Scarangella Adriana (Catania)
Torrìsi Giacomo (Catania)
Tripodi Lisa (Catania)
Ventura Luigi (Catania)
Francesco Venuti (Messina)